An investigation on thermal performance characteristics of hollow-core vacuum insulated panels

Mauricio Aguilar Cardenas

Supervisors: Christopher Kendrick, Shahaboddin Resalati, Martin Heywood

A thesis presented in partial fulfillment for the degree of

Doctor of Philosophy

School of Architecture

Faculty of Technology, Design and Environment

Oxford Brookes University

April, 2020

Abstract

As concerns over climate change stimulate legislation for performance improvement in the building industry, in an effort to mitigate embodied and operational carbon footprint, high performance insulating solutions are gaining attention and invite further research in this area. Hollow-core VIPs are an alternative vacuum insulating technology that can provide thin insulating cladding solutions while avoiding some vulnerabilities of high performance insulating materials such as fumed silica VIPs.

This thesis aims to develop and evaluate the performance of a conceptual prototype of hollow-core VIPs. Initial simulations of a simplified model were used to evaluate desirable values for main parameters such as emissivity and panel thickness. Desirable panel thickness lies between 20 and 50mm to eliminate convection at a pressure of 0.01 Pa and emissivity lower than 0.1 is necessary to stifle radiation. A more detailed model representing a node within a full size VIP was developed and tested in a vacuum chamber and compared to transient simulations to study its thermal performance. Nodes with three structural array configurations were manufactured from stainless steel, PTFE and epoxy resin to analyse performance in different panel thicknesses (25 and 50mm) and with different internal surface emissivity.

Low emissivity configurations indicate thermal resistance over 4.2 $\frac{m^2K}{W}$ in the centre of sample for 50 mm thick panels with PTFE structural elements. The same configuration with high emissivity resulted in a thermal resistance of 0.25 $\frac{m^2K}{W}$. Further analysis was conducted to define panel dimensions in function of thermal conductance limits and structural integrity to provide design constraints on

the design parameters of hollow-core VIPs. PTFE structures were limited by their mechanical properties and were found incapable of achieving a thermal conductance of 0.1 $\frac{W}{m^2K}$. However, an internal array made from stainless steel is proposed with a rounded off tip to minimize contact area and was found to achieve desired values of thermal conductance.

Performance of both structural solutions is greatly affected by solid conduction from the foil at the edge creating the hermetic seal. The conceptual composition of the panel with a stainless steel structure was simulated to achieve an average thermal conductivity of 0.017 $\frac{W}{mK}$. A panel with a PTFE structure resulted in an average thermal conductivity of 0.023 $\frac{W}{mK}$. Moreover, hollow-core VIPs can incorporate a conducting state by changing their internal emissivity with use of electrochromic coatings and increase their thermal conductivity to 0.1 $\frac{W}{mK}$.

The results of this study indicate that hollow core VIPs can function as thin insulating elements with the capacity to change into a conducting state, for near passive means of space conditioning. Nonetheless, hardships of the technology such as material compatibility with high-vacuum environments and competing requirements between structural and thermal performance significantly limit dimensions and composition of this type of cladding solution.

Contents

List of Figures

List of Tables

List of Symbols

κ	Thermal Conductivity $\left[\frac{W}{mK}\right]$
ρ	Density $\left[\frac{kg}{m^3}\right]$
p	Pressue $[Pa]$
C	Thermal Conductance $\left[\frac{W}{m^2K}\right]$
α	Accommodation Coefficient
γ	Specific Heat Ratio
R_g	Molar gas constant
M_w	Molar weight of the gas
T	Temperature
d	Distance
A	Area
σ	Stefan-Boltzmann constant
ϵ	Emissivity
t	Thickness
h	Heat Transfer Coefficient
Q	Heat Rate $[W]$
Q''	Heat Flux $\left[\frac{W}{m^2}\right]$
Kn	Knudsen Number

λ	Molecular mean free path
η	Coefficient of viscosity
C_v	Specific heat capacity at constant volume
C_p	Specific heat capacity at constant pressure
F	View factor; Form factor
Pr	Prandtl number
μ	Dynamic viscosity
R	Thermal resistance $\left[\frac{K}{W}\right]$
R''	Thermal resistance $\left[\frac{m^2K}{W}\right]$
$U-$	Lower limit of uncertainty when used as subscript
$U+$	Upper limit of uncertainty when used as subscript
h_c	Thermal contact conductance $\left[\frac{W}{m^2K}\right]$
W	Compressive load $[Pa]$
M	Surface hardness $[Pa]$
H	Height $[m]$
P	Maximum compressive load $[N]$
E	Modulus of elasticity $[Pa]$
I	Moment of Inertia $[m^4]$
σ''	Compressive stress $[Pa]$
v	Poisson's ratio
r	Radius
y_{max}	Maximum Deflection $[m]$
w	Uniform distributed load $\left[\frac{N}{m}\right]$

ζ	Constant depending on dimensions and support method

Abbreviations

DSMC Direct Simulation Monte Carlo

EPS Expanded Polystyrene

MD Molecular Dynamics

PIR Polyisocyanurate Rigid Foam

PUR Polyurethane Rigid Foam

VIP Vacuum Insulated Panels

XPS Extruded Polystyrene

Glossary

Accomodation Coefficient (α) Parameter describing the gas-wall interaction. It describes change in momentum, translational, and rotational energy of the molecule at the gas-wall interface.

Array Separation (d) Distance between parallel structural elements inside hollow-core vacuum insulated panels

Contact area ($A_{contact}$) Area of contact between structural elements and face plates of samples or simulated hollow-core VIP nodes

Array Conductance (C_{array}) Solid thermal conductance of structural elements. Calculated from array separation, structural elements' height and panel dimensions. Units in $/fracWm^2K$

Edge Conductance (C_{edge}) Thermal conductance of foil creating hermetic seal at the edge of the panel. Units in $/fracWm^2K$

Effective Conductance ($C_{effective}$) Thermal conductance of the system. Sum of the thermal conductance of the structural array, face plates, rarefied gas and edge foil. Units in $/fracWm^2K$

Direct Simulation Monte Carlo DSMC Direct Simulation Monte Carlo is a probalistic method for simulating molecular interaction by solving the Boltzmann equation. This method improves computational efficiency by simulating a number of particles that representing a larger set.

emissivity (ϵ) Factor describing the efficiency of a surface in transfering radiative energy averaged over all directions and wavelengths.

Free Molecular Flow Regime of rarefied gas flow where effects from intermollecular collisions become negligible. This occurs when the mean free path between molecules is larger than the distance between boundaries.

Height (H) Dimension of strucural elements along the axis parallel to heat flux in the panel. If the panel has dimensions length and width along axis "x" and "y" of cartesian space, Height is the dimension along the "z" axis.

PIMPLE algorithm Combination of the SIMPLE and PISO algoritm, PISO stands for pressure implicit of split operations. It is a method for solving the Navier-Stokes equations with time discretization allowing for larger time steps than permitted by the PISO algorithm.

SIMPLE algorithm Semi-Implicit-Method of Pressure Linked Equations. It is a method for solving the Navier-Stokes equations. The discretized momentum and pressure corrections equations are solved implicitly, where the velocity correction si solved explicitly.

Thermal Conductance (C) Total heat transfer coefficient through a system per unit area per degree. It doesn't include heat transfer coefficients from external surfaces.

Thermal Contact Conductance (h) Heat transfer coefficient per unit area per degree at the interface between two regions with imperfect contact.

U-Value Inverse of the sum of all thermal resistances in a system including including heat transfer coefficients in the external surfaces.

View Factor (F) The fraction of the radiation leaving a surface that is intercepted by surface another surface. This factor is calculated from the intensity of radiation by emission and reflection, and the solid angle subtended by the first surface when viewed from the second surface.

Acknowledgments

I would first like to express my gratitude to my supervisors, Christopher Kendrick, Shahaboddin Resalati and Martin Heywood. I would also like to thank professor Ray Ogden for giving the opportunity to join his lab and explore a new and interesting research area.

Thanks to Ray Solter and Ian Spacksman, who were instrumental in the manufacturing of the testing equipment.

This work would not have been possible without my financial sponsors. I would like to thank Oxford Brookes University and Conacyt Mexico, who provided me with the means to fund my doctoral studies and avoid starvation.

I would also like to thank my family for their unrelenting support. I'll always remember my father's pride watching me progress through this stage in life.

Last but not least, I would like to dedicate this thesis to my wife, Marimar, my guiding light through the maze of life.

Chapter 1

Introduction

Improving the energy efficiency of the built environment can significantly reduce energy demand and the inherent negative environmental impact from hydrocarbon sourced energy generation. The potential benefits become evident considering that over 20% of the world's total generated energy is allocated to buildings [1], and nearly 50% of that amount supplies the demand for space conditioning in developed countries [2]. Energy outlook models forecast significant increase in buildings' energy consumption, especially in developing economies, as rural populations shift towards urban lifestyles [1]. Consequently, concerns over the consequences of climate change have resulted in coordinated efforts towards a more sustainable development.

1.1 Building Regulations and Performance Targets

Trends focused on improving ecological conditions were first set in the United Nations Framework Convention on Climate Change (UNFCCC) in 1992 [3], and sup-

plemented in The Kyoto Protocol in 1997 [4]. Which, in Europe, led to the energy package of 2007, also known as the "20, 20 by 2020" package, set to reduce greenhouse gas emissions by 20% (later increased to 30%) and provide 20% of energy demand from renewable sources [5]. In order to reach these goals several directives regarding the building industry were set to reduce the effects from energy consumption in buildings; some of the directives defined by the European Parliament are[6, 7]:

- Directive 2009/28/EC on energy use from renewable sources.
- Directive 2010/31/EU on buildings' energy performance.
- Directive 2012/27/EU on energy efficiency.
- Directive 2018/844/EU amending directive on energy performance of buildings.

The European effort to reduce greenhouse gas emissions from the building industry has led to improved building codes. The UK introduced in 2006, the Code for Sustainable Homes, which is a holistic guideline for low energy and low impact construction [8]. This code rated buildings from 1 to 6 based on their overall performance and was mandatory for new homes until 2010, when it became voluntary. The initiative that established the Code for Sustainable Homes eventually led to changes in Part L of the building regulations, concerned with buildings' energy efficiency, but eliminating the preceding holistic approach. The new building regulations require that new or refurbished construction meet certain emission rates and energy demand targets, estimated according to a National Calculation Methodology, which in the UK is the Standard Assessment Procedure (SAP) 2012 in compliance

with the Energy Performance of Buildings Directive [9]. In these calculations the efficiency of the building fabric is emphasized and limited to a U-Value of 0.3 $\frac{W}{m^2K}$ for walls and 2 $\frac{W}{m^2K}$ for windows [10], amongst other criteria. Moreover, the sustainability trend has given rise to third party certification schemes such as LEED [11] and BREEAM, which categorize buildings on a holistic approach using rubrics similar to the Code for Sustainable Homes. These codes stress the importance of an improved building envelope, as it will be responsible for a significant amount of energy transfer in or out of the building regarding space conditioning. Achieving the required performance established by building codes and standards moving toward nearly Zero Energy Buildings is not a trivial task. In alignment with UK building regulations, the CO_2 Target Emission Rate (TER) and Target Fabric Energy Efficiency Rate (TFEE) must not be exceeded by the dwelling. The former is calculated according to: a) provision of space heating and hot water, b) use of pumps and fans, c) use of internal lighting; the latter is calculated according to a notional dwelling constructed with rigorous thermal properties such as external wall U-Value of 0.18 $\frac{W}{m^2K}$ and window U-Value of 1.8 $\frac{W}{m^2K}$ [10]. Both TER and TFEE are directly affected by the building fabric construction as it will have a direct effect on the internal temperature and consequently space heating or cooling demands. Although U-Value limits established by building regulations are more lenient than those of the notional construction used in the calculations of the TFEE rate, the building fabric must meet the required energy performance goals either through a modest amount of high performance materials or a larger amount of less efficient materials.

1.2 Insulating Materials

Insulation materials are characterized by a high thermal resistance, consequently hindering heat transfer through the material. These are commonly employed in the building industry to shield internal spaces from external climatic conditions. The application, placement and use of insulation materials is dependent on the design, construction method, material properties and desired outcome. For example, glass wool is a flexible, economic and common insulation material commonly found in timber constructions between studs and other structural elements; XPS foam can be sandwiched between floor layers in a ground slab, to prevent undesired heat loss to the ground.

The most common insulating materials in Europe can be summed up in two categories, inorganic fibrous materials like glass wool and rock wool, and organic foam materials like expanded polystyrene (EPS) and extruded polystyrene (XPS), and to a lesser extent polyurethane and polyisocyanurate rigid foams (PUR, PIR), Figure 1.1. The former dominates the market with a 60% share, the latter accounts for 27% of market volume [12]. In addition to these categories, other common insulating materials include cellulose and cork insulation, although these don't have a market share comparable to inorganic fibrous materials or organic foamy materials.

Glass wool and rock wool have a thermal conductivity between 0.030 - 0.046 $\frac{W}{mK}$ [16, 17] and cost approximately 14.5 $\frac{£}{m^3}$ and 17.8 $\frac{£}{m^3}$ respectively for 100mm thick rolls; batts tend to be several times more expensive [18, 19]. EPS and XPS foams have a conductivity between 0.025 and 0.041 $\frac{W}{mK}$ [16, 20] and cost 86 and 218 $\frac{£}{m^3}$ respectively for 100mm thick batts [21, 22]; the latter is an upper echelon Kingspan product with a higher price tag than other XPS foams. The difference between these

two categories in performance is negligible, and while rolls of fibrous insulation tend to be considerably cheaper, the cost of fibrous insulation batts approaches that of foams. PUR-PIR foams, while contained in the previous category for organic foamy materials have a slightly lower conductivity, as low as 0.019 $\frac{W}{mK}$ [16, 23], and a higher price tag at 156 $\frac{£}{m^3}$ [24]. It's not surprising that these materials hold the majority of market share considering that more efficient solutions like aerogel blankets and vacuum insulated panels (VIPs) come at a much higher price. Aerogel blankets used for building insulation have a thermal conductivity between 0.014 and 0.017$\frac{W}{mK}$ [25], but a 5mm thick aerogel blanket can cost over 8100 $\frac{£}{m^3}$ [26]. VIPs can have a center of panel thermal conductivity as low as 0.004 $\frac{W}{mK}$ [27], but cost between 2500 and 20000 $\frac{£}{m^3}$ for VACUPOR NT-B2-S panels; prices depend on panel dimensions [28].

While building regulations are stringent in the resulting performance they don't mandate any one building material or construction type, as such, multiple solutions can be approached, each with its own benefits and drawbacks. A simple example trying to achieve a wall U-Value of 0.3 $\frac{W}{m^2K}$, assuming uniform layers and neglecting heat bridges, can be constructed comparing glass wool and aerogel. If glass wool

Figure 1.1 has been removed
from this version of the thesis
due to copyright restrictions

Figure 1.1: Common Insulating Materials. a) Glass wool insulation. Image from [13]. b) Expanded polystyrene (EPS) insulation. Image of Polarguard EPS foam board [14]. c) Polyisocyanurate rigid foam (PIR) insulation. Image of Kingspan's thermafloor TF70 [15].

insulation is used, which has a thermal conductivity of 0.046 $\frac{W}{m^2K}$ [16], the insulation layer would need to be 15 cm thick according to Fourier's Law [29]. The same requirement could be fulfilled with aerogel, which has a thermal conductivity as a low as 0.014 $\frac{W}{m^2K}$ [25], with a layer less than 5 cm thick. Clearly, the high performance aerogel blanket allows for much thinner walls, which ultimately means more usable floor area, although the material is several times more expensive [16, 30, 31, 26]. This difference is exacerbated when trying to fulfill more demanding criteria, such as Passivhaus.

As regulations move toward stricter regulation, as has been seen in the case of the UK, where wall U-Value limits were 1.7 $\frac{W}{m^2K}$ in 1965, 1.1 $\frac{W}{m^2K}$ in 1974, 0.7 $\frac{W}{m^2K}$ in 1981 and now 0.3 $\frac{W}{m^2K}$ [32, 10], construction methods have evolved accordingly, shifting away from uninsulated brick walls to more complex wall solutions that mitigate heat transfer [33]. It is reasonable to postulate, if the trend continues towards even stricter regulations, construction solutions will require larger amounts of common insulating materials, or more efficient insulators. The economic viability of switching to sustainable development sooner than later[34], and government commitment for reducing energy consumption through building related applications [4, 5] has driven and continues to stimulate extensive research and innovations in building technology; e.g. the UK has funded over £70 million for innovation in the construction industry in 2018 innovation grants[35].

Extensive research has been conducted in pursuit of materials with better thermal performance. These materials or insulating technologies are sometimes referred to as superinsulators, achieving thermal conductivity as low as 0.014 $\frac{W}{mK}$ in the case of aerogels and vacuum insulated panels (VIPs) [36, 25, 30, 27, 37, 38], Figure 1.2.

Aerogels are state-of-the-art insulators, and their fabrication and application

has been subject to thorough research. While fabrication is still expensive, these materials have already been introduced to the market in the form of blanket-type insulators and even incorporated into glazing solutions [36, 39, 40, 41]. However, due to the limited product range, availability and high cost, these products are still not widely adopted [36].

Figure 1.2 has been removed
from this version of the thesis
due to copyright restrictions

Figure 1.2: Super insulating materials. a) Nano-encapsulated aerogel. Image from [42].b) Spacetherm (aerogel) blanket. Image from [26]. c) Vacuum insulated panel (VIP). Image of Kingspan's OPTIM-R panel [43].

1.3 Vacuum Insulation

Vacuum insulating technology can be traced back to Professor James Dewar's flasks [44] but was introduced to the building industry in the form of glazing on a patent by Zoller in 1924[45] in which two panes of glass were separated by a vacuum gap, this patent marks the starting point for an area of research that would inspire modern vacuum glazing and, indirectly, other vacuum insulating technology as VIPs. Vacuum insulating technology works by suppressing convective heat transfer through the gap when a critical low pressure is achieved and the gas shifts from a continuum flow regime into a free molecular flow [46]. Vacuum glazing has been manufactured using solder glass edge sealing, and indium alloy edge seals, both with internal low emittance coating resulting in a measured center of pane thermal transmittance

U-Value of 0.8 $\frac{W}{m^2K}$ [47] and 0.86 $\frac{W}{m^2K}$ [48] respectively. Application of vacuum insulation in opaque panels has been mostly investigated in Vacuum Insulation Panels (VIPs), which consist of a porous core, evacuated and wrapped in an airtight foil.

1.3.1 Composite Vacuum Insulated Panels

VIP solutions may include as core material fumed silica, perlite, polyurethane foams, glass fiber, or other mesoporous materials, enveloped by a multi-layer metalized polymer film [44, 49, 50, 51]. At a high vacuum heat transfer through the core is negligible [50, 52, 53, 54] and most heat transfer occurs through the panel's envelope [55].

Optimal VIP performance is outstanding, but fragility and cost renders them a niche product in the construction industry. It was estimated that in 2005, products outside of the inorganic fiber and organic foams categories accounted for less than 5% of market share in Germany [56]. Updated information for UK market share was not available in reputable sources, nonetheless, the previous source is indicative of trends in the European market, where super-insulators are not yet widely adopted. As mentioned previously, VIPs are eight times more expensive than conventional insulators and aerogels are more than fifteen times more expensive [27, 37]. However, in markets with high floor area price, the increase of usable floor area provided by thiner walls represents economic viability for super insulating solutions over conventional insulating materials [23].

A significant drawback to VIPs is that thermal conductivity will increase over time, due to water vapour and air diffusion through the envelope. Although envelope properties and ambient conditions can affect panel aging, all VIPs will deteriorate

over time [23]. Additional drawbacks include the fragility of the panel, which includes perforation vulnerability, and the lack of size adaptation by cutting on site [23]. Repercussions of the limitations are greater than may seem at first glance, e.g. any irregular stud distance may not accommodate a standard size VIPs and will force the use of other materials with different properties, improper handling and friction of the envelope may cause a loss of vacuum, hanging a picture in your wall may puncture a panel. Integration of VIPs in construction then require additional considerations to protect the panels. As a response to these vulnerabilities, VIPs have been sandwiched between additional superficial layers such as EPS or rubberized films for both reasearch and comercial applications [27, 28].

1.3.2 Hollow-core Vacuum Insulated Panels

Looking at the evolution of building regulations, especially in harsh weather, where the building envelope continues to be improved we can identify a clear necessity for a thermally efficient building fabric, although, one that can be widely incorporated into the market without the cost limitations and fragility of current super insulators like aerogel blankets or VIPs. In pursuit of overcoming these limitations, the design of a hollow-core VIP with a rigid envelope has begun to attract attention. However, at the time of writing, only a single peer reviewed paper on this technology was found and it dealt mostly with fabrication rather than design and characterization of its thermal properties [57]. Designing a hollow-core vacuum insulated panel, with a rigid envelope, could overcome the fragility of conventional VIPs and provide a more efficient insulator than common insulating materials. Moreover, it could potentially function as a dynamic element capable of switching between an insulating and a

conducting state, thus reducing some of the heating or cooling demands.

A hollow-core panel works on the same principles of VIPs but, as the name says, lacks any core material. As such, the panel requires a structural array to maintain its shape and rigidity. Figure 1.3 shows a diagram of the panel. The structural array could be designed in multiple configurations such as staggered glass bars or glass spheres. Investigation and fabrication of this type of panel has not been widely pursued, and while some examples have been documented in the past such as that by Nemanic [57], the subject still lacks investigation into the feasibility, configuration, material selection, thermal performance and processing of hollow-core vacuum insulating panels. This subject is still an attractive area of research due to the panel's potential on good insulating properties, range for extreme temperature application, higher resistance to mechanical stress and improper handling that could otherwise compromise the vacuum in softer panels.

At the time of writing the only example found in peer reviewed journals [57] focused on fabrication methods rather than on panel configuration and its effect on thermal performance. No additional sources were found to comment on the thermal performance of hollow-core VIPs or analysis methods directly applied to this technology. This research narrows the gap in knowledge by providing the following information regarding hollow-core VIPs:

- Measuring the thermal performance of hollow-core vacuum insulation by laboratory testing and numerical simulations;

- Proposing an alternative method of numerical analysis that incorporates heat transfer through a rarefied gas region in multi-region solvers which are incapable of directly handling molecular dynamics;

- Identification of key parameters and constraints, structural and thermal, necessary for the design and configuration of hollow-core VIPs;

In addition, this project investigates the potential for a hollow core panel to change its thermal conductance and function as a dynamic insulator with a conducting and insulating state.

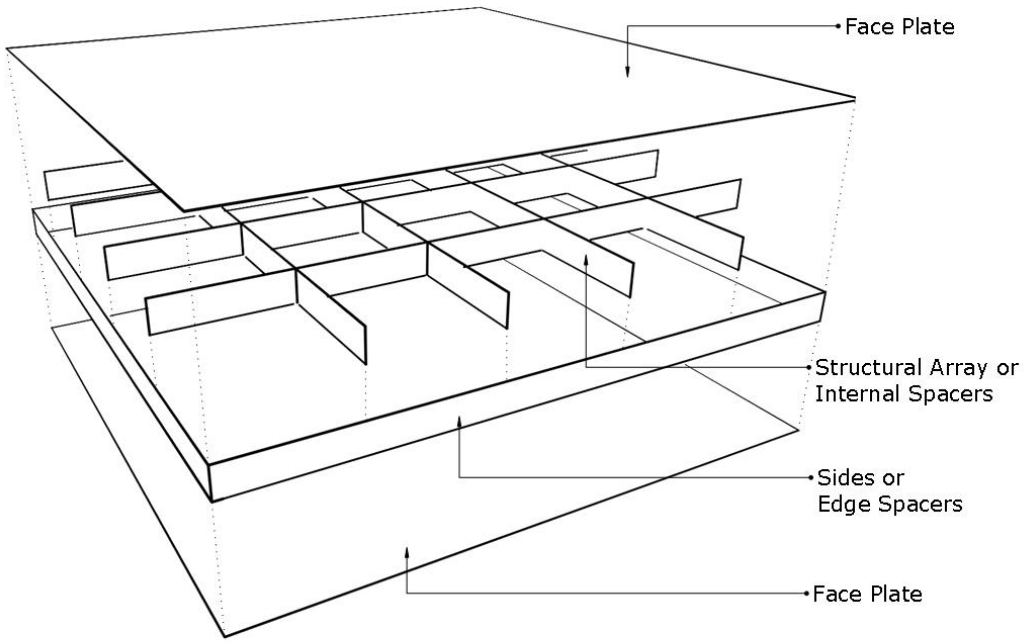

Figure 1.3: Hollow core vacuum insulated panel diagram.

1.4 Aims and Objectives

The research reported in this thesis focuses on hollow core vacuum insulating panels, a possible building cladding solution that has not yet been addressed formally and whose characteristics and performance have not been studied with adequate rigor to determine if it is or not a feasible solution.

The overall aim was to develop a conceptual prototype of a hollow-core vacuum insulated panel with better insulating properties than common insulating materials. A detailed study is conducted to determine the thermal conductance and establish the contribution of heat transfer mechanisms in thin hollow core vacuum insulated panels, and the dependency of these on vacuum pressure, geometric configuration, material properties and other relevant factors in order to produce design constraints for such cladding systems.

The objectives that support this aim are:

- Identify key parameters in the thermal performance of hollow-core VIPs;
- Analyse how key parameters are involved in heat transfer and to what extent these can affect the performance of the panel;
- Identify key parameters in the structural integrity of the panel;
- Analyse the relationship between competing requirements, structural and thermal, towards configuring a feasible hollow-core VIP;
- Evaluate the thermal performance of hollow-core VIPs and how these compare with current insulating solutions for the building industry;
- Identify limitations of this type of insulating technology.

1.5 Thesis Outline

In Chapter 2 a literature review describes in greater detail the current state of technology and what methods have been investigated towards altering thermal performance of a building cladding element. In Chapter 3 the numerical solvers and methods used to perform thermal simulations are discussed and validated against analytic solutions. The basic algorithms and physical models are described. In Chapter 4 simulations on a simplified case are performed to assess participation of heat transfer mechanisms in variable vacuum conditions and to determine the most suitable parameter for manipulating heat transfer across the panel. Chapter 5 measures the thermal resistance of several prototypes representing nodes in a large scale hollow-core VIP. Chapter 6 improves the previous simplified case by incorporating structural supports and validates results against empirical measurements conducted in a controlled laboratory environment. The design constraints of competing structural and thermal requirements are addressed in Chapter 7 to obtain design parameters and limits. A conceptual design is postulated and evaluated as a dynamic thermal cladding element. The thermal resistance range between insulating and conducting state is discussed. Chapter 8 presents key findings of this project along with project limitations and discussions on further work.

Chapter 2

Literature Review

As the building industry strives for better performance, insulating materials play a lead role in providing adequate thermal insulation for the building envelope, which results in lower energy consumption for space conditioning and a lower carbon footprint for the operating cost of the building.

Common insulating materials are categorized into inorganic fibrous insulations and organic foamy materials. The former includes materials like mineral and glass wool, the latter includes EPS, XPS, PUR and PIR foams. Beyond these materials are super insulating solutions, like aerogel and vacuum insulated panels (VIPs). These solutions have a lower thermal conductivity but are more expensive and have additional drawbacks that have hindered their market adoption.

Vacuum insulating technology is an attractive solution to high performance demands with a thin form factor, and it has seen application in diverse areas such as lab equipment, drink thermos, fenestration and now building cladding. This technology was introduced to the building industry in the form of vacuum glazing, and has since expanded into pyrogenic silica VIPs. Current VIPs have a very low thermal

conductivity, but can be easily damaged and have been shown to deteriorate over time. A different solution relying on the same principle, but with a hard shell and a hollow core is researched as an alternative to both common and super insulating materials.

Hollow core vacuum insulated panels can be self supporting cladding elements that eliminate the need of additional housing and are more resilient. In addition, the lack of a core material provides an environment suitable for heat transfer manipulation, which could help the panel adapt to different conditions.

Prior to evaluating the characteristics and performance of hollow core VIPs, a comprehensive review of current insulating solutions is provided. Amongst which are found the predecessors of the hollow core VIPs, vacuum glazing, evacuated solar collectors and fumed silica VIPs. Considering that hollow core VIPs could respond dynamically to environmental conditions and become a switchable element, heat transfer manipulation methods and devices are also researched to examine their functionality and application.

2.1 Common insulating materials

The most common insulating materials include inorganic fibers, rock and glass wool, and organic foam structures, expanded polystyrene (EPS), extruded polystyrene (XPS), polyurethane rigid foam (PUR) and polyisocyanurate rigid foam (PIR). The former category accounts for 60% of the European market share, and the latter accounts for 27% of market share [16, 12].

Other insulating materials that will not be reviewed are cellular glass (closed cell structure), foamed glass, calcium silicate foam, ceramic fibers, and expanded

perlite, but a comprehensive review on these can be found in [56, 58].

Material properties for common common insulating materials can be found in Table 2.1. Most common insulating materials are available in a wide variety of densities and dimensions, as they have different applications in the building.

Table 2.1: Thermophysical properties for common insulating materials.

Material	Type	κ $\frac{W}{mK}$	ρ $\frac{kg}{m^3}$	T_{max} $^\circ C$	Refs
PUR-PIR	Organic, foamy	0.019– 0.030	25–100	120	[23, 12, 59, 30, 58, 60]
XPS	Organic, foamy	0.025– 0.050	20–80	80	[12, 30, 58, 60, 23]
EPS	Organic, foamy	0.029– 0.041	10–50	80	[12, 30, 58, 60, 61]
Glass wool	Inorganic, fibrous	0.030– 0.046	08–150	500	[62, 12, 30, 58, 60]
Rock wool	Inorganic, fibrous	0.030– 0.046	13–240	800	[60, 62, 12, 58]

κ is the thermal conductivity
T_{max} is the maximum service temperature

2.1.1 Fibrous Insulation

Glass and rock wool are commonly categorized as mineral wool materials (Figure 2.1), and are often sold as a hybrid solution. Mineral wool has become very popular due to its noble properties, offering benefits against cold and warmth, sound absorption and fire protection. Moreover, it is easy and safe to handle from a health standpoint and is resistant to ageing. Typical thermal conductivity values of mineral wool are between 0.03 and 0.046 $\frac{W}{mK}$. However, these values are heavily dependent on moisture content and mass density, and have been known to increase from 0.037 to 0.055 $\frac{W}{mK}$ with a 10% volumetric water content increase [23].

These insulating materials can be perforated, cut and adjusted at the building site without affecting its thermal performance, making them an attractive solution for both professional and DIY(do it yourself) solutions.

2.1.1.1 Glass Wool

Glass wool is made from limestone,sand, soda ash, recycled glass and other minerals. These are melted at 1400 °C, spun into fibers and mixed with organic resins. Finally, the fibers are sprayed with a binder, which is then hardened to give the final product its structural stability. The typical composition of glass wool is approximately 70% recycled glass, 0.5 to 7% binder resin and 0.5% mineral oil. The remaining components like limestone are derived from the glass manufacturing process [56]. The thermal conductivity of glass wool is commonly found to be between 0.03 and 0.046 $\frac{W}{mK}$ [23, 60], and can be affected by material density and other material properties. A 100mm thick roll, with a density of 10 $\frac{kg}{m^3}$ sold by a UK retailer is said to have a nominal conductivity of 0.044 $\frac{W}{mK}$; the same retailer offers a 75mm thick batt with a density of 36 $\frac{kg}{m^3}$ with a conductivity 0.032 $\frac{W}{mK}$ [18]. A varied product range is offered for different applications in the building industry, adjusting to building elements and building methods.

Glass wool is very versatile and can be applied in floors, roofs and walls, as

Figure 2.1 has been removed
from this version of the thesis
due to copyright restrictions

Figure 2.1: Fibrous Insulating Materials. a) Glass wool insulation. Image from [13]. b) Rock Wool insulation. Image of Knauf Earthwool Building Slab - RS100 [63].

such it is found in a variety of thicknesses in both roll and batt form. It does require a weather barrier to prevent direct contact with water or humidity, as this can deteriorate the material's performance [23]. Consequently, glass wool is never exposed to weather and is never applied as external insulation without a protective barrier or membrane [56].

Pricing for glass wool insulation will depend on thickness and form. The batt will tend to be more expensive than rolls, and thicker products will always be more expensive. A 100mm thick loft insulation roll, with a thermal conductivity of 0.044 $\frac{W}{mK}$ is currently sold for 1.45 $\frac{£}{m^2}$, which equates to 14.5 $\frac{£}{m^3}$. A batt form solution from the same retailer is sold for 5.43 $\frac{£}{m^2}$ or 72 $\frac{£}{m^3}$, albeit with a lower thermal conductivity of 0.032 $\frac{W}{mK}$ [18].

2.1.1.2 Rock Wool

Rock wool is based on natural, non renewable minerals like volcanic rock. Similar to glass wool the materials are melted, spun into fibers and impregnated with binders and oils. Rock wool commonly contains approximately 30% recycled raw material (glass), 0.5 to 7% binder resin and 0.5% mineral oil, the remainder is comprised of natural minerals [56, 12].

Rock wool shares many similarities with glass wool, amongst which is the thermal conductivity, at a nominal value of 0.036 $\frac{W}{mK}$ [56, 23, 60] and large product range. However, it is consistently denser than glass wool providing better fire resistance and a greater service temperature range up to 800 °C [60].

Similar to glass wool the application of rock wool extends to the entirety of the building envelope where there is no direct contact with the external environment or water.

A 100mm thick loft insulation roll, with a 0.044 $\frac{W}{mK}$ thermal conductivity is currently sold for 1.78 $\frac{£}{m^2}$, which is approximately 22% more expensive than glass wool, although both solutions are quite accessible [19]. Rock wool shares the same advantages as glass wool, albeit with a better fire resistance, higher density and higher service temperature. However, the embodied energy is four times greater than glass wool [56, 60].

2.1.2 Foam Insulation

The most common types of foam insulation applied in buildings are expanded polystyerene (EPS), extruded polystyrene (XPS), polyurethane rigid foam (PUR) and polyisocyanurate rigid foam (PIR) [30].

Figure 2.2 has been removed
from this version of the thesis
due to copyright restrictions

Figure 2.2: Foam Insulating Materials. a) Expanded polystyrene (EPS) insulation. Image of Polarguard EPS foam board [14]. b) Extruded polystyrene (XPS) insulation. Image of Danosa Danopren product range [64]. c) Polyisocyanurate rigid foam (PIR) insulation. Image of Kingspan's thermafloor TF70 [15].

2.1.2.1 Expanded polystyrene (EPS)

Expanded polystyrene is perhaps the most common material amongst foams, holding a 13% of market share [30]. EPS is composed of polymerised polystyrol (2%) and air (98%). The foam is manufactured by heating small beads of polystyrene containing

an expansion agent (pentane C_6H_{12}) with water vapor, which expands to form closed cells [23]. The resulting structure are discrete voids of air in a polymer matrix. This foam is low density, hydrophobic and non-absorbent [30].

EPS has a thermal conductivity between 0.03 and 0.04 $\frac{W}{mK}$, but can vary depending on temperature, moisture and density [12, 30, 58, 60, 61]. EPS has been found to increase its thermal conductivity from 0.036 to 0.054 $\frac{W}{mK}$ with increasing moisture content from 0 to 10% [23].

The cost in the UK for 100mm thick EPS board with a thermal conductivity of 0.038 $\frac{W}{mK}$ is aproximately 8.6 $\frac{£}{m^2}$ at the time of writing. This equates to 86 $\frac{£}{m^3}$ [21]. This foam is very adaptable as it can be easily modified to great precision without altering its characteristic properties. While this material has good water and moisture resistance properties, it has a low service temperature and is very vulnerable to sun degradation and fire [12].

2.1.2.2 Extruded polystyrene (XPS)

Extruded polystyrene is produced from melted polystyrene with the addition of an expansion gas ($HFC, CO_2 or C_6H_{12}$). The melted polymer is extruded through a nozzle, releasing gas pressure and causing mass expansion. XPS has a closed pore structure similar to EPS but is commonly found in higher density.

Common thermal conductivity values for XPS foam are between 0.025 and 0.05 $\frac{W}{mK}$ but has been found to increase its 0.04 to 0.066 $\frac{W}{mK}$ with increasing moisture content from 0 to 5% [12, 30, 58, 60, 23].

The cost of a 100mm thick Kingspan GreenGuard GG300R with a thermal conductivity of 0.036 $\frac{W}{mK}$ is 21.8 $\frac{£}{m^2}$ [22].

This material has excellent water and moisture resistance properties, hence its

use beneath ground floor slabs and foundations. However, just like EPS it is vulnerable to direct sunlight and fire. Moreover, its service temperature is limited to 80 °C, making it unsuitable for high temperature applications [12, 30, 58, 60].

2.1.2.3 Polyurethane (PUR) and polisocyanurate (PIR) foams

Polyurethane is manufactured through a chemical reaction between isocyanates and polyols (alcohols with several hydroxyl groups) [23]. Polyisocyanurate (PIR) is produced by the same chemical reaction but with different proportions between the reactants, generating a different molecular structure [65]. The insulation materials may be produced as boards or a continuous surface on a production line. PUR is also used as a sprayed expanding foam at the building site. PUR and PIR foams have a typical thermal conductivity between 0.02 and 0.03 $\frac{W}{mK}$, but can vary depending on moisture content and mass density [12, 59, 30, 58, 60]. Moisture content increase from 0 to 10% has been shown to increase PUR's thermal conductivity from 0.025 to 0.046 $\frac{W}{mK}$ [23].

At the time of writing, Celotex 100mm GA4100 PIR Insulation Board with a thermal conductivity of 0.022 $\frac{W}{mK}$ was available from UK retailers for 15.6 GBP per m^2 [24].

Health and environmental concerns attached this product are significant. Some of the expanding agents used in the production of PUR foams are long lasting green house gases. Moreover, PUR foam combustion releases toxic gases like hydrogen cyanide and other isocyantes [60, 23, 30].

2.2 Vacuum Insulating Technology

Professor James Dewar introduced vacuum insulating technology when he invented the vacuum flask in 1892. The original flask was made of glass and uncoated. Initial attempts at switching to a metallic flask failed due to gas adsorption at the surface, spoiling the vacuum. Over the course of his work he achieved functional metallic vacuum flasks by integrating charcoal into the flask, cooling the system and coating the interior surfaces with silver [44].

Vacuum insulating systems rely on high vacuum, typically at pressure levels below $10^{-4} mbar$, to suppress convection and gas conduction, and highly reflecting surfaces to reduce radiative heat transfer [46, 66, 44].

Commercial availability of vacuum flasks began in 1904 in Germany, and by 1907 the trademark had been sold to companies in the United States, Canada and England [44]. The cylindrical shape of flasks is important as the walls are capable of resisting the atmospheric pressure load of $10^5 Pa$. Transferring this technology into flat panels requires a load bearing structure or material to prevent the evacuated walls from collapsing. This adaptation was first proposed in a patent by Zoller filed in 1913, in which two glass sheets were separated by vacuum [45], setting the start point for vacuum glazing and vacuum insulated technology in the building industry. Years later, in 1930, the first vacuum panel was proposed in a patent granted by the German Reichsatentamt to O. Hemman and Sterchamolwerke [67].

Vacuum insulation offers several advantages over conventional insulation materials. Construction with conventional materials will result in substantially thicker building elements by comparison to VIPs to achieve the same heat exchange coefficient. Increased building envelope thickness results in unfavorable net-to-gross

floor area and building volume. In addition to complex details and joinery solutions, thicker elements represent a larger material consumption, although this doesn't necessarily mean higher embodied carbon.

Vacuum insulation solutions have been proposed as a composite element, commonly referred to as a sandwich [44, 68], or as a hollow-core solution [57], Figure 2.3. Hollow-core constructions, lack a core material and rely primarily on the sheet and spacing/structural elements to bare all mechanical stress, while composite panels rely on the core material for support. Structural or spacing elements will tend to represent a direct path for heat conduction. By comparison, composite panels exhibit less heat loss through its edges by having a thinner sheet face and edges, distributing mechanical stress along its inner core.

Investigation into hollow-core vacuum insulated panels is limited to the research conducted by Nemanic, focusing mainly on manufacturing rather than thermal characteristics [57].

Image (a) has been removed from this version of the thesis due to copyright restrictions

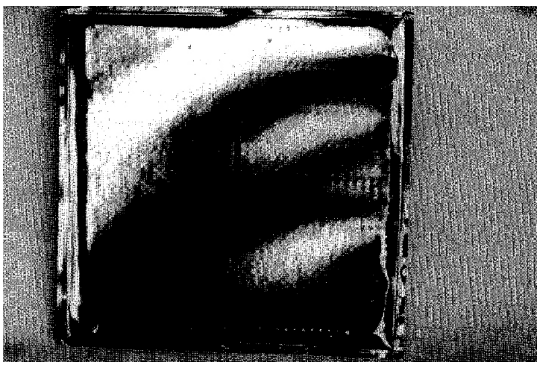

(b)

Figure 2.3: Vacuum Insulated Panels. a) Vacuum insulated panel (VIP). Image of Kingspan's OPTIM-R panel [43]. b) Hollow-core vacuum insulated panel with staggered glass tube structure. Reprinted from [57] Copyright (2019), with permission from Elsevier, license number 4626221304698.

2.2.1 Vacuum Glazing

After Zoller's patent the only publications with regards to vacuum glazing were other patents (a detailed list can be found in [47]) until Benson and his group began publishing conference papers [69]. Benson calculated that vacuum glazing could achieve a thermal conductance of 0.6 $\frac{W}{m^2K}$ with two glass panes laser welded at the edge and separated by glass spheres [69], but was not successful in fabricating it. Robinson and Collins describe the manufacturing process and thermal performance measurements for the first successful attempt at evacuated glazing in which they achieve a gas thermal conductance of 0.2 $\frac{W}{m^2K}$ and overall thermal conductance matching Benson's calculations [70].

The development of a practical evacuated window must incorporate a hermetic seal at the edge, a low and stable pressure between the glass panes, and a low emittance coating on at least one of the internal surfaces, Figure 2.4.

Earlier designs of vacuum glazing used 3–to–4 mm soda lime glass separated by fused solder glass pillars [70], but were later substituted by Inconel 718 (nickel based alloy) pillars [47] and stainless steel pillars [48]. The seal along the edge was achieved by using solder glass matching the lime glass' thermal expansion, and consequently heating the entire structure to 450 °C for 1 hour. Finally, the sample was evacuated after cool down. The evacuation process involved heating the sample up to 250 °C to eliminate adsorbed gases from interior surfaces [47]. Newer designs achieved hermetic seals using indium alloy [48], which requires lower temperatures (less than 200 °C)and permits the application of low temperature coatings that would otherwise degrade using the previous sealing method.

Measurements of the glazing conductance have been conducted using a small

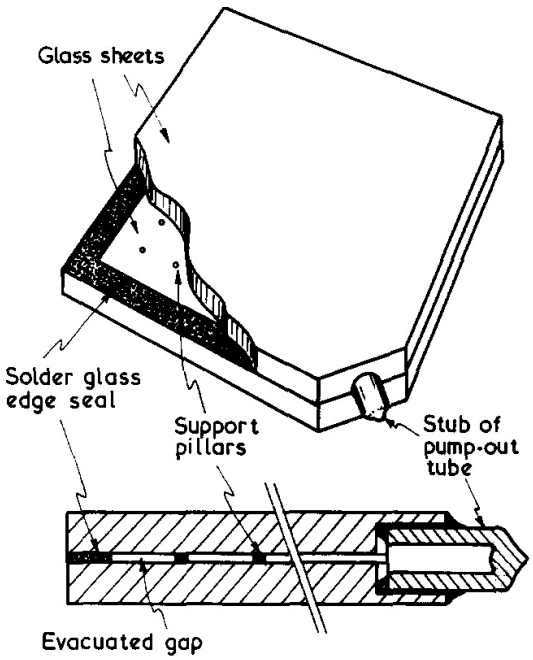

Figure 2.4: Schematic diagram of the evacuated window. Reprinted from [70] Copyright (2019), with permission from Elsevier, license number 4617200972417. Later designs, such as that by [47, 48], improve on the pump nozzle design and reduce leaks experienced by Robinson and Collins.

area guarded hot plate apparatus that measures heat flux between support pillars and in the vicinity of support pillars. Two measurement methods were used, the first involves temperatures near room temperature, the second involves a rapid temperature increase on one side of the sample and measuring temperature increase on the opposite side. The rate of increase on the cold side of the sample is dependent on the thermal conductance of the sample [47]. Although this method requires calibration against samples with known properties, it provides accurate and reproducible data over a wide temperature range.

Precise evaluation of heat transfer through the different elements of the vacuum glazing solution requires considering conduction through the rarefied gas, radiative exchange through the vacuum, conduction through the edge seal and the pillar

structure. In addition to these, the frame will have an insulating effect over the edge of the welded glass panels and will need to be considered in evaluating the complete glazing system.

2.2.1.1 Gaseous conduction

Gas conductivity is independent of pressure over several orders of magnitude, however, measurements have shown that at very low pressures the thermal conductivity of a gas decreases linearly with pressure. The heat conduction theory at these pressures has been developed from two standpoints, the first is Knudsen's theory that considers individual molecule's energy transfer to the surface, the second is Smoluchowski's temperature discontinuity [66]. Some of the most notable research groups in vacuum glazing evaluate gas conduction using Knudsen's method [70, 47, 48].

According to Knudsen's theory, the thermal conductance due to conduction through low pressure gas is written as [71, 66]:

$$C_{gas} = \overline{\alpha} \left[\frac{(\gamma+1)}{(\gamma-1)}\right] \left[\frac{R_g}{8\pi M_w T}\right]^{1/2} p \tag{2.1}$$

Where, $\overline{\alpha} = \frac{\alpha_1\alpha_2}{[\alpha_2+\alpha_1(1-\alpha_2]}$, and α_1 and α_2 are the accommodation coefficients of the gas molecules with the two surfaces, γ is the specific heat ratio of the gas, p is gas pressure, R_g is the molar gas constant, M_w is the molar weight of the gas, and T is the intermediate temperature between the opposing surfaces' temperature.

For a $0.2mm$ vacuum gap, as described by Collins et al., and Fang et al., and considering a combined accommodation coefficient of 0.9 for water molecules, the necessary pressure to ensure negligible gas conduction is $0.1Pa$ [47, 48]. Vacuum degradation beyond this pressure limit and in a viscous flow region would require

a different approach, for two parallel flat surfaces gas conductance is described by [71]:

$$C_{viscous} = \frac{\kappa_{gas} A(T_1 - T_2)}{d} \tag{2.2}$$

Where, d is the distance separating the surfaces, A is surface area, and κ_{gas} is the gas thermal conductivity.

2.2.1.2 Radiative heat flow

Radiative heat transfer between two flat parallel surfaces depends heavily on the optical properties of the surfaces. If the surface emittance ϵ is not strongly dependent on angle and wavelength the radiative conductance can be approximated as [72]:

$$C_{radiation} = 4\epsilon_{effective}\sigma T^3 \tag{2.3}$$

Where $\epsilon_{effective} = [\epsilon_1^{-1} + \epsilon_2^{-1} - 1]^{-1}$ and σ is the Stefan-Boltzmann constant.

For surfaces where emittance is heavily dependent on wavelength and incidence angle, a detailed derivation of the solution can be found in [72].

The effect of coatings on vacuum glazing has been researched over a wide range of emissivity values; Table 2.2 summarizes the center of glazing and full window U-Values for $40x40cm$ samples with different combinations of emissivity on the internal glass surfaces.

The use of low-e coatings on both glass panes has been shown to significantly reduce the U-value of the glazing system. However, employing a low-e coating with an emittance coefficient of 0.02 shows negligible improvement when applied to both glass panes [48].

Numerical simulations have shown that incorporating an electrochromic coating on vacuum glazing results in increased internal glass temperature and heat transfer inwards with incident solar radiation of 300 $\frac{W}{m^2}$ [73, 74], providing useful gains in heating dominated climates. However, at greater solar radiation incidence ($1000\frac{W}{m^2}$) indoor glass temperature can reach 50 °C when the electrochromic layer is facing outwards and over 100 °C when facing inwards [75], potentially damaging the glazing system and hazardous for the user.

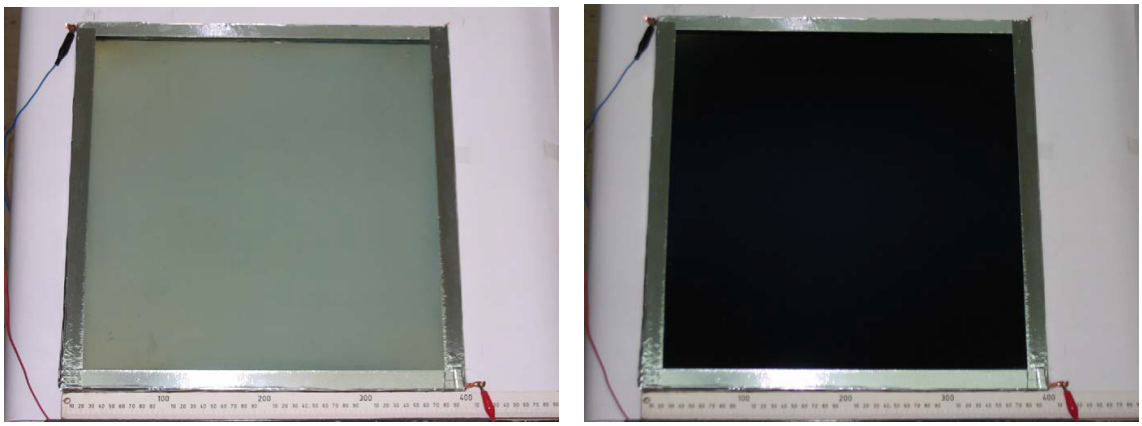

(a) Glass pane with electrochromic coating in as prepared state. Reprinted from [76] Copyright (2019), with permission from Elsevier, license number 4632051437053.

(b) Glass pane with electrochromic coating in colored state. Reprinted from [76] Copyright (2019), with permission from Elsevier, license number 4632051437053.

Figure 2.5: Electrochromic coating on glass, a) as prepared state, b) colored state

The effect of emissivity on thermal transfer in vacuum glazing is a clear indicative that radiation can take a significant role in vacuum insulated systems.

2.2.1.3 Pillar conduction

Support pillars in vacuum glazing have been manufactured from soldered glass [70, 78] shown in Figure 2.6, alumina, stainless steel [48] and Inconel [47]. The pillar design will have to consider the total array conductance and necesary strength to

Table 2.2: Simulated and measured U-values for vacuum glazing systems with different emissivity. Center of glazing and total window values presented.

Window	**Method**	ϵ_1	ϵ_2	**EC absorp.**	**U-Value**		**ref**
					Center $\frac{W}{m^2K}$	**Total** $\frac{W}{m^2K}$	
				%			
EC-VG 1	Simulated	0.02	0.02	80	1.06	0.51	[73]
EC-VG 2	Simulated	0.02		80	1.10	0.56	[73]
VG 1	Simulated	0.02	0.02		0.66	0.54	[73]
VG 2	Simulated	0.02			0.72	0.58	[73]
EC-VG 3	Simulated	0.16	0.16	80	1.29	1.06	[77]
EC-VG 4	Simulated	0.12	0.16	80	1.22	0.97	[77]
EC-VG 5	Simulated	0.04	0.16	80	1.13	0.85	[77]
EC-VG 3	Measured	0.16	0.16	80	1.30	1.07	[77]
EC-VG 4	Measured	0.12	0.16	80	1.20	1.00	[77]
EC-VG 5	Measured	0.04	0.16	80	1.15	0.87	[77]
EC-VG 6	Measured	0.15	0.12	WO_3	1.31	1.18	[76]

EC- electrochromic; VG- vacuum glazing; WO_3 Tungsten Oxide coating; empty emissivity values indicate uncoated surfaces

support at least the compressive stress of ambient pressure and the glass weight [78, 48]. Moreover, in the design of a pillar structure array for vacuum glazing, mechanical tensile stress on the outside surface of the glass is also an important consideration; Collins has proposed $4MPa$ as a tolerable level of stress for untempered glass [78].

When glass pane thickness is much larger than pillar height and the material of the pillars has a greater conductivity than that of the glass, as is the case for alumina, stainless steel and Inconel, the thermal resistance of the pillar array is defined by the spreading resistance of heat flow in the glass sheet, rather than by the thermal resistance of the pillar itself. In this case the thermal conductance of a single pillar is defined as [78, 79]:

$$C_{pillar} = 2\kappa_{glass}a \tag{2.4}$$

Figure 2.6: Diagram of pillar construction. Pillars have been manufactured from Inconel, stainless steel, alumina and glass. Solder glass pillars in image fuse with the glass plane during the edge seal process. Reprinted from [78].

Where "a'' is the pillar radius and κ_{glass} is the thermal conductivity of the glass.

When the thermal conductivity of the pillar is similar to that of the glass panes, the thermal resistance of the pillar array is well estimated by the series combination of the spreading resistance and the material resistance of the pillar; material

resistance becomes more evident with increasing pillar height [78].

For an equidistant square pillar array, where inter pillar distance is "d''", the thermal conductance of the pillar array is defined by [78, 79, 48]:

$$C_{array} = \frac{2\kappa_{glass}a}{d^2} \tag{2.5}$$

Finite element modeling has shown excellent agreement with this analytic approach [79]. Moreover, the uniformity of heat flux near the pillars has been modeled and confirmed by infrared thermography [73], which has an effect on radiative heat transfer in that region. However, over 90% of the area shows uniform heat flux density, allowing the array to be treated as a contiguous region in FEM simulations [48].

Experimental and numerical analysis on the participation of the pillar array have shown that while pillar height does have an effect on the overall thermal conductance of the glazing system, heat transfer is dominated by the spreading resistance of the glass. Therefore, pillar height on the analysis of vacuum glazing can be ignored [79]. It should be noted that pillars in the cited research have a height no larger than 0.72mm; pillar design with dimensions exceeding those of the previous research may find beneficial to determine the participation of pillar material resistance.

2.2.1.4 Edge conduction

Heat flow near the edges in highly insulated glazing has been modeled analytically, in a simple one dimensional model, and numerically with a three dimensional finite element model. Both models show close agreement [47].

For highly insulating glazing, the temperature at the edges of the glass ap-

proaches center-of-pane temperature exponentially with a characteristic distance $(\kappa_{glass}t/h)^{1/2}$, where "$t$" is the thickness of the glass and "h" is the heat transfer coefficient at the external surface of the glass. The analytic model then equates heat transfer through the edge per unit length to that which would flow along the glass pane of thickness "t" and length equal to the previous characteristic distance [47].

This model can be extended to account for insulation along the edge provided by the frame. For a frame design where insulation extends over the surface of the vacuum glazing panel on both sides with a distance of w_1 and w_2, the total heat flow per unit length of the edge seal is written as [47]:

$$Q_{edge} = \frac{(T_1 - T_2)\kappa_{glass}t}{\left(\frac{\kappa_{glass}t}{h_1}\right)^{1/2} + w_1 + w_2 + \left(\frac{\kappa_{glass}t}{h_2}\right)^{1/2}} \tag{2.6}$$

This model is only accurate when heat transfer through the glazing is negligible and when the conductance of the glazing is small by comparison to external heat transfer coefficients [47].

The participation of an insulated frame reduces the thermal conductance of the vacuum glazing by increasing lateral heat flux along the glass pane and into the frame. Moreover, the temperature gradient between center of panel and the edge is narrowed, reducing tensile stress and probability of failure in the edge region [48].

2.2.1.5 Total thermal conductance

The total thermal conductance through the glass sheets can be obtained by combining heat transfer from gas conduction, pillar conduction and radiation [47].

$$C_{center-of-glazing} = C_{gas} + C_{radiation} + C_{pillars} \tag{2.7}$$

The air-to-air thermal conductance at the center of glazing is defined by the combination in series of the glazing conductance plus the heat transfer coefficients at the external surface.

$$\frac{1}{U_{center-of-glazing}} = \frac{1}{h_1} + \frac{1}{C_{center-of-glazing}} + \frac{1}{h_2} \tag{2.8}$$

The total air-to-air thermal conductance of the vacuum glazing is the sum of the participation from the edge and the participation at the center of glazing [47].

$$U_{total} = U_{center_of_glazing} + U_{edge} \tag{2.9}$$

2.2.2 Evacuated Solar Collectors

Solar energy is an abundant resource used to produce electrical or thermal energy by use of photo-voltaic cells or solar collectors. Solar collectors are devices that collect thermal energy by absorbing solar insolation and carry it via fluids. Fixed or non-tracking collectors include devices such as evacuated tube or flat plate collectors.

Flat plate collectors consist of a transparent glass cover, and absorber plate, a channel for fluid flow and a back plate, as shown in Figure 2.7. As solar irradiance heats the absorber plate that energy is transfered to a fluid in contact with the absorber plate. The glass cover, back plate and lateral insulation are in place to mitigate undesired heat loss and improve system efficiency [80].

Evacuated tube collectors consist of a heat pipe inside a glass enclosure which is evacuated to minimize heat loss from convection. Fluids inside the heat pipe transfer thermal energy using evaporation-condensation cycles. Research has found this system's efficiency is not significantly affected by incidence angle and allows a

Figure 2.7 has been removed
from this version of the thesis
due to copyright restrictions

Figure 2.7: Diagram of an evacuated flat plate solar collector. Reprinted from [81].

range of orientation between 25°C and 60°C [81].

Research conducted in solar collectors has investigated selective coatings with high solar absorbance and low thermal emittance [82], trough and plate geometry [83], effect of different insulators [84] and innovative fluids with increased thermal conductivity [85]. It was found that selective coatings can produce a system efficiency of 0.77 at 20 °C [82], and up to 0.91 at 60 °C [86]. It was also found that geometry and insulators suppressing convection significantly increased system performance [80].

Evacuated flat plate collectors combine the aesthetics and high fill factor of flat pate collectors with the reduced heat loss of coefficients of evacuated tubes. An array of pins support the glass enclosure resisting atmospheric pressure. It has been found that an internal pressure of 0.5Pa is necessary to suppress convection.

Although, using a non-selective high emittance coating on the absorber plate yields lower performance than conventional flat plate collectors with selective coatings. However, including a selective coating on evacuated flat plate solar collectors results in higher efficiency than even the best conventional flat plate collectors, trough collectors or evacuated tubes [87].

Conventional flat plate and evacuated tube collectors are commonly found as commercial solutions for domestic hot-water supply, due to the low (60 °C) medium temperature requirements [81, 88]. Evacuated flat plate collectors can achieve higher temperatures and have been used for industrial process heat applications and desalination [87, 89].

2.2.3 Composite Vacuum Insulated Panels

Vacuum insulation panels or VIPs rely on a core void of fluids to achieve low values of heat transfer. The extraordinary low thermal conductivity of vacuum insulation panels or VIPs is achieved by virtually eliminating convection, stifling radiative heat transfer and reduced solid conduction through the panel's core. This can be accomplished at different pressures depending on the panel's composition.

Composite VIPs' constitution is commonly limited to a porous core material, a barrier envelope and occasionally supporting materials, such as getters or desiccants, to regulate the presence of gases or moisture. Metalized polyethylene foils are used for the envelope, being one of few solutions capable of fulfilling the permeation rates and durability requirements for building applications. Materials with larger pores, such as fibers and foams require envelopes 100 times more gas tight in order to maintain a service life over 30 years [44].

Core materials can be described by three broad categories: fibrous, cellular and granular. Fibrous materials are characterized by high porosity (up to 90%). Cellular insulation, such as Polyurethane or expanded Polystyrene foam, can be closed or open cell materials with low-density, low-heat capacity and relatively good compressive strength. Granular insulation is composed by bonded particles or fragments of inorganic materials such as perlite, diatomaceous silica, and vermiculite [90]. Nanostructured porous materials are favored since these are the least sensitive to pressure increase [44]. Different pressure levels will be required depending on the material, ranging from 20×10^{-3}bar, in the case of pyrogenic silica [52], to 0.01×10^{-3} bar with fibrous materials [49].

Pioneering research for VIPs came from soviet scientist Kaganer [91] in 1969. He measured the thermal conductivity of powdery and fibrous materials as a function of external load, gas pressure and temperature. Using a linear superposition of gaseous, solid and radiative conductivity he was able to find pore sizes for various powder materials using the following equation [91].

$$\kappa_{eff} = \kappa_{solid} + \kappa_{rad} + \frac{\kappa_{G0}}{(1 + 2\beta Kn)} \tag{2.10}$$

Where κ_{eff} is the effective thermal conductivity, κ_{solid} is the solid thermal conductivity, κ_{rad} is the radiative thermal conductivity, κ_{GO} is thermal conductivity of still air at ambient pressure and Kn is the Knudsen number.

Years later the scientific community corroborated Kaganer's findings but amended the equation finding that the effective thermal conductivity of the VIP can be calculated as the sum of all thermal transfer mechanisms plus a coupling term [44]:

$$\kappa_{eff} = \kappa_s + \kappa_g + \kappa_r + \kappa_c \tag{2.11}$$

Where;

κ_{eff} is the total effective conductivity

κ_s is the solid conductivity

κ_g is the gaseous conductivity

κ_r is the radiative conductivity

κ_c is the coupling term

The coupling term is negligible at low pressures but can take a more significant role with increasing pressure as the gas begins to short contact resistance in the microscopic structure of the core material [44]. Since empiric testing cannot fully isolate individual heat transfer mechanisms, theoretical analysis on each of these can provide detailed information on the performance of the VIP and offer insight on potential improvement. Heat transfer mechanisms vary between material categories. The internal structural composition of each material will affect heat propagation through the solid matrix. E.g. cellular materials exhibit a different composition from fibrous materials; see Figure 2.8.

2.2.3.1 Solid Conduction

Deriving accurate models for the prediction of solid conduction is not a trivial task for any core material due to the complexity and randomness of particle size and arrangement. However, assuming uniform distribution and particle size, simple models

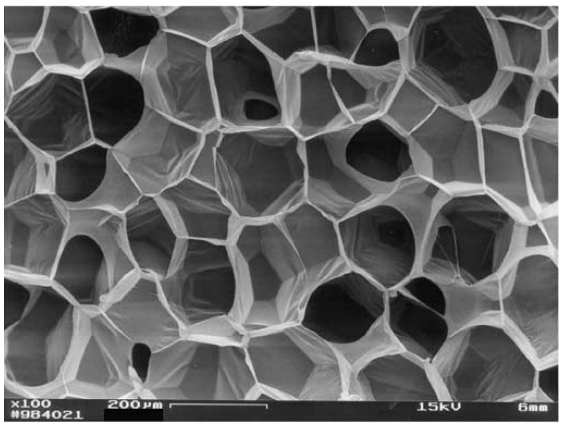

(a) Cellular structure of XPS foam ($33kg/m^3 Density$). Reprinted from [92] Copyright (2017), with permission from Elsevier, license number 4044731296024.

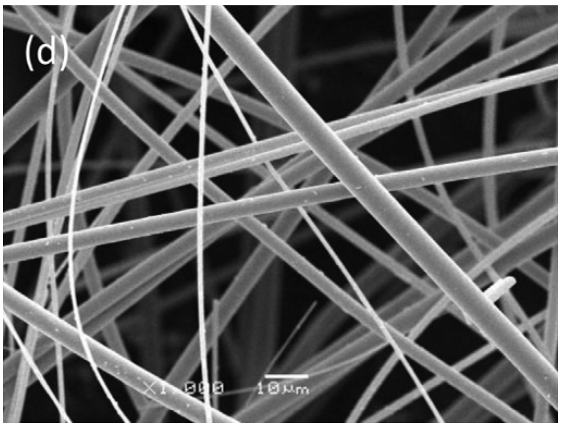

(b) Fibrous structure of glass fibre material. Reprinted from [51] Copyright (2015), with permission from Elsevier, license number 4044740402340.

Figure 2.8: Microscopic Structures of different types of insulating materials

have been proposed for granular, fibrous and cellular core materials. Figures 2.9 and 2.10 show the simplification of the microscopic structure for fibrous and cellular insulation on which the respective models are constructed. A similar approach is taken for granular materials, assuming a uniform hexagonal arrangement for spheres of equal size [49].

Equations 2.12 [93], 2.13 [94] and 2.14 [95] are part of the analytic models describing the thermal conductivity of a layer composed of granular, fibrous and cellular materials, respectively. It should be noted that results from the granular equation, as well as other sphere arrangements proposed by [93], estimate the powder layer's thermal conductivity to be higher than empirical measurements reported by Fricke [96].

$$\kappa_{s-powder} = \kappa_p \left(\frac{96(1-v^2)p_{atm}}{E} \right)^{1/3} \tag{2.12}$$

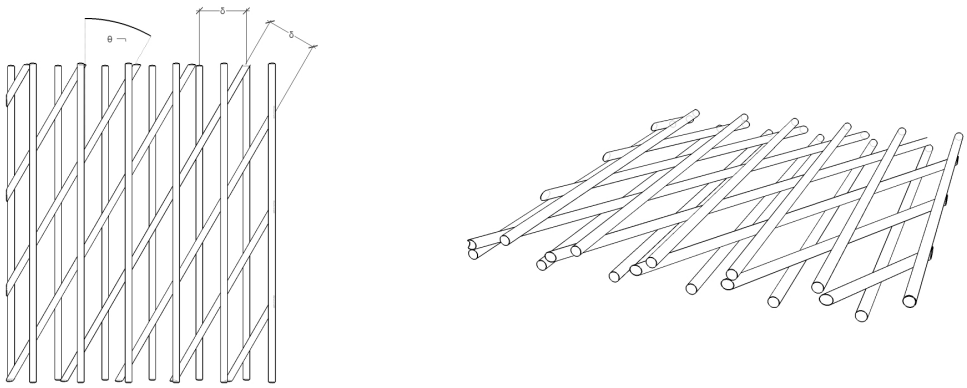

(a) (b)

Figure 2.9: Geometric arrangement for fibrous insulation simple model (a) Plan view of the simple model (b) Tilted view shows staggering of fibres. Recreated from [49] Copyright (2009), with permission from Elsevier, license number 4044740714521.

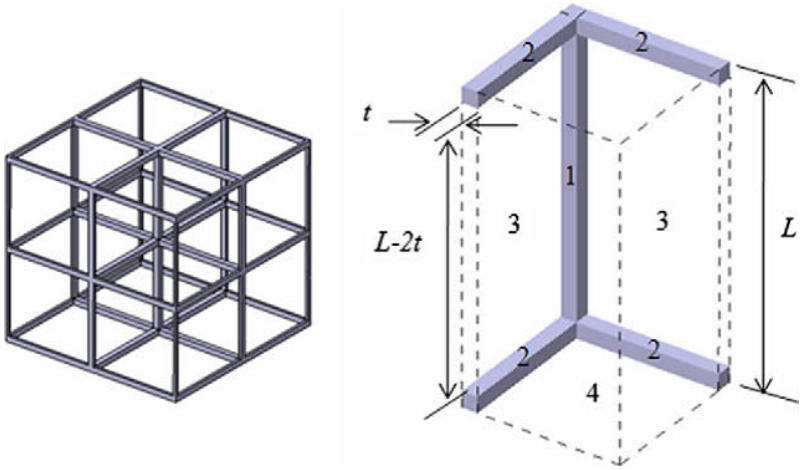

Figure 2.10: Graphic representation of the cubic structure in cellular insulation. The image on the right represents the symmetric elementary unit, which is $\frac{1}{4}$ of a single cell (in this case cubic). Reprinted from [49] Copyright (2009), with permission from Elsevier, license number 4044740714521

$$\kappa_{s-fiber} = 16\kappa_f \left[\left(\frac{\sqrt{2}\pi^4 E_0}{24p\left(1-\Pi^4\right)\left(1-v^2\right)} \right)^{1/3} + \frac{\pi^2}{4\left(1-\Pi\right)^3 \sin^2\theta} \right]^{-1} \tag{2.13}$$

$$\kappa_{s-cellular} = \frac{4\kappa_s t^2}{L^2} \tag{2.14}$$

Where;

$\kappa_{f,s,c}$ is the thermal conductivity of the fiber, sphere or cell $[W/mK]$

E_0 is Young's modulus for the fiber material $[Pa]$

p is the external pressure $[Pa]$

Π is the porosity of the layer

v is the Poisson's ratio of the fibre material

θ is the angle between fibrous layers

In addition to analytic models, the thermal conductivity of core materials in-vacuo has been measured empirically. Table 2.3 summarizes the thermal conductivity of several core materials employed in VIPs. Thermal conductivity of these materials was measured with an evacuable guarded hot plate device LOLA II, which includes a piston system to apply a variable pressure to load onto the evacuated sample. Sample mean temperature was varied between 10 and 400 °C [94, 96]. Calculated values relied on mathematical models built assuming uniform particle distribution, a cubic model was used for the open-cell foam, and an equidistant and staggered fibre model was used for the glass fibre insulation [49].

2.2.3.2 Gaseous Conduction

The thermal conductivity of the the rarefied gas can be calculated by the last term in equation 2.10. Where the gas thermal conductivity κ_g is a function of the thermal

Table 2.3: Solid thermal conductivity for various core materials under evacuated conditions (10Pa gas pressure) and under ambient compressive load.

Material	**Method**	**Load** bar	ρ $\frac{kg}{m^3}$	κ $\frac{W}{mK}$	**ref**
Diatomite	Measured	1	350	<0.01	[96]
Perlite	Measured	1	150	<0.01	[96]
micro silica	Measured	1	360	<0.01	[96]
opacified silica aerogel	Measured	1	150	0.003	[96]
borosilicate glass fiber paper	Measured	1	90-150	0.001 - 0.002	[94]
Alumina fiber fleece	Measured	1	70	0.003	[94]
PU foam	Calculated	1	70	0.005	[49]
Glass fiber	Calculated	1	250	0.0021	[49]

conductivity of still air κ_{G0}, β coefficient (1.6 for air) and the Knudsen number Kn, which is the ratio of the molecular mean free path and pore width ϕ [91, 66, 44]:

$$\kappa_g = \frac{\kappa_{G0}}{1 + 2\beta Kn} \tag{2.15}$$

The variation of the gas thermal conductivity κ_g with gas pressure p can be rewritten as [44]:

$$\kappa_g = \frac{\kappa_{G0}}{1 + \frac{p_{1/2}}{p}} \tag{2.16}$$

Where $p_{1/2}$ is the gas pressure at which the gas thermal conductivity equals half the conductivity of the still gas ($\kappa_g = \kappa_{G0}/2$). From this equation can be interpreted that nanostructured materials with pore width $\phi = 200nm$ require a pressure below 1000Pa to avoid gaseous conduction. Coarser materials with a pore width $\phi = 20\mu m$ require pressure lower than 10 Pa to suppress gaseous conduction [44].

2.2.3.3 Radiative heat flow

Radiative heat transfer is attenuated by scattering, absorption and emission of the core structure. A common method to evaluate radiative heat exchange in thermal insulation structures relies on diffusion approximation. This method is limited to optically thick elements, which concerns most cases of insulating materials. The radiative conductivity for an optically thick specimen with a mean temperature T_m is [44]:

$$\kappa_r = \frac{16n^2\sigma T_m^3}{3E_R(T_m)} \tag{2.17}$$

Where $T_m = (T_1 + T_2)(T_1^2 + T_2^2)/4$, n is the index of refraction and E_R is the Rosseland mean extinction coefficient, which is the reciprocal of of the mean free path λ_{ph} of the thermal photons and is correlated with density ρ and mass specific extinction $e(T_m)$ [44].

$$E_R(T_m) = e(T_m)\rho = \frac{1}{\lambda_{ph}} \tag{2.18}$$

Using these equations we can evaluate that for opacified silica kernels with $\lambda \approx 100nm$ the VIP will need to be 20mm thick for infrared radiation transfer to occur diffusively rather than ballistic. Consequently, the radiative conductivity of an opacified silica core with a mean temperature $T_m = 300K$, $e_{T_m} \approx 50 - 60\frac{m^2}{kg}$ and $\rho \approx 150\frac{kg}{m^3}$, is $\kappa_r \approx 0.001\frac{W}{mK}$ [44].

The following table includes the radiative conductivity for several filling materials, including powders, fibers and foams.

Table 2.4: Calculated radiative thermal conductivity for several core materials.

Material	T_m K	**e** $\frac{m^2}{kg}$	ρ $\frac{kg}{m^3}$	κ_r $\frac{W}{mK}$	**ref**
Glass fibers	300	50	250	0.001	[97, 49]
SICSIP28	300	61	232	0.003	[98]
SIP	300	20	180	0.005	[96, 49]
PU foam	300	44	70	0.003	[99, 49]

SICSIP28 precipitated silica with silicon carbide powder, SIP precipitated silica

2.2.3.4 Edge Conduction

VIPs have an excellent thermal resistance at the center of panel, with thermal conductivity values near $0.004\frac{W}{mK}$ [96, 44], however the heat bridging effect at the edges has been the focus of research in pursuit of lower overall thermal conductivity. Heat loss through the edges occurs by solid conduction through the film sealing in the vacuum. Barrier films are composed of polymeric substrates (PP, PE, PET, PA) with a thin layer of aluminium ($20 - 100nm$ thick). These multi-layered films are characterized by very low permeability rate to dry gases and water vapor [100]. Thicker membranes (6–12μm) will have lower permeation rates, but increase heat bridging effects [101].

Table 2.5 presents the thermal conductivity of some materials used for barrier films. From these values the heat flux through the film can be calculated as a parallel resistances. However, the type of film and wrapping at the edge needs to be considered since multi layered films that seal and wrap around the edge will triple the width of the conductive material over the length of this overlap, increasing solid conduction through the edge [100].

Laboratory testing has shown that including the edge effect results in noticeable

Table 2.5: Thermal conductivity of barrier film materials

Material	**kappa** $\frac{W}{mK}$
Aluminum (foil)	160
Aluminum (coated)	200
PE low density	0.32
PET	0.24

Source: [102]

decrease of the overall thermal resistance. Measurements conducted by Ghazi on fumed silica VIPs of size $500 \times 500mm$ with metalized barriers of thicknesses 90nm, 300nm and 8 μm, the edge effect will reduce the center of panel thermal resistance by 25%, 28% and 68%, respectively [102].

2.2.3.5 Limitations

The outstanding thermal performance of VIPs is not without limitations. Weaker aspects of VIPS, such as permeation over time, fragility and cost have stifled their adoption in the building sector.

The difficulty in manufacturing these panels, from producing the core material and barrier film to evacuating the panel, result in an expensive product that can cost well over 100 times per volume by comparison to common insulating materials.

In addition to cost, the deterioration over time has also been a source for concern. While observations and calculations suggest that permeation through current barrier films on European climates should result in VIPs thermal conductivity lower than 0.007 $\frac{W}{mK}$ over 50 years [44], manufacturing imperfections and prolonged service life can significantly reduce the performance of VIPs [27]. It has also been shown that stress can produce delamination between the layers of the film [103], compromising

the vacuum.

Moreover, improper handling of the panel at any given time may puncture the envelope and render the panel useless. Mechanical rubbing against adjacent surfaces caused by thermal expansion or building shifts can also result in envelope weakening or rupture.

The outstanding performance of the technology calls for further research in the subject towards creating a commercially appealing product through competitive pricing or added benefits.

2.2.4 Hollow-core Vacuum Insulated Panels

Hollow-core panels, sometimes referred to as edge-spacing panels, eliminate the need of a core material by diverting structural loads from the core to the envelope and internal structural array. This type of vacuum insulating solution substitutes the nano-structured core material for a macroscopic structural array with reduced contact area to avoid solid conduction as much as possible. At the time of writing, the only documented case of hollow-core vacuum panels was that of Nemanic, which included an internal structure composed of staggered glass bars or glass beads [57], as shown in Figure 2.11. Hollow-core VIPs could provide a more durable panel with a longer service life, as the rigid envelope will be much more resilient that multi-layer barrier films employed in composite VIPs.

Investigation conducted by Nemanic found that lateral solid conduction through the envelope is a considerable drawback, since materials suitable for this type of construction have high thermal conductivity. Although he failed to provide quantitative data on the subject it was found that stainless steel (0.1 - 0.15mm thick)

Figure 2.11: Internal structure of Nemanic's hollow-core VIP. The image on top shows staggered glass bars, the image below shows stacked glass beads. Reprinted from [57].

was the best solution for a foil. In addition to the thermal aspects of the envelope it was found that roll resistance welding was the most adequate technique for sealing the edge in regards to laboratory samples. Evacuation of the sealed panel was hindered by limited conductance of the pumping tube and gap, large surface to volume ratio S/V (his 5mm gap VIP had an S/V ratio similar to Dewars glass, larger than cathode-ray tubes but much less than powder filled insulating panels), and compromised by long weld lines [57].

Nemanic was explicit in the hardships of manufacturing such a panel, and while he did provide insight into the mechanisms that drive thermal exchange through this type of panel, he did not provide information on the thermal performance of the manufactured prototype. It follows that research must be conducted to measure the thermal conductance of this type of insulating panel and to define composition necessities in function of thermal performance and structural stability.

2.2.4.1 Solid Conduction

Solid conduction in hollow-core VIPs occurs through the internal structure and the edges of the panel. Thermal bridging through the edges of the vacuum panel should not to be confused with thermal bridges resulting from the installed product, which may result from additional building elements foreign to the panel.

The solid conduction or heat rate , "Q", of the edge-spacer panel can be approximated by the general form of Fourier's Law [29]. For pragmatism in the building industry the steady state calculation are useful due to the prolonged application of the system and sides are assumed adiabatic due to the large surface are where cladding is usually applied. However, in reality, the system's response will be subject to temporal variations of heat rate and the panel's sides perpendicular to the

heat flux will not be perfectly isolated and will also be exchanging heat. In certain systems where a single mechanism (e.g. conduction, convection, radiation) is vastly dominant, the overall heat transfer of the system may be approximated by superposition of independent heat transfer mechanisms [44].

The theoretic and unobstructed solid conduction will be affected by the connections between solids. Thermal contact conductance between solids shows significant variations depending on the characteristics of contacting solids, pressure load, surface roughness and other properties [104, 105, 106, 107]. Consequently, initial analysis may assume a perfect connection without added thermal resistance, but as the project progresses, detailed models will incorporate the added thermal resistance at all connections to yield more accurate results.

Moreover, it is important to understand the possible and likely dependence of all heat transfer mechanisms; such a relationship may account for disparities encountered between empiric measurements and numerical simulations or analytical solutions.

2.2.4.2 Gaseous Conduction

A gas can be modeled at a macroscopic or microscopic level. The macroscopic level regards the gas as a continuum and its description is in terms of spatial and temporal variations of velocity, density, pressure and temperature. The microscopic level describes the gas as a collection of discrete particles and its description is in terms of individual molecular properties, such as position, velocity and state. The average molecular values for a discrete fraction of the gas equate to the macroscopic properties of the gas. When the gradients of the macroscopic variables become steep enough to match the order of the mean free path of molecules, the transport terms in

the Navier-Stokes equation become inaccurate, I.e. the gradients of the macroscopic model depend on intermolecular collisions and as density is reduced the rate of collisions becomes too low to maintain these macroscopic gradients [46]. Flow analysis in regimes beyond the continuum flow requires solving the Boltzmann equation. For non-trivial problems solutions of the Boltzmann equation require physically based numerical methods, such as the deterministic molecular dynamics method, MD, or the probabilistic Direct Simulation Monte Carlo Method, DSMC. For this project the DSMC method will be used as it is less computationally demanding.

The degree of rarefaction and consequently type of flow can be determined by its Knudsen number, Figure 1, which is amongst other factors a function of gas pressure and geometric dimensions. The Knudsen number can be calculated by [29]:

$$Kn = \frac{\lambda_{mfp}}{L} \tag{2.19}$$

Where L is the cross-sectional length between boundaries.

Figure 2.12 has been removed from this version of the thesis due to copyright restrictions

Figure 2.12: Flow regime classification by Knudsen Number. Adapted from [46].

Given the nature and scope of this project the mean free path of the molecules,

λ_{mfp}, can be calculated as hard spheres. For noble gases it can be an accurate approximation but for complex molecules it neglects dipole moments and electrical interactions [29].

$$\lambda_{mfp} = \frac{k_b T}{\sqrt{2}\pi D^2 p} \tag{2.20}$$

Where k_b is the Boltzmann constant, D is the diameter (m) of the molecule considered as a sphere, and p is the pressure $[Pa]$.

Prior to numerical simulations analytical evaluation of a simplified model can be conducted through Smoluchowski's temperature discontinuity model. Smoluchowski observed a temperature discontinuity in low pressure environments, which for parallel plates describes the heat flux $\left(\frac{W}{m^2}\right)$ as [66]:

$$Q'' = \frac{\kappa_{G_0}}{d + 2\beta}\left(T_1 - T_2\right) \tag{2.21}$$

Where;

κ_{G_0} is the thermal conductivity of the still gas $\left[\frac{W}{mK}\right]$

d is the distance between the parallel temperature boundaries $[m]$

β can be expressed as [66]

$$\beta = \left(\frac{\kappa}{\eta C_v}\right)\left(\frac{2}{\gamma + 1}\right)\left(\frac{2 - \alpha}{\alpha}\right)\lambda_{mfp} \tag{2.22}$$

According to [108] $\frac{k}{\eta C_v}$ can be substituted by $\frac{1}{4}(9\gamma–5)$ and thus making it dependent only on the ratio of specific heat capacity:

$$\beta = \left(\frac{9\gamma - 5}{2\gamma + 2}\right)\left(\frac{2 - \alpha}{\alpha}\right)\lambda_{mfp} \tag{2.23}$$

Where;

γ is $\frac{C_p}{C_v}$

λ_{mfp} is the mean free path of the gas molecules (m)

α is the accomodation coefficient

2.2.4.3 Radiation

Radiative heat transfer can be calculated by analytical expressions described in [29]. The chosen method involves calculating the view factor (also referred to as shape factor) between participating surfaces and solving overall heat exchange in the system treated as a resistance network. For radiative heat exchange between two surfaces the view factor between parallel surfaces i and j can be derived from the following expression:

$$F_{ij} = \frac{1}{A_i}\int_{A_i}\int_{A_j}\frac{\cos\theta_i \cos\theta_j}{\pi R^2} dA_i dA_j \tag{2.24}$$

Where;

R is the shortest distance between the centres of both surfaces

θ_{ij} is the angle between the surface normal and R

For two parallel plates of equal size the resulting view factor is [29]:

$$
\begin{aligned}
F_{ij} =& \frac{2}{\pi \overline{X}\overline{Y}} \left\{ \ln \left[\frac{\left(1+\overline{X}^2\right)\left(1+\overline{Y}^2\right)}{1+\overline{X}^2+\overline{Y}^2} \right]^{1/2} \right. \\
&+ \overline{X}\left(1+\overline{Y}^2\right)^{1/2} \tan^{-1} \frac{\overline{X}}{\left(1+\overline{Y}^2\right)^{1/2}} \\
&\left. + \overline{Y}\left(1+\overline{X}^2\right)^{1/2} \tan^{-1} \frac{\overline{Y}}{\left(1+\overline{X}^2\right)^{1/2}} - \overline{X}\tan^{-1}\overline{X} - \overline{Y}\tan^{-1}\overline{Y} \right\}
\end{aligned} \tag{2.25}
$$

Where $\overline{X}$ and $\overline{Y}$ are the width and length divided by the distance between plates.

Postulating that radiation between two opaque objects whose absorptivity, emissivity, and reflectivity are independent of direction and wavelength the emissivity is equal to the absorptivity. Following the previous assumptions the radiative heat flux of surface i is expressed as:

$$
q_i = \frac{E_{bi} - J_i}{\left(1-\epsilon_i\right)/\epsilon_i A_i} \tag{2.26}
$$

Where;

E_{bi} is the emissive power (W/m^2) of the surface treated as a black body

J is the radiosity (W/m^2) of the surface

The resistance between the blackbody emissive power and radiosity of each surface is the surface resistance expressed as:

$$
R_{surface} = \frac{1-\epsilon_i}{\epsilon_i A_i} \tag{2.27}
$$

Where A is the surface area and ϵ is the emissivity.

It should be noted that atmospheric gases have a transmittance lower than one for certain wavelengths, predominantly in the Infrared spectrum . However, for this research it is postulated that the high vacuum of the internal cavity will act as a non-participating medium. As such, the net radiative heat flux between two grey bodies in an enclosure would be treated by a resistance network according to the following diagram 2.13.

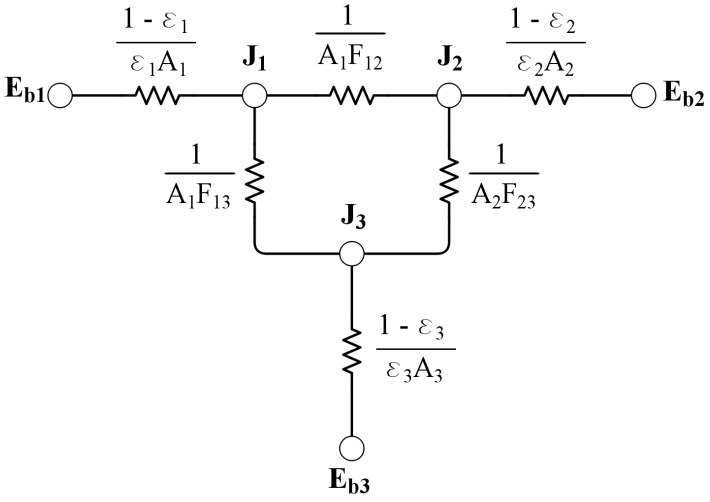

Figure 2.13: Resistance network between two grey bodies within an enclosure through a non-participating medium

The enclosure, represented as surface 3 in Figure 2.13, is treated as a perfect black body that absorbs all incident irradiation and as such the resistance expressed in equation 2.27 becomes 0. If this 0 value is then substituted in equation 2.26 its radiation can be evaluated as equal to its blackbody emissive power; the same happens when the surface area approaches infinite. When a surface is much larger than the other surfaces in the system it is convenient to treat it as infinite, as it will eventually intercept radiation not transferred between the smaller objects.

This resistance network shows how gray surface radiation is black body radiation restricted by emissivity, an optical property of the radiating surface. In addition, the resistance network also shows how the radiative resistance between two radiating surfaces is a function of view factor. From this network it can be interpreted that larger emissivity and view factor coefficients will present lower resistance to radiative exchange.

The resistance presented by the medium is the inverse of the product of the view factor and the area of one of the involved surfaces:

$$R_{medium} = \frac{1}{F_{ij} A_i} \tag{2.28}$$

Where F_{ij} is the view factor between the radiating bodies. From the summation rule we can then infer that F_{13} and F_{23} will be equal to 1–F_{12}.

The resulting equations from the previous network are:

$$\begin{aligned} \frac{E_{b1} - J_1}{(1-\epsilon_1)/\epsilon_1 A_1} &= \frac{J_1 - J_2}{1/F_{12} A_1} + \frac{J_1 - E_{b3}}{1/F_{13} A_1} \\ \frac{E_{b2} - J_2}{(1-\epsilon_2)/\epsilon_2 A_2} &= \frac{J_2 - J_1}{1/F_{21} A_2} + \frac{J_2 - E_{b3}}{1/F_{23} A_2} \end{aligned} \tag{2.29}$$

The solution to these equations provides a balanced energy exchange with detailed flux at any point in the radiation network. Surfaces can be subdivided for greater accuracy; however this will involve deriving the view factor for multiple subsurfaces and can prove to be a tedious task for analytical analysis. The numerical solution employed uses the same method for each individual cell in the region, thus providing a more accurate model with great detail in the radiative transfer gradient.

2.3 Heat Transfer Manipulation

Heat transfer manipulation can be achieved by controlling heat transfer mechanisms, either jointly or isolated. In opaque environments this modulation has commonly been achieved by controlling convection, either at microscopic or macroscopic scales, within a sealed element. However, alternative designs have also investigated the effects on regulating solid conduction and radiation. Effective designs of dynamic insulation include the implementation of a bidirectional thermodiode [109] [110] , altering the pressure of a gas medium [111], and controlling the spacing between multi-layered polymeric membranes [112, 113] amongst others.

2.3.1 Conduction

Manipulating conductive heat transfer is proposed has been proposed by [114, 112, 113], although each solution differs in composition the underlying principle is the same, creating a thermal short by connecting the hot and cold side under specific conditions.

A theoretical solution for adaptable insulation proposes the use of multiple polymeric membranes and air gaps as wall insulation. Although the analytical model suggests high sensitivity to variable emissivity values in the innermost-outermost wall membranes, the primary manipulation mechanism relies in affecting heat conduction across the composite wall construction. The adaptability of the insulation occurs by having air gaps between multiple insulation membranes, which could be collapsed to increase the thermal conductivity when desired.

The final results explore one of the more feasible wall configurations analyzed,

comprised of 9 air gaps of $1.56cm$ each, internal polymeric membranes of $2mm$ in thickness with a conductivity of $0.2Wm^{-1}K^{-1}$, total wall thickness of $15cm$ and thermal conductivity for outermost wall materials of $0.8\frac{W}{mK}$. The resulting thermal resistance from feasible wall composition is 3.23 and $3.7\frac{m^2K}{W}$ for summer and winter, respectively [112]. The resulting estimated thermal conductance range from 0.309 to $0.27\frac{W}{m^2K}$, constituting a modulation variation of 13%.

It should be noted that the analysis carried out does not consider any mechanism for collapsing interior membranes, or even a fastening method for preventing the membranes from bending and creating heat bridges. While the analytical method does include approximations to the radiative heat exchange, through both solid and gaseous elements, it fails to explore 2D heat transfer, view factor and particular wavelength interactions. In addition, the assumption that air gaps remain completely stagnant, neglecting buoyancy from temperature changes, could distant results of the discussed model from actual thermal behavior.

Another solution involves heat activated bimetallic conductors that transfer heat from source to heat sink. An isolated region of adhered metallic layers with different thermal expansion properties would become deformed under the proper thermal conditions. These isolated regions of multi-layer metallic envelope would become flexible at certain temperatures, thus collapsing to the vacuum and creating direct contact with the opposite panel wall, effectively conducing heat by direct contact. The critical "bending" temperature could be achieved, by passive means, through external temperature conditions and radiation, or by internal electric resistances [114]. Take into consideration that deforming the envelope to achieve contact with the opposing envelope wall would require enlargement of the isolated region as the distance between panel walls increases. Therefore, this method for dynamic thermal

manipulation would not be capable of precise thermal conduction modulation in thicker panels, and would be limited by fixed increments.

2.3.2 Convection

Manipulating heat exchange can also be achieved by controlling convective heat transfer. Solutions created around controlled convection rely on fluid flow mechanics to stifle or boost heat exchange. E.g. The buoyancy of a hot fluid is used to divert heat into a specific direction or region. Methods proposed to manipulate heat transfer by altering convective exchange include utilizing latent heat of vaporization [115, 110], buoyancy[116], changing gas flow [117], and gas pressure [118, 119, 111, 120, 121].

2.3.2.1 Latent Heat Mechanisms

Thermodiodes or heat pipe mechanisms use the latent heat of vaporization, e.g. energy necessary for phase change, and buoyancy to exchange heat in a closed loop. On one end the fluid is exposed to elevated temperatures, which results in heat transmission through the liquid or gas medium towards the opposite end.

To control operation temperature different fluids can be employed such as methanol, ethanol, water, ammonia, mercury, etc. Alternatively, the pressure within the tube can be controlled to affect the partial pressure of the fluid and therefore its boiling point (Claperion-Clausius relation) and consequently its thermal conductivity. The heat pipe effect has been used in cooling panels by means of siphon heat pipes which limit the heat flow by fluid conduction to a single direction, and have been demonstrated to achieve a conductivity of up to $0.36 W m^{-1} K^{-1}$ when desirable and

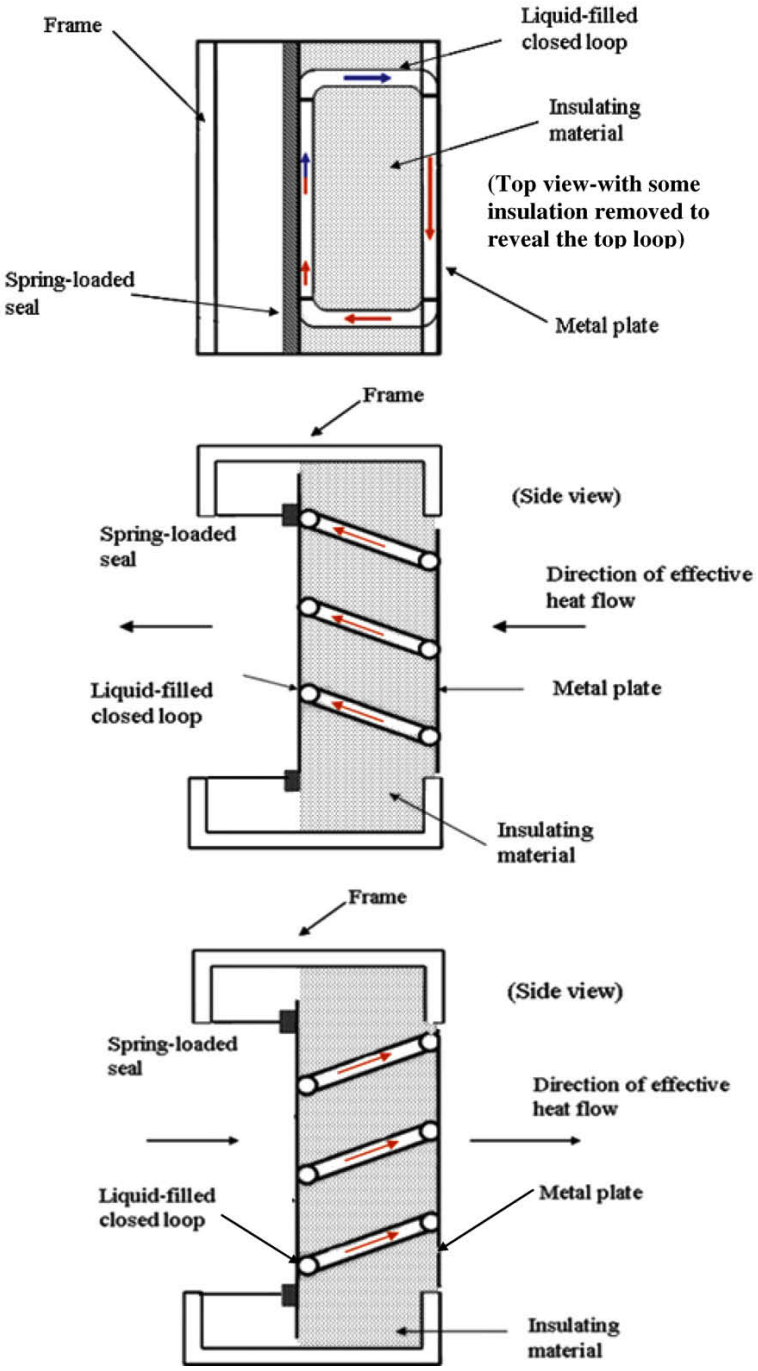

Figure 2.14: Diagram of bidirectional thermodiode. Reprinted from [110] Copyright (2019), with permission from Elsevier, license number 4632150998853

$0.07 W m^{-1} K^{-1}$ when undesired, that is when external temperatures are lower than internal temperatures. Since internal conditions of the pipe exist in near vacuum when the fluid is in liquid state, undesired convection is negligible. The most significant adverse effect is by solid conduction (heat bridges) through the walls of the pipe [115].

A bi-directional thermodiode involves a system where the direction of the heat flow can be easily altered and therefore loose or gain heat, depending on ambient and internal conditions. The dynamic behaviour of heat transfer has been studied in bayonette-type heat pipes [109], and similar parallelogram shapes [115]. However, to actively and intentionally control the direction of heat flow thermodiodes, rectangular heat pipe loops have been designed capable of changing elevation of the collector side of the panel by comparison to the radiator side [110].

2.3.2.2 Controlled Gas Flow

A patent solicited in 1969 [117] describes a method for controlling heat transfer by convection within a sealed panel by controlling gas flow and its inherent interaction with the surrounding solid surfaces.

The method described involves a panel with conductive fins, mounted internally at both sides of the panel, with a perforated reflective plate in a middle hermetic chamber filled with gas. The fins mounted internally serve to increase the area subject to heat transfer. Consequently, when subjected to eddy currents caused by the vibration of the inner perforated plate, convection would transfer heat across the insulation panel. Inversely, when static, the fins would stifle convection due to lack of a free convective path. The interior hermetic cavity holds a perforated plate influenced by electromagnetic vibrators to move and, consequently, produce eddies

that would increase heat transfer [117]. The method described permits a reversible function, heating or cooling, depending on the activation schedule for convective transfer.

A different approach described by Pflug involves a translucent element composed by two external glass panes, and an internal movable translucent insulation element surrounded by air, changing position to hinder or allow buoyant flow. With this method the overall U-value roughly varies by 100%, depending on the temperature difference [116]. The efficiency of heat transfer is affected by the placement of the interior insulation layer, which placed at any vertical limit would virtually eliminate convection. Of multiple variations on placement on the interior insulator(s), calculations performed on the thermal conductance demonstrates a lower limit of 0.65 and $0.74\frac{W}{m^2K}$ at temperature differences ($\Delta°C$) of $15°C$ and $30°C$ respectively, and an upper limit of 1.83 and $2.03\frac{W}{m^2K}$ for $\Delta°C$ values of $14°C$ and $28°C$ respectively [116]. Precise modulation to achieve any desired thermal conductance (U-value) may prove challenging since it would require precise estimation of complex fluid dynamics. In addition, current research doesn't mention the inclusion of any automated mechanism with which to control the position of the intermediate layer. Nonetheless, the panel itself suggests buoyancy could be used as a passive control for heat exchange.

2.3.2.3 Gas Pressure Mechanisms

Prior to the development of insulation technology with variable thermal exchange properties, a method for creating a vacuum insulation panel explored the idea of reclaiming hydrogen from a metal hydride [118]. The same principle of releasing a small amount of gas to affect the internal pressure of a vacuum panel was later put to use as a mechanism to dynamically alter the thermal exchange properties of an

insulation element [119, 111].

Similar ideas explored partial pressure as a method for controlling thermal exchange, yet relied on other means to evacuate fluid from the chamber. A solution for a thermally controllable container to be used in space describes the principle of pressure on gas conductivity. The proposed technology would rely on the vacuum of space to perform the labour of evacuating the gas [120]. A rudimentary method describes the same principle applied to walls or similar structures by connecting these to a vacuum pump [121].

The release and re-adsorption of hydrogen gas, in amounts of 20 to $50mbar$, has the potential to affect the thermal conductivity of a panel by a factor of 40. A relatively small, $5Wm^{-2}$, is required to maintain the gas pressure by heating up the metal hydride [119]. Caps and Benson describe, in their respective patents [111] [113], the effect of hydrogen gas released from a metal hydride , such as zirconium hydride, in a vacuum insulation panel (not specified in patent description) to alter pressure from $0.01mbar$ to $100mbar$ approximately. The behaviour of the panel with spun glass fibre (10 micron diameter) as core material results in a range of thermal conductivity of 0.002 to $0.2Wm^{-1}K^{-1}$ respectively. Variations between $0.01mbar$ and $10mbar$ resulted in an approximate thermal conduction increase by a factor of 50. The use of porous nanoparticles, such as fumed silica, is not as sensitive to hydrogen pressure variations as glass fibre, maintaining high levels of insulation even at a pressure of $100mbar$. This method provides a feasible method for altering the thermal conduction of building elements since only few grams of metal hydride are required per m^2, and 5 watts to release the gas. The release of hydrogen gas requires heating the metal hydride above $400°C$, and the adsorption process requires temperatures lower than $300°C$. The gas release process takes 10 minutes, assisted

by electric heating of the metal, while the adsorption process takes 20 minutes [111].

The application of the technology devised by Caps [111] was applied as part of a solar collector system, where the insulation panel was placed in contact with a steel plate optimized for a maximum absorptivity coefficient. The insulation panel was responsible of manipulating heat exchange by convection from the heat received by conduction from the "absorber" metallic plate. The switching of the panel is explored as functions of temperature difference and solar irradiance [119].

A negative aspect to this solution is the continuous dependence on energy to activate the release of gas from the metal hydride. To avoid constant energy consumption into heating the metal hydride a hydrogen gate is introduced. The hydrogen gate will allow the propagation of hydrogen molecules after its release but will block re-adsorption of such gas, even when the metal hydride is at cooler temperatures, until desired. The hydrogen gate is proposed of palladium or a suitable palladium alloy permeable to hydrogen gas at certain temperatures. The reported thermal resistance for a panel of 0.5 by 0.5 m with an interior cavity of 2.5 mm ranged between values 0.2 to 0.7 $\frac{m^2K}{W}$ [113]. The previous resistance values correspond to U-Values of 5 to 1.4 $\frac{W}{m^2K}$.

An investigation on the re-adsorption process would need to be conducted to determine its viability with regards to the time needed and its efficiency in complex geometries. The tortuous path present in nano-porous fumed silica or other similarly complex structures could potentially limit the release and re-adsorption process to a confined region in the vicinity of the hydride element.

2.3.3 Radiation

Materials that change their optical properties can control, to some extent, radiative energy transfer. These materials, thermochromic or electrochromic, will have two or more states with distinct absorption spectra. Solid electrochromic materials commonly found deposited as films, such as tungsten trioxide (WO_3), will not require constant charge to maintain the switched state. Such materials are sought for commercial applications in car mirrors, smart windows, aircrafts, battery indicators, etc. [122, 123].

Electrochromic devices are comprised of two electrodes separated by an electrolytic layer, commonly found as multiple films sandwiched together. These electrodes are made from materials such as nickel hydroxide ($Ni(OH)_2$) or tungsten trioxide (WO_3) which change optical properties under an appropriate electrical charge. By electrically controlling the ion flow between the electrochromic layer through an ion conductive layer and into a counter-electrode layer the emissivity properties of the electrochromic material are changed. To reverse ion migration the DC current applied must be reversed, consequently reversing the polarity of previous layers. The migration can be interrupted at any given point thus achieving intermediate emissivity values. The materials can be chosen according to desired wavelength emission. A multilayer device of NiO, Ta_2O_5 and WO_3 over a silver substrate was shown to change its emittance from 0.057 to 0.595 over a spectral range of 0.3 to 13.8 μm when exposed to radiation from a 300 K blackbody [124]. Even though the absorption band tested comprises approximately 50% of the total emitted energy by the black body, the emittance modulation measured demonstrates the potential for such coatings, especially in infrared environments. Electric current is not required

to maintain emissive properties and is only applied during the ion transition process. However, this process is not instantaneous and therefore the emissivity cannot be updated in very small time steps.

Similar to electrochromic devices, thermochromic materials will change their absorption spectra as a function of temperature, e.g. vanadium oxide, titanium oxide (Ti_2O_3), nickel sulfide (NiS), and vanadium oxy fluoride ($VO_{2-x}F_x$). Vanadium oxide can vary its infrared emittance from 0.2 to 0.8 within 5 °C temperature difference [113].

The application of optically changing coatings or films is promising due to the low energy consumption, significant change in emissivity and the flexibility to deposit the films in different materials and different geometries.

2.4 Structural Behaviour

The hollow-core panel will experience significant compressive stress due to the pressure differential between ambient pressure and the contained vacuum within the panel. It follows that the panel, and the elements which compose it, should be able to withstand this stress.

In flat evacuated windows with a pillar array structure, where the compressive stress from ambient pressure is similar, the critical structural conditions are tensile stress on the external face leading to micro-fractures in the glass and occurrence of conical fractures where the glass pane is in contact with the pillars [78]. Considering that a metallic skin will wrap the hollow-core VIP, external tensile stress is not as problematic as undesired deflection of the skin, which could alter heat transfer from desired conditions and could affect brittle coatings if these exist. Similarly, conical

fractures will not occur in the steel skin. However, if the internal structure is slender in proportion, it can fail by buckling to compressive stress. As such the limiting structural requirements are buckling of the internal structure and bending of the panel skin or envelope.

2.4.1 Buckling

The compressive load is assumed to be uniform and distributed equally amongst all structural elements and that structural elements are spaced apart in an equidistant rectangular array. Evaluation of the maximum load can be calculated from the elastic buckling of a column or the elastic buckling of a plate. These are in agreement within a short range but show divergence as the structural element becomes shorter in length.

2.4.1.1 Elastic buckling of columns

The structural element, or spacer, is evaluated as a column pinned at both ends. The maximum load is the defined as [125] :

$$P_{max} = \frac{\pi^2 EI}{H^2} \tag{2.30}$$

Where

- E = Modulus of elasticity $[Pa]$
- I = Moment of inertia $[m^4]$
- H = Column height

The moment of inertia is defined by:

$$I = \frac{1}{12} d t^3 \tag{2.31}$$

Where t is the spacer thickness.

By substitution we can correlate the dimensions of the array as follows:

$$H = \left(\frac{\pi^2 E I L_{spacers}}{p_{amb} A_{panel} d} \right)^{1/2} \tag{2.32}$$

And can be rewritten as:

$$H = \left(\frac{\pi^2 E S d t^3}{p_{amb} A_{panel} 12} \right)^{1/2} \tag{2.33}$$

Where S is the total number of spacer segments in the panel; $L_{spacers} = S * d$. Both equations relate critical force load to height of the spacers and their maximum segment length, d.

2.4.1.2 Elastic buckling of plates

The problem is now evaluated as a rectangular element, pinned on all sides, with uniform compressive stress, σ'', on opposite edges of length d. The compressive stress is described as [125]:

$$\sigma'' = K \frac{E}{1 - v^2} \left(\frac{t}{d} \right)^2 \tag{2.34}$$

Consequently, the maximum load, P_{max}, is obtained by multiplying the compressive stress by the area receiving the compressive force.

$$P_{max} = K \frac{E}{1 - v^2} \left(\frac{t}{d} \right)^2 (td) \tag{2.35}$$

The value K is dependent on the ratio H/d, and these values are tabulated in [125, 126]. If we plot these and perform a regression, Figure 2.15, we can approximate the relationship to the ratio H/d by the power law in the regression, where H/d is plotted along the x axis. This power law regression permits the reverse evaluation of a safe design ratio, H/d, by first establishing a critical force or stress.

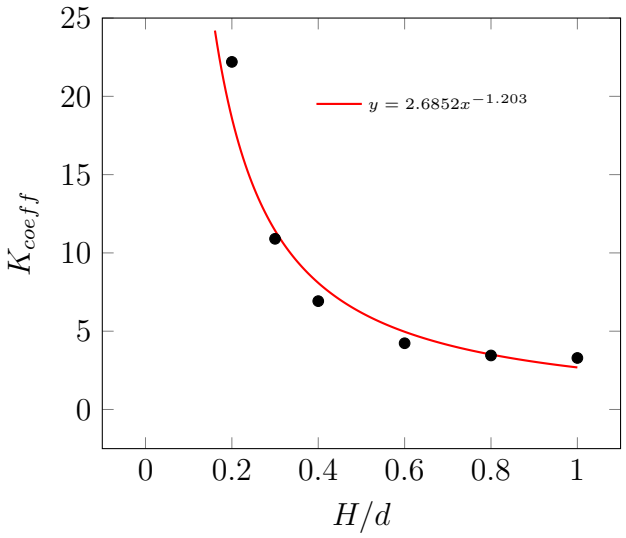

Figure 2.15: K coefficient for H/d ratios as tabulated by [125]. Power regression in red; correlation coefficient = 0.95.

Values beyond a ratio of 2.7 are closely bounded by a K value of 3.29. The data has been truncated beyond a ratio of 1 since these dimensions are unlikely to occur in the current application, moreover, ratios between 1 and 3 vary by less than 10%. In addition, at larger ratios this method for evaluating critical stress in elastic conditions becomes inaccurate as the material begins to yield and exhibits plastic deformation [126].

2.4.1.3 Conclusion on Elastic Buckling

The plate analysis is more conservative at smaller H/d ratios. An inversion of this conservative behavior is observed around a 0.2 ratio (Figure 2.16). Larger ratios will have to be disregarded as the previous plate analysis is inaccurate past a H/d ratio of 1, where the previous power law stops and where the material approaches a yielding point lower than calculated from the plate buckling analysis. Nonetheless, the results have been plotted, indicating with a dotted line where the analysis is insufficient and results in inaccurate values.

The plate analysis is favored as a clear failure point becomes evident from the predicted "safe" H/d ratios.

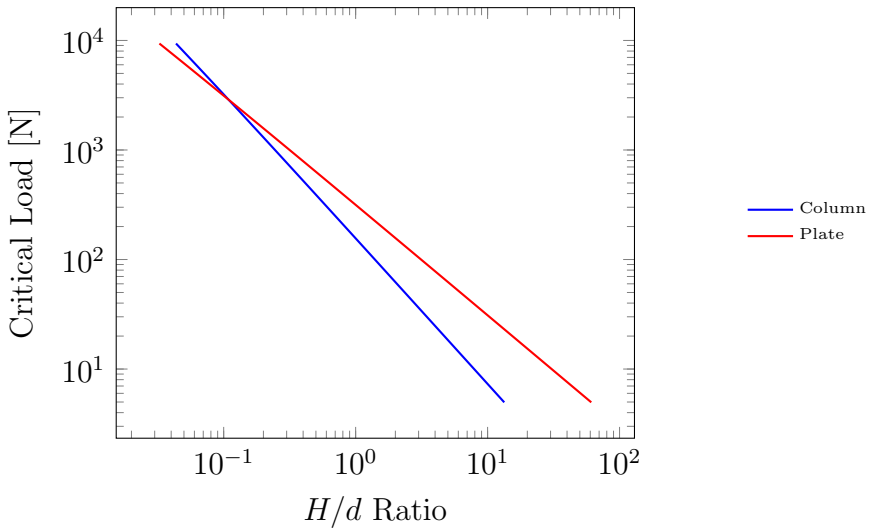

Figure 2.16: Maximum Load plotted against H/d ratio on a log-log base 10 chart. Plate analysis show more conservative results at smaller ratios and differs greatly from column analysis as the ratio grows. The H/d ratio is evaluated from the previous equations and as such is subject to inaccurate values past the proportional limit of the material, when plastic deformations should be taken into consideration.

2.4.2 Plate Bending

By continuity of the plate all sides of the rectangular plate are considered as fixed. According to [125] the max deflection y_{max} of the plate is obtained by the following equation:

$$y_{max} = \frac{-\zeta W b^4}{E t^3} \tag{2.36}$$

Where ζ is given by tabulated data and for a length to width ratio of 1, $\zeta = 0.0444$ for rectangular plates with simply supported edges or 0.0138 for fixed edges[125]; W is the uniform load, in this case ambient pressure; E is the elastic modulus and t is the thickness.

A parametric study calculated using the previous equation for stainless steel plates with different thickness and variable spanning distance indicates how increasing plate thickness will greatly improve tolerated spanning distance, as shown in Figure 2.17. The most conservative tolerance comes from spanning distance over 100, followed by tolerance defined as half of plate thickness. From this study it can be interpreted that flat plates thinner than 3mm will not be able to cover a distance over $300mm$ with tolerances of $\frac{t}{2}$ or $\frac{Span}{200}$. A $1mm$ thick AISI 304 stainless steel plate would fulfill $\frac{Span}{200}$ deflection criteria up to $80mm$ separation. A $3mm$ plate would withstand up to $260mm$ separation under the same criteria.

Both represent significant constraint of the maximum allowed distance between structural elements. Increasing the thickness of the plate will continue to increase the maximum allowed distance between structural supports, although at a costly expense of significant weight increase. These observations suggest that alternative plate stiffening techniques could provide a more efficient solution allowing for larger

spans with reduced deflection.

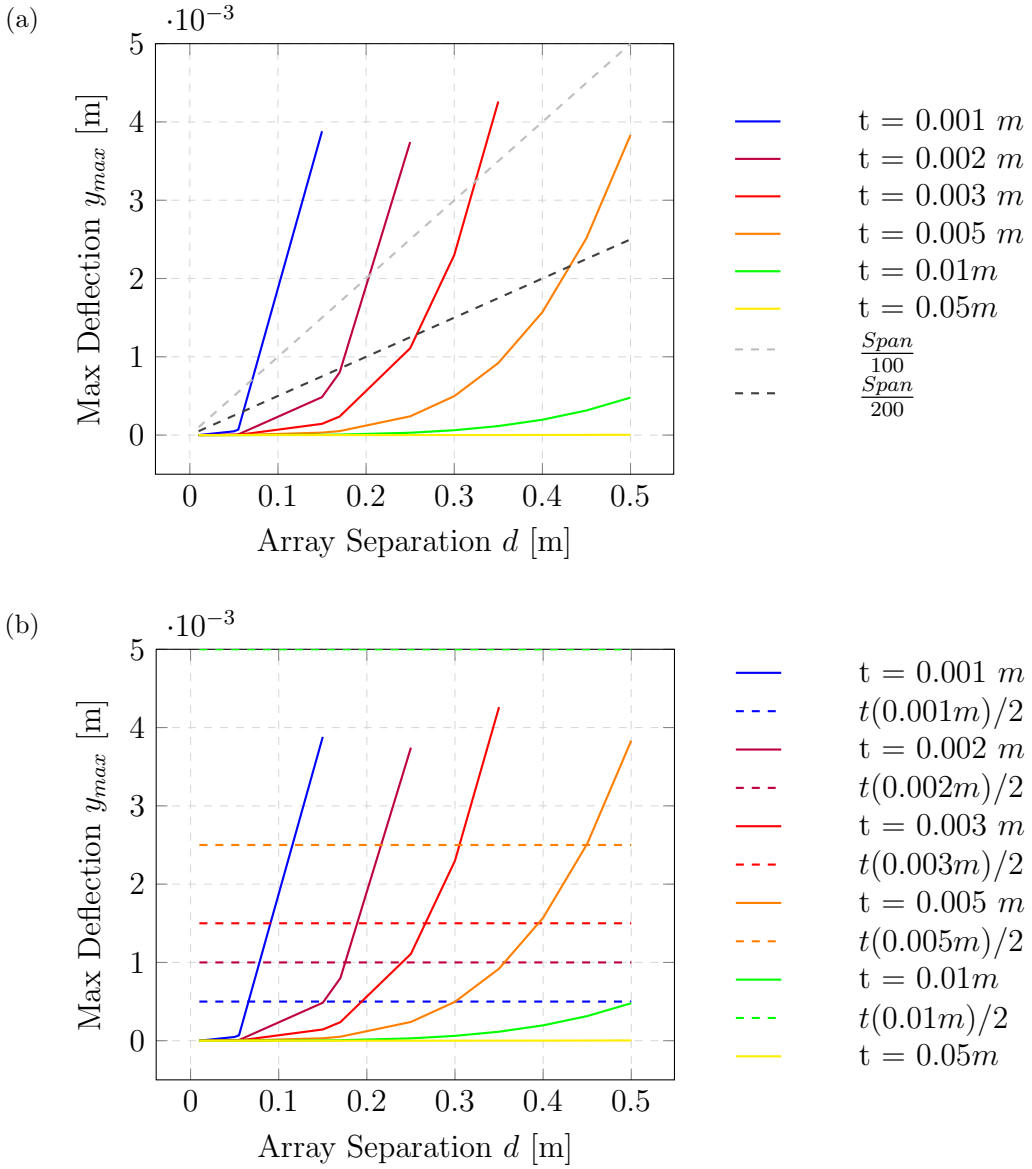

Figure 2.17: Bending parametric study for stainless steel rectangular plates of uniform thickness with fixed edges. Calculated maximum deflection as a function of spanning distance. Solid lines indicate plate deflection for different plate thicknesses. a) Calculated deflection compared to tolerated deflection defined by Span distance divided by 100 & 200. Points in curve over the dashed line exceed tolerances. b) Calculated deflection compared to tolerated deflection determined as half of plate thickness. Points in curve over the dashed line of the same color exceed tolerances.

As an example to overcome this limitation it can be postulated that each face of the panel, subject to uniform ambient pressure loads, is going to be supported by an additional layer of arched structures holding the steel face in tension when the arch is loaded by compression, as shown in Figure 2.18.

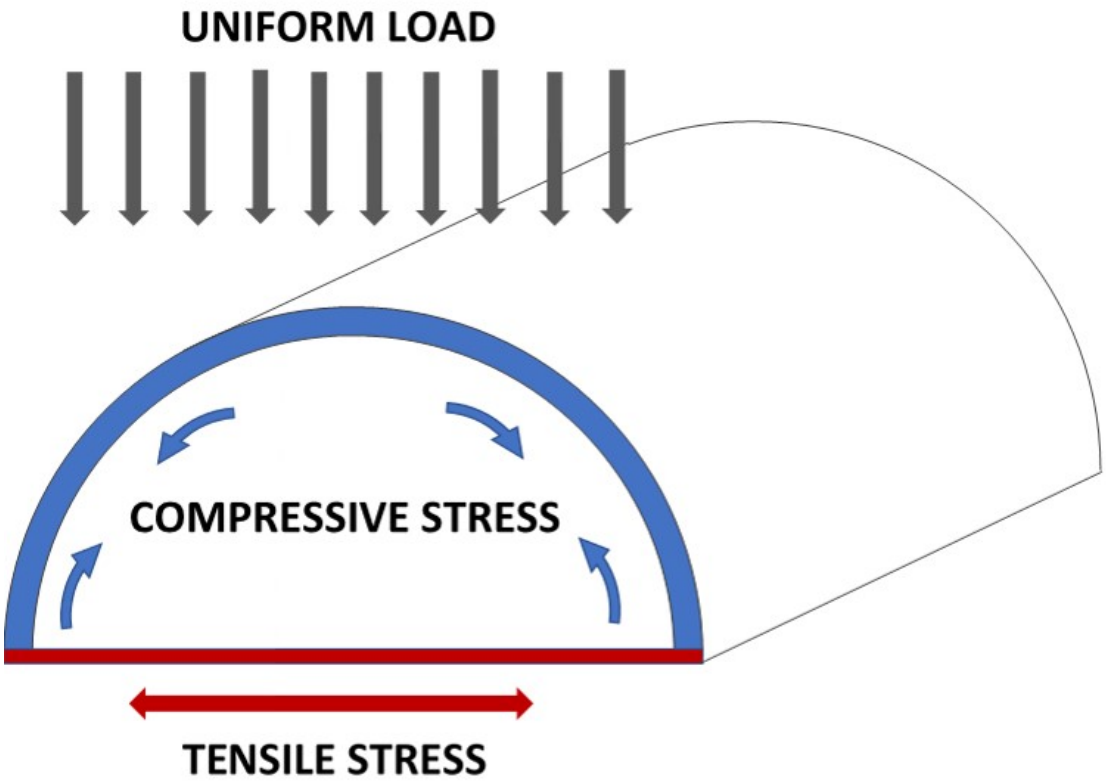

Figure 2.18: Diagram of vaulted skin support structure. The panel's face plate or skin is shown in red and being subject to tensile stress as the arched structure bends outwards when subject to a uniform load.

In this support system, a series of adjacent arches would redirect the compressive load from ambient pressure into tensile stress on the steel face holding the vacuum, thus preventing deflection and reducing the required thickness of the face plate. Arch, or vault, dimensions can be increased or decreased depending on the desired outcome. A single arch spanning the entire width of the panel would result in an

unruly arch height, thickening the high performance thin vacuum box by several orders of magnitude. A more subtle approach would utilize 49mm radius arches made from 0.5mm gauge AISI 304 stainless steel arch, that is, each arch spanning up to 98mm width and adding 49mm thickness per side, for a total added thickness of 98mm. With this application, the maximum total thickness of the hollow core VIP could be between 120mm and 150mm, depending on the thickness of the internal vacuum. The limitation then becomes the bending of the arch structure along the axis perpendicular to the arch cross-section, i.e. Bending of the vault along its longitudinal axis.

To determine the maximum longitudinal span of the vault it's necessary to define its moment of inertia about its centroid. According to [125] the moment of inertia of a hollow semicircle is defined by:

$$I_x = \frac{\pi}{8}(r^4 - r_i^4) - \frac{8}{9\pi}\frac{(r^3 - r_i^3)^2}{r^2 - r_i^2} \tag{2.37}$$

Where r is the external radius, r_i is the internal radius.

Having defined the moment of inertia of the arch its maximum deflection along its longitudinal axis can be calculated using beam theory. The added rigidity of the steel tie binding the arch is neglected for a more conservative approach. The maximum deflection of a simply supported beam will come at its half length and is expressed by [125]:

$$y_{max} = \frac{-5wl^4}{384EI} \tag{2.38}$$

2.5 Conclusion

Research innovating on insulating solutions has investigated several systems relying on vacuum enclosures to eliminate convection. Amongst developed vacuum insulating technology are found vacuum glazing, evacuated solar collectors, composite vacuum insulated panels and hollow-core vacuum insulated panels. The composition of these systems has been investigated in regards to their geometrical proportions, material composition, optical properties, internal pressure and other variables that affect their thermal conductance.

The following list provides findings from research conducted in these systems that can provide useful insight in the general aspect of vacuum insulation.

- Evacuated flat plate solar collectors require 0.5Pa to eliminate convection and significantly increase system efficiency.
- Vacuum glazing requires 0.2Pa internal pressure to virtually eliminate convection.
- The rarefied gas gap in vacuum glazing has been measured to have a thermal conductance of 0.2 $\frac{W}{m^2K}$.
- To eliminate gas conduction, gas pressure must be reduced to a point where the molecular mean free path is greater than the distance between boundaries.
- Selective coatings with high solar absorbance and low thermal emittance are necessary for high performance flat plate collectors.
- In vacuum glazing and evacuated solar collectors radiative heat losses can greatly affect the system's performance.

- Electrochromic coatings have been shown to change their emittance from 0.057 to 0.595 in the temperature range expected in building applications.
- Sealing the edge of a vacuum enclosure has been achieved with Indium alloy and solder glass for glass contact, and with several welding techniques for metal foils.
- Edge conduction through the foil is a significant heat bridge in VIPs and hollow-core VIPs.
- Stress from pressure differential in evacuated systems can fracture glass enclosures.
- Structural supports for vacuum enclosures include staggered glass bars, stacked glass beads and pillar arrays made of glass, Inconel, and stainless steel.
- A hollow-core panel will need to consider bending of the face plates or fascias, and buckling on the internal structure in addition to thermal conductance of the system.
- Flat stainless steel plates thinner than $3mm$ will not be able to cover distances over $300mm$ without deflecting beyond accepted tolerance.
- Plate stiffening techniques are necessary to overcome elastic bending limitations experienced by the metallic envelope of hollow-core VIPs.

While the research conducted by Nemanic [57] described the underlying principles and manufacturing process of hollow-core VIPs it failed to address important issues regarding the thermal performance and structural stability of this type of

technology. It follows that this research project must address the gaps in knowledge from previous studies:

- How to predict, analyse and evaluate heat transfer in hollow-core VIPs without treating heat transfer mechanisms independently?
- What is the necessary pressure on the internal cavity to suppress gas conduction in hollow-core VIPs?
- How do individual heat transfer mechanisms compare in terms of participation in overall heat transfer?
- How are panel properties, such as dimensions, optical properties and gas composition defined in function of thermal conductance?
- How is panel design constrained by competing requirements, structural and thermal?
- What values of thermal conductance can be achieved by hollow-core VIPs, and does it work as an insulating solution?

Chapter 3

A numerical method for heat transfer simulation in hollow-core VIPs.

3.1 Introduction

Heat transfer through a vacuum cannot be accurately predicted by solving the Navier-Stokes equations as the transport terms in the conservation equations fail when their gradient is of the same scale as the molecular mean free path [46]. However, macroscopic flow properties can be obtained from mean values of molecular interactions. Thus, a molecular simulation like OpenFoam's Direct Simulation Monte Carlo solver, capable of predicting the behavior of a rarefied gas will yield the macroscopic properties of the gas, such as pressure and density, and will also measure the gas' response to its boundary conditions such as heat flux. When the gas reaches a steady state the rarefied gas' effective thermal conductivity can be calculated,

according to Fourier's law, from the predicted heat flux through the fluid region. It is through this property than molecular simulations can be linked to more computationally efficient solvers capable of handling multiple regions simultaneously, such as OpenFoam's chtMultiRegionSimpleFoam and chtMultiRegionFoam solvers.

Simulation results from CFD solvers, in this case OpenFoam 4.0, are initially validated by comparing simple cases to their analytical solutions; these will be corroborated by empirical measurements in the following chapters.

3.1.1 OpenFoam

Not all numerical solvers are capable of handling this problem, as it requires solving molecular interactions in a rarefied gas, in addition to common heat diffusion and radiation equations through multiple coupled regions. OpenFoam is an open-source software with an extensive toolkit including features for solving complex fluid flows, acoustics, mechanical stress, chemical reactions and more. The toolkit includes dsmcFoam, a probabilistic solver for molecular dynamics, as well as chtMultiRegionFoam and chtMultRegionSimpleFoam, multi-region solvers for transient and steady state simulations capable of handling radiation, contact conductance and other thermal transfer nuisances. By employing these two features we can predict the behavior of hollow-core VIPs, which consist of vacuum and solid regions, without massive computational resources and without the necessity to develop specialized software, see Figure 3.1.

OpenFoam [127], as other numerical solvers, is constrained by equations that describe physical phenomena; these equations are denominated governing equations. The governing equations concerning the project are the continuity, momentum and

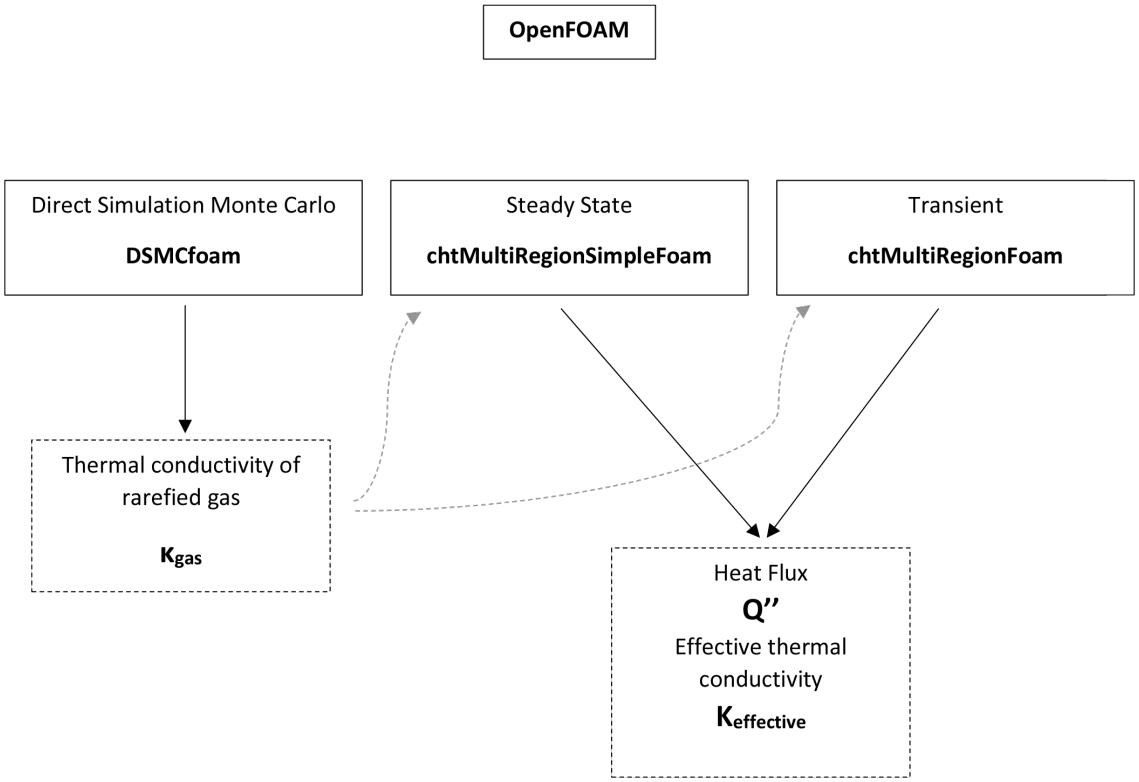

Figure 3.1: Diagram of Openfoam utilization. Results from DSMCfoam are used to calculate the thermal conductivity of the rarified gas, which is then incorporated into multi-region solvers.

enthalpy equations, which describe mass, moment and enthalpy conservation, respectively. The enthalpy equation is of particular interest since it introduces temperature as a necessary variable. These past equations can derive more complex and specific equations depending on the problem. The molecular solver employed, dsmcFoam, is based on the kinetic theory of gases and utilizes the Boltzmann equation to describe the gas flow. This equation is a conservation equation describing the influx of particles in the element due to all involved processes [46].

OpenFoam solvers are professionally developed and validated prior to any release, nonetheless the software has been previously validated on multiple occasions by

un-affiliated researchers. Natural convection has been modeled using buoyantSimpleFoam and compared to experimental data [128], showing close agreement on velocity and temperature distribution [129]. Solver scalability over multiple processors, turbulence models, discretization schemes and pressure-velocity coupling methods has been verified against proprietary software, Fluent, and experimental data. The SIMPLE and PIMPLE algorithms show accurate flow results within 5% and 3% of experimental data for a backward facing step and flow over sphere cases. Results are within 6% of proprietary software, FLUENT, and show greater scalability [130]. Time discretization schemes, specifically time-backward or implicit schemes, as first order Euler scheme and second order Crank-Nicolson scheme, have been validated against well know solutions and show adequate convergence at internal time steps as large as $0.001s$; minor modifications in the internal code regarding face flux have shown to achieve faster convergence with second order temporal integration [131]. Several other notable studies and validations regarding CFD [132, 133, 134, 135, 136, 137, 138], heat transfer [139, 140, 141], molecular dynamics[142, 143, 144, 145] and other phenomena [146, 147, 148] have been conducted using OpenFoam, acknowledging its capability as an industrial and academic research resource.

3.1.2 Flow regime by Knudsen number

The degree of rarefaction of a gas can be described by the unitless Knudsen number, Kn, which is the ratio of the mean free path, λ, to the characteristic dimension, L. The Navier-Stokes are valid for Knudsen numbers lower than 0.1, larger Knudsen numbers indicating a higher degree of rarefaction require solving the Boltzmann

equation [46].

$$Kn = \frac{\lambda}{L} \tag{3.1}$$

3.1.3 Aims and Objectives

The studies in this chapter aim to evaluate the capacity of open source software OpenFoam as a tool for heat transfer analysis through multiple regions in a vacuum environment. The following list presents objectives of this chapter comparing the accuracy of OpenFoam simulations against analytical solutions:

- Compare OpenFoam's DSMC solver against Smoluchowski's equation for parallel plates separated by a rarefied gas.

- Compare OpenFoam's Simple solver against analytical solution for a solid-fluid interface.

- Compare OpenFoam's Simple solver and Laplacian Equation solution for solid-solid and solid-fluid interface.

- Compare OpenFoam's View Factor solver for radiative heat transfer against an analytical solution for parallel plates with variable emissivity values.

3.2 Method

3.2.1 Calculating the rarefied gas thermal conductivity with Direct Simulation Monte Carlo

An isolated analysis is conducted on the vacuum region to calculate, according to the kinetic theory, its effective gas conductivity. In the numerical solution the analysis is conducted through an OpenFoam solver called dsmcFoam, Direct Simulation Monte Carlo. The analytical counterpart validating the numerical approach utilizes Smoluchowski's temperature discontinuity [66] on heat exchange through a rarefied gas between parallel plates. Opposing parallel plates have a fixed temperature boundary condition, while the remaining boundaries are treated as adiabatic.

3.2.1.1 OpenFOAM DSMC solver

One of OpenFoam's native features, called dsmcFoam, is employed to calculate the molecular interactions of the rarefied gas without incurring in a massive computational expense. The solver, dsmcFoam, is capable of handling transient multi-species flows.

The Direct Simulation Monte Carlo method, DSMC, provides a probabilistic solution to molecular interaction. The basis of the solver is numerically solving the Boltzmann equation, eq. 3.2.

$$\frac{\partial}{\partial t}(nf) + c\frac{\partial}{\partial r}(nf) + F\frac{\partial}{\partial c}(nf) = \int_{-\infty}^{+\infty}\int_{0}^{4\pi} n^2(f^* f_1^* - f f_1)c_r \sigma d\Omega\, dc_1 \qquad (3.2)$$

In this method, each simulated particle represents larger number of real particles. The application of the DSMC method is restricted to dilute gas flows. This method's approximation relies on uncoupling molecular motion from intermolecular collisions over a small time step, smaller than the average rate of collision. It is recommended that cells in the simulated region are smaller than the molecular mean free path. Each time-step molecules are moved over the appropriate distance, followed by the calculation of a representative set of intermolecular collisions, and as long as the time step is small relative to the rate of collision the results will be independent of the time step. The DSMC method employs simulated molecules of the correct physical size [46]. This means that simulated molecules, of the correct physical size, representing a larger set of "real" molecules are moved every time step and collisions are calculated to determine if and how many of these collide with each other and/or with boundary conditions.

Solving the Boltzmann equation is not a trivial task but a probabilistic approach where only a fraction of particles need to be simulated provides a more efficient solution accessible to most modern computers. A description of the terms found in the DSMC solver and the Boltzmann equation can be found in Appendix A.Figure 3.2 presents a flowchart on the dsmcFoam algorithm.

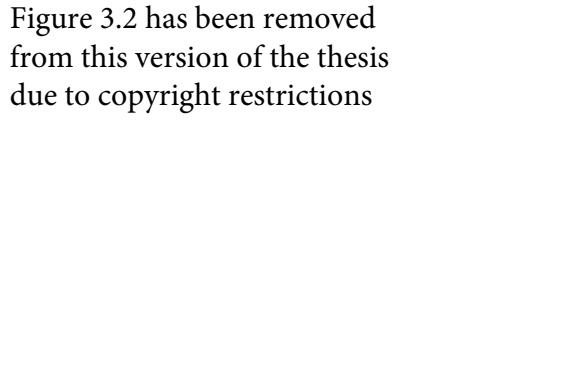

Figure 3.2: dsmcFoam flowchart. Adapted from [144].

3.2.2 Multi-Region temperature coupled solvers

The OpenFoam native solvers package include chtMultiRegionSimpleFoam and chtMultiRegionFoam, tools for solving mass and heat transfer across multiple regions of different physical properties, the former on a steady state basis and the latter on an unsteady simulation. The steady state solver, chtMultiRegionSimpleFoam, relies on a combination of the buoyantSimple solver and the Laplacian equation, the former solves the fluid region as a compressible fluid and the latter solves the solid region. The unsteady solver, chtMultiRegionFoam, utilizes the PIMPLE solver and the Laplacian equation. The PIMPLE solver, as the SIMPLE solver, treats the fluid as compressible, but does so over an implicit time discretization scheme. The conditions of the current project with relatively minor temperature differences and with a stationary and contained rarefied gas, assume negligible changes in pressure, consequently neglecting viscous dissipation and/or flow dilatation, which suggest treating the fluid as incompressible [149] or with fixed pressure and velocity.

It should be noted, for rarefied gases, the rate of intermolecular collisions is small enough that gradients in the macroscopic properties of the fluid cannot be maintained and solving the Navier-Stokes equation for fluid flow produces inaccurate results [46]. Consequently, the transport implications of the rarefied gas are solved with molecular simulations, and when solving the Navier-Stokes equation during chtMultiRegionFoam simulations, the moment equations for the fluid are not solved by specifying a "frozenFlow" variable in the dictionaries and only the energy equation is solved, by solving for enthalpy. Considering a frozen flow that will not update pressure or velocity in the system, only the internal energy component in enthalpy is of consequence. This problem doesn't include any internal energy sources rendering

thermal energy as the only form of energy considered.

The conserved enthalpy equation is derived from the conservation of energy equation. The total energy of the fluid is the sum of internal energy, e, and kinetic energy, K. Mechanical and source terms are eliminated because the sample isn't doing any work or generating energy, leading to the enthalpy equation employed in the simulation.

$$C_p \frac{\partial}{\partial t} \rho T = -C_p \nabla \cdot (\rho U T) + \nabla \cdot (k \nabla T) + Rad \tag{3.3}$$

Where the first term describes energy transfered by fluid flow, the second refers to diffusive heat transfer and the last is the radiative heat exchange, which is calculated by the View Factor method. A detailed derivation and explanation of the equations employed in the simulation can be found in Appendix B.

Having described the physical principles which are used by the solvers we can now move on to describe the process used by the steady state and transient solvers. Keep in mind the previous equations were described for a transient process, directly applicable to the PIMPLE solver. The SIMPLE solver, being a steady state solver, uses the same principles without temporal rate of change.

3.2.2.1 OpenFOAM SIMPLE solver

The SIMPLE algorithm stands for Semi-Implicit-Method of Pressure Linked Equations. This algorithm is used for steady state problems and does not include time derivation. This solver follows a segregated solution strategy, by which it sequentially solves for the system variables (velocity U, pressure p, and other turbulence variables). The non-linear term from the momentum equation is resolved by comput-

ing it from the preceding velocity and pressure values from the preceding iteration or the initial guess. Figure 3.3, show the flowchart for the SIMPLE algorithm. The first step is solving the momentum equation, resulting in a velocity field, U^*. At this moment, the continuity equation is not guaranteed. Next, the momentum and continuity equations are used to construct a pressure equation, thus avoiding decoupling velocity and pressure. After obtaining a pressure field, p^n, the velocity field is corrected, ideally delivering a divergence free velocity field, U. The last step is solving equations for turbulence. The process is repeated until convergence.

Figure 3.3 has been removed
from this version of the thesis
due to copyright restrictions

Figure 3.3: SIMPLE algorithm flowchart. Adapted from [150]

3.3 Results

3.3.1 DSMC validation against analytical solutions

Due to the molecular interaction of rarefied gases at low pressures the macroscopic fluid flow properties cease and heat transfer becomes dominated by gas conduction. Instead of convection, heat transfer mechanisms are ruled by molecular interaction and described by the kinetic theory of gases. The accuracy of the molecular solver used for rarefied flows, dsmcFoam, was tested against analytic solutions derived for free molecular flow by Smoluchowski [66].

The expression used for analytically estimating the gas-conductive heat rate between two parallel plates follows the principles of Temperature Discontinuity phenomenon described by Smoluchowski [66] and previously described in Section 2.2.4.2. In this expression the rarefied gas conductivity is calculated as:

$$Q'' = \frac{k_{G_0}}{d + 2\beta} (T_1 - T_2) \tag{2.21}$$

$$\beta = \left(\frac{9\gamma - 5}{2\gamma + 2}\right) \left(\frac{2 - \alpha}{\alpha}\right) \lambda_{mfp} \tag{2.23}$$

It should be noted that the previous expression calculates the rarefied gas conductivity with regards to the average gas conductivity at ambient pressure within the temperature range, k_{G_0}.

As an initial consideration the Knudsen number $\frac{\lambda_{mfp}}{d}$ is used to determine the type of flow and restrict use of the previous equations to only transitional and free molecular flows. The mean free path was approximated according to the elastic

sphere model commented in Section 2.2.4.2.

$$\lambda_{mfp} = \frac{k_b T}{\sqrt{2}\pi d^2 p}$$

The test case involves heat transfer through a 1 by 1 by $0.01m$ region with air at different levels of rarefaction, Figure 3.4. Air is treated as a mixture of Nitrogen 77% and Oxygen 23% for simplicity. The boundary conditions for the opposing plates are 300 and $500K$, this temperature range was chosen exclusively for initial solver testing, and although this range isn't representative of common building application the large resulting heat flux is more efficient in exposing divergence between analytic and numeric solutions. The accommodation coefficient for Smoluchowski's expression is set at 0.823, as measured by Klett and Irey [151]. The variable levels of rarefaction according to the calculated Knudsen number indicates the gas switches from a free molecular flow to the slip-flow regime, rendering Smoluchowski's expression unfit for the latter.

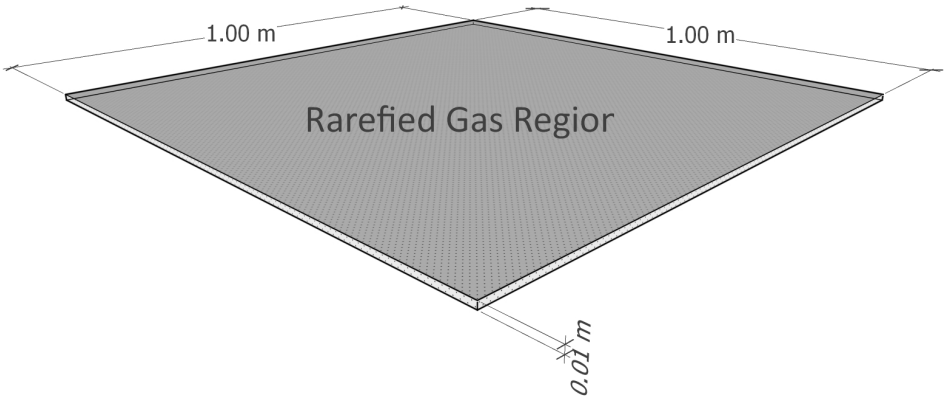

Figure 3.4: Rarefied gas region for simple DSMC model

When comparing results from the simulated cases against the analytic expressions (Figure 3.5) discussed previously it becomes evident that as the Knudsen flow regime changes from transitional to continuum (Figure 3.6) the solutions begin to diverge. The last case involving a 50 Pa pressure is not suitable to be predicted by the analytic solution. Nonetheless, the simulated results within the free molecular flow and transitional regime agree closely with the expected results.

More detailed validation cases have been conducted for molecular collision calculation, rarefied and hypersonic flow over flat and curved geometries, Poiseuille flow and other molecular dynamic scenarios [143, 144, 152, 153]. DsmcFoam shows close agreement with analytic solutions, Table 3.1, with less than 5% difference within the intended pressure range.

Table 3.1: Gaseous conduction results between simulated (DSMC) and analytic analysis.

Pressure	**Heat Flux Q"**		**Difference**
	Analytic	Simulated	
Pa	$\frac{W}{m^2}$	$\frac{W}{m^2}$	%
0.012	2.45	2.58	4.84
0.12	23.74	24.38	2.61
1.29	188.65	170.72	-10.50
13	526.56	580.91	9.36
50	616.59	1464.00	57.88

3.3.2 Multi-region solver validation against analytical solutions

The simulated model consists of two air regions with steady flow at opposite sides of the solid wall. Air regions have an input speed of 1 $\frac{m}{s}$ (Figure 3.7a) and a fixed

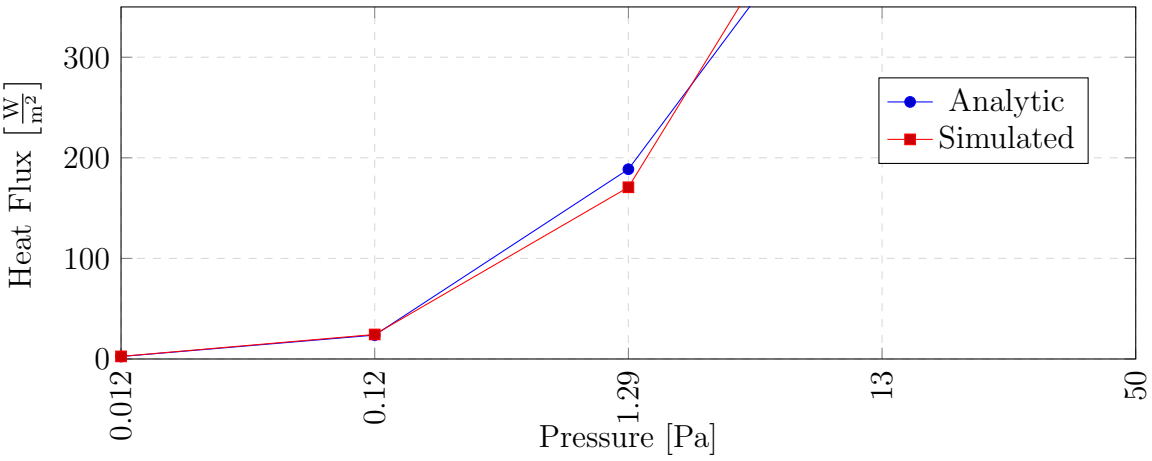

Figure 3.5: Heat Exchange results between simulated and analytic equations. The results diverge as the pressure increases resulting in smaller Knudsen numbers. At 50 Pa the flow regime should be analysed as a continuum flow rather than a transitional/rarefied flow as Smoluchowski's expression provides inaccurate data.

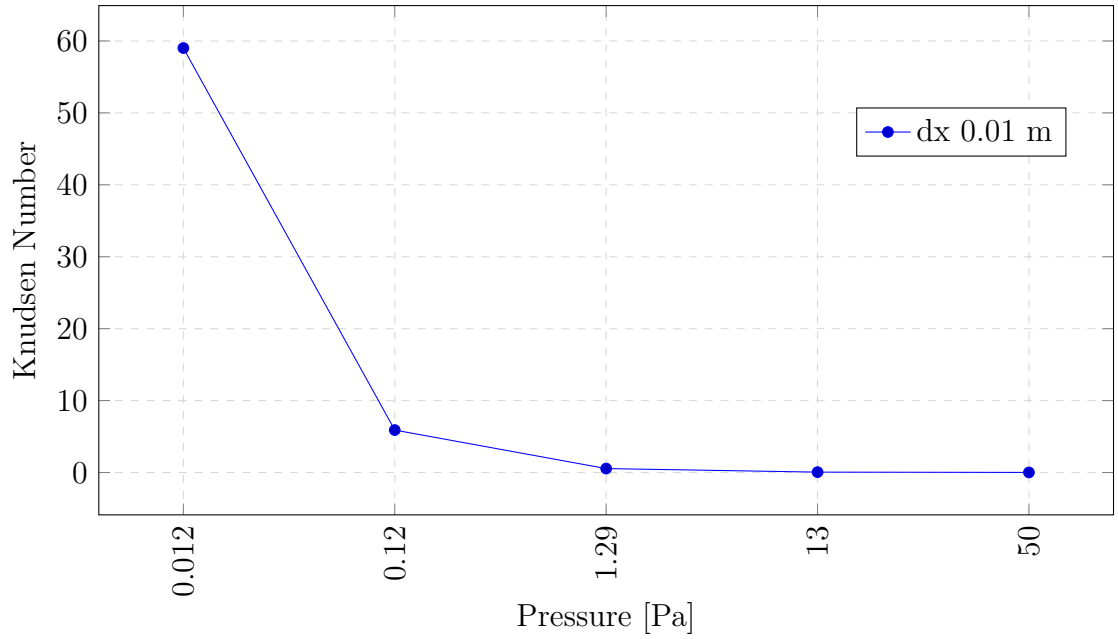

Figure 3.6: Knudsen number indicating level of rarefaction for different pressures in the test case. At 0.012 Pa the flow is in the free molecular or collisionless regime, from 0.12 to 1.29 Pa the flow is in the Transitional regime, at 13 Pa the flow is in the Slip Flow regime and at 50 Pa the flow is borderline in the continuum flow type.

input temperature of 300 and 500 K respectively (Figure 3.7b). The wall has an initial temperature of 400K. The resulting temperature profile plotted vertically across the model agrees with the expected results as described in literature [29]. The simulation has demonstrated the temperature gradient in both solids and fluids is behaving as expected in a solid to gas interface (Figure 3.8) as well as for solid to solid interface (Figure 3.9) .

Additional detailed studies verifying the discretization methods, turbulence models, interpolation schemes and other solver properties have been thoroughly conducted by [132, 133, 134, 135, 136, 137, 138, 139, 140, 141], providing confidence in OpenFoam's multi-region solvers for both steady state and transient simulations.

The temperature gradient in the wall (from 0.4 to 0.6m) is small, consistent with the high conductivity ($180\frac{W}{mK}$) assigned to this region. Sampling the temperature at opposing sides at mid-length of the solid wall we get a max temperature of 399.298K and a min temperature of 399.207K. The heat flux through the wall is the calculated as

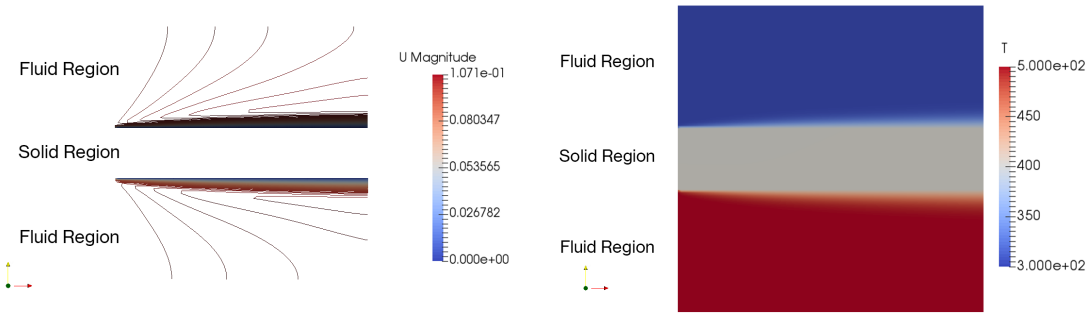

(a) (b)

Figure 3.7: Results from the Plane Wall exercise as described in [29] simulated in openFoam (a) Wind Speed profile. A boundary condition can be clearly observed adjacent to the wall with a laminar flow extending perpendicular to this boundary (b) Temperature Profile

$$Q'' = \frac{k}{L}(T_{0.4} - T_{0.6}) \tag{3.4}$$

The resulting heat flux is 81.9 $\frac{W}{m^2}$. The openFoam heat flux tool (wallHeatFlux) reads 82.8 $\frac{W}{m^2}$ at this same position.

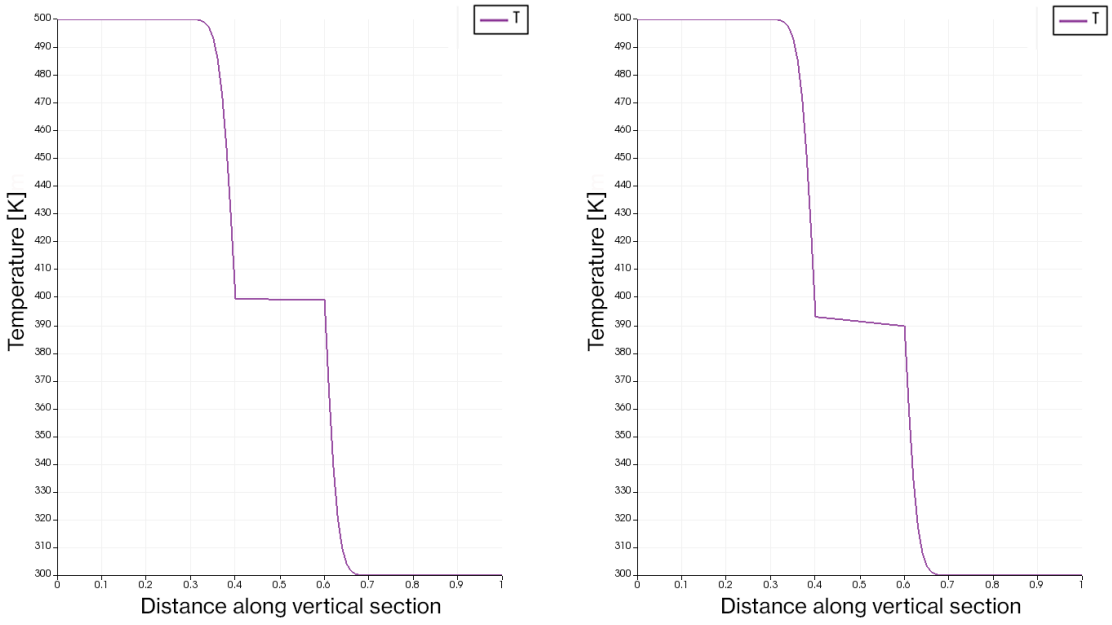

(a) (b)

Figure 3.8: Simulation results from steady state solver chtMultiRegionSimpleFoam.Temperature gradient plotted vertically through the center of the model. The ordinate units are degrees Kelvin. The abscissa units are meters. a) The solid wall has a conductivity of 180 $\frac{W}{mK}$ b)The solid wall has a conductivity of 5 $\frac{W}{mK}$

Changing the conductivity of the wall to 5 $\frac{W}{mK}$ displays a noticeable difference on the temperature gradient of the wall element (Figure 3.8). Similarly, by changing the case to include three adjacent wall elements with different thermal conductivity values, the expected variation in temperature gradient is appreciated (Figure 3.9), indicating adequate handling of solid to solid interfaces. It can be observed that

this numerical simulation is capable of predicting heat exchange between multiple regions of different properties.

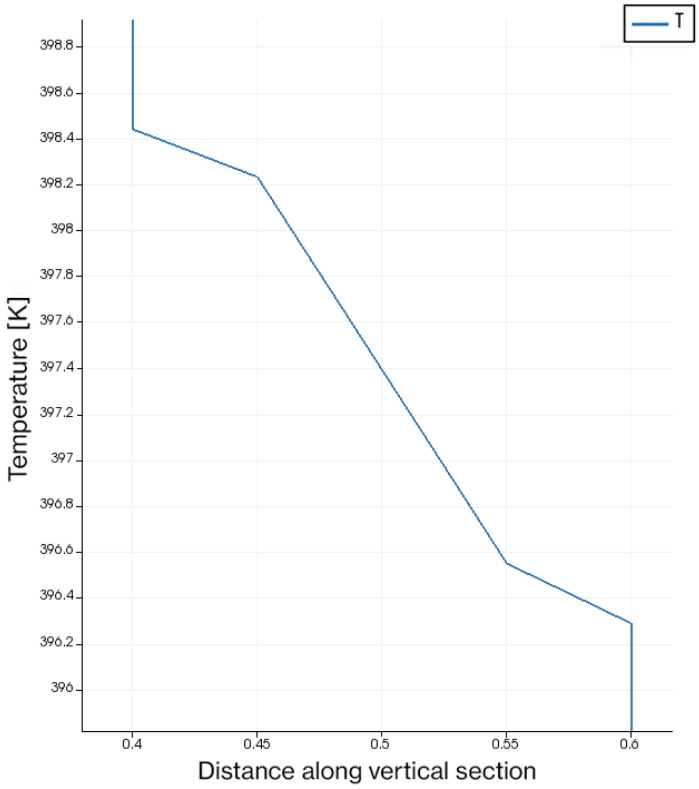

Figure 3.9: Simulation results from steady state solver chtMultiRegionSimpleFoam.Temperature gradient plotted vertically through the center of the model of a multi-layer solid wall. The ordinate units are degrees Kelvin and the abscissa units are meters. The multi-layered wall represents an element built with a series of materials with different thermal conductivity. This wall is simulated with a series of thermal conductivity values of 80, 20 and 65 W/mK respectively from left to right.

Results for radiative heat flux are validated in a simple case involving two parallel plates of equal size. The view Factor radiation model employed in OpenFoam can be adequately validated by the following expressions described in [29, 154] and mentioned previously in Section 2.2.4.3.

Using this analytical method, the radiative heat flux of both plates was compared to that resulting from OpenFoam simulations. The evaluated region consists of a fluid (at this stage the composition is meaningless since we are only measuring radiation through a non-participating medium) measuring 1 by 1 m in length, width with variable thickness. The hot and cold walls have an area of 1 m^2. The accuracy of the simulation was tested in variable plate separation conditions with a constant emissivity of 0.07, simulating that of polished steels plates [155]. By setting the interface between the solid and gas regions to fixed temperature values (373 and 273 K for the hot and cold plate respectively) we can evaluate the radiative heat transfer virtually uncoupled from convective effects resulting in adequate conditions for comparison against the analytic method.

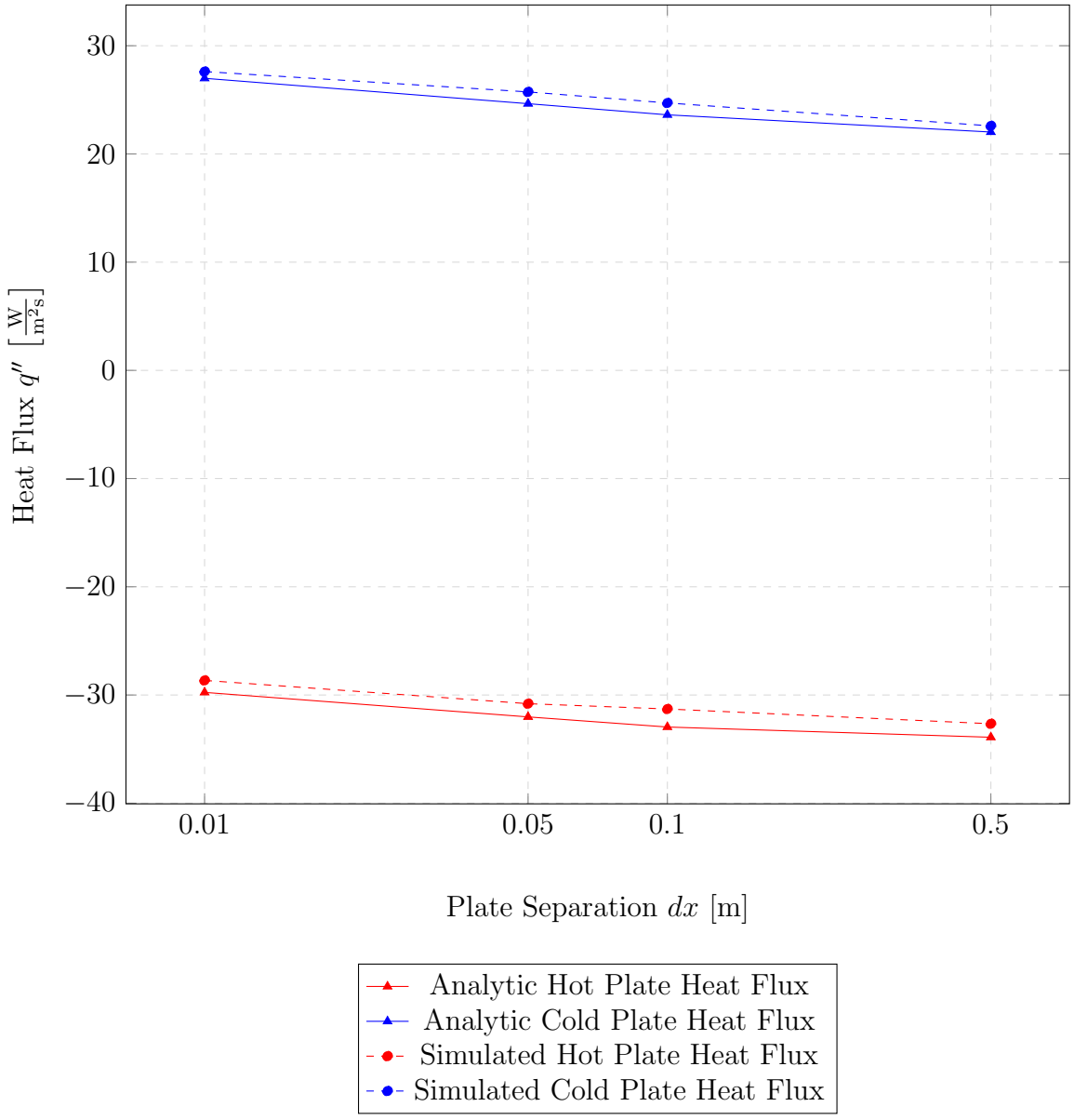

Figure 3.10: Heat Rate Comparison between Analytic and Simulated Solutions. Values agree within 5% of the analytic solution. It should be noted that the case with the narrowest spacing takes more time to achieve convergence. Since multi region solvers aren't capable of interrupting the simulation based on convergence criteria, care should be taken to ascertain these criteria are met.

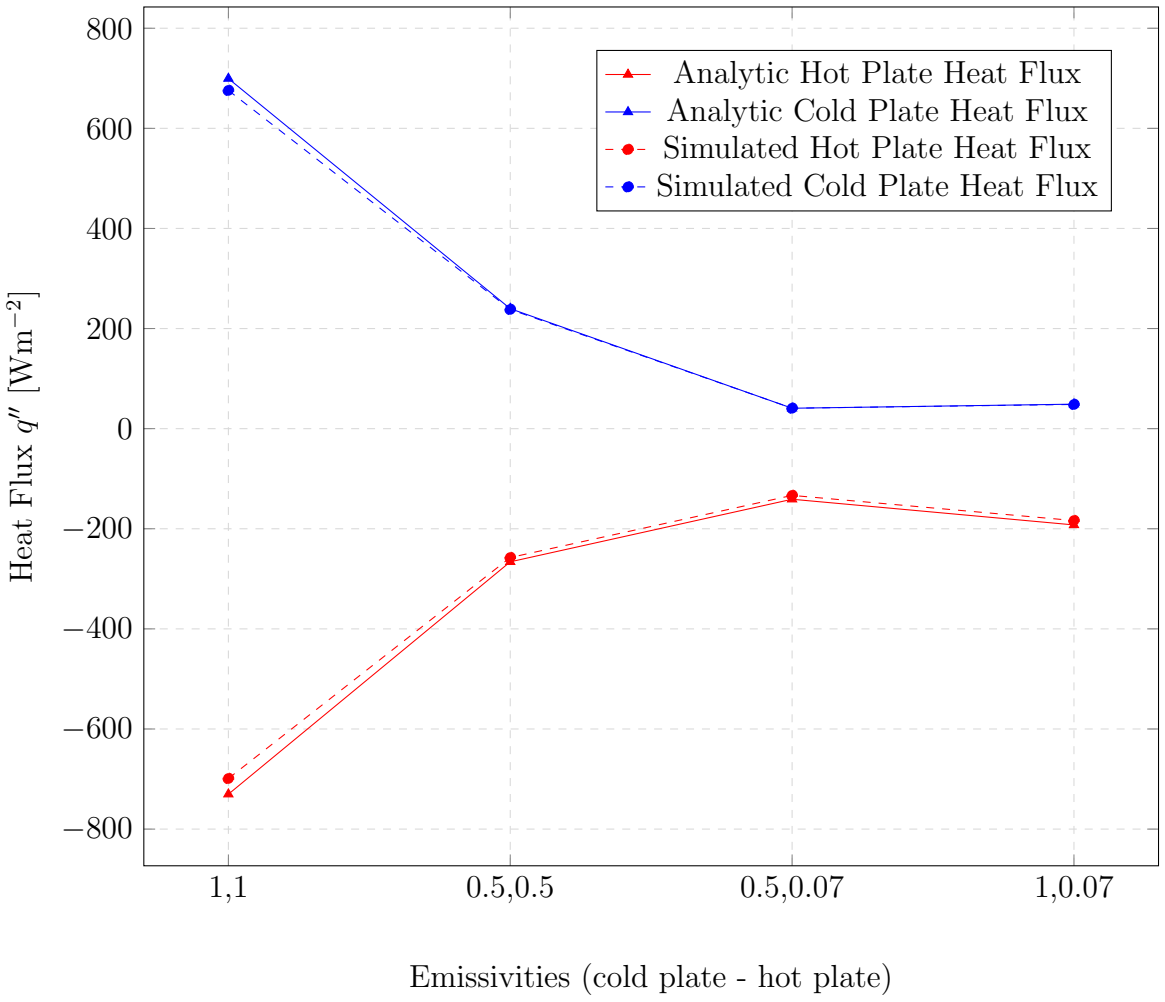

Figure 3.11: Radiative Heat Flux Comparison between Analytic and Simulated Solutions with different emissivities. Largest discrepancy between simulated and analytic values is 5.7%, found in the 0.5 to 0.07 emissivity case measuring heat flux from the hot plate. The heat rate at the cold plate falls within 3.5% agreement in the worst case.

By comparing the heat flux from the analytic and simulated solutions we can observe a close agreement in the data, within 5% (Figure 3.10), in several degrees of separation. In addition to dimensional variations, changes in emissivity were also tested (Figure 3.11) and the results from the numerical simulation agree closely with the analytic method. From this simple case it can be concluded that radiative heat transfer simulated in OpenFoam using the viewFactor model is accurate enough to proceed with more detailed models and simulations.

Table 3.2: Radiative Heat Flux Comparison between Analytic and Simulated Solutions

Separation m	**Analytic Hot Plate Flux** Wm^{-2}	**Analytic Cold Plate Flux** Wm^{-2}	**Simulated Hot Plate Flux** Wm^{-2}	**Simulated Cold Plate Flux** Wm^{-2}
0.01	−29.759	26.989	−28.651	27.610
0.05	−32.024	24.645	−30.800	25.732
0.1	−32.959	23.614	−31.290	24.713
0.5	−33.906	22.024	−32.660	22.592

Simple models of well-known solutions, solvable by analytic methods, show that OpenFoam is capable of great accuracy in heat transfer simulations. Convergence monitoring is important to ascertain a concluded simulation; otherwise, discrepancies in the coupling interfaces may provide inaccurate heat flux and temperature gradients.

3.4 Conclusions

OpenFoam's native solvers dsmcFoam and chtMultiRegionSimpleFoam, for molecular and multi-region simulations have shown accurate results against analytic solu-

tions and empiric measurements, qualifying them as suitable research tools capable of handling the thermal interactions experienced by a vacuum panel, or other vacuum insulating technologies.

The DSMC solver was accurate to within 5% when the fluid was in the free molecular flow regime, beyond this point the solver was accurate to within 10% for fluids in the transitional and slip flow regime. It should be noted that Smoluchowski's equation is only accurate for a free molecular flow. The SIMPLE solver and Laplacian equation were accurate in heat flux simulations up to 3% by comparison to analytical solutions describing solid-fluid and solid-solid interfaces. OpenFoam's implementation of the View Factor method agreed within 5% to analytical solutions.

After these initial tests all chapter objectives were met and results confirm that OpenFoam is accurate in heat transfer simulation and validate its capacity to undertake the following studies.

Chapter 4

The effect of varying model properties on thermal performance

4.1 Introduction

Numerical analysis is conducted on a simplified model under variable conditions to isolate and evaluate the effect of diverse variables that affect the overall thermal resistance of the panel. A simple box, comprised of $1mm$ thick steel sheet and measuring $1m$ length by $1m$ width with variable depth (Figure 4.1), is subject to multiple steady state simulations of variable parameters including changes in internal emissivity, gas composition and pressure. Mechanical stress and similar structural considerations are neglected and the "box" is assumed to have no deformations or any other response to the conditions imposed on it. The interaction between the gas and radiation has been neglected for all wavelengths and gas is always treated as a non-participating medium.

Results from this simplified numerical model can be corroborated against analyt-

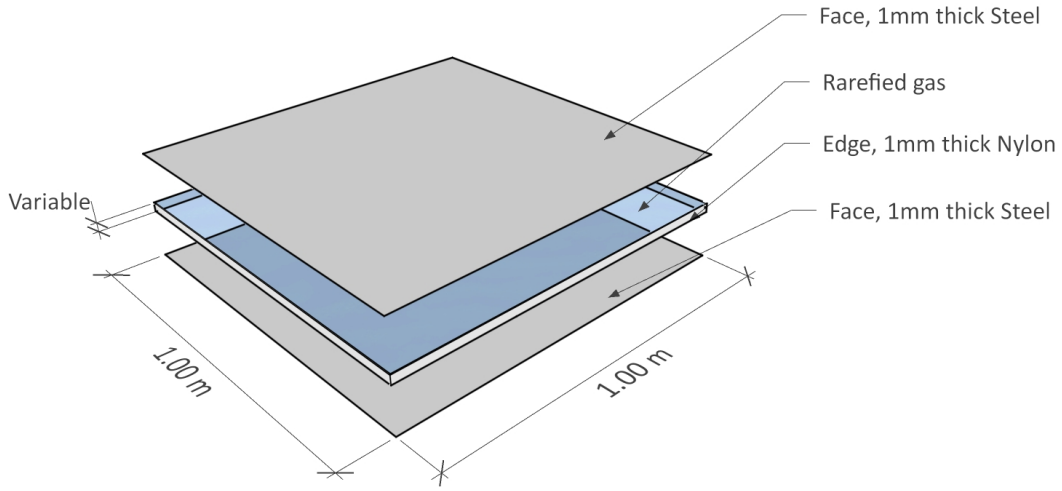

Figure 4.1: Simple model diagram.

ical equations that would otherwise require non-trivial solutions for more elaborate or complex geometries. Observing the effects of variable panel properties can help identify sensitive characteristics that may be regarded as vulnerabilities or opportunities for heat transfer manipulation.

4.1.1 Aims and Objectives

The aim of this chapter was to understand which physical properties have the greatest effect on the overall thermal resistance of a simplified version of a hollow-core VIP, and if any could be used as a suitable mechanism for switching between an insulating and conducting state. The simulations on the simplified model tested in this chapter serve to determine general requirements of hollow-core VIPs. The following objectives are defined to ascertain panel requirements:

- Determine adequate panel thickness in regards to thermal performance.

- Determine necessary pressure to suppress gas conduction.
- Study the effect on heat flux of different gas composition.
- Study the effect of internal surface emissivity on heat flux.
- Estimate a thermal conductance range considering fluctuation of all variables.

4.2 Model and Method

4.2.1 Simplified Model Configuration

Having concluded that OpenFoam's native tools provide accurate results within the validation cases we can proceed to introduce a simplified model of the hollow-core VIP. A simplification of the model is useful for observing trends in heat flux fluctuations, helping identify vulnerabilities in the performance of the panel as well as helping to identify the most suitable mechanism for manipulating heat transfer. The following chapter includes validation of a detailed model against empirical measurements. This simplified model is composed by a 1mm thickness steel sheet box measuring 1m wide and 1m long with variable panel thickness. Mechanical stresses from the conditions imposed are neglected. I.e. Deflection, buckling and similar failure modes are not considered and the panel is assumed steady with no kinetic energy. Opposing sides of the panel will have fixed temperature boundaries according to normal building conditions, other boundaries are treated as adiabatic. Internal emissivity of the panel is treated as a variable and will be simulated with different values. The thermophysical properties of the gas are obtained from DSMC simulations and described in the following section. The thermophysical properties

of the model are described in the following table Table 4.1.

Table 4.1: Thermophysical properties of the simplified model

Material	**Thermal Conductivity** $\frac{W}{mK}$	**Emissivity**	**Specific heat** (C_p) $\frac{J}{kgK}$	**density** $\frac{kg}{m^3}$	**Regions**
Nylon*	0.25	0.15	1670	679	Sample sides (edge-spacers)
Steel	43	0.016-0.93	490	8050	Sample sides (hot & cold panel)

*While Nylon's emissivity is closer to 0.85, this material property was reduced to 0.15 to observe radiation between opposing steel plates with less interference from edge elements. This adjustment to Nylon emissivity is meant to reduce radiative participation from Nylon elements in order to observe with greater clarity the desired parameters which are the subject of study in this chapter; the following chapters substitute Nylon for PTFE.

4.2.1.1 Mesh Independence

Mesh independence was tested by simulating the same case with 5 different grids, ranging from 16000 cells for the coarse grid to over 1 million cells for the fine mesh. The model used for mesh testing was of different dimensions and greater detail than the previous simplified model, as this geometry would be directly adopted for the detailed models described in the following chapter.

The model consists of 300 by $300mm$ aluminum plates separated by a $25mm$ thick sample. In addition, the cold plate sits on four heat sinks and is in contact with several rarefied gas regions representing the vacuum inside the sample, surrounding the sample, and surrounding the rest of the model. The sample consists of two steel plates directly in contact with the aluminum plates, structural elements separating the two steel plates, and the vacuum region encased by the previous ele-

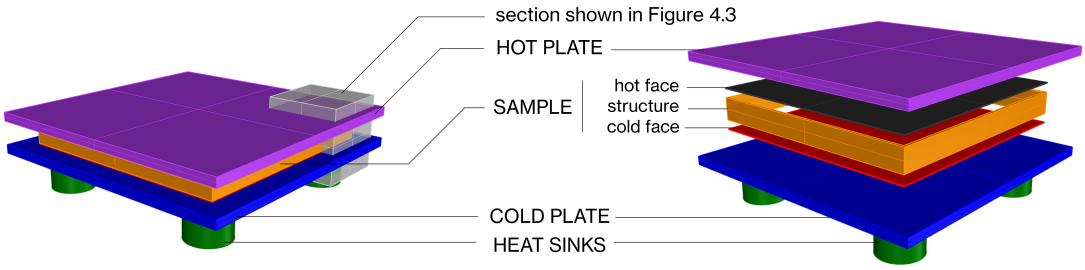

Figure 4.2: Diagram of regions in detailed simulation. Model matches experimental setup discussed in Chapter 5.

ments. More detail can be found in Chapter 5. Mesh refinement was concentrated in the sample elements and adjacent regions creating an interface or patch with the sample. Mesh dependence was measured by the resulting heat flux and temperature at the interface where the heat flux sensors were placed in the empirical measurements. The following figure shows the same fraction of the model with the coarse and fine mesh (Figure 4.3). The thermo-physical properties of the model are described in Table 4.2.

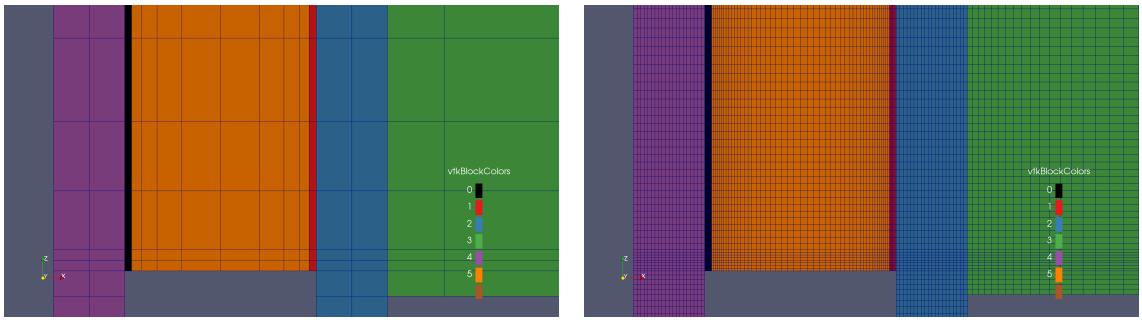

(a) (b)

Figure 4.3: a) Coarse mesh with 16384 cells b) Fine mesh with 1048576 cells. Mesh refinement was concentrated along the axis parallel to heat flux and concentrated within sample elements.

The following table shows the measured heat rates at the interface between the sample and cold plate. This region was chosen because it represents the location

Table 4.2: Thermophysical properties of the models for mesh independence tests.

Material	**Thermal Conductivity** W/mK	**Emissivity**	**Specific heat** (C_p) J/(kgK)	**density** kg/m3	**Regions**
PTFE	0.25	0.9	970	2200	Sample sides (structure)
Aluminum	180	0.06	900	2700	Temperature distribution plates (hot & cold), heat sinks
S.Steel 304	16.4	0.07	500	8000	Sample faces (hot & cold)

of heat flux sensors employed in empirical tests, and is affected by gas conduction, solid conduction and radiative heat transfer. Results from the mesh comparison are summarized in Table 4.3.

Grid independence tests show that heat flux Q and temperature T are virtually unchanging between grid 4 and grid 5. Differences between grid 3 and grid 4 are limited to 2% in heat flux and less than 1% in temperature, Figure 4.4. Grid 3 was selected as the final mesh due to the close agreement in results with finer meshes while taking less than half the time to conclude the simulation by comparison to grid 4, Figure 4.5. It should be noted that cited clock time in Table 4.3 only considers execution time from chtMultiRegionSimpleFoam but neglects added time expense from DSMC simulating the rarefied gas, meshing, and calculation of radiation view factors.

Table 4.3: Simulated Heat rate on mesh independence tests

Grid	**Cells**	**ClockTime** s	$T_{interface}$ K	$Q_{interface}$ W
Grid 1	16384	404	298.77	1.05
Grid 2	65536	889	298.55	1.03
Grid 3	131072	1256	298.43	0.98
Grid 4	262144	2919	298.37	0.96
Grid 5	1048576	10196	298.37	0.96

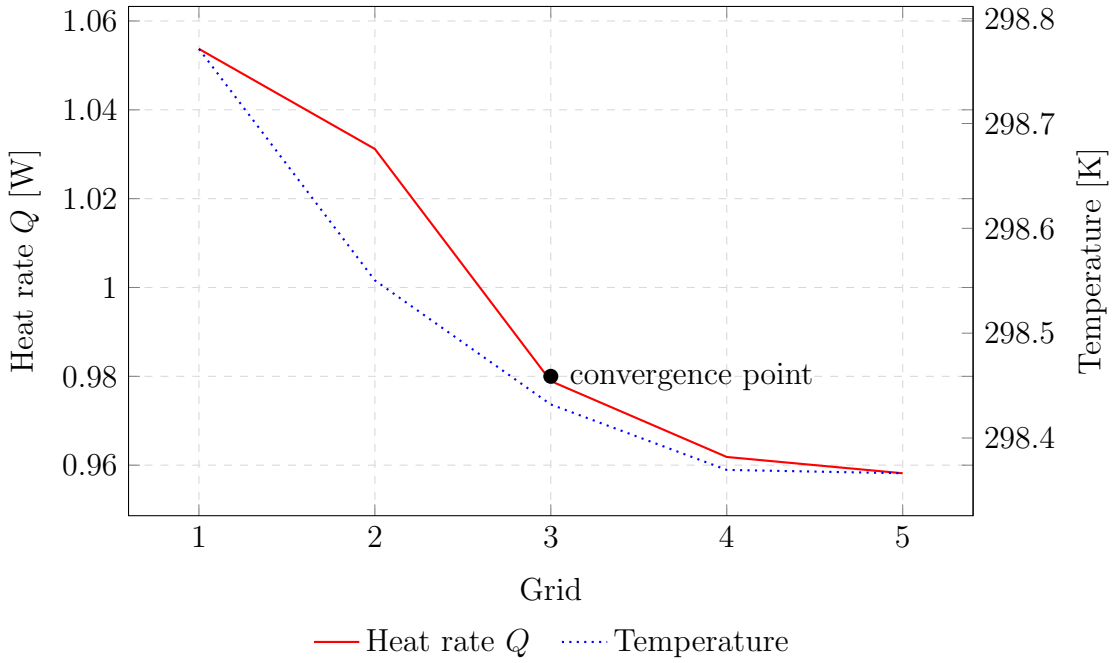

Figure 4.4: Grid independence analysis. Heat rate W and temperature T were probed at the interface between the cold panel (part of sample) and cold plate (part of test rig).

4.2.1.2 Boundary Conditions

The model has three types of boundaries, each with different conditions. The first relates to the opposing sides of the panel, which for the installed product represent

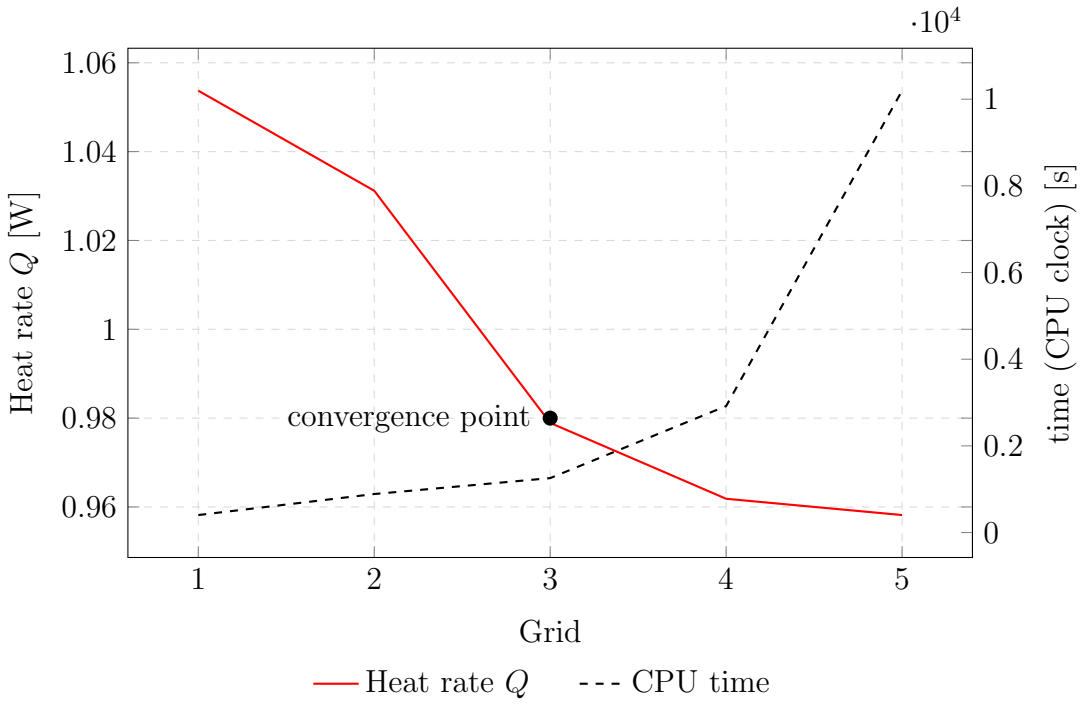

Figure 4.5: Grid independence analysis. Heat rate W and execution time (in CPU clock time) t were probed at the interface between the cold panel (part of sample) and cold plate (part of test rig).

the external and internal sides. These were treated as having a uniformly distributed fixed temperature, a hot and a cold side. For this simple model the hot temperature is 298K and the cold temperature is 273K, representing a common temperature differential in building applications. The second boundary type, perpendicular to the first, and connecting the external and internal sides are the edge-spacing sides of the panel, these were treated as externally adiabatic, internally all properties are calculated after the initial stage. The third and last boundary condition isn't properly a boundary condition but refers to the interface between different regions. The interface between solids is treated as a seamless transition, this means there is no thermal resistance between connecting solids. This will be amended to include

specific contact conductance in the following chapter, with a more detailed model. The interface between the fluid and solid region is treated as a normal solid-fluid interface with radiative exchange through the gas and calculated by the emissivity properties of the solid.

4.2.2 Linking dsmcFoam and SIMPLEfoam/PIMPLEfoam solvers

Understanding that multi-region solvers are incapable of handling the rarefied gas region, the vacuum has to be simulated independently and the resulting macroscopic gas properties, specifically its effective thermal conductivity, needs to be imported to a fluid region in the multi-region solver, which has to be coerced into behaving as the vacuum region would. This procedure is achieved by first simulating a rarefied gas region exposed to the boundary conditions expected in the normal application of the panel. After the dsmcFoam simulation reaches a quasi steady-state, where the gas properties undergo minimal changes over a predetermined time frame, the effective thermal conductivity of the rarefied gas is calculated according to Fourier's Law, and the simulated temperature distribution and heat flux. Once this property is known, a fluid region with the same thermal conductivity is defined in the multi-region solver. In addition, the newly defined fluid region is set as a motionless fluid with constant pressure by setting the correct field values and indicating the solver to avoid updating these fields by treating the fluid as a "frozen flow"; this is specified in the "fvSolution" dictionary for the relevant region, implying that only the energy equation will be solved.

The thermal conductivity of the fluid in the multi-region solvers can be specified

by setting an arbitrary quantity "kappa" or it is calculated from the fluid properties by the Prandtl number, Pr, and dynamic viscosity, μ.

$$k = \frac{C_p \cdot \mu}{Pr} \tag{4.1}$$

The following table specifies the kappa values obtained from the DSMC simulations and input into the multi-region simulations Table 4.4. From the calculated values it can be observed that the DSMC model is not accurate when the flow approaches the continuum regime, Knudsen number < 0.1. This is perhaps due to the time-step dimension, rarefied gasses proved accurate with a delta time of $1x10^{-}6$. Given the time needed for convergence on smaller models, it's logical to assume that as the cell and molecule count increases by several orders of magnitude, the computation time needed for similar accuracy would also increase. Due to time and computational resources constraints, the larger models could not be simulated until full convergence; results from continuum flow simulated in the DSMC solver will be disregarded.

This linking procedure provides us with ideal conditions for a steady state simulation and is also acceptable for transient simulations as long as the temperature remains within the range included in the DSMC simulation and out-gassing or other sources for pressure change are neglected. The multi-region simulation convergence is determined by residuals in the system's enthalpy (h) in the order of 1×10^{-6} and is also verified by observing temperature continuity and equal heat flux magnitude at the interface between regions.

Table 4.4: Thermal Conductivity $\frac{W}{mK}$ for the gas at different levels of rarefaction, results from dsmcFoam Simulations with a temperature range of 273-298 K. Erratic behavior when Knudsen numbers approach 0.1, continuum flow.

	Pressure [Pa]							
	0.001	0.01	0.05	0.1	0.5	1	5	10
Panel thickness m	**Thermal Conductivity** $\frac{W}{mK}$							
0.01	1.8E-05	1.8E-04	8.5E-04	1.6E-03	6.5E-03	1.1E-02	**2.6E-02**	**3.8E-02**
0.02	3.5E-05	3.4E-04	1.6E-03	3.0E-03	1.1E-02	1.6E-02	**3.8E-02**	**6.0E-02**
0.03	5.2E-05	5.1E-04	2.3E-03	4.2E-03	1.4E-02	2.0E-02	**4.9E-02**	**8.3E-02**
0.04	6.8E-05	6.6E-04	3.0E-03	5.3E-03	1.6E-02	2.3E-02	**6.1E-02**	**1.1E-01**
0.05	8.4E-05	8.2E-04	3.6E-03	6.3E-03	1.8E-02	2.7E-02	**7.3E-02**	**1.4E-01**
0.06	1.0E-04	9.7E-04	4.2E-03	7.3E-03	2.0E-02	**2.9E-02**	**8.6E-02**	**1.6E-01**
0.07	1.2E-04	1.1E-03	4.7E-03	8.1E-03	2.2E-02	**3.2E-02**	**9.9E-02**	**1.9E-01**
0.08	1.3E-04	1.2E-03	5.2E-03	8.9E-03	2.4E-02	**3.4E-02**	**1.1E-01**	**2.2E-01**
0.09	1.5E-04	1.4E-03	5.7E-03	9.7E-03	2.5E-02	**3.6E-02**	**1.3E-01**	**2.4E-01**
0.1	1.6E-04	1.5E-03	6.2E-03	1.0E-02	**2.7E-02**	**3.9E-02**	**1.4E-01**	**2.7E-01**
0.125	2.0E-04	1.8E-03	7.4E-03	1.2E-02	**2.9E-02**	**4.5E-02**	**1.8E-01**	**3.5E-01**
0.15	2.3E-04	2.2E-03	8.3E-03	1.3E-02	**3.3E-02**	**5.1E-02**	**2.1E-01**	**4.2E-01**
0.5	6.0E-04	5.4E-03	1.8E-02	**2.7E-02**	**9.0E-02**	**1.6E-01**	**7.6E-01**	**1.6E+00**

Bold values indicate Knudsen numbers smaller than 0.1, approaching a continuum flow.

4.3 Results

Numerical simulations were run with changes in their parameters to evaluate or expose correlations in the heat transport properties of hollow-core vacuum insulations panels. Observing effects in heat transport after changing panel properties can help identify sensitive characteristics that can be regarded as vulnerabilities or opportunities for heat transfer manipulation.

Amongst studied elements are gas composition (air and argon), vacuum gap thickness, gas pressure, and internal emissivity of the panel's faces. The interaction between the gas and radiation has been neglected for all wavelengths and gas is

always treated as a non-participating medium.

4.3.1 Geometric Considerations

It is worth reminding that the simplified model consists of a box with dimensions 1 by 1 m and with variable width; the width measurements simulated are 0.01 through 0.15 m.

Results from the simulations (Figure 4.6) corroborate analytical equations and literature demonstrating that greater pressure levels will significantly increase heat flux; pressure dependence will be treated in greater detail in the following sub section. It is of specific importance to note that at very low pressure levels when the flow type is restricted to Free Molecular Flow or Transition regime the gap spacing has marginal effect on the heat flux when the internal emissivity is low.

The conditions and behaviour of thermal exchange becomes different past a critical pressure. For conditions in the free molecular flow and transition regime, as seen in pressures of 0.01 and 0.1 Pa (Figure 4.6), an increase in vacuum width will improve performance (approximately by 30%) however this is mainly due to reduction in solid conductivity through the edges (Figure 4.7). The simulations conducted maintained a static edge thickness regardless of structural implications. By neglecting the reduction in conductivity through the edges we can appreciate a virtually unchanging heat transfer by gas conduction during a free molecular flow. By comparison, the same geometric conditions at a pressure of 1 Pa go beyond the transition regime and enter a slip flow regime. At this pressure, the same reduction in solid conductivity can be seen as the panel thickness increases; however the most noticeable change is that convective heat transfer is sensibly reduced as the panel

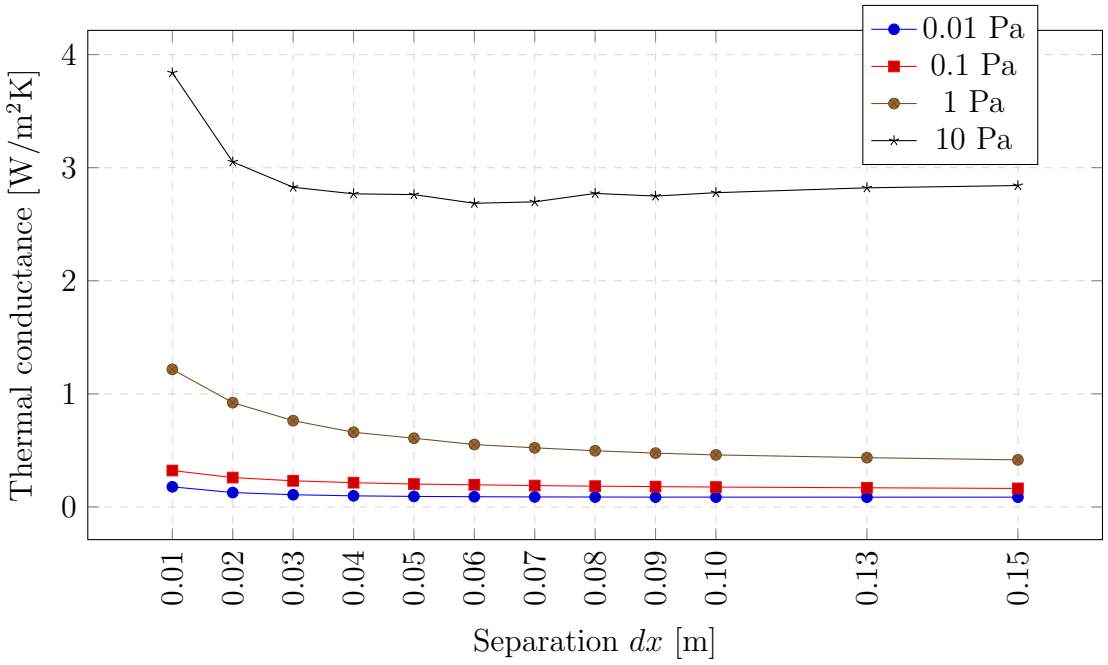

Figure 4.6: Thermal conductance at different internal pressure values and variable panel widths. Results obtained from OpenFoam simulations. Temperature range 273-298 K. Air simulated as 77% N_2 and 23% O_2; Side panel emissivity set as 0.016 for both sides. As expected, greater pressure allows increased heat flux. It should be noted that when the flow type shifts into the continuum regime the results become unreliable as we have considered a frozen flow for these results.

Table 4.5: Thermal conductance $\left[\frac{W}{m^2K}\right]$ at different internal pressure values and variable panel widths. Results obtained from OpenFoam simulations. Temperature range 273-298 K. Air simulated as 77% N_2 and 23% O_2; Side panel emissivity set as 0.016 for both sides.

	Pressure			
Distance m	0.01 Pa	0.1 Pa	1 Pa	10 Pa
0.01	0.178	0.322	1.217	3.839
0.02	0.127	0.260	0.923	3.051
0.03	0.108	0.231	0.763	2.827
0.04	0.098	0.215	0.660	2.769
0.05	0.093	0.203	0.608	2.762
0.06	0.091	0.196	0.552	2.685
0.07	0.089	0.189	0.523	2.698
0.08	0.088	0.184	0.497	2.772
0.09	0.087	0.180	0.476	2.749
0.1	0.087	0.176	0.460	2.779
0.125	0.087	0.170	0.436	2.822
0.15	0.086	0.164	0.416	2.842

thickness increases. The benefit of a thicker panel now approaches 65% performance improvement.

Graphs from a fixed pressure and variable separation show that gaseous conduction is inversely proportional to the panel thickness, Figure 4.8. This relationship is evident in the analytic expressions discussed previously; nonetheless it is important to notice that DSMC simulations display the same behavior; as shown in Figure 3.5. The sensitivity of heat flux to panel spacing remarks certain limitations on geometric characteristics if this is considered as a strategy for heat transfer manipulation. Changes within the elbow of the heat flux function, where the rate of change approaches its largest values, will quickly shift thermal transfer with small changes in panel spacing. Inversely, change in panel spacing when the heat flux function is

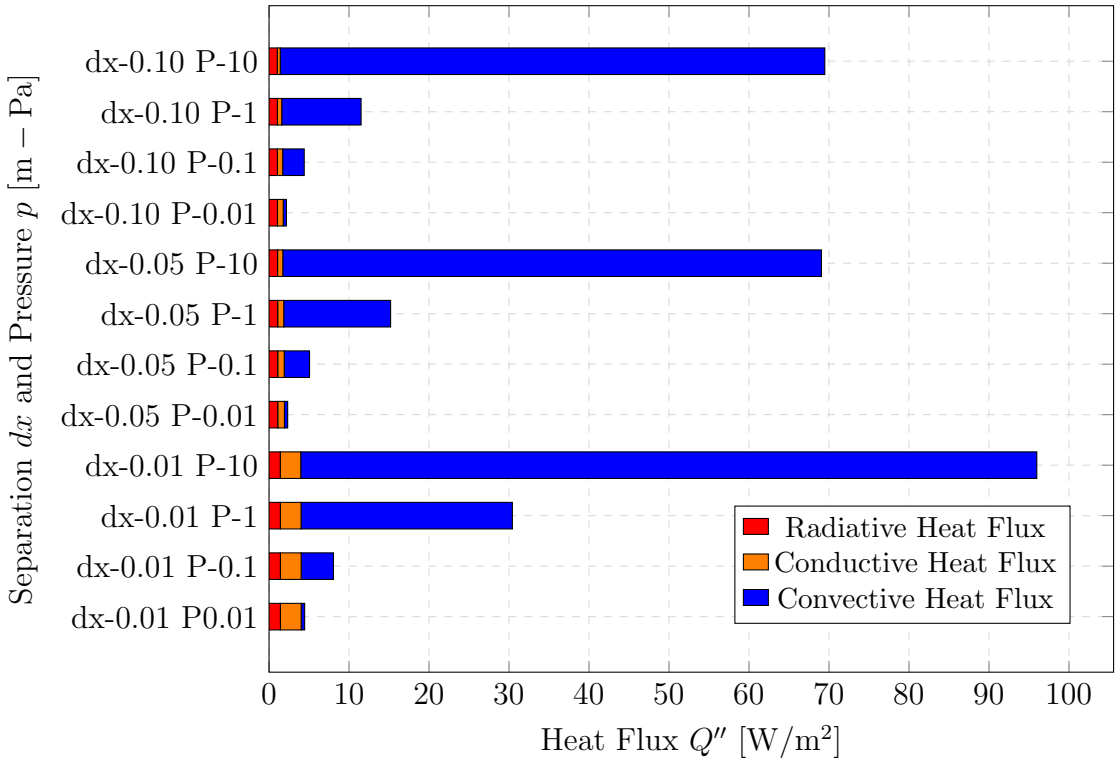

Figure 4.7: Influence of individual heat exchange mechanisms at variable panel thickness and internal pressure. Results obtained from OpenFoam simulations. Temperature range 273-298 K. Air simulated as 77% N_2 and 23% O_2; Side panel emissivity set as 0.016 for both sides.

past the elbow, and the rate of change is small, will have marginal effects.

These results from a simple, yet unfeasible, panel configuration indicate that heat transfer through the fluid becomes a significant influence on the performance of the panel when fluid flow is in the slip flow regime. Moreover, the noticeable contribution of solid conduction at the lowest pressure levels strongly suggest precision modeling of edge-spacer elements so that placement, thickness and materials represent those required to bare the panel's structural stresses and its inherent contribution to heat transfer.

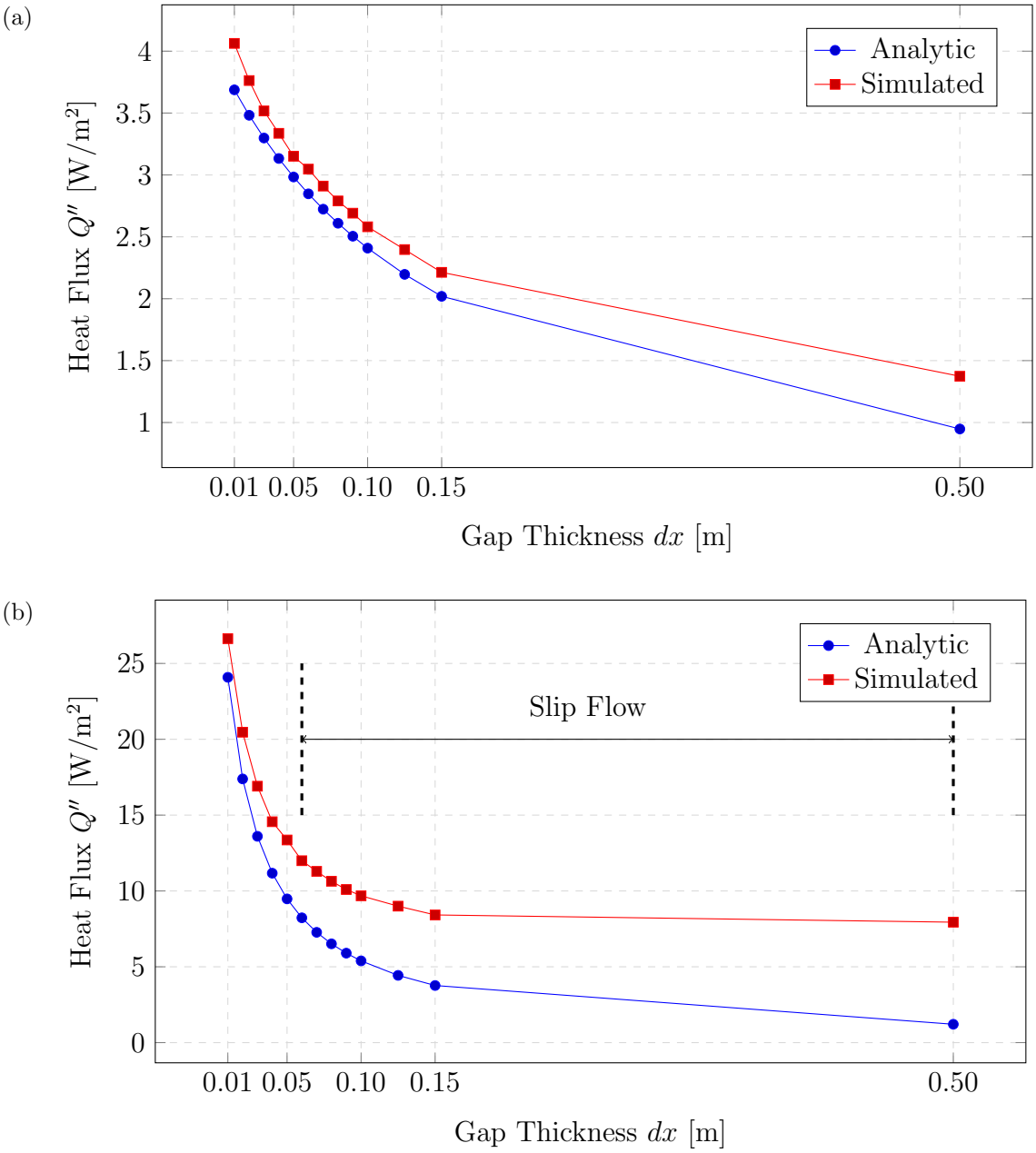

Figure 4.8: Gaseous conduction at a pressure of (a) 0.1 Pa and (b) 1 Pa with different panel separation. Values are compared from analytic expressions described in section 2.2.4.2 and results from dsmcFoam simulations. The gas at 0.1 Pa remains in the transition flow regime but the gas flow at 1Pa changes from a transitional flow to a slip flow with the increasing distance. This flow type evolution correlates to the divergence observed between analytic and simulated results.

The ratio of area (perpendicular to heat flux) to conducting elements' contact area and material resistance should be explored in relation to the overall heat flux to establish a correlation. Such a correlation will facilitate the extrapolation of results from testing smaller samples to larger designs incapable of being fitted into vacuum chambers or hot plate apparatus.

4.3.2 Gas Pressure

A significant trend towards rapid performance deterioration arises when the type of flow evolves from a free molecular flow past the transitional regime and into the slip flow, Figure 4.9. It is at this point that heat transfer through the gas increases substantially and becomes the main transfer mechanism when radiative exchange is kept at a minimum. Panel thickness will mitigate the intensity of gaseous conduction increment during slip flow regime (Figure 4.10). For panels with thickness of 0.05 and 0.1m increasing the pressure from 0.01Pa to 1Pa will increase heat flux by 200% and 150%, respectively. The same pressure changes in the narrower panel of 0.01m will result in 315% heat flux increase.

The semi logarithmic graphs, with a logarithmic scale of base 10 on the abscissa, indicate that gaseous conduction as a function of pressure follows the form of a linear relationship for rarefied gases in free molecular flow. These circumstances suggest that heat flux control through pressure in vacuum panels is manageable. The problem with this approach lies with the pressure control mechanism, i.e. A pressure control system reliant on ambient pressure would have such a vast pressure differential that the linearity of the previous function is quickly swayed by the rate of change of internal pressure. It is perhaps helpful to think that heat flux is linearly related to pressure, but in case of envelope rupture the rate of change of pressure is exponential.

The performance of the vacuum panel will depend primarily on the relationship between the panel thickness and internal pressure, thus dictating the type of flow within the panel and the amount of heat transferred by this type of flow. The superior insulator will operate optimally within the free molecular flow regime. Thicker

insulators will consequently require lower pressure levels to maintain such type of flow. Thinner panels will achieve similar performance in terms of gaseous conduction with higher pressure levels and thus easier to manufacture, however these are more sensitive to changes in internal pressure resulting in rapid performance deterioration.

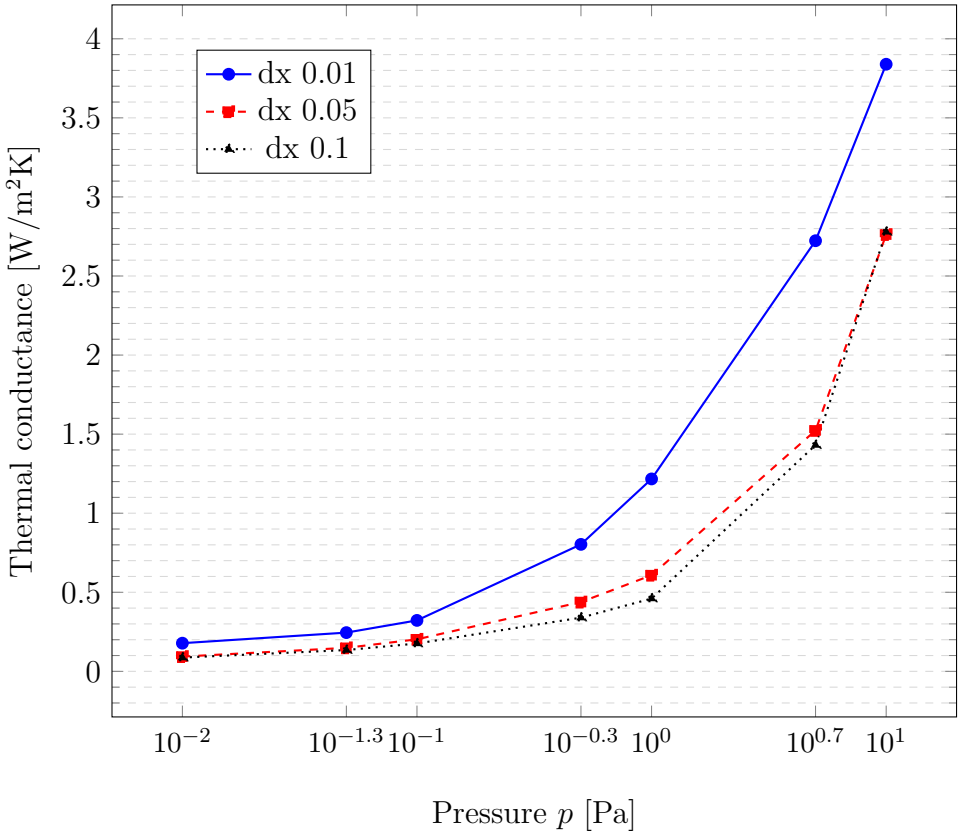

Figure 4.9: Thermal conductance increment with increasing pressure in varying panel thickness. Results obtained from OpenFoam simulations. Temperature range 273-298 K. Air simulated as 77% N_2 and 23% O_2; Side panel emissivity set as 0.016 for both sides. The narrowest panel dimension is significantly affected when the pressure is enough to induce a slip flow regime. Increasing the panel's thickness will mitigate the shift in thermal conductance during the slip-flow regime. The results for the 0.1 m thickness at 10 Pa pressure are invalid as these were simulated with a frozen flow and analytic evaluation suggest a normal continuum flow which requires consideration of advective heat transfer.

Thermal performance variation within types of flow should be considered as a design decision rather than an obstacle. Understanding the relationship between spatial characteristics and vacuum conditions should influence panel design in terms of a balanced performance to feasibility and sensibility configuration. It raises the question of pragmatic manufacturing: Considering the difficulties of achieving high vacuum and the desired performance, which panel and what level of performance is best suited for the building industry?

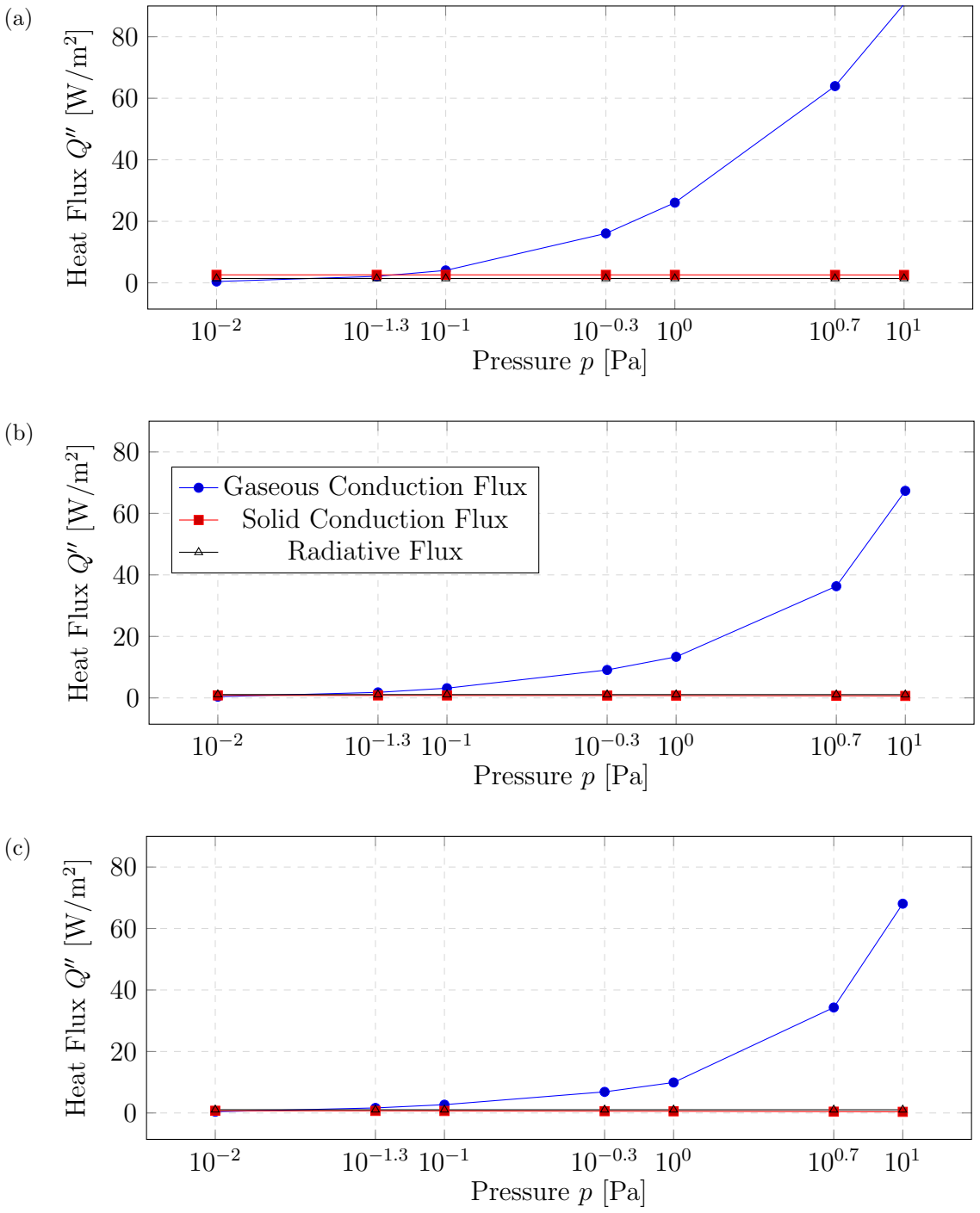

Figure 4.10: Characteristics of Heat Flux at different pressures with a fixed panel thickness of 0.01 m (a), 0.05 m (b), 0.1 m (c) . These results correspond to emissivity of 0.016 and N_2O_2 for the gas.

4.3.3 Gas Composition

Gas conductivity plays a minor role during the free molecular flow regime since gaseous conduction is minimal. The thermal conductance difference between air and argon filled panels is only 1.8-2% (Figure 4.11a) with a pressure of 0.01 Pa throughout all panel separations tested. It is noteworthy that all these configurations at 0.01 Pa exhibit a free molecular flow. By comparison, with a pressure of 1 Pa, when the flow regime has become transitional the gas conductivity is a notable factor and its effect is most noticeable in narrower panels as expected by Increased diffusive heat transfer. The difference in thermal conductance is approximately 30% in the narrowest panel and 20% in the thickest panel (Figure 4.11b).

Detailed analysis into the evolution of heat transfer indicates that heat flux, and inherently thermal conductance, behaves linearly as a function to pressure regardless of gas composition (Figure 4.12). As the flow transitions away from a free molecular flow and into the continuum regime the conductivity of the gas becomes more important in the overall heat transfer.

Including a rarefied gas with low conductivity in the vacuum panel will render the panel slightly more resilient to performance detriment in case of pressure loss. However, in the case of envelope rupture when the vacuum is exposed to trickle filtration from ambient gas, the performance of the panel could not be predicted by these simulations. A two-species diffusion simulation would be needed to determine the dynamics of gases mixing under pressure differential.

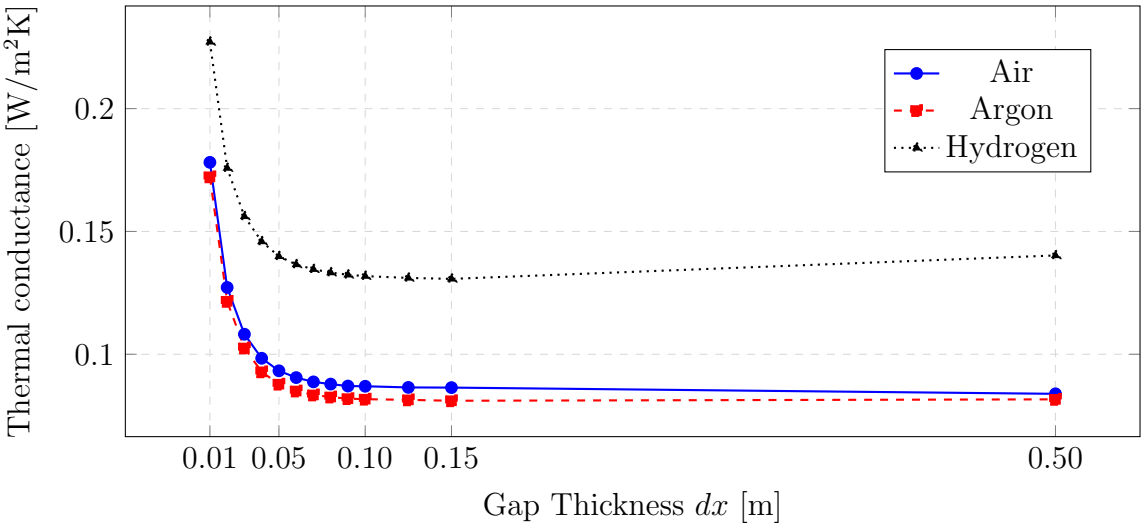

(a)

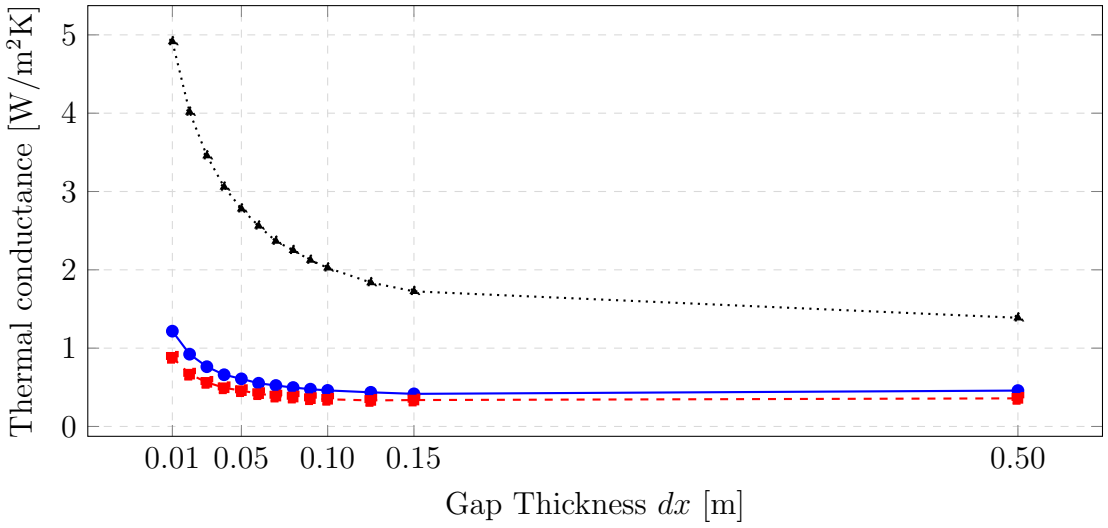

(b)

Figure 4.11: Thermal conductance of panels with variable pressure using Air, Argon or Hydrogen for internal gas; Panels consider an internal pressure of 0.01 Pa (a) and 1 Pa (b). Emissivity is 0.016 and Temperature difference is 298 to 273 K. a) The improvement from gas conductivity is negligible within the free molecular flow. b)The heat flux during transitional flow type is noticeably affected by gas conductivity, especially in narrower dimensions. Results obtained from dsmcFoam simulations.

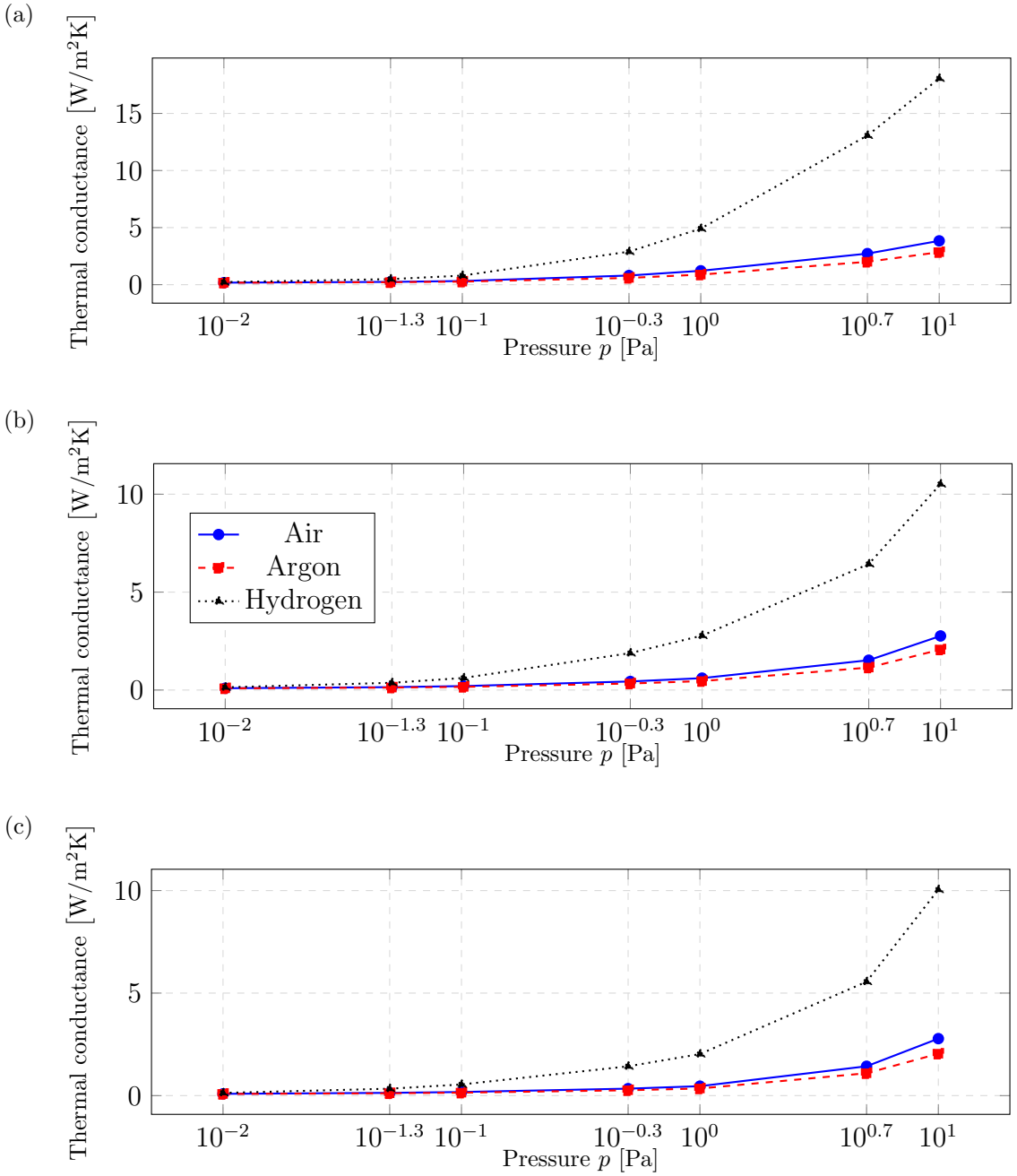

Figure 4.12: Thermal conductance as a function of pressure level in panel thickness of 0.01m (a), 0.05m (b), and 0.1m (c). All surfaces have a 0.016 emissivity. a) As pressure increases and the flow shifts away from free molecular flow gas conductivity becomes increasingly important. b) Sensitivity to changes in pressure is attenuated by the thicker panel. c) The values at 10 Pa are invalid since these fall in the normal continuum type of flow and were simulated with dsmcFoam setup for rarefied gas flow.

4.3.4 Emissivity

The contribution of radiative flux to the overall heat transfer has significant effect on the performance of the panel. A favourable emissivity value, in this case simulated as 0.07, will have a minimal effect on the performance of the panel, rendering gaseous conduction as the most significant exchange mechanism. Nonetheless, radiative exchange has to be suppressed for hollow-core VIPs to achieve values similar to those of composite panels. Contrariwise, an increased emissivity of 0.8 will account for the majority of heat exchange in most cases. The sole exception referring to the thinnest panel with a high internal pressure of 10 Pa (Figure 4.13), where radiative and convective transfer are comparable in magnitude; although the flow's Knudsen number suggests incorporating continuum flow advective transfer mechanisms. The emissivity values chosen here were chosen arbitrarily to exemplify low and high radiation scenarios and are chosen to have the same values over all wavelengths and regardless of temperature.

When radiation is the dominant heat transfer mechanism, changes in convective exchange become less significant to overall heat transfer. By comparing the evolution in thermal conductance of panels with emissivity of 0.07 (Figure 4.9) and 0.8 (Figure 4.14) as pressure changes, the sensitivity to pressure change is almost inconsequential until the flow reaches the slip flow regime. With a low emissivity, changes in pressure from 0.01 to 10 Pa will ultimately result in a heat flux increment by 10 times its original magnitude. Conversely, a high emissivity environment will experience the same change in pressure only as a 78% increase to the original heat flux. Evidently the difference in performance is the result of exposure to a constant radiative exchange of low and high magnitude. While these figures aren't meant

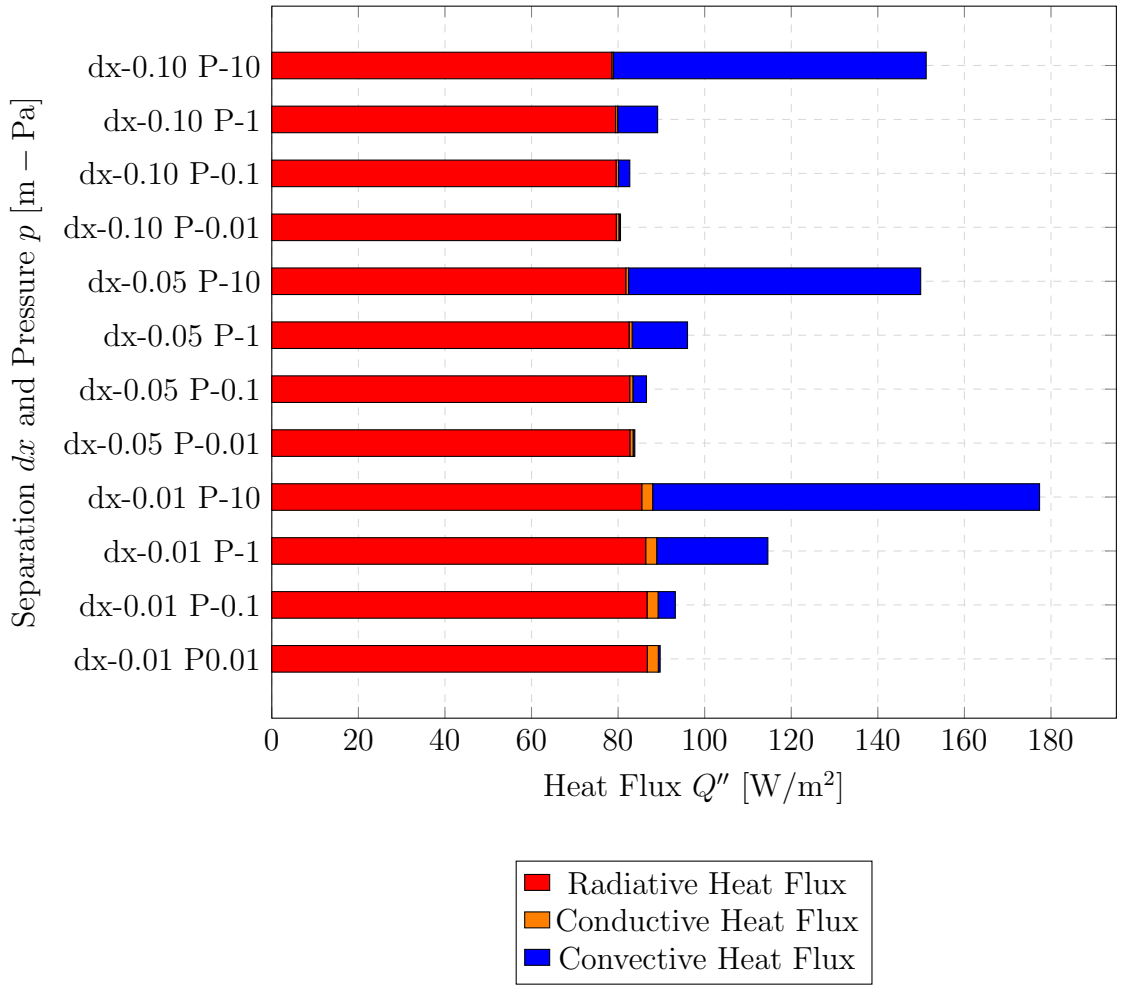

Figure 4.13: Influence of individual heat exchange mechanisms at variable panel thickness and internal pressure; high emissivity 0.8.

to reflect accurate changes in emissivity and their effect on the performance of the panel, they demonstrate the potential for radiative heat exchange as an important mean of control in thermal exchange manipulation strategies. Moreover, VIP panels with a low U-Value by default will benefit by employing different control mechanism towards different goals. Manipulation through emissivity can achieve massive thermal transfer control, however if the emissivity change is considered binary, e.g. high and low, delicate adjustments with minor heat flux increments or decrements will not be possible.

Further research invites for a detailed simulation with emissivity values assigned per wavelength according to performance electrochromic and thermochromic coatings.

Manganite films, specifically $La_{0.7}Sr_{0.3}MnO_3$ (LSMO) films on yttria stabilized zirconia (YSZ) substrate show thermochromic properties that display emissivity variation ranging from 0.17 to 0.59 in the infrared spectrum [156]. While these values show incredible potential for heat transfer manipulation and control, the application in the building industry is limited to a narrower emissivity band. The thermochromic behavior of these films exhibit the most significant change in emissivity from low temperatures of 100 K until 300 K, therefore the curve growth of interest for building insulation is limited to emissivity change from 250-310 K. Within this band the emissivity values available range approximately between 0.45 and 0.55[156].

In addition to thermochromic materials, which adjust emissivity without any active controlling mechanism, electrochromic materials can change optical properties when subject to electrical pulses. The Eclipse variable emissivity device reports the capacity to change emissivity from 0.016 to 0.93 at a wavelength of 8 µm and between temperatures of 300 and 350 K respectively by changing from a bleached to

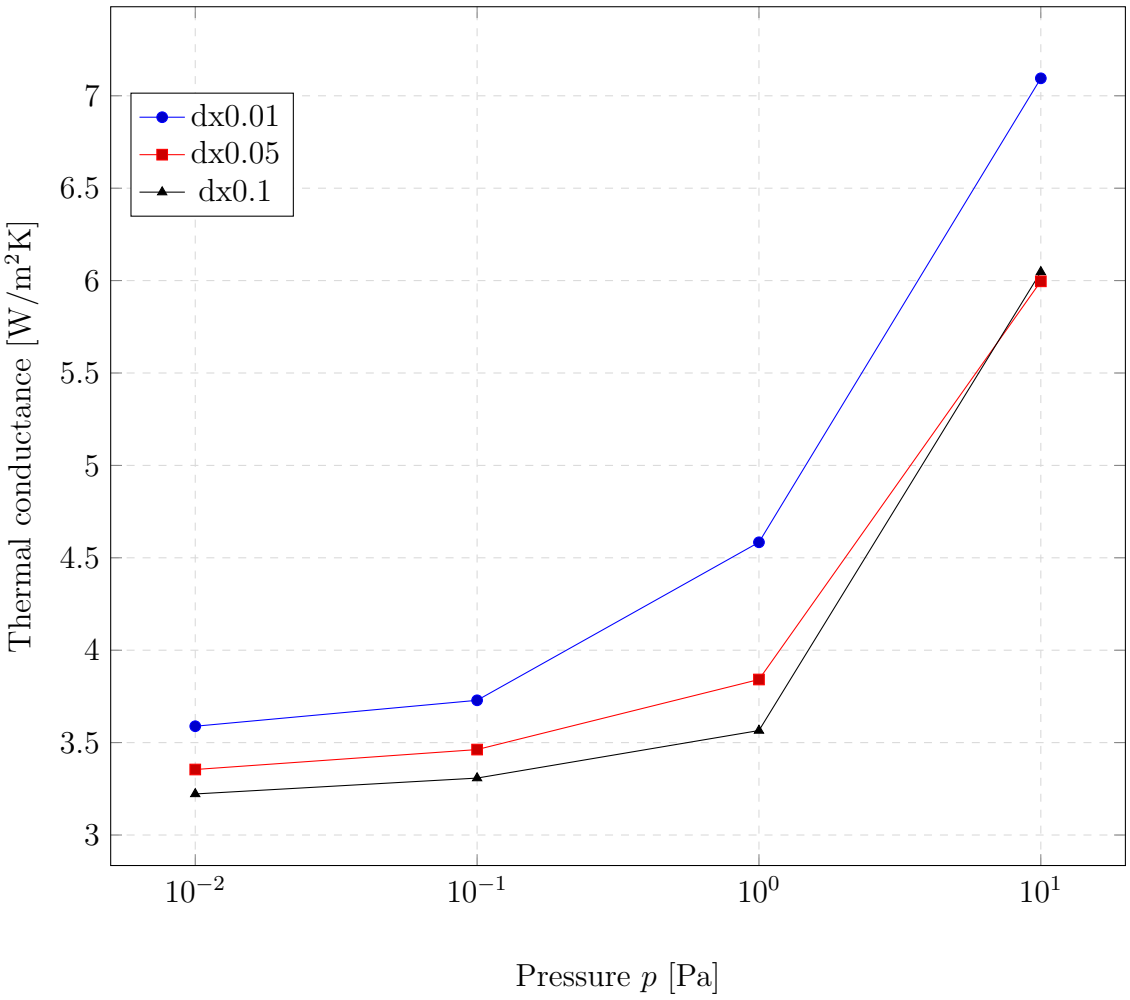

Figure 4.14: Thermal conductance progression with increasing pressure in panels of varying thickness. Emissivity of 0.8

colored state [157]. Similarly, Nickel Oxide (NiO) and Tungsten Oxide (TiO_3) films have been shown to achieve a large modulation capacity by adjusting film thickness. These materials have been determined to change emissivity between 0.057 and 0.595 over a spectral range of 2 -13.8 µm at a temperature of 300 K [123, 158, 124].

4.3.5 Estimated Range of Influence

At performance levels where the thermal conductance approaches 0.1 W/m^{2}K even marginal radiative heat gain from a low-E material (0.07) will be significant, and prevent the panel from reaching the aforementioned limit. In order to achieve performance similar to composite panels, radiative heat transfer must be eliminated. Composite panels achieve insignificant radiation by the complex interaction of photons through the tortuous path in the nanoparticle layer, ultimately resulting in radiation extinction. Hollow core panels will have to rely on highly reflective and inherently low emitting surfaces. This effect can be achieved by radiation barriers of fixed optical properties or by thermochromic or electrochromic films as mentioned previously.

If a near perfect reflective surface is considered, the thermal conductance of hollow core panels could be similar to that of composite panels. The lack of core material then presents the opportunity to control heat transfer without having to deal with the adversities of radiation extinction present in optically thick layers of insulation. Heat transfer control could be pursued by passive means such as thermochromic coatings, or by active means such as electrochromic coatings and/or metal hydrides. Additional means exist to mechanically control conductive transfer, such as bimetallic springs [159], although including complex moving parts also

represent vulnerabilities exposing the technology to potential malfunction or failure.

The best thermal manipulation strategies should rely on pressure and/or emissivity control.. The pressure values considered range from 0.01 to 10 Pa, and constitute a shift in the convective flow from free molecular to slip-flow or even continuum in the thicker panels. Emissivity's lower and upper limits are 0.016 and 0.93 as described by the Eclipse variable emissivity device [157]. These emissivities result in a low and high thermal conductance of 0.17 and 8 W/m^2K respectively, Figure 4.15. Completely eliminating radiation would result in thermal conductance values of 0.113, 0.043, and 0.038 W/m^2K for panels thickness of 0.01, 0.05 and 0.1 m. Complete radiation extinction will continue to improve performance of the panel even by comparison to the reflective state of the Eclipse film (Emissivity of 0.016). However, further control of emissivity by additional means would complicate manipulating heat transfer through the panel.

In addition the Eclipse variable emissivity material, Nickel and Tungsten Oxide films were simulated and show a viable range of thermal conductance for thermal exchange. While the emissivity of these films only spans 0.057 to 0.595 [123, 158, 124], the resulting properties of the panel make for a good insulator and exchange surface, Figure 4.16. Thermochromic materials, with emissivities varying between 0.45 and 0.55 [156, 160] within the temperature bands experienced in the building industry, are not a viable solution as the lowest possible thermal conductance does not fulfill expectations as an effective insulator.

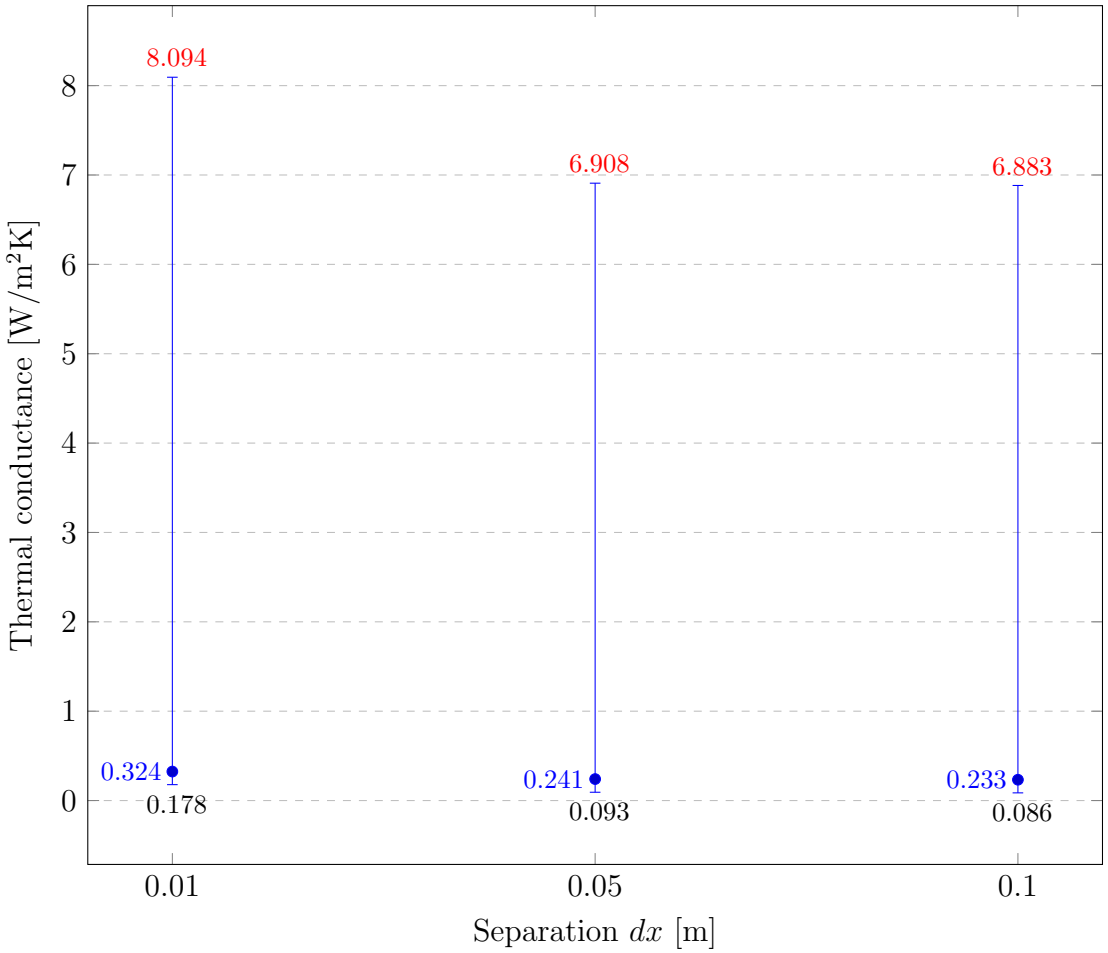

Figure 4.15: Theoretical range of thermal conductance that could be achieved by manipulating pressure and emissivity of the panel. The narrower panel is more sensitive, and therefore presents a wider range of thermal conductance. The initial value shown in blue corresponds to the emissivity of a polished steel plate (0.07). The lowest and highest values correspond to limits described by the Eclipse variable emissivity device [157] as well as a pressure shift from 0.01Pa to 10Pa.

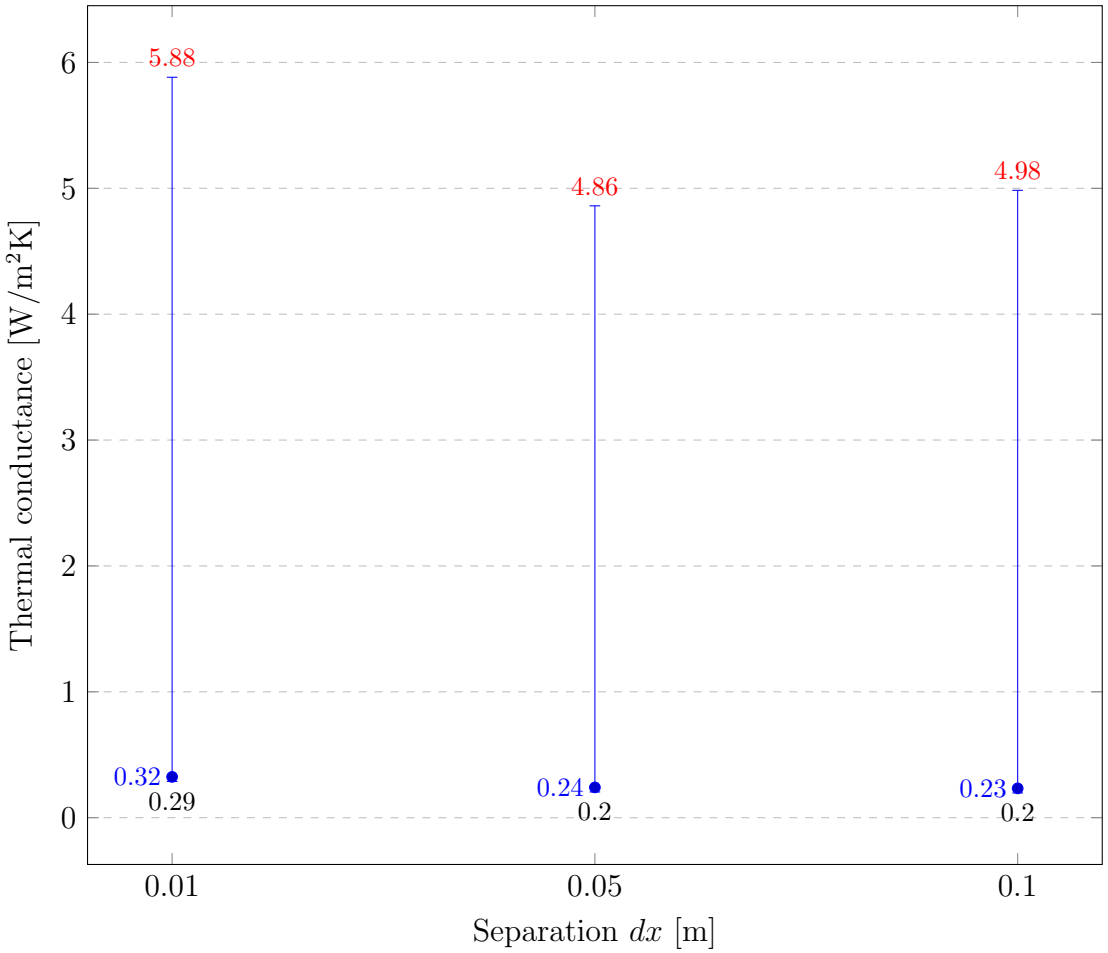

Figure 4.16: Theoretical range of thermal conductance that could be achieved by manipulating pressure (0.01Pa to 10Pa) and emissivity of the panel with Nickel/-Tungsten Oxide electrochromic films.The initial value shown in blue corresponds to the emissivity of a polished steel plate (0.07).

4.4 Conclusions

- Determine adequate panel thickness in regards to thermal performance.
- Determine necessary pressure to suppress gas conduction.
- Study the effect on heat flux of different gas composition.

- Study the effect of internal surface emissivity on heat flux.
- Estimate a thermal conductance range considering fluctuation of all variables.

Initial simulations of a simplified VIP model show that hollow-core panels are highly sensitive to gas pressure and internal emissivity values. Moreover, the geometric configuration of the panel needs to be studied thoroughly during the design process, as changes in dimensions affect the necessary pressure level to suppress convection. For thin panels with thickness in the range of 0.01-0.1 m it has become evident that thicknesses larger than 0.05 m, while providing good insulating properties, require high vacuum pressures difficult to achieve in order to maintain the gas flow type in the free molecular range. In the same measure, very thin panels are highly sensitive to pressure changes and solid conduction. For this type of vacuum technology, the recommended thickness lies between 0.02 and 0.05 m. Tested panel dimensions require a pressure of $0.01Pa$ to achieve free molecular flow and suppress gas conduction. Heat transfered by gas conduction in rarefied gases is limited resulting in negligible difference between gases with different composition and thermal conductivity.

Gas pressure and emissivity need to be regarded as both weak and promising characteristics. Adequate regulation of these properties can greatly affect the performance of the panel. Emissivity lower than 0.1 is necessary to mitigate radiative heat transfer. An emissivity of 0.8 becomes the dominant heat transfer mechanism even on elevated pressure (10Pa) situations. Considering variation in all tested properties yield an estimated thermal conductance range between 0.2 to over 5 $\frac{W}{m^2K}$. While changing gas pressure can have a significant effect in the conductivity of the gas region, achieving and maintaining a high vacuum is an arduous and

time-consuming task, therefore this method is not ideal, and a fixed pressure is recommended. Moreover, the technology for controlling gas pressure in a closed system is currently limited to metal hydrides [118, 57, 44], introducing additional complexity and vulnerabilities in the system. Contrary to affecting gas pressure, changing the emissivity of a surface is well studied phenomenon and several solutions have been developed and studied. While the passive solution of thermochromic coatings is appealing due to its self-regulating nature, the temperature range experienced in most building applications falls short of the necessary temperature required by such coatings to fully change states. The most suitable solution based on previous investigation are electrochromic coatings, such as Nickel Oxide and Tungsten Oxide films. Emissivity values from these films applied to the simplified model suggest the hollow-core VIP could function well as an insulator and as a conductor. Moreover, any improvements in this field could be readily incorporated into the panel without requiring design modifications.

Contribution from solid conduction is noticeable as the panel becomes thiner, even though this simple model lacks any internal support structure. It can be inferred from these results that incorporating a necessary internal structural array will increase thermal conductance significantly.

After meeting all objectives previously established, the gathered information will inform the design of a more precise model that can be compared against empiric measurements. The next model will avoid over simplification and will need to include previously neglected properties, such as the thermal resistance present at the contact interface between two different solids and will include an internal support structure. Results from the following chapter will provide additional validation and verification of the simulation method.

Chapter 5

Measured thermal resistance of hollow core VIP nodes.

5.1 Introduction

This chapter studies heat transfer through a series of prototypes representing individual nodes contained in the array found in a full size hollow-core VIP. Several prototypes were manufactured to represent sections of the panel and placed inside a vacuum chamber to simulate the vacuum conditions found in the evacuated panel.

The test sample is exposed to temperature boundaries found in common building environments, with a maximum temperature of 43 °C ($\pm 1°C$) and with a maximum ΔT of 25 °C. This chapter explores the correlation of the sample's properties and its resulting thermal resistance. Having observed from analysis on the simplified model that hollow core VIPs are sensitive to pressure, geometric configuration and emissivity, these variables are tested in several permutations in order to establish a correlation between the overall thermal resistance and the structural array of the

panel. Table 5.1 summarizes the set of permutations tested, by empirical means and simulation. Figure 5.1 shows diagrams of the spacer configurations included in the tests. It should be noted that the only repeating node is the "cross" configuration, the other configurations correspond to boundaries in the VIP.

The tested samples have an area of 0.0625 m^2, measuring 0.25m in length and width. The opposing parallel plates, meant to represent the external panels of the VIP, have been manufactured of stainless steel grade 304. Two emissivities are tested, the low emissivity version is a highly polished steel plate, and the high emissivity version is a steel plate that has been coated with epoxy resin and black pigment. The structural or spacer elements have a height of 0.025m and 0.05m and have been laser-cut from a 3mm thick PTFE sheet. Materials were chosen due to their low-outgassing properties, available external suppliers and compatibility with manufacturing equipment.

Table 5.1: Test permutations conducted. Three spacer configurations were used: an outer box joined at the edges of the steel plates, and interior symmetric cross and a Box-Cross configuration which included the previous two simultaneously. Two combinations of emissivities were tested: Both plates with low emissivity finishes, both plates with high emissivity. Each of these combinations is carried out with both 25mm and 50mm width PTFE spacers

Emissivity	**Spacer Configuration**		
	Box	Cross	Box-Cross
Low	25mm	25mm	25mm
	50mm	50mm	50mm
High	25mm	25mm	25mm
	50mm	50mm	50mm

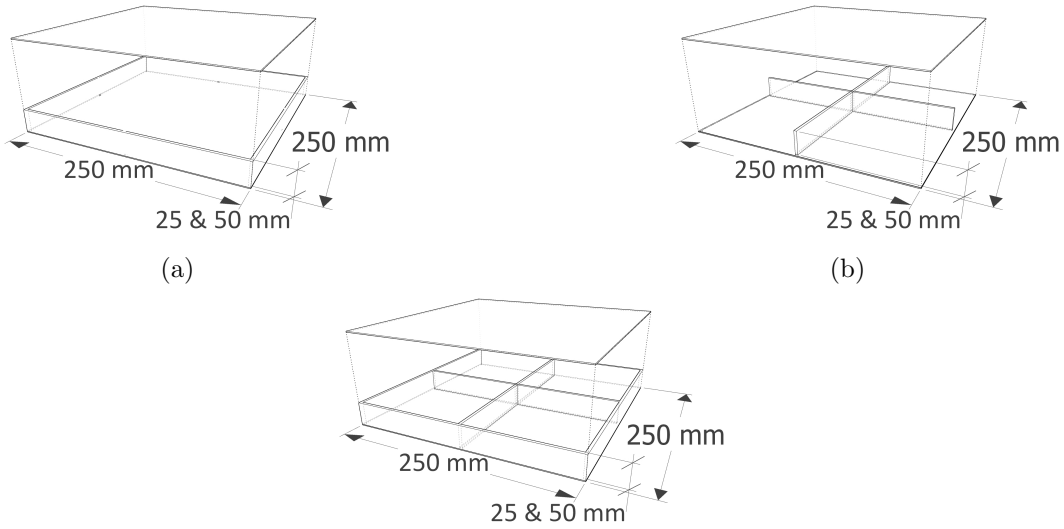

Figure 5.1: Configuration of tested samples. Top and bottom plate sandwich three different configurations of the structural array: a) Box configuration. b) Cross configuration. c) Box-cross configuration. These configurations are used to evaluate heat flux at different positions within the sample. The cross node is a repeating element in the structural array of a full sized hollow-core VIP.

5.1.1 Aims and objectives

The study of this chapter aims to empirically determine the thermal resistance of different sections of a hollow-core VIP.The objectives are:

- Manufacture and calibrate the testing equipment and method.
- Measure heat flux through the samples to establish a thermal resistance.

5.2 Materials and Method

Empiric measurements are limited to temperature and heat flux sampling at the external surfaces of the sample through two sampling points on each side. Available

data feed-through allowed for a limited number of sensors, more details are found in the following subsections.

5.2.1 Testing equipment

A large part of the laboratory equipment used to test the samples had to be manufactured in order to be compatible with a vacuum environment; this was a very time consuming endeavor. This included building the thermally controlled room housing the vacuum chamber, PID controller, the testing rig holding the sample, temperature and heat flux sensors. Preparation of the sample, test rig and sensors is described in greater detail in the following subsections.

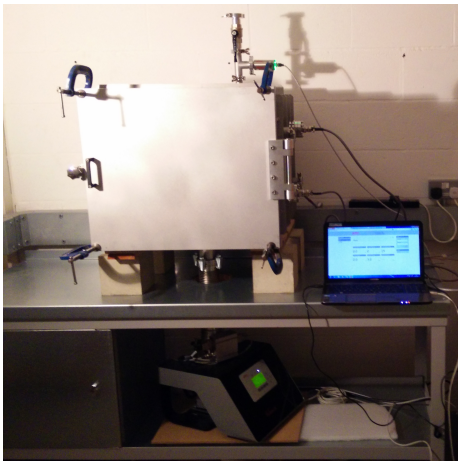

(a)

(b)

Figure 5.2: a) Vacuum Chamber Setup, initial system configuration. b) Testing rig inside chamber, initial configuration. The custom fabricated vacuum chamber sits on a stainless steel bench, the pumping system is located below the chamber. Data logger, PID controller, and additional equipment were later incorporated in an adjacent test bench.

The testing rig, instruments and sample are all placed inside a stainless steel vacuum chamber measuring 600mm length by 600mm width by 500mm depth, Fig-

ure 5.2a. The testing rig, Figure 5.3, was machined at the engineering department with high precision milling equipment providing accuracy up to 1/10 of a millimeter. This testing rig also included radiation shields manufactured from highly polished stainless steel plates that attached to the edges of the bottom plate.

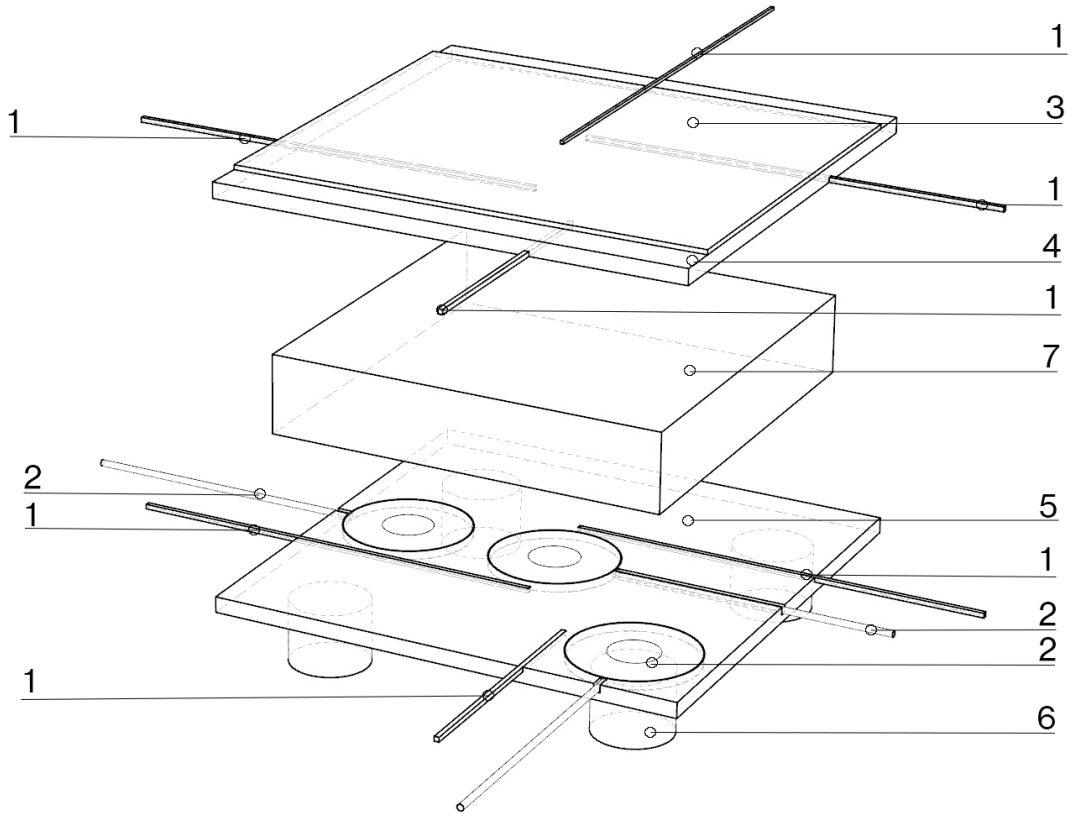

Figure 5.3: Test Rig: 1) PT-100 temperature sensors. 2)Hukseflux HFP01 Heat Flux sensors. 3) Omega Engineering Insulated Kapton Heater KH-1012-P, 10 by 12 in, 2.5$\frac{W}{in^2}$. 4) Hot Plate- Aluminium (6082T6) 10mm thick, 300 by 300mm. 5) Cold Plate Aluminium (6082T6) 10mm thick, 300 by 300 mm. 6) Heat Sinks – Aluminium (6082T6) 50mm diameter bar, 40mm length. 7) Sample.

5.2.1.1 Pump system

The chamber is evacuated by a Oerlikon Leybold Turbolab 80 Turbo Molecular Pump System . The Turbolab 80 pump system includes a turbo molecular pump TurboVac SL 80 H with a DIVAC 0.8 T backing Pump running at 1200Hz at maximum speed [161, 162]. The pressure gauge is a Leybold PENNINGVAC PTR-90N, which uses pirani and cold cathode ionization measurements. This dual measurement technology allows the gauge to measure between ambient pressure (1000 mbar) down to 1×10^{-8} mbar [163]. Due to the large volume of the chamber the lowest observed pressure with an empty chamber was only slightly below 1×10^{-5} mbar.

5.2.1.2 Temperature sensors

Within the test rig, 5 temperature sensors were placed. One over the resistance heater, as part of its thermal controller, two on opposing plates of the test rig next to the central heat flux sensor, two more on opposing plates next to the corner heat flux sensor, Figure 5.4. The sensors used are RS-Pro PT-100, class A, platinum resistance sensors with two leads. These have a thermal response time of 0.1s and, a temperature range from -50 °C to +500 °C, and a tolerance of ± 0.25 °C at 50 °C [164]. Thermocouples were not used because the chamber data feed-through ports are not suitable for thermocouples.

Besides manufacturer specifications, the sensors were calibrated against two mercury thermometers. Both mercury thermometers were compared in icy water and warm water; their reading matched with no discernible differences and the icy water reading was of 0.1 °C. Since the PT-100 sensors could not be fully submerged in water these were attached to an Aluminum rectangular profile that was 95% sub-

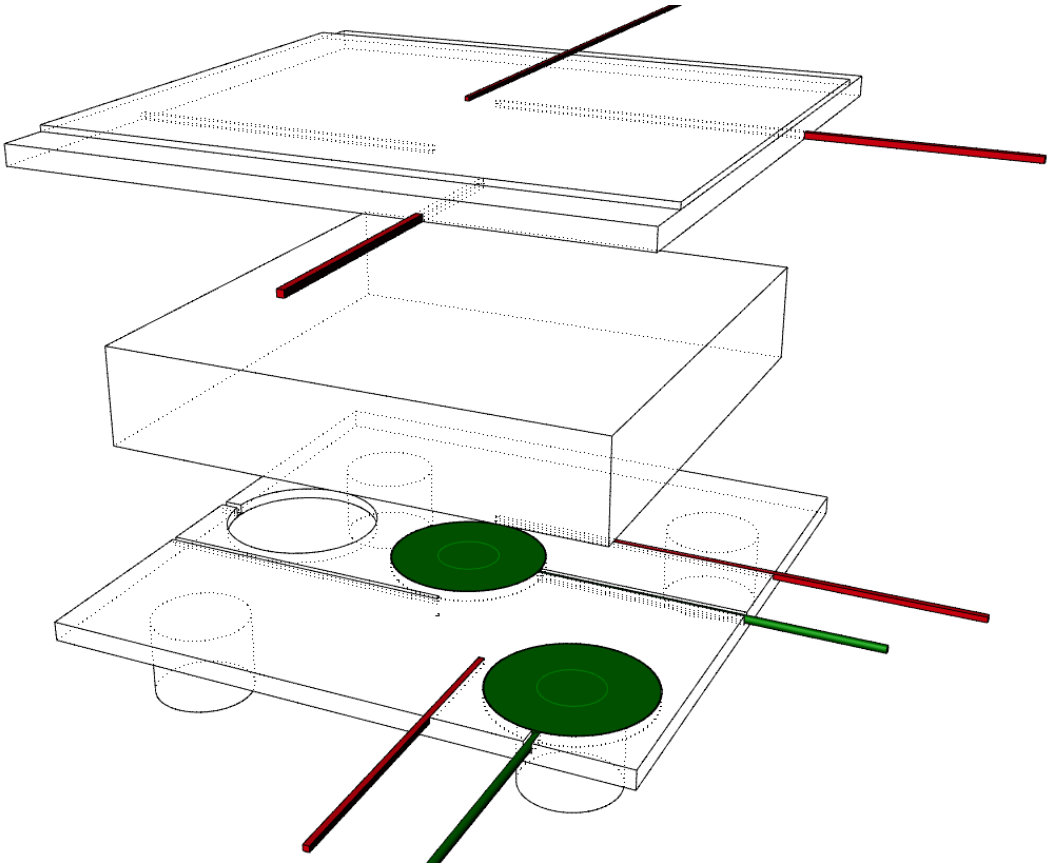

Figure 5.4: Temperature and heat flux sensor placement diagram. Temperature sensor and wire leads are shown in red, Heat flux sensors and wire leads are shown in green. Locations were chosen to take readings from centre and edge of sample.

merged in water. One of the mercury thermometers was also contacting the bar adjacent to the PT-100 sensors. Everything was shielded with Aluminum foil and temperatures were logged for an hour, Table 5.2. Differences beyond manufacturer's tolerance between sensors are attributed to differences in the soldered wires to the leads and the wiring to the data logger, all of which can include variations on the electrical resistance of the circuit.

In addition to the tolerance of the sensor and individual calibration, the connection between the sensor's wires and the chamber feed-through was subject to

Table 5.2: Average temperature sensor readings in cold water.

Mercury °C	**PT #1** °C	**PT #2** °C	**PT #3** °C	**PT #4** °C	**PT #5** °C
1.5	2.69	2.55	2.35	2.33	2.69
deviation	1.19	1.05	0.85	0.83	1.19

small resistance variations. As a precaution the prepared rig and samples were left overnight to achieve steady state and the sensors readings were adjusted to coincide within the aforementioned tolerances.

5.2.1.3 Heat flux sensors

The Hukseflux HFP01 heat flux sensors are factory calibrated and have a nominal sensitivity of $60 \times 10^{-6} V(\frac{W}{m^2})$. The response time to a 95% accuracy is 180s. The measurement range is -2000 to +2000 $\frac{W}{m^2}$ within an operating temperature of -30 to +70 °C. The sensor is comprised of a sensing area in the center with a diameter of 32×10^{-3} m surrounded by a ceramic guard. The overall sensor dimensions are 80×10^{-3} m in diameter with a 5.4×10^{-3} m thickness. While factory calibration uncertainty is ± 3% additional factors render ideal measurements in building physics applications subject to ± 6% uncertainty and improper applications up to ± 20% uncertainty [165]. Figure 5.4 shows the location of the sensors, these were position to sense heat flux at centre and edge of the sample. These sensors have been carefully employed with a thin layer of grease acting as a thermal interface to avoid substantial increase in its effective thermal resistance. Moreover, heat flux deflection by thermal conductivity difference between the sensor and its surrounding material is assumed negligible since the sensor is spaced 0.5 mm from any surrounding material and in a vacuum environment. Estimated overall uncertainty considering factory calibration

uncertainty, non-stability from usage time and additional thermal resistance at the area of contact is ± 10%.

5.2.1.4 Resistance heater

The heater attached to the upper plate is a low out-gassing Kapton Insulated Resistance Heater manufactured by Omega Engineering; model KH-1012-P with a power density of 2.5 $\frac{W}{in^2}$. The heater measures 10 by 12 inches and has a thickness of 0.25mm and includes pressure sensitive adhesive on one side. The operating temperature range is -200 °C to 120 °C [166].

This resistance element was controlled by an Inkbird ITC-100VH-220 PID with one of the previously mentioned PT-100 sensors attached to the heater. The heater was covered with Aluminum foil to mitigate radiative losses to the chamber. This heater was the largest available with low out-gassing properties that could heat a surface evenly thus restricting the sample size to an approximate area.

5.2.1.5 Data gathering

All data was gathered through a Keithley 2700 data logger on 5 second intervals; the equipment is factory calibrated.

5.2.2 Sample

The tested samples were manufactured (shown in Figure 5.5), and simulated, with the intention of representing a fraction of the full sized panel. The “cross” sample represents the repeating node in the panel exluding edges. The “box” and “box-cross” nodes are representative of nodes in the edge of the panel, albeit with dif-

ferent structural separation. The samples are composed of two parallel steel plates separated by PTFE edge-spacer elements. These samples were tested in all permutations possible with two emissivity finishes for the steel plates, two edge spacer lengths and three possible configurations of the edge-spacers. These permutations are commented on with greater detail in the following section. Before any sample was placed inside the vacuum chamber it was thoroughly wiped with acetone and subject to heating with a heat gun during 10 minutes. All points of contact, between the steel plates and the Aluminum plates, between the edge spacers and the steel plates, between the aluminum plate and sensors, were covered with a thin layer of Dow Corning high vacuum grease to act as a thermal interface.

5.2.2.1 Plates

Plates with two different emissivity values are employed to assess the radiative heat transfer magnitude with relation to other heat transfer mechanisms. Moreover, employing two distinct samples will approximate the effect of altering the internal emissivity as could be achieved with electrochromic coatings. The low emissivity plate is a 1mm thick mirror-polished stainless steel plate measuring 250 by 250mm length. The high emissivity plate is a stainless steel plate of the same dimensions that was coated with East Coast Fibreglass Supplies' 2:1 fast acting epoxy resin from their SP Handipack (375ml) with 10% total volume super black epoxy color pigment. The epoxy coating was measured with calipers to be less than 1mm thick but did show noticeable tapering near the edges. The coated plates were left to cure at ambient temperature (20 °C) during 48 hours and were then baked at 100 °C during 6 hours in order to reduce out-gassing. Figure 5.6 presents images from scanning electron microscopy displaying surface uniformity for both coatings.

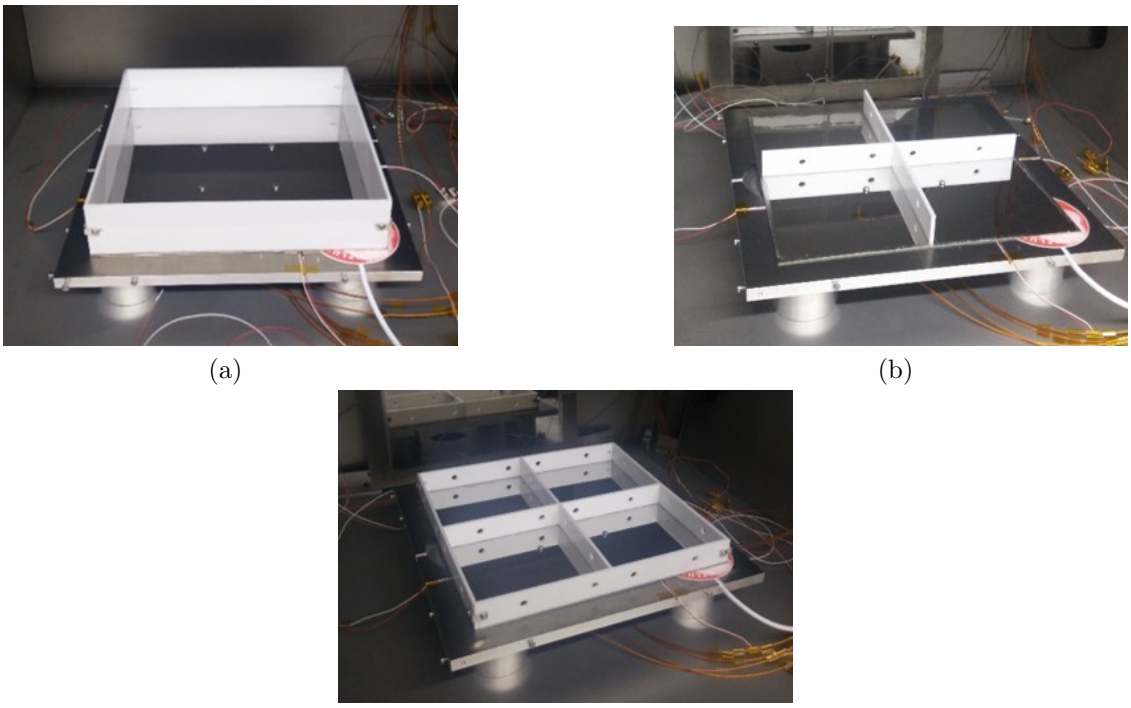

(a) (b)

(c)

Figure 5.5: Manufactured samples. The PTFE structure rests on the polished stainless steel face plate which is bolted onto the temperature distribution aluminium plate. The samples show three different configurations of the structural array: a) Box configuration. b) Cross configuration. c) Box-cross configuration. These configurations are used to evaluate heat flux at different positions within the sample. The cross node is a repeating element in the structural array of a full sized hollow-core VIP.

These plates were bought pre-cut and coated in-house with epoxy resin. Nonetheless, large scale manufacturing could benefit from using a water jet cutter which can operate constantly and produce pieces with a tolerance of $0.03mm$ [167]. Samples could include a layer of electrochromic or selective coatings, which would require a magnetron sputtering deposition [156, 81].

The coated sample was analyzed with a FLIR thermal imaging camera under controlled temperature conditions. Since the surface temperature is known, the emissivity value on the imaging equipment was adjusted until accurate temperature

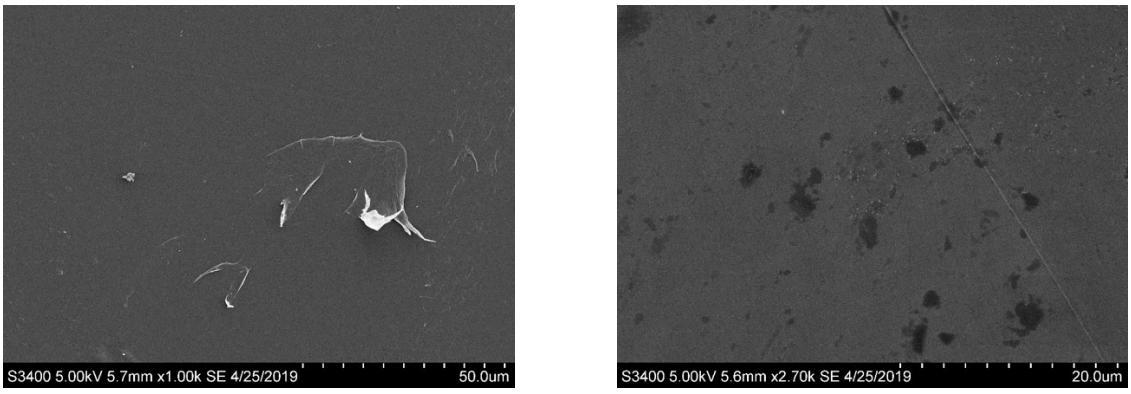

(a) (b)

Figure 5.6: SEM images of sample plates. a) 1000 magnification of epoxy coated plate. b) 2700 magnification of polished stainless steel. The white flecks seen in the PTFE sample are thought to be fibres from a cloth used to wipe the samples. It is important to note how the PTFE coating is even smoother than mirror polished stainless steel.

readings were obtained. While this method was not conducted with great precision, the readings agree with literature [168, 169]. Moreover, 3M Scotch Super 88 vinyl electrical tape covering the thermocouple placed at the center of the sample is seen to merge completely in infrared imaging as show in Figure 5.7, thus implying a similar emissivity coefficient to that of the tape. 3M Scotch vinyl tape has a known emissivity of 0.95 $\pm$0.05 [170].

In addition to literature review and thermal imaging, surface emissivity of both samples was tested by Becker Ltd. conforming to ASTM C1371-15 standard test method. The mirror polished sample was found to have an emissivity of 0.12 and the resin coated sample was found to have an emissivity of 0.9. The detailed report on emissivity measurements can be consulted in Appendix C.

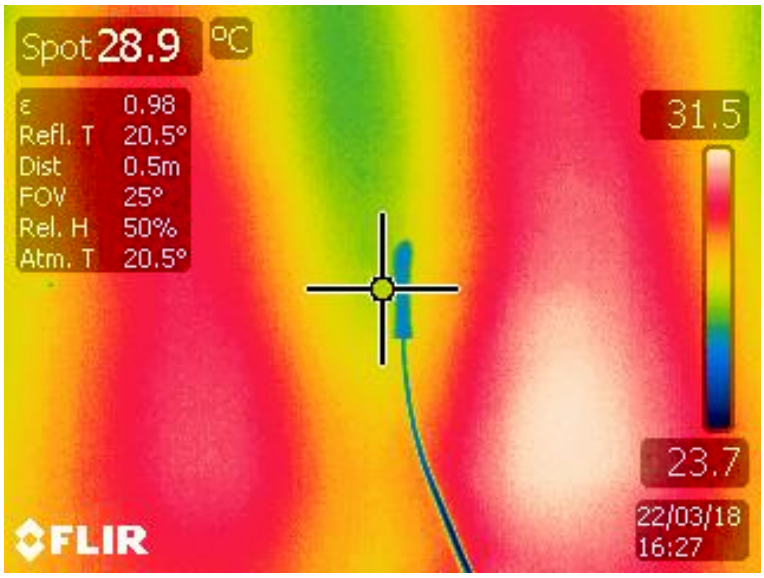

Figure 5.7: Thermal imaging of resin coated sample while maintained at a constant ± 30 °C temperature. Point of measurement is aiming at black electrical tape covering the K-Type thermocouple. It should be noted that the heating mat used here is not the same as used in the vacuum chamber. Uneven heating is clearly discernible.

5.2.2.2 Spacing elements

The structural array elements, or spacers, were laser cut from a single sheet of 3mm natural colored PTFE sheet. These elements were manufactured in order to be assembled as a 250 by 250mm length box or as a 244 by 244mm length cross. The "box" elements had serrated edges to lock in together and were also bolted in place by a small Aluminum 90 °angle with an M3 bolt. The "cross" elements had a single slit through the middle to allow its counterpart to be inserted into place. Both configurations were manufactured in 25 and 50mm widths.

PTFE was chosen because it could be laser cut to a high level of precision and has low enough out-gassing to work in high vacuum. In actuality, steel has much better mechanical and out-gassing properties, but without a water jet cutter achieving

precision pieces would require great dedication in the milling or cutting process as the thin steel plated being used are prone to slight deformations. Nylon and acetal were considered for the structural array, however, these materials have higher outgassing properties than PTFE(TML 0.23%, CVCM 0%). Acetal has a total mass loss (TML) and collected volatile condensable materials (CVCM) of 0.37% and 0.02%. Nylon has a TML of 2.02% and CVCM 0% [171]. Figure 5.8 shows that PTFE has a cracked texture when magnified 25000 times.

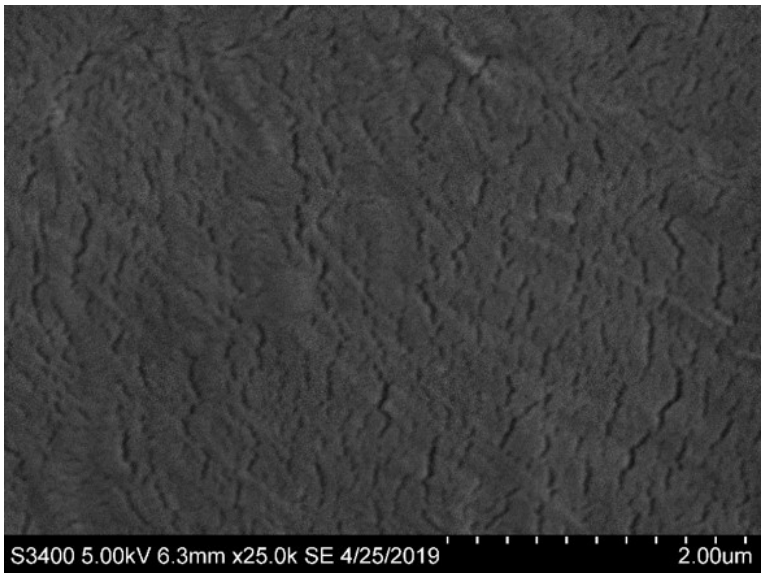

Figure 5.8: SEM imaging with 25000 magnification of PTFE sample.

Large scale manufacturing of the structural elements could employ laser cutter is the material is PTFE. If stainless steel is chosen water jet cutters could produce pieces to a high level of precision [167] or die cutting techniques could be used as an alternative. However, if the stainless steel pieces require a specific treatment on the edge die extrusion would be a better solution.

5.2.3 Testing procedure

The measurement technique is similar to that described by Collins [47], where the gradual increase in temperature on the cold side is measured after the application of a rapid increase in temperature on the hot side. The rate of increase in temperature on the cold side depends on the thermal conductance of the sample.

Prior to the evacuation of the chamber and once the sample and test rig had been set for testing, the chamber was closed and left overnight to achieve an even temperature through all elements contained within. Before evacuation, the internal temperature was sampled and sensors' readings were checked for discrepancies. The temperature, heat flux, and pressure were logged on 5 second intervals from the beginning of the evacuation sequence until the test was concluded.

The chamber was maintained at an internal pressure of 1×10^{-4} mbar during 1 hour before heating the top plate to 40 °C. The default set point for the heater is 25 °C, since these tests were performed during the summer of 2018 in the UK ambient temperature was either close to 25 °C or even slightly warmer. The long progression of the tests gives insight of low flux situations in vacuum and during higher pressures. The sudden increase in temperature, and the panel's response to its inherent high flux, is indicative of the panel's thermal properties such as thermal mass and thermal conductance. The continuous activity during the initial heat phase was logged in order to determine the total energy introduced into the system during that time. The top plate was kept at 40 °C during several hours to obtain a semblance of steady state. Given the fact that the bottom plate is not actively cooled, and instead acts as a heat sink, a true steady state could not be achieved. To avoid improper data comparison, all tests were compared against transient simulations with the same

boundary conditions.

The measured heat flux will be the result of the temperature difference measured between opposite sensors in the top and bottom aluminum plate divided by the total resistance of the sample. Figure 5.9 shows preparation of a sample on the test rig, inside the vacuum chamber.

(a) (b)

Figure 5.9: a) 50mm Sample in thermal measurement rig, the Kapton heater is uncovered to show it spanning most of the Aluminum plate. b) 50mm Cross configuration sample with low emissivity plates before completing rig preparation.

Accurately evaluating the total resistance of the sample is not a trivial task, especially due to the non-linear behaviour of radiative exchange, and the uncertainty introduced by all factors at play. However, if desired, a resistance network can be constructed accounting for the sum of all resistances and making certain assumptions such as estimating radiative resistance through a constant radiative transfer coefficient instead of calculating it by way of the view factor method. Figure 5.10 shows the resistance network for the model, special notice should be made of the fact that this 1D model needs to scale the heat sink resistance of the central sensor to account for the added resistance introduced by lateral resistance from the center of

the cold plate to the heat sink, which doesn't share the same position along the "x" axis. Even though this resistance network can be used to build a simple 1D finite difference model, a better approach was to model a more precise 3D simulation in OpenFoam which should result in similar heat flux measurements. If the behavior of the simulated model is accurate, the total thermal resistance of the VIP can be calculated and consequently its effective thermal conductivity.

The testing technique was calibrated against glass samples of known properties with thickness of 3 and $8mm$. Initially, measurements were conducted for the test rig without any sample but including the thermal interface material (Dow Corning high vacuum grease), as shown in Figure 5.11. These measurements suggest that the layer of grease used for thermal interface has a thermal conductance between 100 and 150 $\frac{W}{m^2K}$. Additional measurements were conducted with Pilkington clear glass (soda lime) samples with 3 and 8 mm thickness, and with a thermal conductivity $\sim 1\frac{W}{mK}$ [172]. Factoring the thermal contact conductance of the grease interface, accurate readings of the thermal conductivity were obtained for both glass samples, Figures 5.12 and 5.13. In both figures, the delay experienced by the heat flux sensors results in near 0 calculated κ values immediately after the temperature increases as the ratio of ΔT to Q'' tends to infinity for a few seconds.

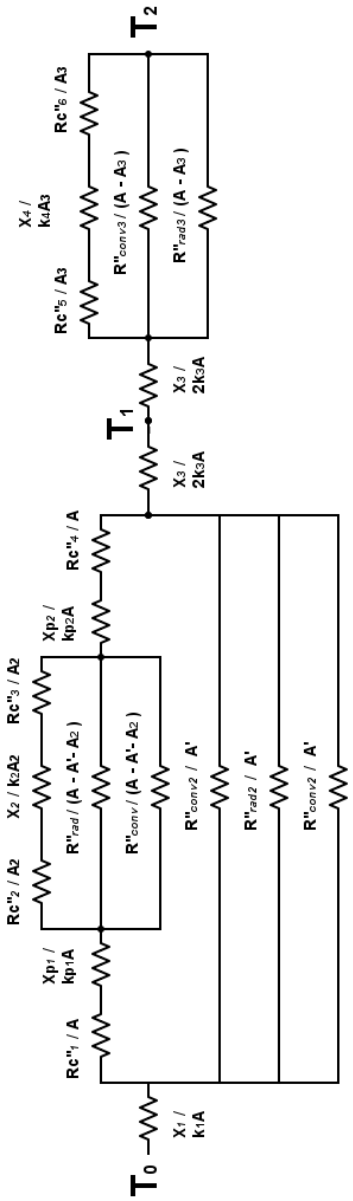

Figure 5.10: Thermal Resistance network of the corner sensor. T_0 is the temperature measured in the top plate, T_1 is the temperature of the bottom plate and T_2 is the temperature from the chamber. R_c'' stands for the contact resistance, k stands for the thermal conductivity, A stands for area, A' stands for the exposed area of the sensor(0 for the actual sensing area, but greater than 0 for the guard), A_2 and A_3 stand for the area of the spacer elements and heat sinks respectively.

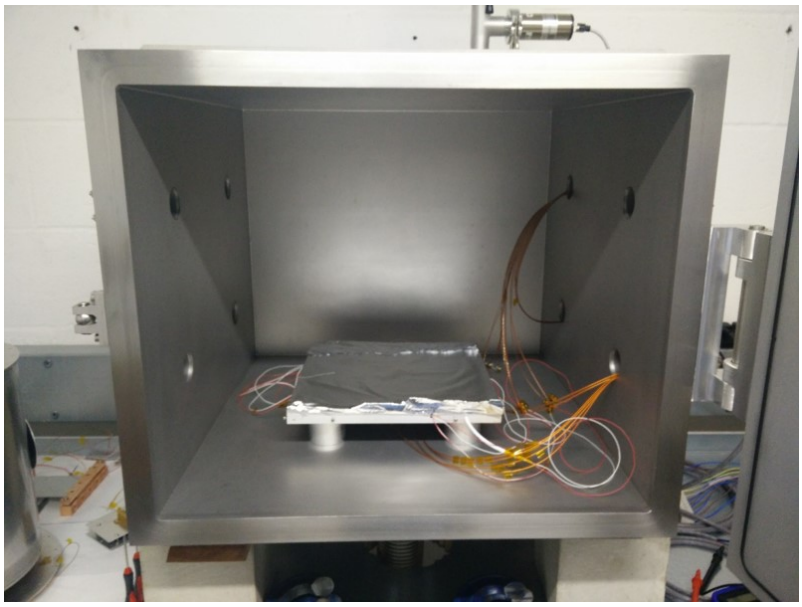

Figure 5.11: Testing Rig Calibration. Heat flux is measured through the rig including a layer of Dow Corning high vacuum grease between aluminium plates. The kapton heater is covered with aluminium foil to reduce radiative heat losses to the chamber.

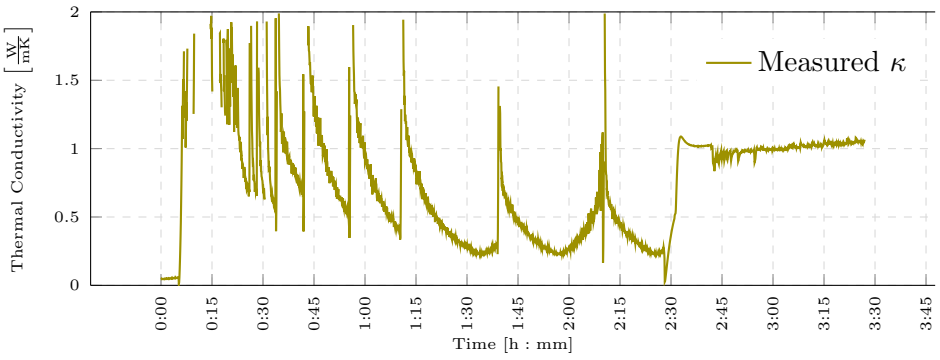

Figure 5.12: Thermal conductivity measurement for 3mm soda lime glass sample calculated from the ratio between measured heat flux and ΔT. Erratic data observed before the plot stabilizes is due to fluctuations during the evacuation process and ΔT values that approach 0 before rapidly heating the sample. Temperature of the hot plate was maintained at 25 °C before being increased rapidly to 40 °C before the 2:30 hour mark.

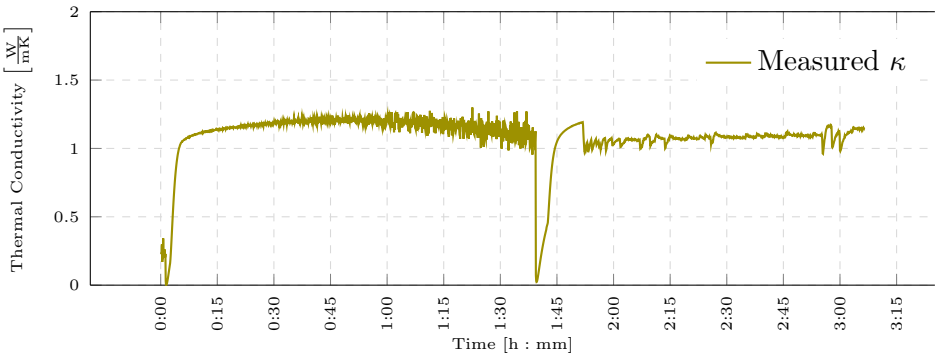

Figure 5.13: Thermal conductivity measurement for 8mm soda lime glass sample calculated from the ratio between measured heat flux and ΔT. This sample was slightly heated (from initial 25 °C to 30 °C) to avoid near 0 ΔT values. Before the 1:45 hour mark the hot plate temperature was rapidly increased to 40 °C.

5.3 Results

Before commenting on the performance between samples it is important to note behavior observed in all tests performed. Figure 5.14 shows the measured heat flux and pressure for the 25mm low emissivity Box sample. A significant pressure drop occurs after approximately 2.5 hours after initiating chamber evacuation, when the chamber pressure reaches 4 mbar the turbo molecular pump begins ramping up and within minutes reduces the pressure by several orders of magnitude. It is also important to note that the pressure then seems to stabilize at around 1×10^{-4} mbar, this is attributed to a large chamber volume and trace out-gassing from the sample. Nonetheless, as seen in previous sections this level of high vacuum is theoretically sufficient to eliminate convective heat transfer and limit gas conduction to have a reduced impact which can be confirmed by the measured heat flux as it quickly tends to 0, especially at the center of the sample where there's no solid conduction.

After the system has remained at a constant 25 °C temperature during an hour the heating set point was changed to 40 °C and the increase in heat flux is noticed, especially in the sensors directly in contact with the PTFE spacer elements. It takes approximately 10 minutes for the top plate to become saturated with energy and stabilize in temperature, shortly after the rate of change in heat flux and temperature of the cold plate become inversely proportional. When we plot the thermal resistance as the ratio between measured heat flux and ΔT, we can observe that thermal resistance becomes constant, Figure 5.15. Prior fluctuations are the result from the irregular ratio between measured heat flux and ΔT, as both of these quantities approach 0. The spike in thermal resistance observed before the curve flattens is due to the delay of the heat flux sensors, as these are much slower than the PT-100 temperature sensors, the ΔT value increases before significant changes in heat flux are registered.

In actuality the bottom plate does not fully stabilize in temperature, Figure 5.16, and will continue to increase as the chamber heats up along with the sample. Achieving a steady state without use of a chilling plate is possible but would require controlled ambient conditions and a very long time, rendering the entire battery of trials an unsustainable long experiment. It is important to reiterate that laboratory equipment limitations would not allow a chiller plate to be used, and thus a true steady state was not possible under current conditions. The state of the experiment then requires a transient analysis, consequently, simulations are conducted using the PIMPLE solver which includes temporal discretization.

The compiled results from the nominal measured heat fluxes on all permutations can be found in Table 5.3, and the respective thermal resistance has been calculated, as shown in Figure fig:barNominalEmpiric. The thermal resistance on all cases is

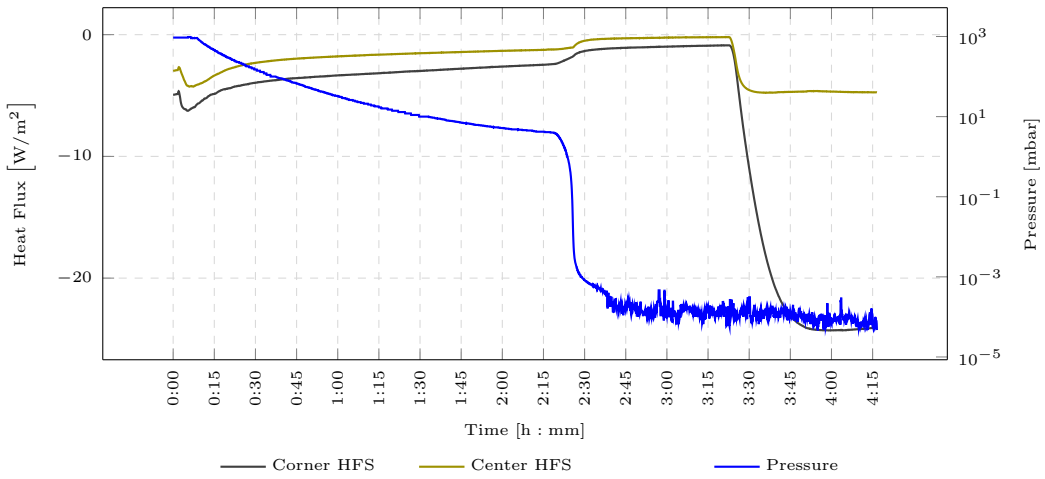

Figure 5.14: Heat Flux measurements for the 25mm low emissivity box sample. Center and Corner heat flux sensors, HFS, show negative values as heat is transferred from the top plate to the bottom plate. The corner sensor displays a noticeably greater flux resulting from heat conducted through the PTFE edges. At 2:20 hours it can be observed how the turbo molecular pump initiates and quickly reduces the pressure from a rough vacuum to a high vacuum.

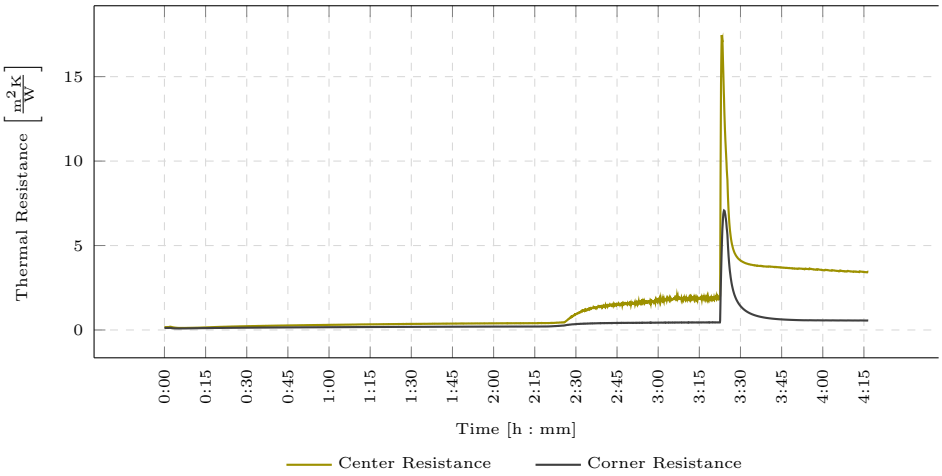

Figure 5.15: Thermal resistance progression for the 25mm low emissivity box sample calculated from the ratio between measured heat flux and ΔT. As the heat flux and temperature gradients become inversely proportional the resistance tends to a constant value.

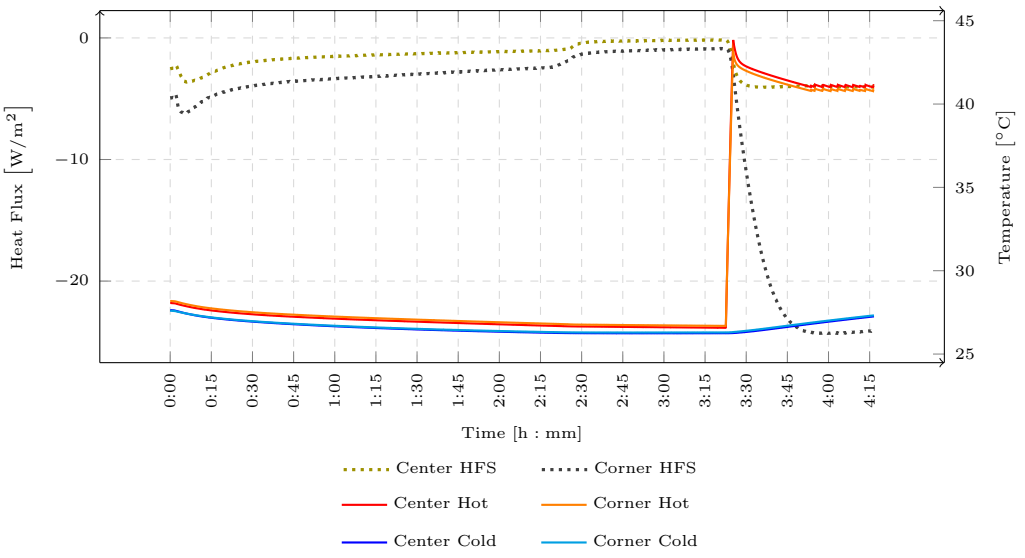

Figure 5.16: Temperature measurements for the 25mm low emissivity box sample. It can be observed that the "cold" temperatures continue to increase as the vacuum chamber, acting as a heat sink, begins to heat up.

subject to an error deviation between ±10% and ±14%; additional information including uncertainty ranges can be found in the extended version of Table 5.3 included in the Appendix D.

Analysis on the thermal resistance values agrees with existing theory regarding solid conduction and radiative exchange, and can be seen by reduced thermal resistance on samples with higher emissivity, increased amount of spacer elements and shorter spacer elements. Expected behaviour between the central and corner sensors, when either sensor is subject to direct heat conduction by solid elements, indicates a higher heat flux than its counterpart, as can be seen in the Box and Cross configurations. Sensors exposed only to radiation will have a different response depending on their position, as these will have a different view factor and consequently a different net radiative exchange. If the measured thermal resistance

Table 5.3: Nominal empiric measurements. Heat Flux Q'' and and Temperatures T values are averaged after the hot plate reached stability at ± 40 °C. Resistance values R are calculated as the ratio between ΔT and heat flux Q''.

		Center Sensor				**Corner Sensor**			
		Q" $\frac{W}{m^2}$	T_C °C	T_H °C	R $\frac{m^2K}{W}$	Q" $\frac{W}{m^2}$	T_C °C	T_H °C	R $\frac{m^2K}{W}$
25 mm	Low E Box	3.94	26.79	41.08	3.63	24.17	26.85	40.84	0.58
	HighE Box	43.51	31.07	40.74	0.22	56.11	30.95	40.50	0.17
	Low E Cross	36.07	28.20	41.02	0.36	6.65	28.23	43.46	2.29
	HighE Cross	48.58	29.80	40.58	0.22	41.44	29.69	40.36	0.26
	Low E Box-Cross	39.56	27.05	41.03	0.35	21.09	27.09	40.69	0.64
	HighE Box-Cross	50.82	29.93	40.70	0.21	43.25	29.77	40.50	0.25
50mm	Low E Box	4.26	20.61	40.85	4.75	25.51	20.62	40.38	0.77
	HighE Box	43.82	30.56	40.55	0.23	43.80	30.45	40.25	0.22
	Low E Cross	24.62	21.64	40.43	0.76	6.67	21.63	40.05	2.76
	HighE Cross	35.30	29.91	40.53	0.30	31.98	29.87	40.30	0.33
	Low E Box-Cross	27.22	28.10	41.05	0.48	13.96	28.14	40.68	0.90
	HighE Box-Cross	38.63	29.40	40.50	0.29	46.81	29.32	40.53	0.24

in low emissivity scenarios is compared between the corner sensor for the cross configuration and the central sensor for the box configuration, both of which are only affected by radiation, a higher thermal resistance can be observed for the center sensor in the box configuration, Figure 5.18. However, behaviour in high emissivity scenarios indicate the opposite, where the corner sensor for the cross configuration has a higher resistance, Figure 5.19. This inverted behaviour is explained by the region's view factor, as the central sensor is exposed to a virtually unencumbered radiative exchange with view factors approaching 1, it's affected to a greater degree by the surface's emissivity coefficient.

It is interesting to note that high emissivity samples show very little variation between the corner sensor and central sensor, indicating that radiative heat flux

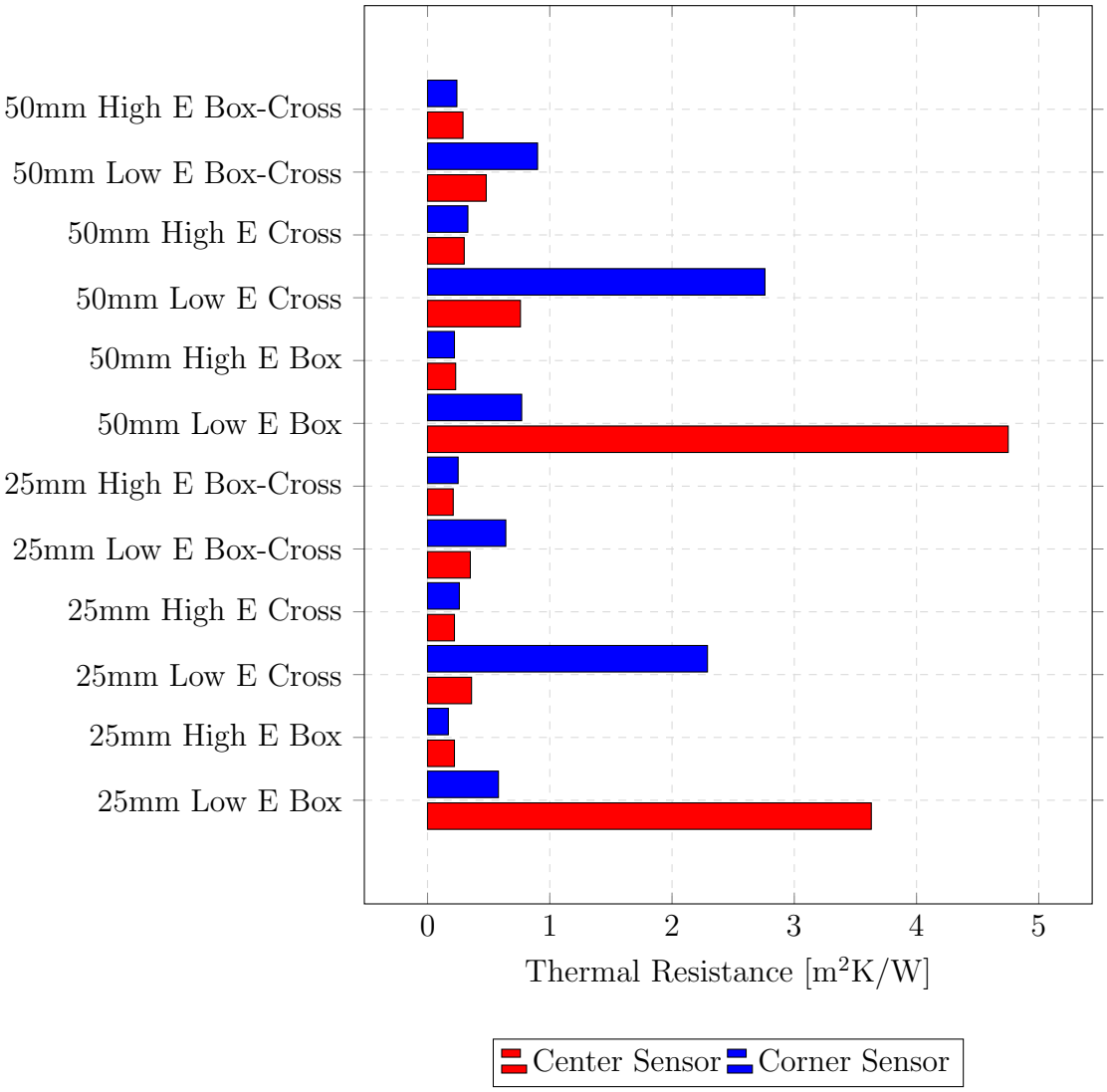

Figure 5.17: Nominal empiric measurements of thermal resistance.

is the dominant heat transfer mechanism, Figure 5.20. Solid conduction remains significant in the shorter 25mm thick samples even in high emissivity environments, resulting in a lower measured thermal resistance by sensors directly aligned with structural elements. This can be seen in the 25mm box and cross configurations, which show a 23% and 15% lower resistance between sensors, respectively. By comparison, the same configurations on the thicker 50mm samples show a 4% and

9% reduction in resistance between sensors. This goes to show that as the panel widens, conduction becomes less significant and radiation accounts for the majority of heat transfer.

Contribution of solid conduction can be observed clearly in low emissivity samples since it is the dominant heat transfer mechanism. Configurations with low internal emissivity show higher thermal resistance on the sensors not aligned with structural elements. Box and cross configurations show a resistance difference between sensors by a factor of 6. As the panel thickens, the effect of solid conduction is proportionally less drastic since the solid resistance increases linearly with length. This behavior can be observed by comparing the measured resistance between the 25mm and 50mm low emissivity cross samples, which show a resistance difference between sensors by a factor of 6.4 and 3.6, respectively.

A significant change in thermal resistance is found between low emissivity and high emissivity cases. Comparing readings from sensors without spacer elements in direct contact, the measured thermal resistance in low emissivity samples is over 8 times greater than its high emissivity counterpart for cross configurations. A similar difference is found in box configurations, where the observed thermal resistance for the low emissivity samples is over 16 times greater than the high emissivity configuration.

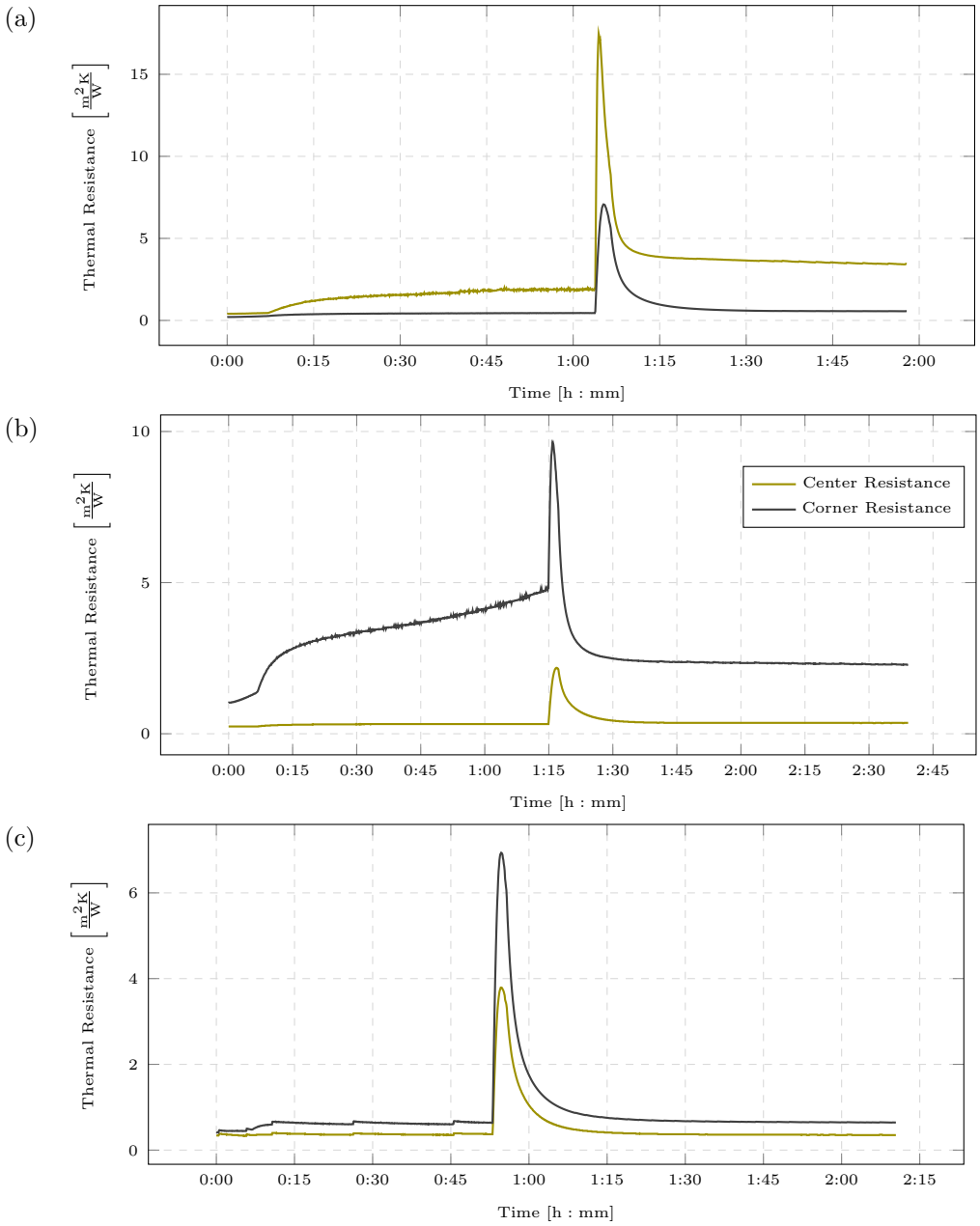

Figure 5.18: Thermal resistance over time for 25mm thickness samples with internal low emissivity surfaces: a) Box configuration b) Cross configuration c) Box-Cross configuration. Results plotted from the moment the turbo molecular pump is activated at 4mbar. The spike indicates when the resistance heater increased temperature to 40 °C. The measured thermal resistances of Box and Cross configurations have comparable values between opposite sensors, as these coincide with solid conduction elements. It should be noted that the corner resistance in Cross configuration is never as high as the center sensor in Box configuration.

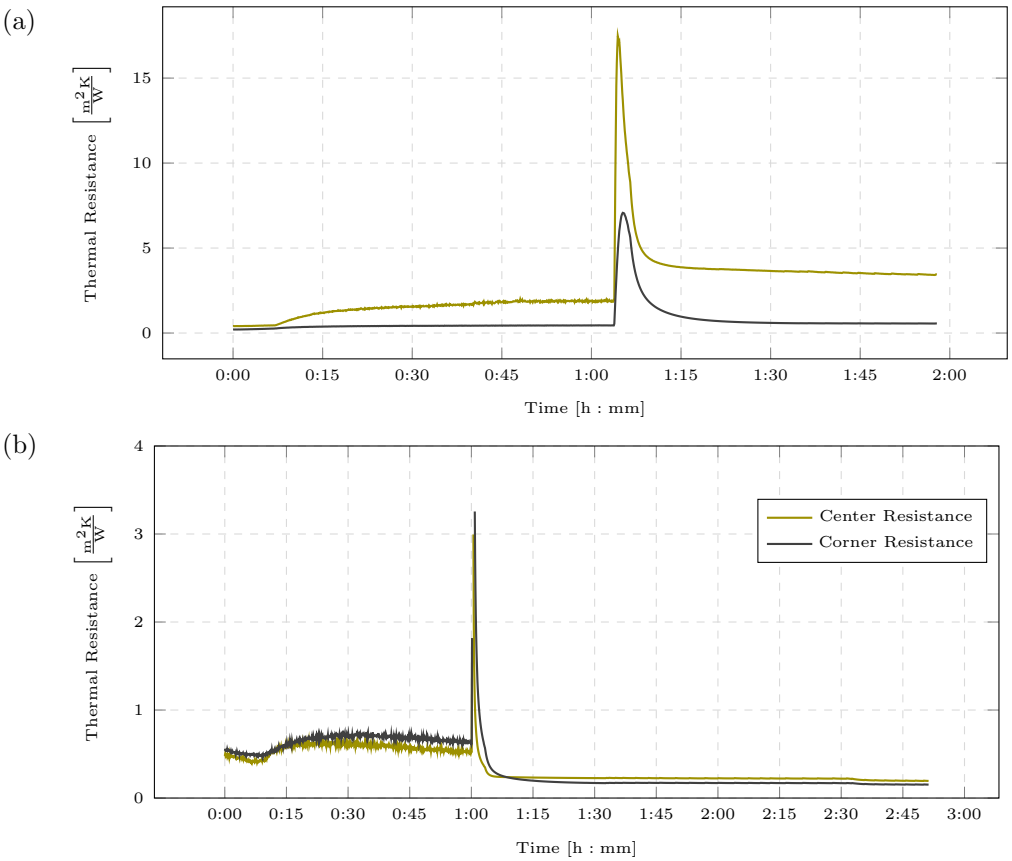

Figure 5.19: Thermal resistance over time for 25mm thickness Box configuration samples with different internal emissivity configurations: a) Low emissivity b) High emissivity. Results plotted from the moment the turbo molecular pump is activated at 4mbar. The spike indicates when the resistance heater increased temperature to 40 °C.

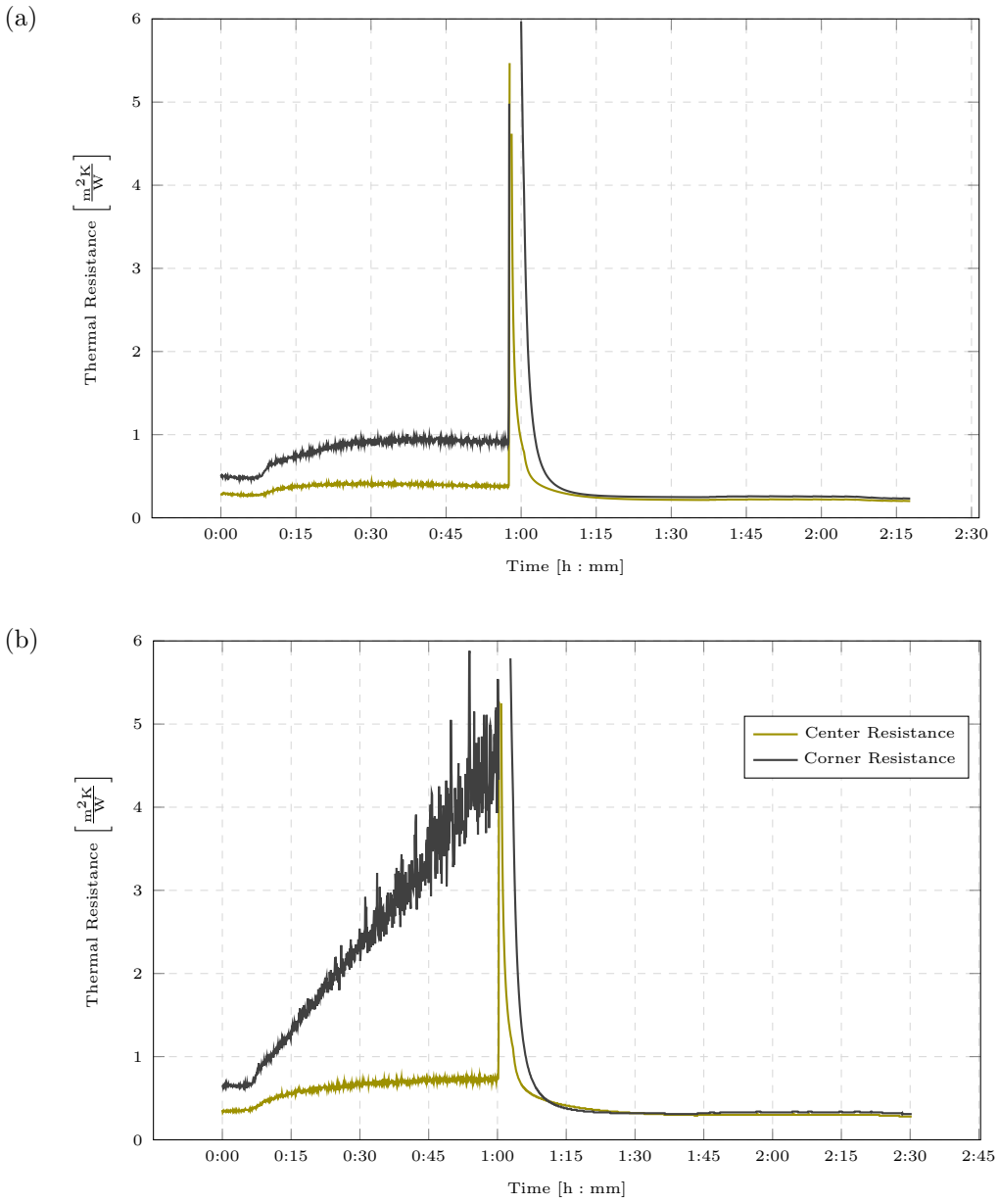

Figure 5.20: Thermal resistance over time for Cross configuration samples with high internal emissivity and variable thickness: a) 25mm b) 50mm. Results plotted from the moment the turbo molecular pump is activated at 4mbar. The spike indicates when the resistance heater increased temperature to 40 °C. Values above the y-axis domain aren't plotted. Both cases show almost identical thermal resistance between sensors, indicating radiation is capable of conducting heat at a similar rate as the solid elements.

5.4 Conclusions

The testing equipment employed in measuring thermal resistance by the rapid temperature increase method described by Turner and Collins [173] was calibrated against glass samples of know thermal conductivity and produced accurate measurements.

Thermal resistance measurements were conducted over a series of samples representing sections of a hollow-core VIP by a rapid temperature increase technique. The calculated thermal resistance shows erratic behavior during the evacuation process and when either ΔT or heat flux approaches zero. The rapid temperature increase technique proved accurate when measuring soda lime glass samples of 3 and 8mm thickness.

Samples with a structural array along the perimeter show good thermal resistance in the center of sample, 4.75 $\frac{m^2K}{W}$, under low emissivity conditions. High emissivity conditions on the same configuration for both $25mm$ and $50mm$ thick samples indicate nearly identical resistance $\sim 0.22\frac{m^2K}{W}$. It can be inferred from this data that solid conduction is not as noticeable as radiative transfer when there is no direct contact with solid elements, regardless of lateral heat flow through the face plates of the samples. Moreover, most samples with high emissivity resulted in thermal resistance $\approx 0.25\frac{m^2K}{W}$, confirming the importance of surface emissivity when seeking either a conducting or insulating state.

The lowest thermal resistance ($0.17\frac{m^2K}{W}$) was observed in the $25mm$ thick high emissivity Box samples when measured adjacent to the perimeter of the sample (close to the structural array). Comparing thermal resistance in sampling points without direct solid conduction between "Box" and "Cross" configurations indicate

that a larger magnitude heat flux is found in the periphery of the samples. Since the radiative view factor should be closest to unity at the center of the sample, this observation suggests that radiation from the testing rig is affecting the sample's periphery.

Objectives were met as samples were successfully tested for their thermal resistance. Although it becomes difficult to discern participation of individual heat transfer mechanism through these results, the observed thermal resistance can be compared against numerical solutions that can provide precise data into temperature and heat flux gradient as well as participation form individual heat transfer mechanisms.

Chapter 6

Simulated thermal resistance of hollow core VIP nodes.

6.1 Introduction

Analysis on a simplified vacuum box was important to ascertain correct behavior from the software when predicting gas conduction in rarefied fluids and the thermally coupled response of multiple regions, as well as exposing opportunities to manipulate heat transfer towards achieving a dynamic insulating solution. Having tested the method for simulating heat transfer in the conditions of the project, albeit simplified, we can proceed to build a more detailed model representative of a real prototype, and compare simulated and measured results. The new more detailed model, being a representation of a laboratory sample, is still constrained by limitations imposed by the available facilities and equipment.

The testing rig and sample configurations are modeled in OpenFoam and tested under the same conditions, the measured and simulated results are compared to

evaluate discrepancies, and finally the differences between each permutation show a correlation of heat flux to the configuration of the panel.

6.1.1 Aims and objectives

The studies conducted in this chapter aim to provide additional validation to the numerical method and to elucidate on the participation of individual heat transfer mechanisms in the tested samples. The objectives of this chapter are:

- Configure transient models to accurately simulate the behavior observed during empirical measurements.
- Study the effect of individual heat transfer mechanisms on overall heat exchange.
- Determine threats to the insulating properties of this technology.

6.2 Model and Method

Pairing simulated and measured results provides additional robustness to the data obtained, and in certain cases provided evidence of contaminated testing conditions. Simulations mimicking empirical tests need to be conducted using a transient solver since a steady state could not be achieved in the laboratory tests. The rarefied gas simulations do not need alteration in the dsmcFoam solver, since this is a transient solver by default. The dimensions and boundary conditions of the gas region are set to match those of the conducted experiments. Since the rarefied gas is subject to a relatively small temperature difference and due to the computational demand of DSMC simulations, which still require very small time steps, the initial uniform

temperature in the region is set as the average value between hot and cold temperatures in order to reduce the simulation time. The obtained thermal conductivity of the rarefied gas is introduced in the multi region simulations as has been previously described. The multi region solver employed is the native chtMultiRegionFoam solver, which solves the PIMPLE algorithm with a frozen flow, meaning that only the enthalpy equation is solved in the fluid region.

The full model starts from a steady state, whose temperature is set by values observed during tests after the evacuation of the chamber and prior to the activation of the resistance heater. At the beginning of the simulation, a fixed temperature boundary modeled after the observed stable hot temperature ($\pm 40°C$) is immediately introduced in the uppermost patch of the hot plate, at the position of the heater. The base of the heat sinks is also treated as a fixed temperature boundary, and set by the initial steady state temperature. Although the base of the heat sinks undergo minor temperature fluctuations, these are approximated as fixed temperature boundaries due to the large thermal mass of the vacuum chamber, which also acts as a massive heat sink.

Results from these simulations provide detailed information that is not available from empirical observations. Moreover, once the simulations are verified against measured results, these can be expanded to simulate a great deal of model permutations. While model parameters are set according to the thermo-physical properties of the manufactured samples, these parameters are subject to variations which affect the outcome of the simulation. Accordingly, a thorough analysis on the uncertainty of the model is conducted to provide error bars on the nominal simulation outcome.

6.2.1 Model configuration

Simulated models have been configured to accurately match the properties of the tested samples, as such, no two simulations have matching temperature boundaries. These models do not include the "vaulted" skin treatment discussed in Section 2.4.2 and in Chapter 7. A consequence of minor variations in temperature boundaries is that heat flux and its rate of change cannot be directly compared between sample configurations without misleading results. Therefore, the final comparative analysis is conducted on the differences between the predicted thermal resistance.

6.2.1.1 Mesh and regions

At an average temperature of 30 °C, as experienced by the heated sample, the approximate mean free path λ_{mfp} of air calculated as a hard sphere is 0.5m. The DSMC model measuring 250mm by 250mm with a maximum thickness of 50mm has maximum cell dimension of 12mm, which is much smaller than the mean free path, and is within recommended mesh properties described in section 3.2.1.1. The DSMC mesh has 4000 cells, all of which are regular hexahedra and the maximum aspect ratio is 2.5.

All chtMultiRegionFoam models have 131072 regular hexahedra cells with a maximum aspect ratio is 17.78. Table 6.1 describes the size of each region by sample configuration. The reader is reminded that mesh independence of the model was commented in Section 4.2.1.1.

Table 6.1: Mesh cell count by region. The cross configuration lacks a boundary between the vacuum contained within the sample and the surrounding vacuum, resulting in a merged region.

Configuration	**Regions**	**# Cells**
Box	Hot Plate	20480
	Hot Panel	5832
	Edges	4992
	Interior Vacuum	30000
	Sorrounding Vacuum	18880
	Cold Panel	5832
	Cold Plate	20480
	Heat Sinks (x4)	3174
	Underneath Vacuum	21402
Cross	Hot Plate	20480
	Hot Panel	5832
	Edges	2352
	Vacuum	51520
	Cold Panel	5832
	Cold Plate	20480
	Heat Sinks (x4)	3174
	Underneath Vacuum	21402
Box - Cross	Hot Plate	20480
	Hot Panel	5832
	Edges	7344
	Interior Vacuum (x4)	37648
	Sorrounding Vacuum	18880
	Cold Panel	5832
	Cold Plate	20480
	Heat Sinks (x4)	3174
	Underneath Vacuum	21402

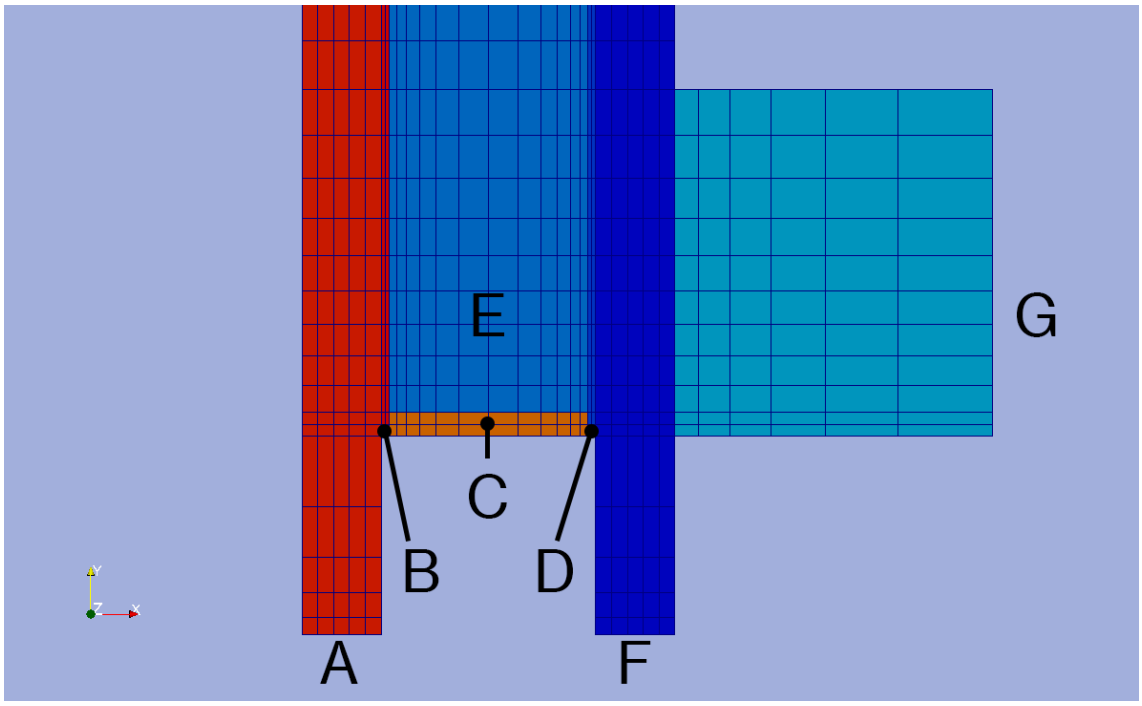

Figure 6.1: Orthogonal mesh of the model. Cross section parallel to heat flux. Mesh was kept relatively coarse since previous tests showed mesh independence. "A" is the hot temperature distribution plate; "B" is the hot face plate of the sample; "C" is the edge or structure of the sample; "D" is the cold face plate of the sample; "E" is the rarified gas; "F" is the cold temperature distribution plate; "G" is a heat sink (1 of 4).

6.2.1.2 Boundary conditions

Boundary types and conditions are of great significance since the state of the model depends directly on the constrains imposed at the limits of the geometry and the interfaces between different regions. The boundary conditions found at the limits of the model fall into two categories, fixed temperature with uniform distribution and adiabatic. The first type, fixed temperature, sets the hot and cold temperatures from average values measured during empiric tests. The hot temperature refers to the average stable temperature maintained by the Kapton heater and is found on

the top face of the Hot Plate region. The cold temperature, which is also the initial steady state temperature found throughout the model, is found at the base of the regions termed Heat Sinks. These temperatures have minor variations depending on the model configuration, but can be reviewed from Table 5.3. The remaining external faces, which do not directly encounter any adjacent region, are treated as adiabatic.

Interfaces between regions, also referred to as patches, have different behavior even though these are treated with the same type of boundary patch. These differences result from the source of thermal conductivity (a fluid or a solid), contact resistance and radiative exchange. Patches connecting solids include thermal contact resistance but neglect radiative exchange. Patches between solid and fluid regions don't have a contact resistance but include radiative exchange calculated from the view factor model. In this model there are no fluid to fluid interactions. Thermal conductivity is always treated as fixed, uniform and isotropic.

Table 6.2: Boundary patches between adjacent regions in OpenFoam model. This type of interface permits introducing a thermal baffle, which is used to model the thermal resistance found from imperfect contact between solids.

Interface	**Contact**	**Thermal Conductivity**	**Radiation**
turbulentTemperature-RadCoupledMixed	solid to solid*	fixed kappa from thermophysical properties dictionary	None
	solid to fluid	fixed kappa for solids and fluids^{+}	View Factor

* This type of boundary allows the variables: thicknessLayers and kappaLayers; these are used to establish the contact resistance.
\+ Kappa is defined from DSMC simulations of the rarefied region.

6.2.1.3 Material properties

The material assignment per region can be found in Table 6.4 and the corresponding thermo-physical properties of each material are shown in Table 6.3.

Table 6.3: Thermophysical properties of materials employed in OpenFoam simulations. Rarefied gas properties obtained from DSMC simulations.

Material	κ $\frac{W}{mK}$	**Emissivity**	**Cp** $\frac{J}{kgK}$	ρ $\frac{kg}{m^3}$	**Regions**	**Reference**
PTFE	0.25	0.92	970	2200	edge spacers	[174, 175]
Aluminium 6082-T6	180	0.145	900	2700	hot & cold plates, heat sinks	[176, 177, 178]
Steel 304 (Polished)	16.2	0.1	500	8000	hot & cold panels	[155, 178, 179, 180]
Steel 304 (Resin Coated)	16.2	0.885	500	8000	hot & cold panels	[168, 169]

Table 6.4: Material assignment per region for OpenFoam simulations using chtMultiRegionFoam solver.

Configuration	**Regions**	**Material**
Box	Hot Plate	Aluminium
	Hot Panel	Steel
	Edges	PTFE
	Interior Vacuum	Air (0.01Pa)
	Sorrounding Vacuum	Air (0.01Pa)
	Cold Panel	Steel
	Cold Plate	Aluminium
	Heat Sinks (x4)	Aluminium
	Underneath Vacuum	Air (0.01Pa)
Cross	Hot Plate	Aluminium
	Hot Panel	Steel
	Edges	PTFE
	Vacuum*	Air (0.01Pa)
	Cold Panel	Steel
	Cold Plate	Aluminium
	Heat Sinks (x4)	Aluminium
	Underneath Vacuum	Air (0.01Pa)
Box - Cross	Hot Plate	Aluminium
	Hot Panel	Steel
	Edges	PTFE
	Interior Vacuum (x4)	Air (0.01Pa)
	Sorrounding Vacuum	Air (0.01Pa)
	Cold Panel	Steel
	Cold Plate	Aluminium
	Heat Sinks (x4)	Aluminium
	Underneath Vacuum	Air (0.01Pa)

6.2.1.4 Thermal contact resistance

Thermal contact resistance found at the interface between materials is the result of imperfect contact between surfaces. Surfaces that appear smooth and planar to the naked eye will have macroscopic irregularities that limit the contact area and thus heat transfer. This resistance becomes a significant factor in our laboratory tests and simulations since the samples are subject to very low pressure loads, are partially manufactured from low emissivity materials and lack interstitial gas. Data has shown that at low pressure loads heat transfered at the contact interface occurs mainly through the gas [181], which in our case is a low conductivity rarefied gas. The overall conditions of the experiment result in contact resistance values several orders higher than in normal ambient conditions.

While there is extensive literature on thermal contact conductance mathematical models and measurements for high pressure loads in a vacuum regarding Al to Al and/or Al to Steel contacts [106, 182, 104, 107], fewer sources are found for measurements with low pressure loads within the desired temperature range[183, 184], or with the inclusion of interstitial materials [185].

Due to the lack of available data in the correct conditions, the Aluminium to Aluminium contacts have been calculated based on the correlations investigated by Thomas and Probert. This correlation, shown in equation 7.1 was plotted against 350 data points from recorded data in literature and showed a correlation coefficient over 0.9 [105].The calculated load is based on the measuring rig mass plus any additional torque added by screws. Heat sinks are held by a single M3 Aluminium screw with a measured torque of 2 N-m; the screw was meant to fix the position rather than apply a significant force.The surface roughness employed in the calcu-

lation could not be measured due to lack of equipment, but it is estimated based on measurements conducted on similar manufacturing procedures investigated in [186]. The resulting nominal contact conductance for Al-Al contact at the base of the rig is estimated at 11 $\frac{W}{m^2K}$ with an uncertainty of $\pm 68\%$.

$$ln\left(\frac{h_c A}{\sigma\kappa}\right) = (0.72 \pm 0.044) ln\left(\frac{W}{\sigma^2 M}\right) + 0.66 \pm 0.62 \tag{6.1}$$

Where:

- h_c is the thermal contact conductance $\left[\frac{W}{m^2K}\right]$
- A is the nominal contact area $[m^2]$
- κ is the thermal conductivity $\left[\frac{W}{mK}\right]$
- W is the compressive load $[Pa]$
- σ is the surface roughness [m]
- M is the surface hardness $[Pa]$

Given the limited amount of data points found for Al-Al with a contact interface [182], the data could not be extrapolated to the necessary applied pressure load. Consequently, the effect of the high vacuum grease at the contact interface was estimated by the reduced heat flux measured with the rig without a sample. The resulting flux was compared against the analytical solution neglecting contact conductance. The observed performance of the rig with a thin layer of Dow Corning high vacuum grease acting as the thermal interface suggests a thermal contact conductance between 100 and 150 $\frac{W}{m^2K}$. The small magnitude relative to measurements

found in literature is attributed to the low pressure load experienced. While measurements observed in the previous cited sources consider a pressure load over 70 $\frac{kN}{m^2}$, the calculated pressure load at the measured interface is of only 265 $\frac{N}{m^2}$. Taking the previous thermal contact conductance value of 100 $\frac{W}{m^2K}$ as the nominal value, the same uncertainty of ±68% is considered. For dissimilar elements contact, found between the different components of the sample, there is no available measured data in literature with the adequate conditions. However, measured samples of dissimilar metals in a vacuum at high pressure loads show similar contact conductance between Steel to Aluminum interfaces and Aluminium to Aluminium interfaces. The data does however show a direction dependency, greater agreement between Al-Al and SS-Al joints was found when steel was located at the origin of the heat flux [187]. The limited available information suggests using the measured Al-grease-Al contact conductance with a high uncertainty percentage. Therefore, dissimilar metal contact with thermal interface is proposed equal to Al-Al contact with thermal grease. Unfortunately, thermal contact conductance measurements between stainless steel and PTFE are not found in literature. Consequently, the contact conductance for metal to PTFE with thermal interface is estimated as the range between nominal values for Al-Al contacts with and without a thermal interface. The resulting nominal thermal contact conductance is 55 $\frac{W}{m^2K}$ with an uncertainty of ±79%. These values agree with correlations and measurements described in ECSS standards [188].

6.2.2 Uncertainty analysis

Uncertainty analysis was conducted on a steady state model with the exact same properties as the transient model, albeit, without temporal discretization. Uncer-

tainty regarding thermal contact conductance has been discussed in the previous subsection. Uncertainty in thermal conductivity is ±10% as suggested by ECSS guidelines for homogeneous materials [189]. Emissivity uncertainty was determined by the range in measured values published in [176, 177, 178, 155, 179, 180, 168, 169] for polished steel, Aluminium and resin surfaces; these are higher than the recommended ±0.03 in ECSS standards. Table 6.5 presents a summary of uncertainty deviations for different variables. Combined uncertainty was obtained by summation in quadrature method, these values can be found in Tables E.1, E.2 and in Appendix E.

Simulated temperature at the interface, where PT-100 sensors were placed, showed less than 0.1% variation, as such these fluctuations are neglected in subsequent analysis. Tables E.1 & E.2 summarizing heat flux fluctuation by combined uncertainty can be found in the Appendix E. A brief excerpt, showing exclusively 25mm Box configurations, is shown in Table 6.6. As expected, uncertainty in the dominant heat exchange mechanism will have the most noticeable contribution to deviation from nominal values. ; e.g. Surface emissivity fluctuation is most noticeable in sensors without direct solid conduction. An interesting observation lies in the asymmetric behaviour of contact conductance at interfaces in direct contact with the sample. Reducing and increasing thermal contact conductance does not result in comparable effects on heat flux. Reducing contact conductance compounds the insulating effect of the sample, while the effect of increasing contact conductance appears to be limited by the insulating properties of the sample.

Table 6.5: Summary of uncertainty per variable included in simulations. Uncertainty analysis conducted in OpenFoam with chtMultiRegionSimpleFoam solver.

Contact Conductance			**Thermal Conductivity**			**Emissivity**		
Al-grease-(Al/SS)	Al-(Al/SS)	PTFE-grease-*	Al	Steel	PTFE	Al	Steel	Resin
±%	±%	±%	±%	±%	±%	±%	±%	±%
68	68	79	10	10	10	38	25	10

Table 6.6: Uncertainty analysis results for 25mm thickness Box configurations. Simulations conducted with OpenFoam's chtMultiRegionSimple solver. Abbreviations : GI - grease interface, MI - metallic interface, SPI - PTFE interface, AC- Aluminium conductivity, SC- Steel conductivity, PC- PTFE conductivity, AE- Aluminium emissivity, SE- Steel emissivity, RE- resin emissivity

Case	**Variable**	**Center Q" [W/m2]**			**Corner Q" [W/m2]**		
		U-	Nominal	U+	U-	Nominal	U+
Box Low E	GI	0.14	4.67	0.01	-11.41	36.30	5.60
	MI	0.04		-0.05	0.08		-0.09
	SPI	0.18		-0.07	-16.86		6.32
	AC	-0.01		0.01	-0.04		0.03
	SC	0.01		0.00	0.94		-0.86
	PC	0.02		-0.02	-2.24		2.12
	AE	0.07		-0.07	0.09		-0.10
	SE	-1.29		1.32	-0.99		0.99
	RE	0.00		0.00	0.00		0.00
	SUM %	**28.11%**		**28.37%**	**56.55%**		**24.26%**
Box High E	GI	-11.22	67.74	2.69	-15.85	74.51	5.79
	MI	0.01		-0.01	0.00		0.00
	SPI	0.11		-0.06	-18.41		7.56
	AC	-0.22		0.18	-0.10		0.08
	SC	0.07		-0.07	0.43		-0.39
	PC	0.02		-0.02	-1.81		1.72
	AE	0.07		-0.07	0.17		-0.18
	SE	0.00		0.00	0.00		0.00
	RE	-9.87		10.92	-4.20		4.46
	SUM %	**22.06%**		**16.61%**	**33.18%**		**14.31%**

6.2.3 OpenFOAM PIMPLE solver

The PIMPLE algorithm, used for transient problems, is a combination of the SIMPLE and PISO algorithms. PISO stands for Pressure Implicit of Split Operations and its stability is limited by Courant number, which often dictates small time steps. The combination of both algorithms allows transient problems to be solved with larger time steps. If the variable "nOuterCorr" is set to 0 the PIMPLE algorithm is reduced to the PISO algorithm. For this project the previous variable is set to its default value, 1. The algorithm follows the progression described in Figure 3.3.

Figure 6.2 has been removed
from this version of the thesis
due to copyright restrictions

Figure 6.2: PIMPLE algorithm flowchart adapted from [130]

6.3 Results

Nominal predicted thermal resistance values are included in Table 6.7, additional details including uncertainty range are included in Appendix F. Simulated thermal performance trends follow analytic solutions for areas subject to direct solid conduction, when in direct contact with PTFE elements, suggesting increased thermal performance with increasing panel thickness; indication of these effects are found when comparing the corner area for box configurations, the center area for Cross configurations and both areas for the combined Box-Cross configurations. It is interesting to note that proportional change in resistance, when solid conduction is significant, between center and corner areas is not comparable. The primary difference between these two areas, is the local view factor and consequently the net radiative exchange; solid interface area is also different by over 10%. I.e. radiation is not uniform through out the region and is substantially different between Box, Cross and Box-Cross configurations.

Nominal resistance values between areas subject to solid conduction between Box and Box-Cross configurations, corner areas, agree within 8% for high emissivity models as shown in Table 6.7. The same can be said for comparison between center areas for Cross and Box-Cross configurations. Within Box-Cross models, a noticeable difference occurs between the 25mm and 50mm thick models. In the former, the difference in thermal resistance in areas subject to solid conduction is greater at the periphery of the model by comparison to Box and Cross configurations. In the latter, the trend is reversed and the difference in thermal resistance in areas subject to solid conduction is greater at the center of the model. This effect is thought to be caused by increased radiative exchange by proportion to solid conduction in thicker

models, lateral heat flux through PTFE elements, and reduced solid conduction from increased material resistance. The compound effect of all these phenomena narrows the difference in thermal resistance between BOX-CROSS and BOX models at the edge of the panel to a point where the difference in thermal resistance seen in the center of the model is greater.

The participation of individual heat transfer mechanisms can be found in in Table 6.8. It is important to note the extremely low effect of gas conduction, always below 1% in overall heat transfered, except in low emissivity models, where it accounts for 3%. Moreover, as the panel becomes thicker and pressure is kept constant at 0.01Pa, gas conduction increases as the rarefied gas approaches the transitional flow regime. As mentioned previously, solid conduction becomes less important with increasing cross-sectional length. Radiation contribution increases by approximately 1% with increasing thickness.

Figure 6.4 shows how heat flux is concentrated around solid elements in low emissivity models. Although contact area is small by comparison to the overall model area, solid conduction still accounts for over 40% of transfered energy. By comparison, Figure 6.4 demonstrates how radiation can take a dominant role and provide near uniform heat transfer over the region with high emissivity surfaces.

While models show a stabilizing thermal resistance after the initial effects of thermal mass, Figure 6.6, the highest heat flux magnitude occurs approximately 30 minutes after heat is introduced into the system, Figure 6.5, at which point thermal energy storage has been saturated and the temperature differential is at its maximum value.

Table 6.7: Nominal results from transient heat transfer simulations using OpenFoam's solver chtMultiRegionFoam. Average values are presented after resistance becomes steady. Resistance values R are calculated as the ratio between ΔT and heat flux Q'' and integrated over a mesh area of the approximate size and position as the sensors employed in empirical measurements.

		Center Area				**Corner Area**			
		Q" $\frac{W}{m^2}$	T_C °C	T_H °C	R $\frac{m^2K}{W}$	Q" $\frac{W}{m^2}$	T_C °C	T_H °C	R $\frac{m^2K}{W}$
25 mm	Low E Box	3.26	27.14	41.00	4.26	25.59	27.13	41.00	0.54
	HighE Box	45.48	29.96	41.00	0.24	45.69	29.99	41.00	0.24
	Low E Cross	29.26	27.91	41.00	0.45	4.78	27.90	41.00	2.74
	HighE Cross	40.13	30.21	41.00	0.27	39.81	30.13	41.00	0.27
	Low E Box-Cross	22.87	27.07	41.00	0.61	17.34	27.04	41.00	0.80
	HighE Box-Cross	39.27	30.39	41.00	0.27	40.39	30.33	41.00	0.26
50mm	Low E Box	4.59	21.53	41.00	4.24	23.86	21.23	41.00	0.83
	HighE Box	46.82	29.41	41.00	0.25	38.29	29.31	41.00	0.31
	Low E Cross	36.52	21.20	41.00	0.54	6.87	21.18	41.00	2.89
	HighE Cross	33.98	29.98	41.00	0.32	36.73	30.11	41.00	0.30
	Low E Box-Cross	18.40	27.73	41.00	0.72	13.72	27.78	41.00	0.96
	HighE Box-Cross	34.95	29.48	41.00	0.33	37.13	29.37	41.00	0.31

Table 6.8: Percentual participation of individual heat transfer mechanisms in transient simulations.

		Gas %	**Rad** %	**Solid** %
25 mm	Low E Box	2.41	46.13	51.46
	HighE Box	0.33	91.69	7.98
	Low E Cross	2.97	56.33	40.70
	HighE Cross	0.34	95.02	4.63
	Low E Box-Cross	1.83	31.01	67.16
	HighE Box-Cross	0.36	86.94	12.70
50mm	Low E Box	3.99	47.69	48.32
	HighE Box	0.36	92.68	6.96
	Low E Cross	3.58	56.67	39.75
	HighE Cross	0.41	95.14	4.44
	Low E Box-Cross	2.46	32.21	65.33
	HighE Box-Cross	0.46	87.92	11.62

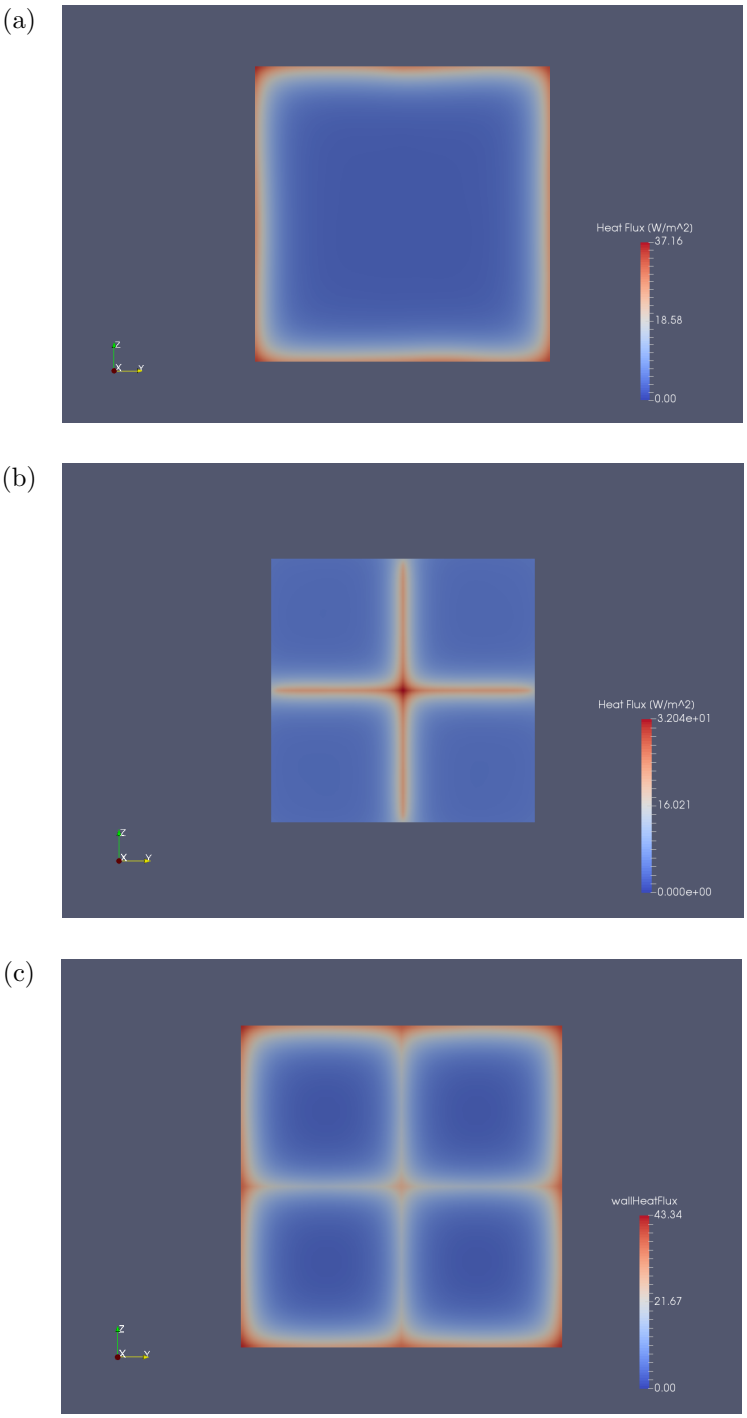

Figure 6.3: Heat flux map at the interface between the Aluminium plate and sample at time 3600s for 25mm thick low emissivity configurations: a) Box b) Cross c) Box-Cross. Simulations conducted in OpenFoam chtMultiRegionFoam.

(a)

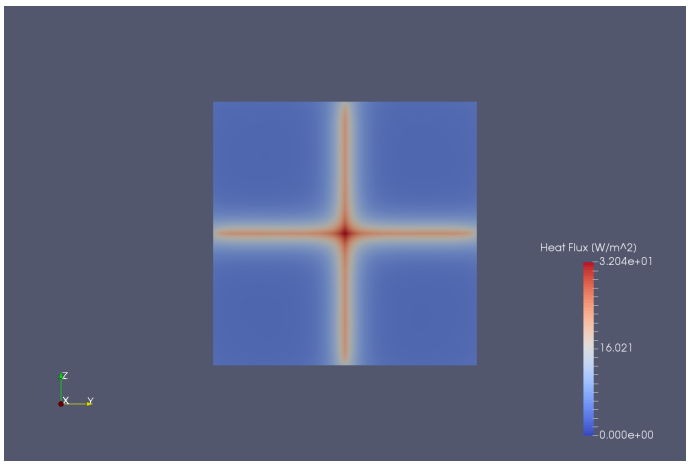

(b)

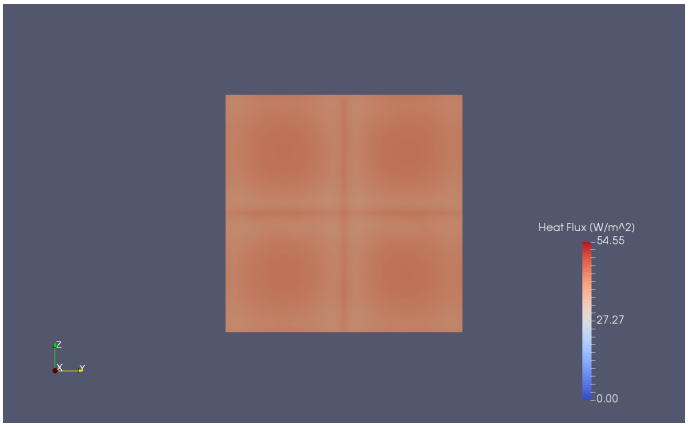

Figure 6.4: Heat flux map at time 3600s for 25mm thick Cross configurations: a) Low emissivity b) High emissivity. Simulations conducted in OpenFoam chtMultiRegionFoam.

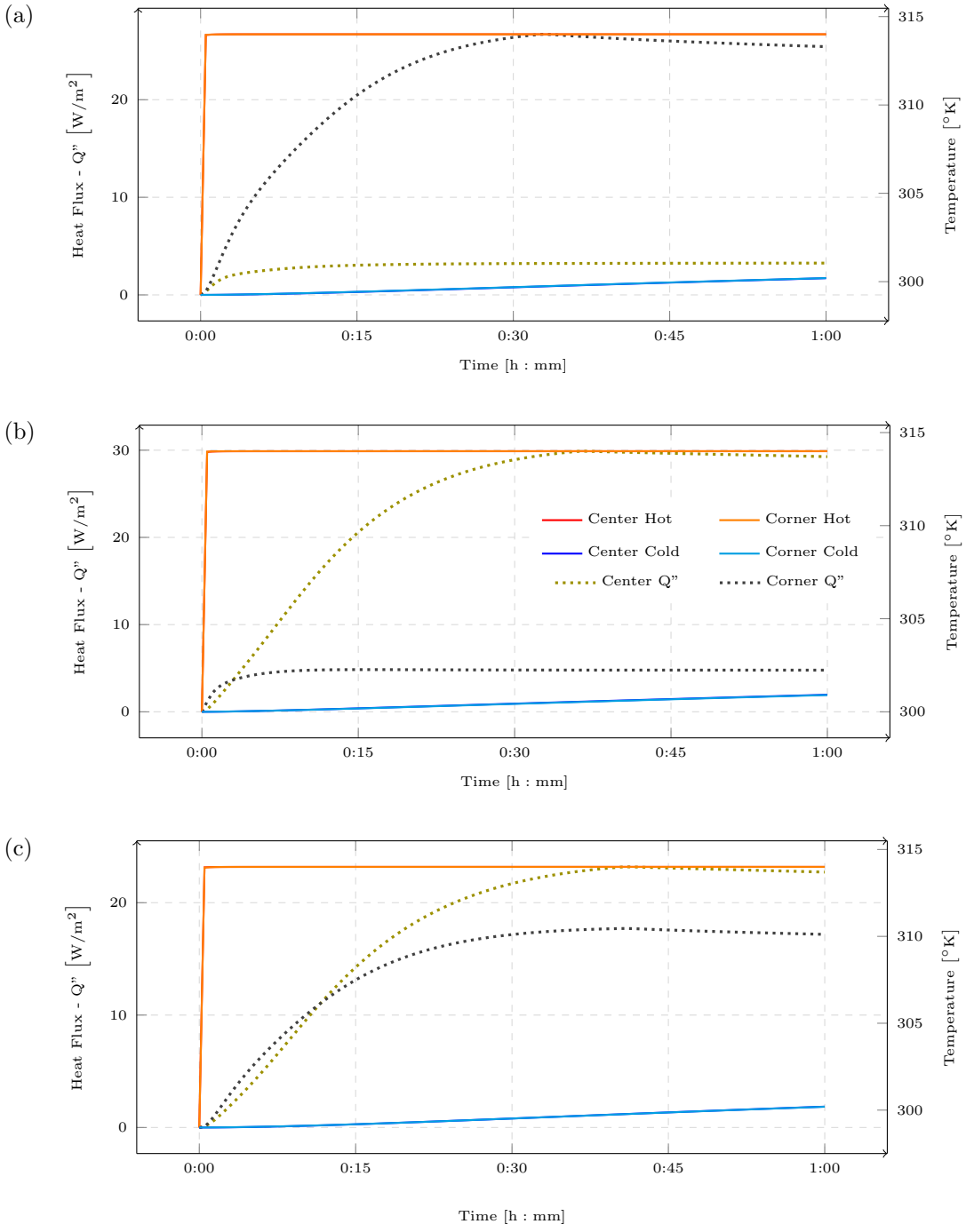

Figure 6.5: Transient heat transfer simulations for 25mm thick low emissivity configurations: a) Box b) Cross c) Box-Cross. Heat flux and temperature plotted against time for areas approximating positions and size of sensors employed in empirical measurements.

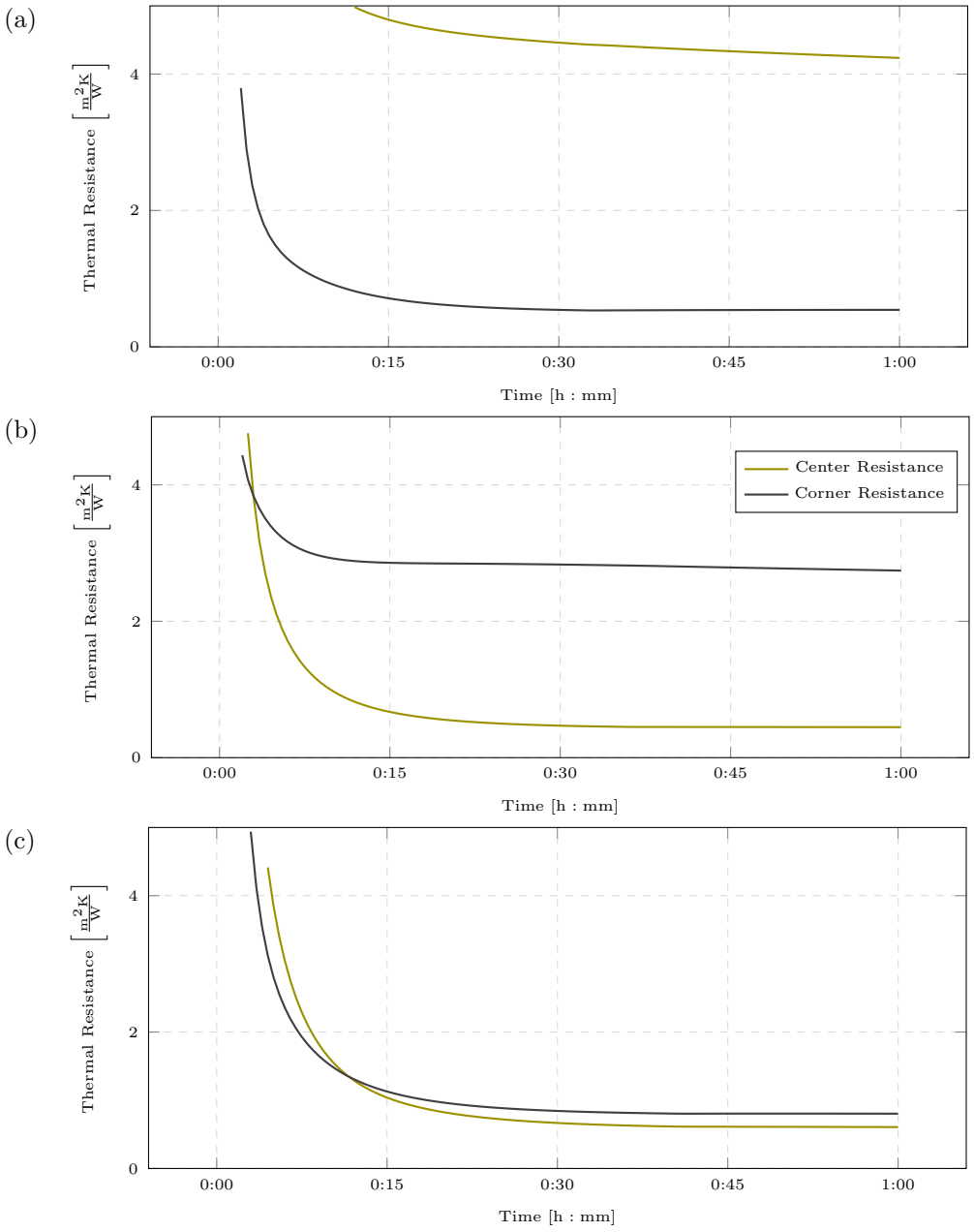

Figure 6.6: Simulated thermal resistance over time for 25mm thick, low emissivity configurations : a) Box b) Cross c) Box-Cross.

6.4 Comparison between simulated and measured results

Thermal resistance between measured samples and simulated models can be found in Table 6.9. All cases agree within their error ranges providing confidence in the modeling method but indicating the importance of narrowing such uncertainties. High emissivity cases agree within 5% where the measuring area is not in contact with PTFE elements. There is agreement between 5 and 20% in simulated and measured results where solid conduction is dominant, such as the corner sensor for Box configurations or the center sensor for Cross configurations. The biggest difference between nominal results is observed in low emissivity cases where radiation is the primary transfer mechanism, such as the center sensor for Box configurations and the corner sensor for Cross configurations. In these cases nominal results are offset by up to 50%, although within tolerated error margins are set by the uncertainty study. Considering the overwhelming importance of radiation in these cases, and hence surface emissivity, even minor imperfections in the simulated values or the measured samples, where emissivity shifts from 0.07 to 0.1, can result in sensible discrepancies. It is important to remember these cases are subject to the largest uncertainty by the same reasons.

The thermal resistance progression, after effects of thermal energy storage, are almost identical between simulated and measured cases, Figure 6.7 provides the example for the 25mm thick low emissivity Box. The difference in the shape of the curve is explained by the overshoot experienced by the thermal controller in the measured results, where the top Aluminium plate initially reaches up to 43 °C,

before settling at around 40.8 °C. These deviations from the thermal controller set point of 40 °C are thought to be due to radiative losses from the Kapton heater and changes in thermal mass in the system.

Figures 6.8, 6.9, 6.10 plot the position of simulated and measured thermal resistance with regards to each other.

Table 6.9: Thermal resistance values with uncertainty range for measured and simulated cases.

		Center Sensor						**Corner Sensor**					
		Measured			Simulated			Measured			Simulated		
		R_{U-} $\frac{m^2K}{W}$	R $\frac{m^2K}{W}$	R_{U+} $\frac{m^2K}{W}$	R_{U-} $\frac{m^2K}{W}$	R $\frac{m^2K}{W}$	R_{U+} $\frac{m^2K}{W}$	R_{U-} $\frac{m^2K}{W}$	R $\frac{m^2K}{W}$	R_{U+} $\frac{m^2K}{W}$	R_{U-} $\frac{m^2K}{W}$	R $\frac{m^2K}{W}$	R_{U+} $\frac{m^2K}{W}$ W
25 mm	Low E Box	3.18	3.63	4.10	3.32	4.26	5.92	0.51	0.58	0.65	0.44	0.54	1.25
	HighE Box	0.19	0.22	0.25	0.21	0.24	0.31	0.15	0.17	0.19	0.21	0.24	0.35
	Low E Cross	0.31	0.36	0.40	0.34	0.45	1.22	2.01	2.29	2.59	2.15	2.74	3.78
	HighE Cross	0.19	0.22	0.25	0.24	0.27	0.38	0.22	0.26	0.29	0.24	0.27	0.33
	Low E Box-Cross	0.31	0.35	0.40	0.47	0.61	1.63	0.56	0.64	0.73	0.64	0.80	2.05
	HighE Box-Cross	0.18	0.21	0.24	0.24	0.27	0.38	0.22	0.25	0.28	0.23	0.26	0.39
50mm	Low E Box	4.21	4.75	5.34	3.31	4.24	5.87	0.69	0.77	0.87	0.64	0.83	2.07
	HighE Box	0.20	0.23	0.26	0.21	0.25	0.32	0.19	0.22	0.25	0.26	0.31	0.44
	Low E Cross	0.68	0.76	0.86	0.41	0.54	1.42	2.44	2.76	3.11	2.28	2.89	3.92
	HighE Cross	0.26	0.30	0.34	0.28	0.32	0.44	0.28	0.33	0.37	0.26	0.30	0.36
	Low E Box-Cross	0.42	0.48	0.54	0.54	0.72	1.89	0.78	0.90	1.02	0.75	0.96	2.40
	HighE Box-Cross	0.25	0.29	0.33	0.29	0.33	0.45	0.21	0.24	0.27	0.27	0.31	0.45

"R" indicates the nominal thermal resistance;"R_{U-}" and"R_{U+}" indicate the thermal resistance extended by the system's uncertainty.

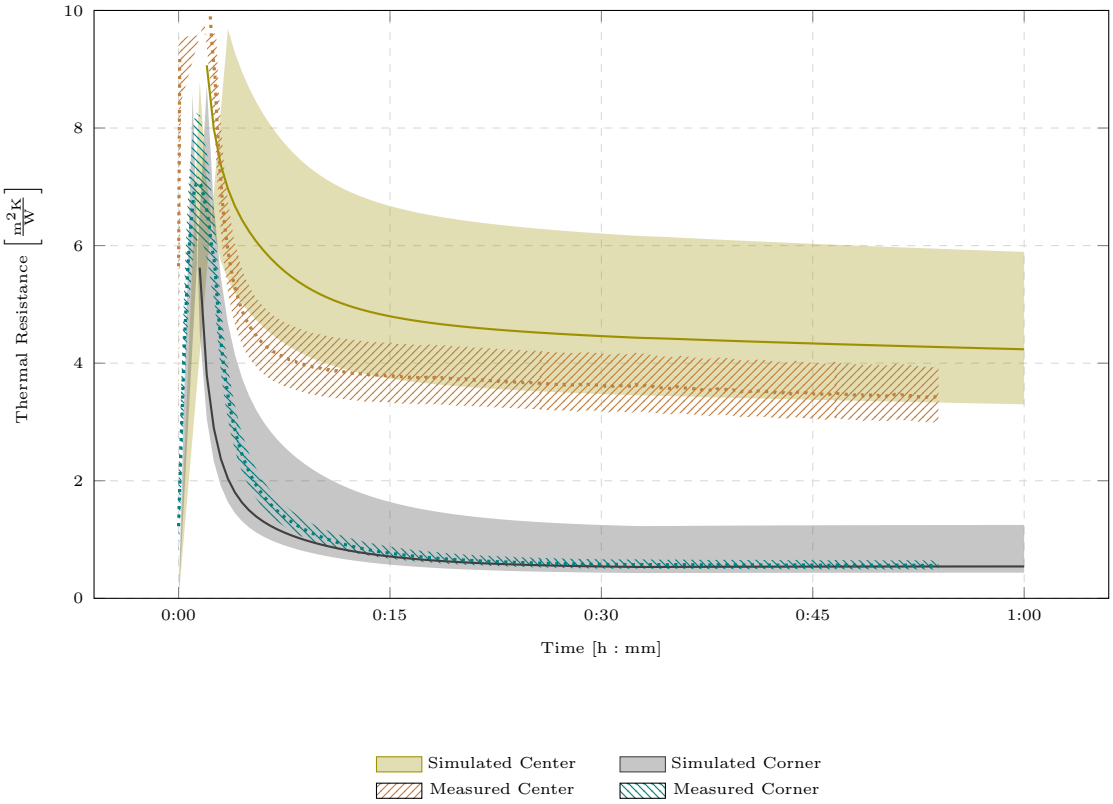

Figure 6.7: Thermal resistance comparison between empirical and simulated results for the 25mm Box low emissivity configuration. After heat is introduced, the thermal resistance spikes due to the significant influence of thermal mass, however, after the first few minutes the thermal resistance becomes constant. Predicted and measured resistances are plotted with error bands, overlap within the bands demonstrate that the model is accurate within expected uncertainty.

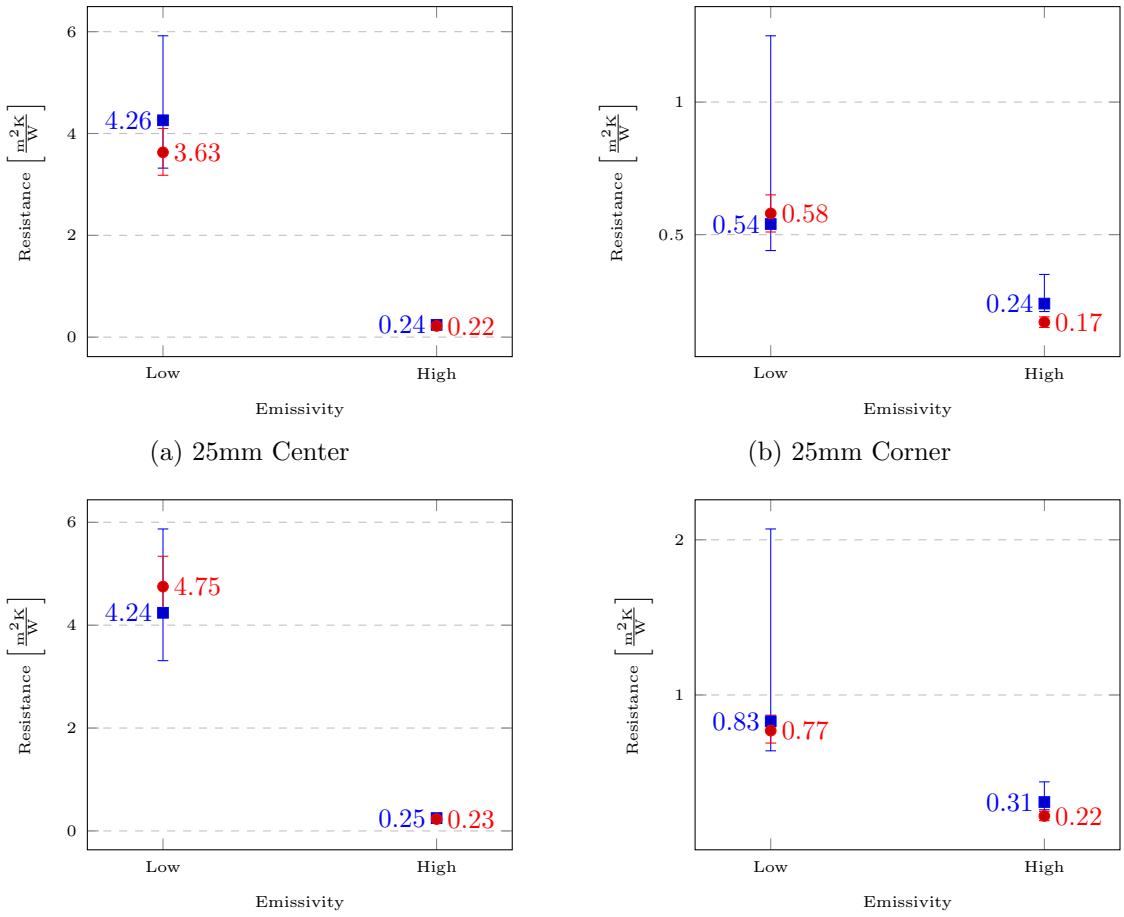

(a) 25mm Center

(b) 25mm Corner

(c) 50mm Center

(d) 50mm Corner

Figure 6.8: Thermal resistance comparison between simulated and measured results with error bars for BOX configurations. Simulated values are plotted with a blue square, measured results are plotted with a red circle. We can see significant agreement between measured and simulated values, although low emissivity scenarios are most prone to discrepancies, especially when radiation is the primary transfer mechanism.

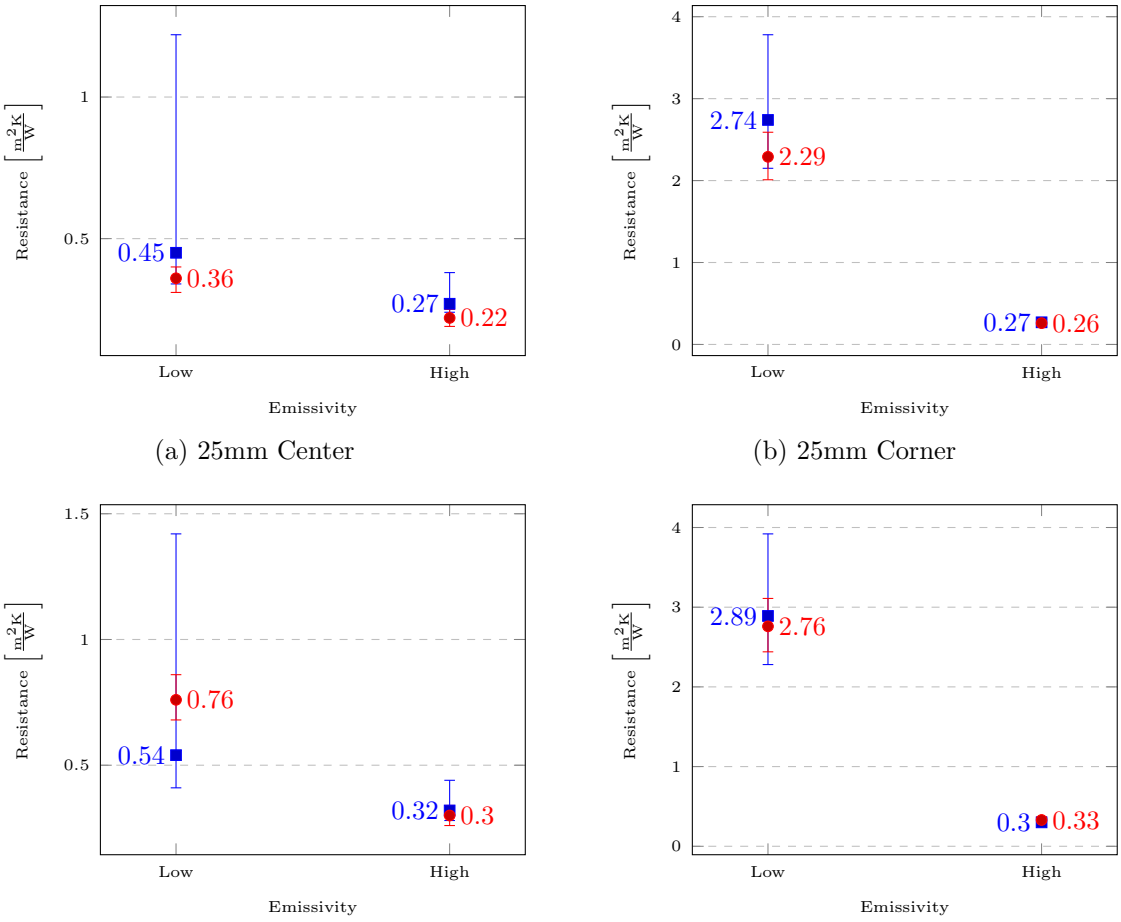

(a) 25mm Center

(b) 25mm Corner

(c) 50mm Center

(d) 50mm Corner

Figure 6.9: Thermal resistance comparison between simulated and measured results with error bars for CROSS configurations. Simulated values are plotted with a blue square, measured results are plotted with a red circle. We can see significant agreement between measured and simulated values. The corner sensor for low emissivity scenario shows predicted values greatly exceed measured values, again when limited radiation is the primary transfer mechanism.

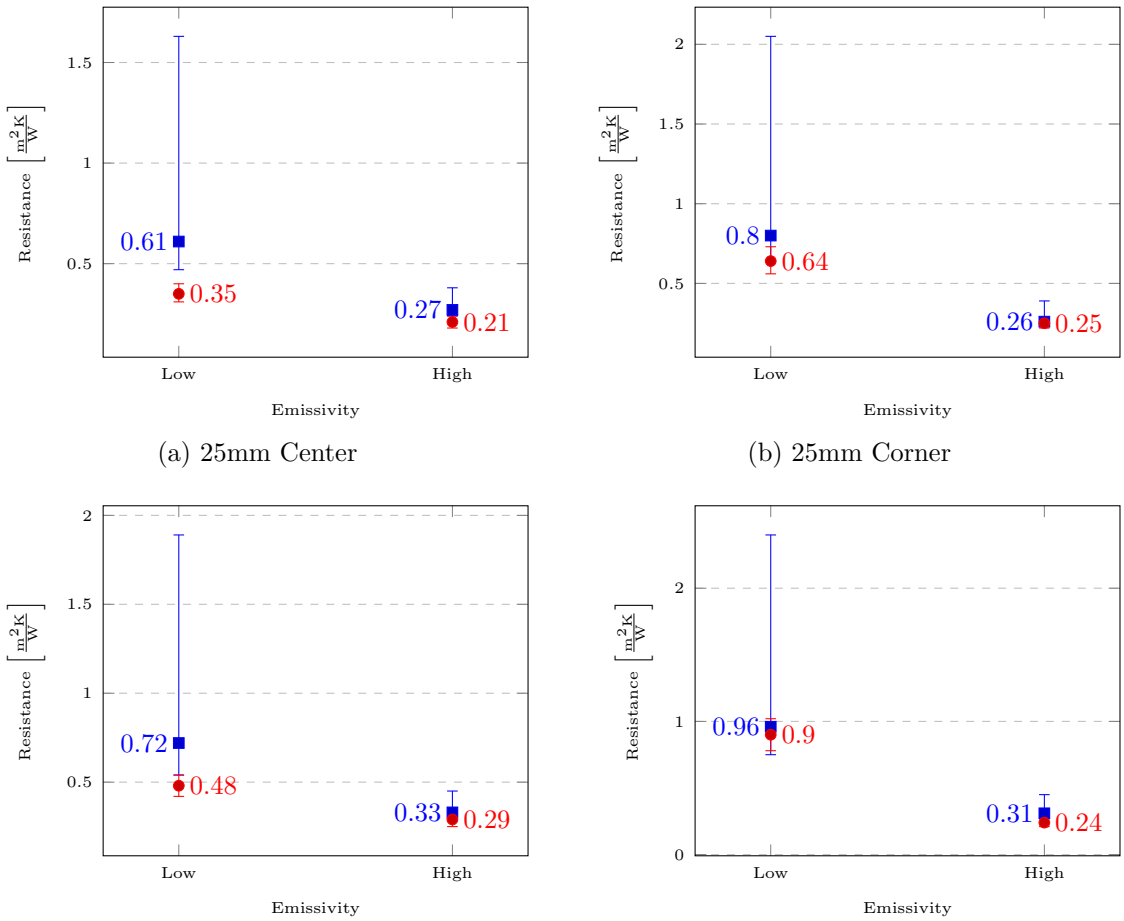

(a) 25mm Center

(b) 25mm Corner

(c) 50mm Center

(d) 50mm Corner

Figure 6.10: Thermal resistance comparison between simulated and measured results with error bars for BOX-CROSS configurations. Simulated values are plotted with a blue square, measured results are plotted with a red circle. Agreement in this configuration demonstrate accurate results when radiation and conduction primary transport mechanism.

6.5 Conclusions

Comparison between simulated and measured thermal resistance show good agreement, providing confidence in the simulation method and meeting the first objective of the chapter. The largest uncertainties in the system lie in thermal contact conductance and surface emissivity for low emissivity scenarios. Although current uncertainties result in large error bands on the overall performance of the panel, increasingly so as the panel becomes more thermally insulating, these can be narrowed down at the manufacturing stage where machining precision can be optimized. The accuracy of simulated results on such a complex model comprised of several regions interacting in a high vacuum environment suggest that this method can be used to accurately predict performance of hollow-core vacuum insulated panels. While the tests conducted are restricted to uniform box-like geometry, this method could function for other geometric alternatives and including any variation of material properties.

The disposition of such numerical methods capable of handling the complex mechanics of heat transfer across a solid-to-vacuum composite element can serve to inform the design process, reduce the need for prototype testing, evaluate for optimal configuration and properties, and explore vulnerabilities and limiting conditions such as emissivity, functional pressure levels and contact conductance.

Results from sample testing and modelling indicate that a hollow-core VIP panel can become a sufficiently good insulator, as seen in the low emissivity Box samples, where the maximum measured thermal resistance is 4.75 $\frac{m^2K}{W}$ and could potentially increase with lower surface emissivity. However, the effects of solid conduction (heat bridges) in efficient insulators, even in very small surface areas with low thermal con-

tact conductance, account for a significant percentage of thermal energy transferred; $\approx 40\%$ for low emissivity "Cross" configurations. Heat transfered through the rarefied gas accounts for up to 4% in low emissivity cases, and less than 0.5% in high emissivity cases. Radiative participation is responsible for $\sim 50\%$ of heat transfered in low emissivity scenarios and increases to $\sim 90\%$ in high emissivity scenarios. Observation from these tests indicate that radiation has a significant effect on the thermal properties of the model and suggest that it's a mechanism well suited for dynamic change between an insulating and a conducting state. Conduction and radiation represent the biggest threats towards achieving adequate insulation performance.

Gathered data indicates that thermal resistance can range from ~ 0.2 to $\sim 6\frac{m^2K}{W}$ when there is no direct contact with the structural array, and from ~ 0.2 to $\sim 2\frac{m^2K}{W}$ near structural array elements, taking into consideration both low and high emissivity states.

While these model iterations were limited by time constraints, available resources and facilities, obtained results and modelling technique can be used to balance competing requirements, the panel's overall thermal conductance and structural integrity, which will then lead to a feasible design configuration of a large scale building element.

Chapter 7

Design constraints and performance of the hollow core VIP

7.1 Introduction

Let the hollow core VIP be defined as an insulating panel comprised of opposing panel faces, or plates, supported by a structural array and a lateral foil sealing the vacuum. The three design constraints to be addressed are thermal conductance of the structural array and foil separating panel faces, plate deflection and maximum plate load, and compressive stress on the internal structural elements. The foil is neglected in mechanical constraints since deflection can be overcome by welding it in tension.

The structural elements in the array, which serve to separate the panels that hold the vacuum, will be referred to as spacers. The array separation, the length

between parallel elements in the array, is described by the variable d. Spacers' height is described by the variable H.

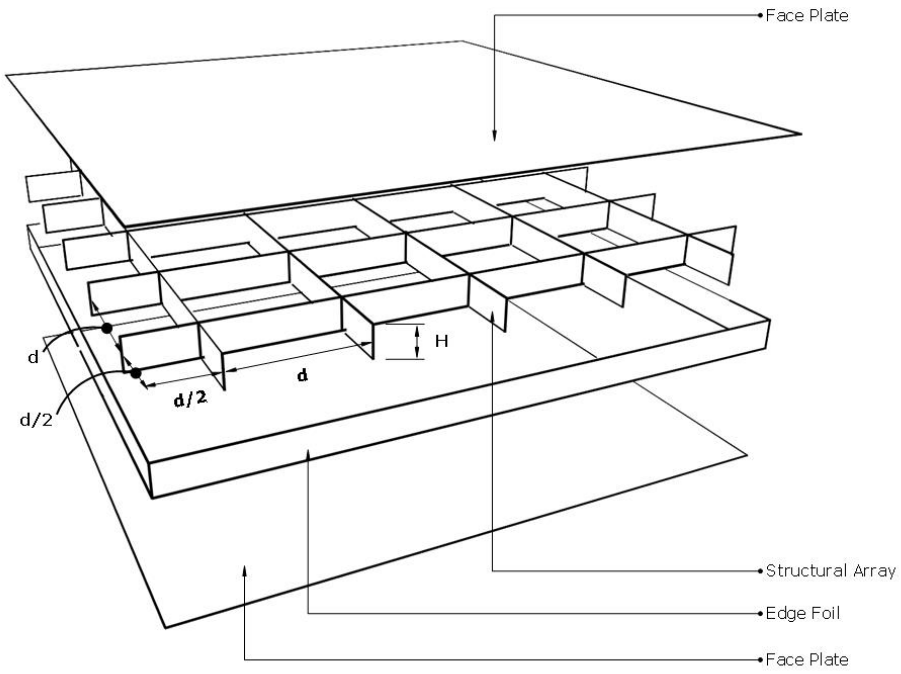

Figure 7.1: Hollow core vacuum insulated panel diagram.

7.1.1 Aims and Objectives

The studies conducted in this chapter aim to configure a hollow-core panel by balancing competing requirements, structural and thermal, and to use the simulating method to evaluate its overall thermal performance. Objectives for this chapter are:

- Express thermal conductance as a function of panel thickness and array dimensions and constrain it to a value defined by building regulations.

- Evaluate the maximum tolerated stress of the structural array and panel face plates and express these as a function of height and array separation.

- Combine thermal and structural design constraints into a feasible configuration for a hollow core VIP.

7.2 Thermal conductance

Analysis on the thermal conductance of the structural array is conducted by first looking at a single node of the repeating structure. There are many solutions to a structural array, and previous research has investigated conductance on glass pillars [78], staggered hollow glass tubes and glass spheres [57], this project investigates the thermal conductance of a uniform orthogonal array of thin continuous planar elements, like a widely spaced grate.

A node is defined as a repeating element in the structural array, with length and width "d''", with depth "H", and whose centroid is the point where perpendicular spacer elements intersect Figure 7.1. The node closest to the edge of the panel is separated from this edge by a distance of $d/2$.

If perfect contact between the face plate and the structural array is considered, the thermal resistance per unit area of a single node equals that of the material's resistance:

$$R''_{node} = \frac{H}{\kappa} \tag{7.1}$$

However, in the case where thermal contact resistance from imperfect contact at the interface is present, this term $\left(\frac{2}{hc}\right)$ becomes more noticeable as the material

thermal conductivity increases. Including the contact area, $A_{contact}$ as shown in Figure 7.2, which can be significantly reduced depending on the choice of materials results in the following thermal resistance $[\frac{K}{W}]$ for a single node.

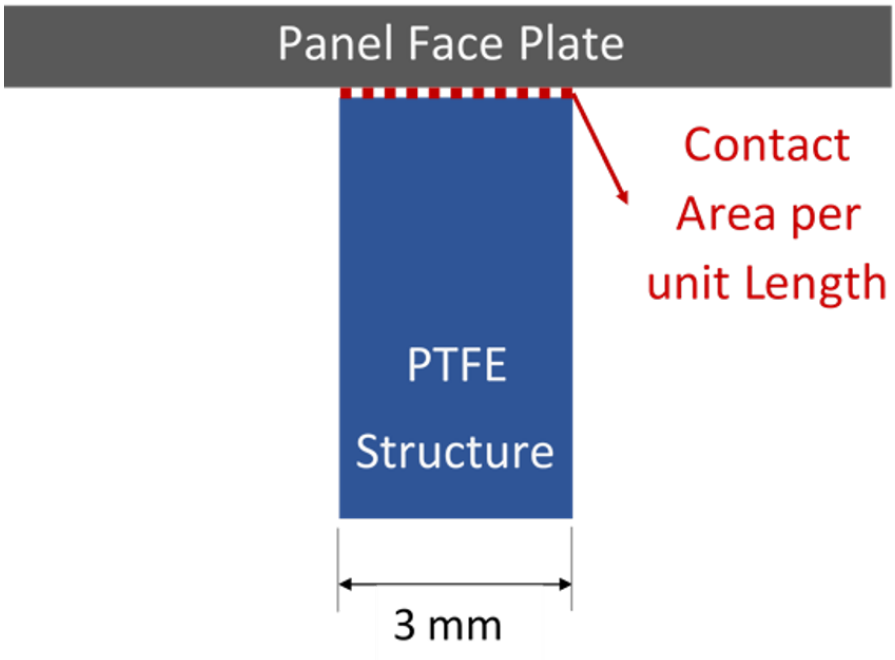

Figure 7.2: PTFE structure contact area diagram.

$$R_{node} = \left(\frac{2}{h_c} + \frac{H}{\kappa}\right) \times \frac{1}{A_{contact}} \tag{7.2}$$

Where h_c is the thermal contact conductance in $[\frac{W}{m^2K}]$ and κ is the material's thermal conductivity.

It becomes evident that for low conductivity materials contact conductance becomes trivial unless a very poor contact occurs, which is unlikely in the case of hollow core VIPs due to the considerable pressure differential. Inversely, for highly conductive materials, even slight imperfections at the contact interface can have a noticeable effect on the total thermal resistance. The thermal conductance, C_{node},

of the structural node can then be expressed as the inverse of its resistance.

$$C_{node} = \frac{h_c \kappa A_{contact}}{2\kappa + H h_c} \tag{7.3}$$

This calculation is effective for a center of panel but must include the heat transfered through the foil sealing the edge of the panel, since this can be a significant heat bridge in the panel. Heat transfered through the foil is analyzed as a perfect contact since it must be welded to the face plates to contain high vacuum pressure levels. The participation of the foil in the overall heat exchange will depend on the panel size and length to width ratio.

In a square or rectangular configuration, a width to length ratio of 1 will provide the smallest perimeter to area value. As the width to length ratio departs from unity the edge length or perimeter increases while maintaining the same area, thus increasing the panel's heat flux. Figure 7.3 shows the percent increase of perimeter for different length to width ratios. For a 2 to 1 ratio the perimeter increases by 6%, for a 3 to 1 ratio the perimeter increases by 15%, consequently, the dimensions of the panel will have a significant effect on its thermal performance. In addition to the Length-to-Width ratio, the area of the panel is also important. In rectangular configurations the area increases geometrically while perimeter increases linearly, as such larger panels will outperform smaller panels due to heat transfered through the edges. This phenomenon is exacerbated with larger length-to-width ratios, Figure 7.4. Although these geometric properties suggest manufacturing the largest possible panel, with equal length to width, they are meant to inform the design process rather than impose a specific solution.

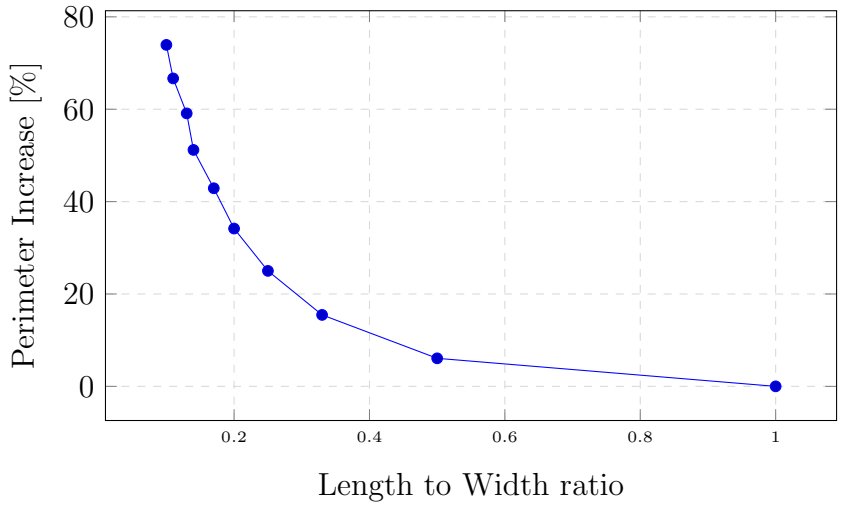

Figure 7.3: Effect of Length to Width ratio on perimeter increase for a $10m^2$ area. As the ratio departs from 1 the perimeter increases; at a 2:1 ratio the perimeter has increased 6%.

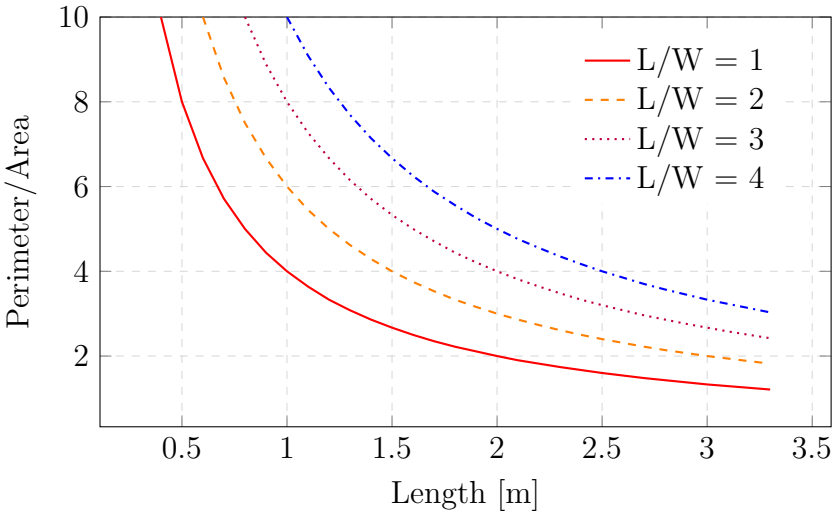

Figure 7.4: Perimeter to Area values for different Length to Width ratios. This graph shows that increasing the area diminishes the Perimeter to Area value, and that the most efficient length to width ratio for rectangular configurations is 1.

Having stated the importance of panel dimensions on the perimeter to area relationship and the inherent effect on heat flux, the thermal resistance $\left[\frac{K}{W}\right]$of the edge foil is described by:

$$R_{edge} = \frac{H}{\kappa_{edge}} \frac{1}{A_{edge}} \tag{7.4}$$

Where A_{edge} is is the edge foil's contact area, and is defined for a panel with length, a, and width, b, as:

$$A_{edge} = (2a + 2b)t \tag{7.5}$$

The thermal conductance of the edge per unit area can then be defined as:

$$C_{edge} = \frac{\kappa_{edge} A_{edge}}{abH} \tag{7.6}$$

The effective thermal conductance of the array, including the edge foil, can be established as the sum of the edge foil's thermal conductance per unit area and the array's thermal conductance per unit area. For a rectangular array, the number of nodes in the array per unit area is equal to $1/d^2$, the thermal conductance of the array per unit area can be defined as:

$$C_{array} = \frac{h_c \kappa A_{contact}}{2\kappa + H h_c} \times \frac{1}{d^2} \tag{7.7}$$

Finally, the effective thermal conductance of the panel including participation from the edge:

$$C_{effective} = \frac{h_c \kappa_{array} A_{contact}}{2\kappa_{array} + H h_c} \times \frac{1}{d^2} + \frac{\kappa_{edge} A_{edge}}{abH} \tag{7.8}$$

Having expressed the thermal conductance of the structural array in function of array separation d and height H, this equation can be rewritten to obtain the maximum allowed dimensions of the array (d and H) according to any given value for the effective conductance of the array. For the configuration described, the resulting equation is quadratic.

$$0 = H^2 abh_c d^2 + H\left[(2ab\kappa_{array}d^2) - \left(\frac{abh_c\kappa_{array}A_{contact}}{C_{effective}}\right) - \left(\frac{\kappa_{edge}A_{edge}h_c d^2}{C_{effective}}\right)\right] - \frac{2A_{edge}\kappa_{edge}\kappa_{array}d^2}{C_{effective}} \tag{7.9}$$

The tolerances of the array configuration can now be analyzed. Keeping in mind that for low emissivity samples the solid conduction accounted for approximately 40% (Table 6.8) of total energy transfered, the desired effective array thermal conductance is 0.1 $\frac{W}{m2K}$. The previous value in addition to radiative transfer and gas conduction would render the panel to have an estimated thermal conductance of 0.3 $\frac{W}{m2K}$, which is the limiting value for wall elements in UK's building regulations [10].

For a 3mm thick PTFE structural array with a contact conductance of 55 $\frac{W}{m^2K}$, as that of the measured samples, the tolerable dimensions for a series of array conductances can be seen in Figure 7.6a. Higher thermal contact conductance at the interface can be expected due to the substantial increase in compressive load from the pressure differential between ambient and high vacuum conditions as the soft PTFE is pressed into stainless steel. Figure 7.5 shows how PTFE conforms to steel when subject to compressive stress.

Any point above the curve in the graphs would result in lower thermal conduc-

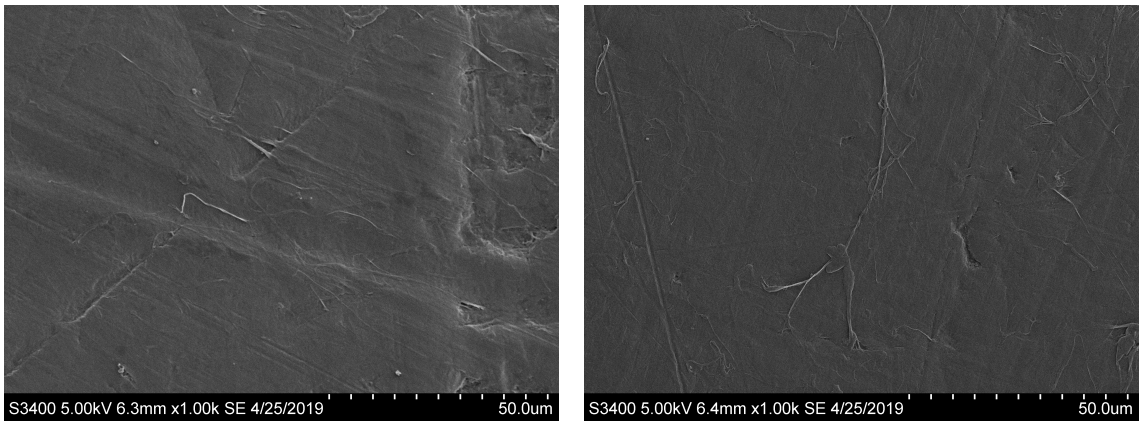

(a) (b)

Figure 7.5: SEM imaging of a)uncompressed PTFE sample and b) PTFE sample compressed with 750N in a hydraulic press; both samples were gold plated with a 10nm thick layer. The compressive load per unit area is equal to that experienced by the evacuated panel against ambient pressure. The uncompressed sample shows a highly irregular surface; the compressed sample has a flatter surface with some indentations as it conformed to the surface of the steel press.

tance than specified by the curve. Consequently, the safe desired performance is found within the shaded region in Figure 7.7.

The same analysis is performed for AISI 304 stainless steel, which has a much higher thermal conductivity than PTFE, at 16.2 $\frac{W}{mK}$ but has better mechanical properties which also affect other design considerations, as will be explored in the following subsections. Three cases regarding a 1mm thick AISI 304 stainless steel are analyzed: a) A flat contact across the entire width as shown in Figure 7.8a. b) A flat contact at half width, as if the object was slightly sharpened as shown in Figure 7.8b. c) Curved contact as if the end was rounded off to have a radius of 0.5mm as shown in Figure 7.8c. The first two cases consider a contact conductance of 280 $\frac{W}{m^2K}$ for steel to steel interface based on experimental data from [104] at similar temperature and compressive stress. The last case assumes perfect contact

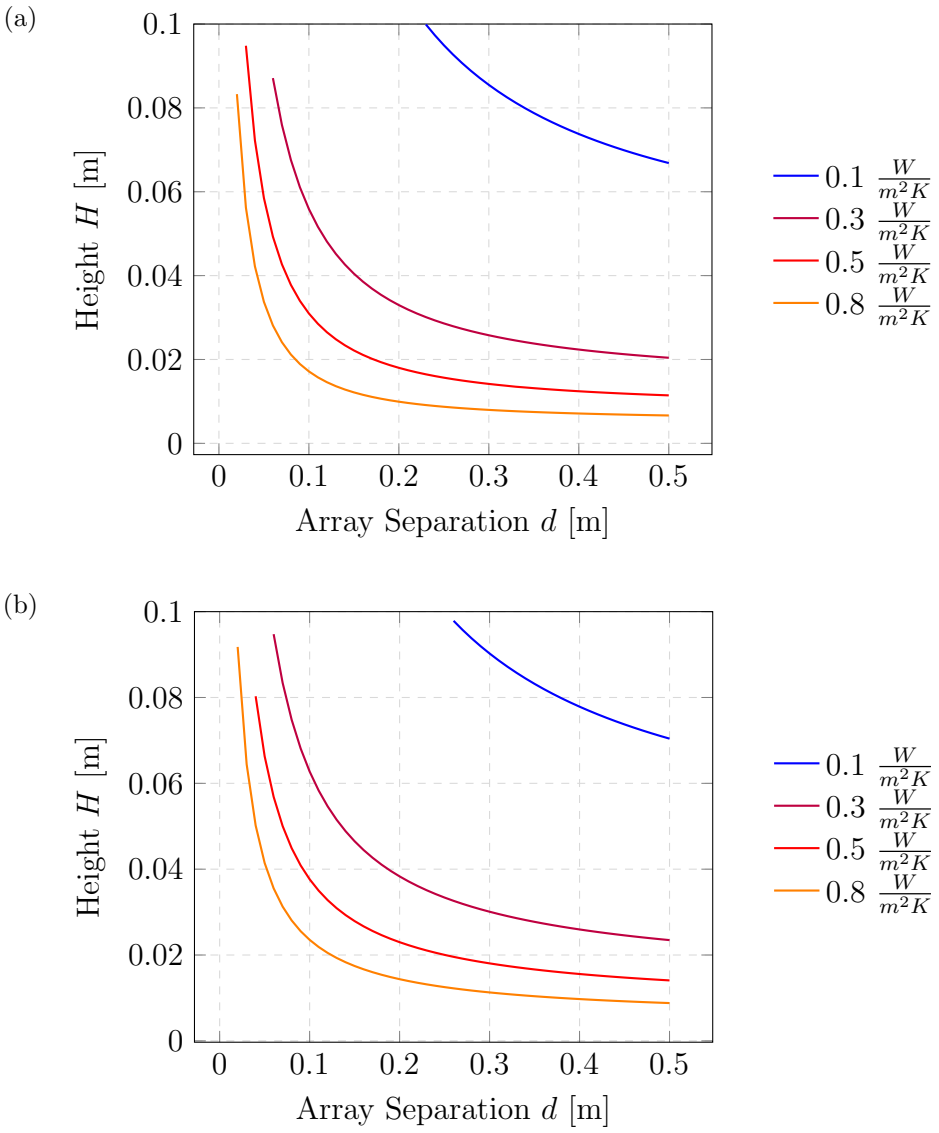

Figure 7.6: Limiting dimensions for PTFE array according to multiple array conductance values. a) Includes a thermal contact conductance of 55 $\frac{W}{m^2K}$ at the interface. b) Perfect contact at the interface. The difference between a and b is negligible due to the insulating nature of PTFE. Nonetheless, due to the large contact area, achieving an array thermal conductance of 0.1 $\frac{W}{m^2K}$ may result in challenging array dimensions.

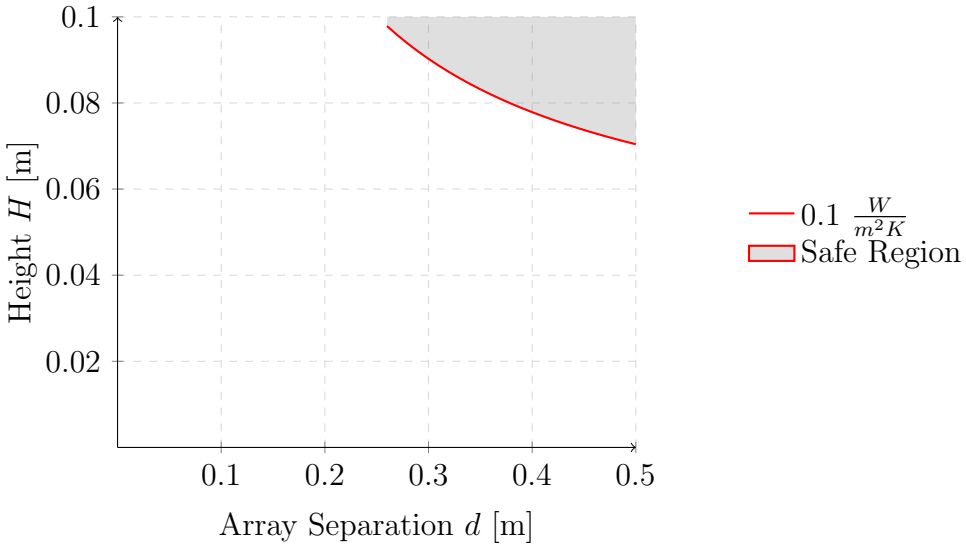

Figure 7.7: 3mm thick PTFE structural array dimensions needed to maintain an array conductance of or below 0.1 $\frac{W}{m^2K}$ considering perfect contact at the interface. Anywhere within the shaded region would provide values within the tolerated conductance.

within the area resulting from deformation of two elastic solids in contact under pressure [190]. In support of perfect contact after deformation, Figure 7.9 shows the polished surface of stainless steel conforming to a $50mm$ long dull blade under a load of $1kN$, which is the same load per unit length as would be experienced by the curved contact. However, due to the uneven edge of the blade, its effect on load distribution, and the limited surface imaged by the SEM it is not possible to draw an accurate direct comparison between Hertz formula and the observed indentations.

The contact area, $A_{contact}$, from the last case is calculated according to Hertz equations for non conforming cylinders, where the flat surface is a cylinder whose radius tends to infinity. The contact area of the node is equivalent to $2a \times 2d$, where a is the half width of the contact area and is calculated as [190]:

$$a = \left(\frac{4PR}{\pi E*}\right)^{1/2} \tag{7.10}$$

Where P is the compressive load per unit length, R is the equivalent radius $(1/R \equiv 1/R_1 + 1/R_2)$, and $E* \equiv \left(\frac{1-v_1^2}{E_1} + \frac{1-v_2^2}{E_2}\right)^{-1}$

Clearly, the high conductivity of stainless steel makes it impossible to produce an

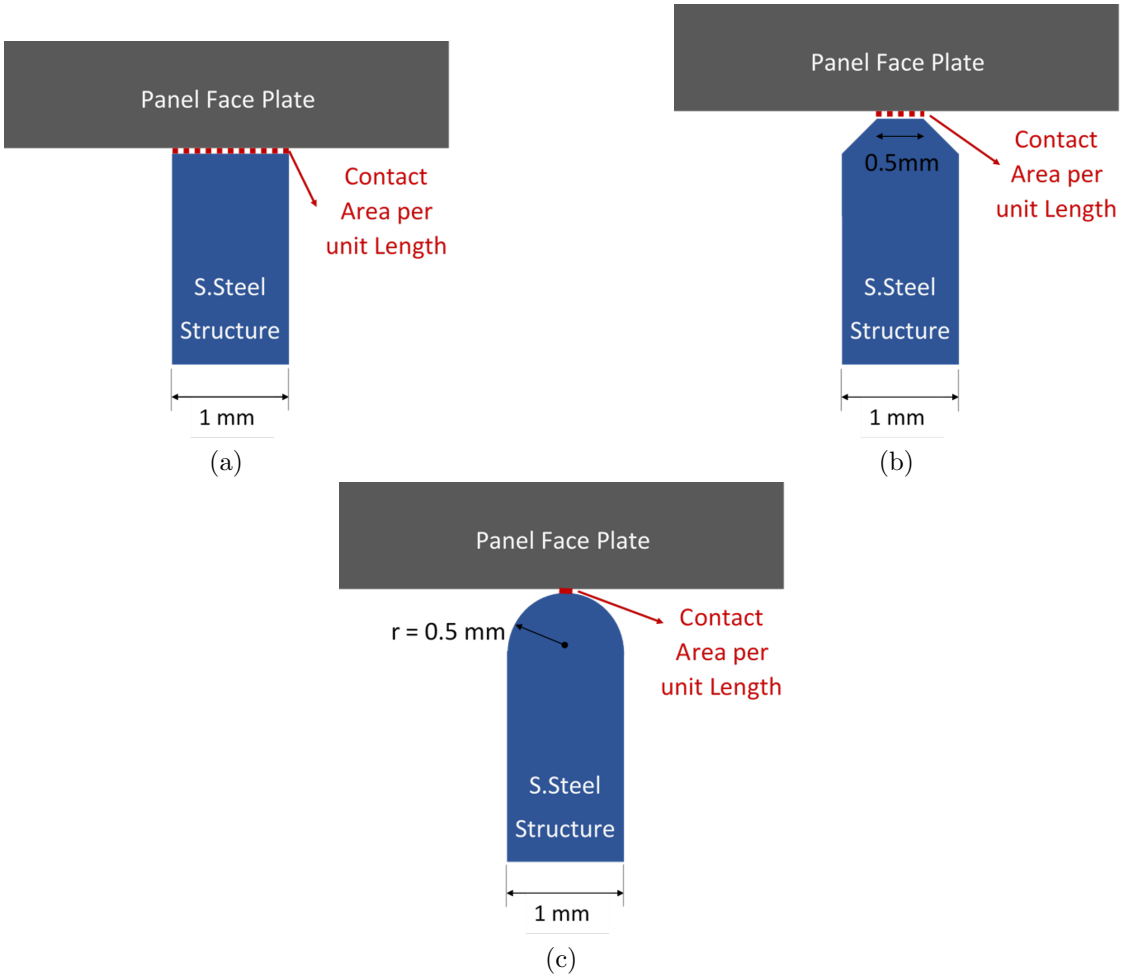

Figure 7.8: Contact area for stainless steel structural solutions: a) Flat contact across entire element, b) Flat contact across tapered element, c) Contact area between non conforming solids. The last case assumes the steel face plate will not deform or conform beyond the calculated deformation of pressed contact between elastic non conforming solids as described by Hertz's equations.

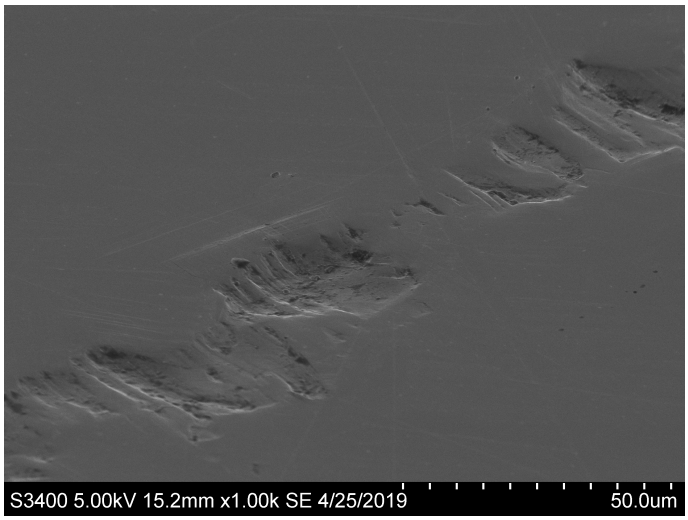

Figure 7.9: SEM imaging of finely polished AISI 304 Stainless Steel with indentation caused by a $50mm$ long dull blade pressed with $1kN$ of force.

adequately insulating array with a flat contact, Figures 7.10a 7.10b. However, the hardness of steel allows to round off the tip , significantly reducing contact area and yielding adequate insulating properties. Therefore, a rounded off (0.5mm radius) 1mm thick AISI 304 Stainless Steel array is a better solution even in comparison to the PTFE array from a theoretical stance, Figure 7.11. However, in non-ideal scenarios, where even small deflection from the panel face plate occurs, the resulting contact area would be significantly affected.

Having produced a relationship between array dimensions and its estimated solid thermal conductance we must now compare this criterion with the structural necessities of the panel.

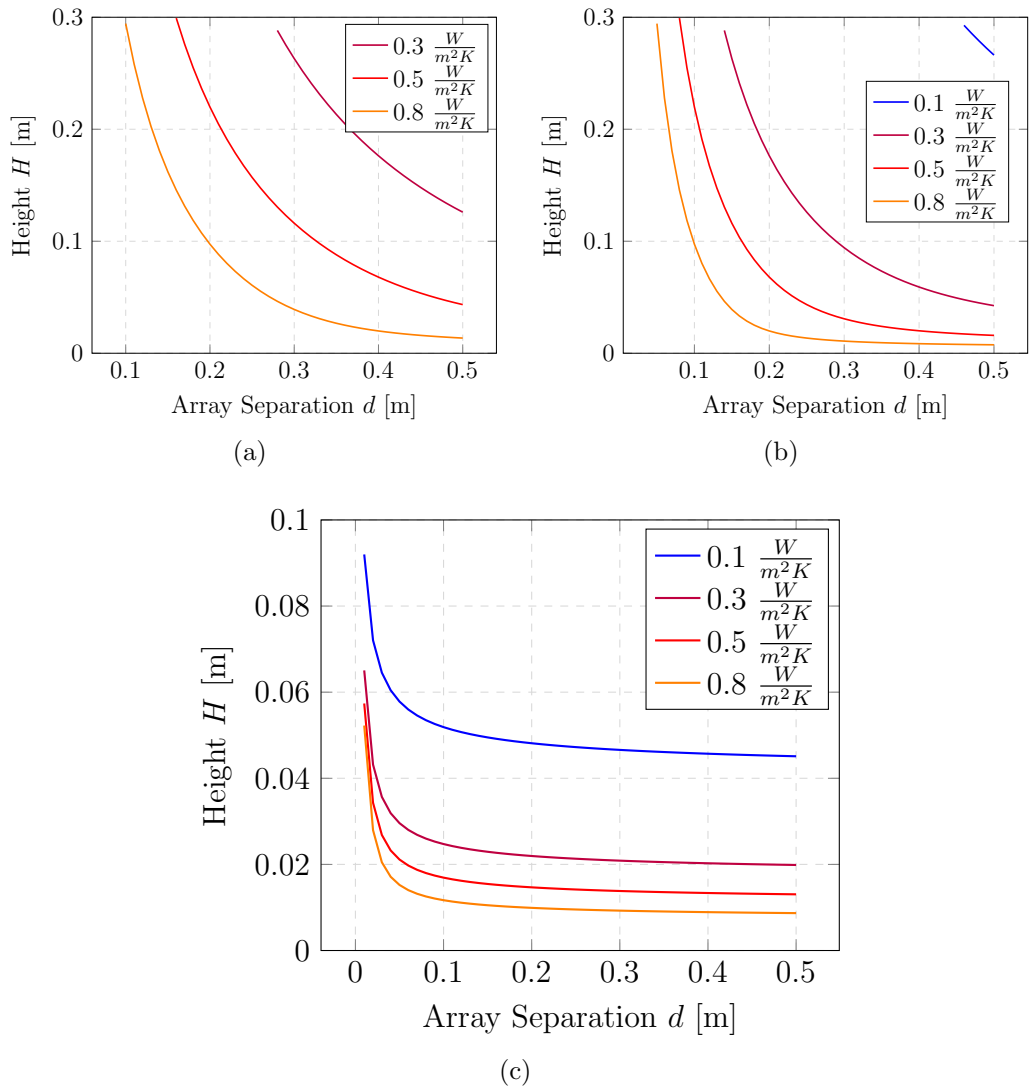

Figure 7.10: Limiting dimensions for a AISI 304 Steel array according to multiple array conductance values and different types of contact between the array and the panel's face plate. a) 1mm flat contact with thermal contact conductance at the interface of 280 $\frac{W}{m^2K}$ at the interface. b) 0.5 mm flat contact with thermal contact conductance at the interface of 280 $\frac{W}{m^2K}$ at the interface. c) Contact between a 0.5mm curved thin element and a flat plate.

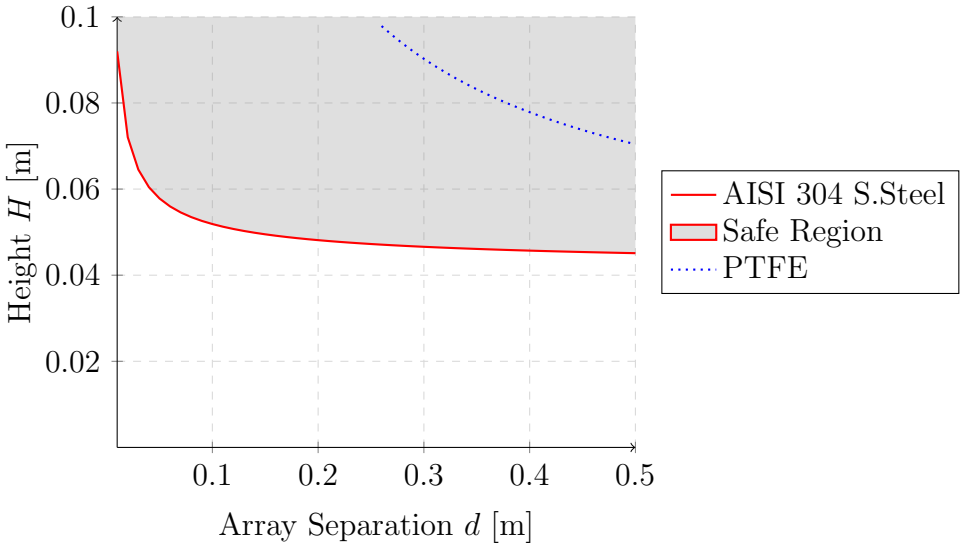

Figure 7.11: 1mm thick rounded off AISI 304 Stainless Steel vs 3mm thick PTFE structural array dimensions needed to maintain an array conductance of or below 0.1 $\frac{W}{m^2K}$. Anywhere within the shaded region would provide values within the tolerated conductance.

7.3 Compressive stress on structural array

The structural elements separating the panels which hold the vacuum will have to, at the very least, be capable of supporting the compressive load exerted by ambient pressure. Further research could incorporate additional stresses experienced in practical applications such as wind loading.

The maximum load, P_{max}, can be defined under two conditions, when these are substituted the relationship can be plotted as a function of spacer height, h, against array separation, d. The maximum load is first evaluated as the net force exerted by the differential between ambient pressure and in-vacuum pressure. Since the vacuum levels treated in this project are less than one millionth of ambient pressure we can approximate net compressive stress equal to ambient pressure, p_{amb}. Consequently

the maximum load is defined as:

$$P_{max} = \frac{p_{amb} A_{panel}}{L_{spacers}/d} \tag{7.11}$$

Where

- P_{max} = maximum compressive load $[N]$
- p_{amb} = Ambient pressure $[Pa]$
- A_{panel} = Area of panel $[m^2]$
- $L_{spacers}$ = Total length of spacer array $[m]$
- d = Spacer segment length $[m]$

7.3.1 Results on critical loads and elastic buckling

Results from the previous expressions have been plotted in Figure 7.12a and 7.12b. Even though the evaluated material, PTFE, has a relatively low Elasticity Modulus ($4 \times 10^8 Pa$), acceptable element dimensions are calculated. E.g. A structurally adequate element, under elastic buckling conditions, could be designed with a height of 0.025m and length of 0.3m for 3mm thick PTFE material.

Finally the safe design dimensions of a structural PTFE array, as the one included in the tested samples, in regards to elastic buckling are found in the area beneath the curve of elastic buckling of plates, Figure 7.13a. In this project, we were limited by fabrication solutions to soft materials with low out-gassing, resulting in the use of PTFE, nonetheless other materials with different mechanical properties can be chosen to improve the structural array dimensions, as seen in the case of 1mm thick

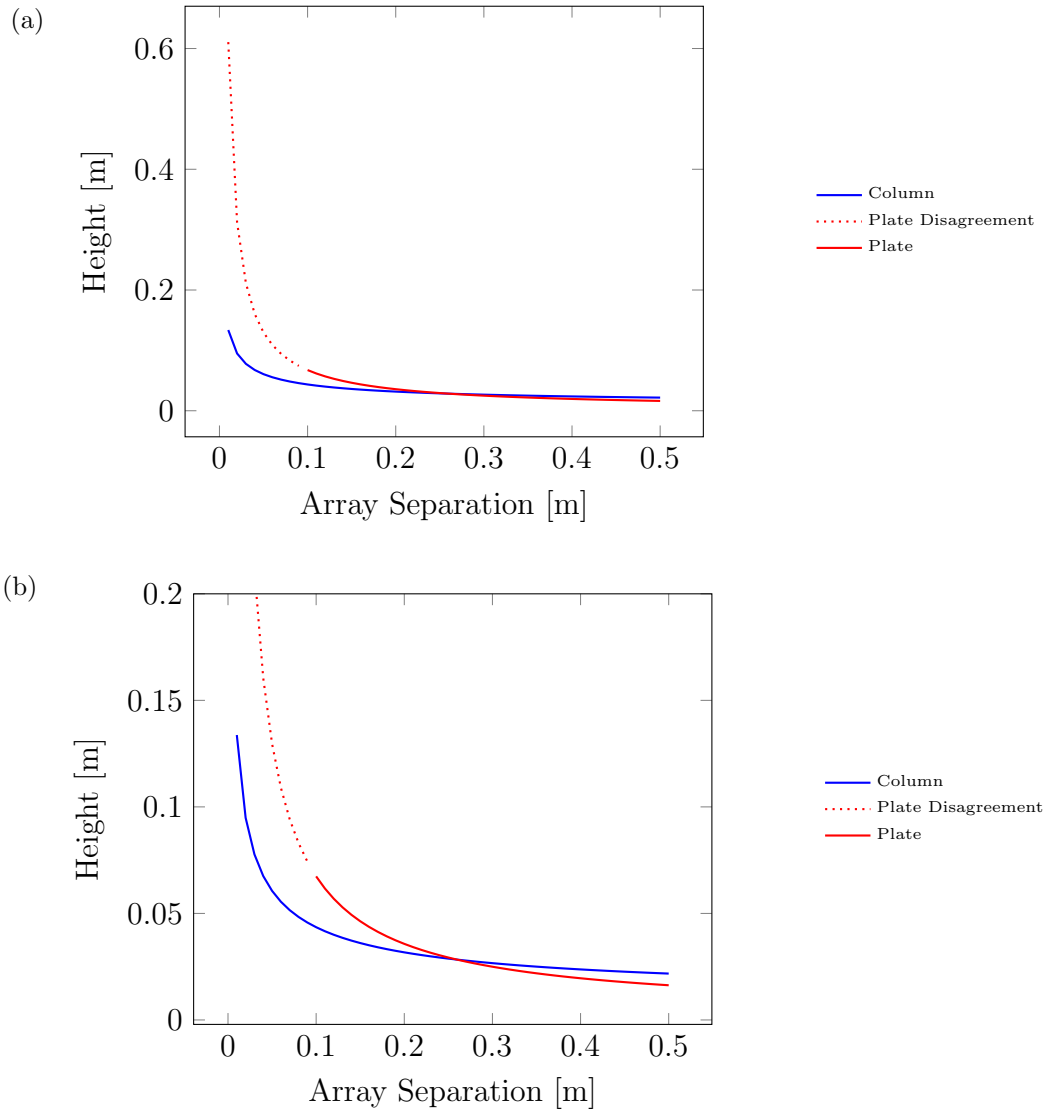

Figure 7.12: Elastic buckling of PTFE spacer elements. Plate and column analysis plotted on a height to array separation chart. The dotted line represents inaccurate data of the plate analysis when the plastic deformation is likely to occur and as such equation 7.7 is insufficient. a) Domain from 0 t0 0.05. b) The range is truncated to show greater detail in the smaller H/d ratios.

AISI 304 stainless steel, Figure 7.13b, where a separation of 1m between structural spacers still allows for a 3.5cm spacer height. Materials with better mechanical properties often result in increased thermal conductance, therefore, choosing an adequate material solution requires considering both of these opposing properties.

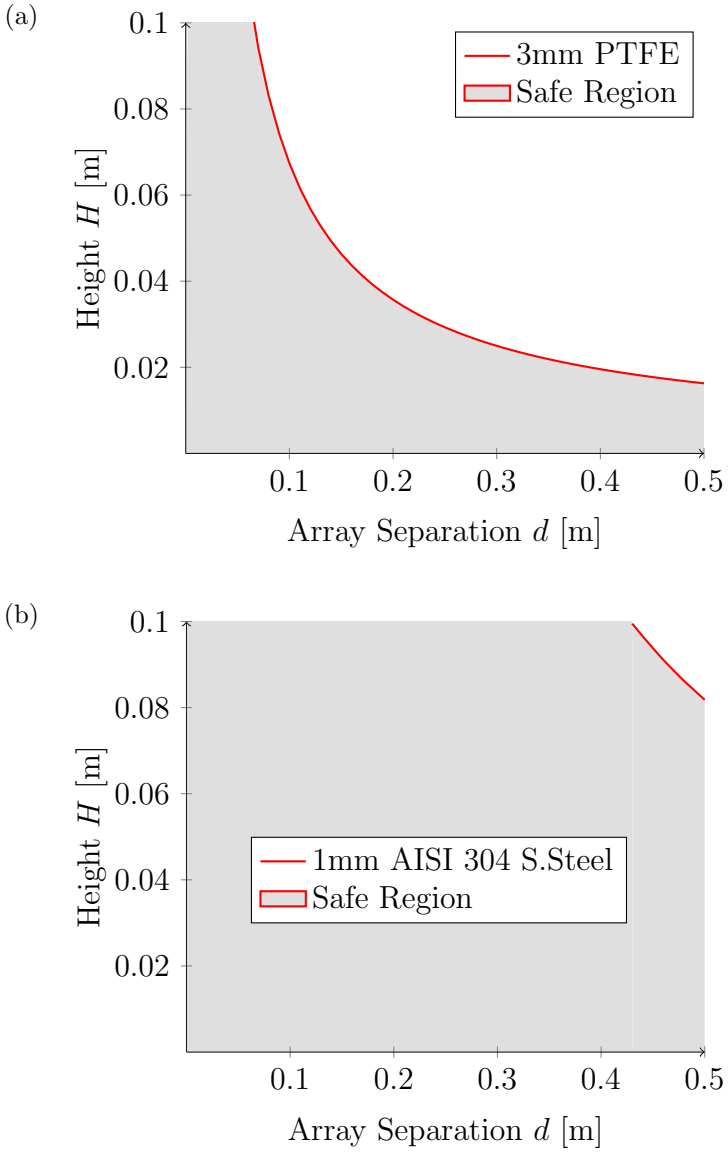

Figure 7.13: Safe structural dimensions in the shaded region for a) 3mm thick PTFE elements b) 1mm thick AISI 304 Stainless Steel elements. The improved mechanical properties of steel allow for much larger array H/d ratios than PTFE, allowing an element height over 3cms at a separation of 1m.

7.4 Plate deflection

The maximum allowed plate deflection is limited to 1/200 of the span. Even though this limitation was designed for vertical deflection of suspended ceilings according

to Eurocodes standards [191], the implications of structural stability can be applied to elements on a smaller scale.

As stated in Section 2.4.2, stainless steel flat plates thinner than $3mm$ are incapable of withstanding array separation larger than $300mm$ without significant deflection. It follows that plate stiffening is necessary to withstand larger spans. A skin treatment consisting of consecutive vaults tied by a steel plate allows for large spans without deforming in the plane of the arch. The limiting dimension then becomes the maximum span along the axis of the vault.

Limiting the maximum deflection to Eurocodes standard for a suspended ceiling as 1/200 of the span, equation 2.38 can be rewritten into obtaining the maximum length of the support arch or vault element. However, if the interior is coated with brittle materials the maximum deflection will need to be adjusted accordingly. This directly affects any electrochromic coating applied on the steel sheet holding in the vacuum, the coating's maximum allowed deflection will need to be greater than the maximum allowed deflection when placing the support elements.

$$l_{max} = \left(\frac{384EI}{-1000w} \right)^{1/3} \tag{7.12}$$

As the arch radius increases, so does its maximum length, Figure 7.14. Choosing a limitation can be done in order of maximum desired weight, maximum span length or arch radius, which is representative of the added thickness to the panel. Following the last option the added thickness is limited to 0.035m per side. Consequently the safe design criteria in terms of maximum spacer distance is 0.40m; plotted as a function of spacer separation d to spacer height H it's seen as a constant independent of spacer height h, Figure 7.15.

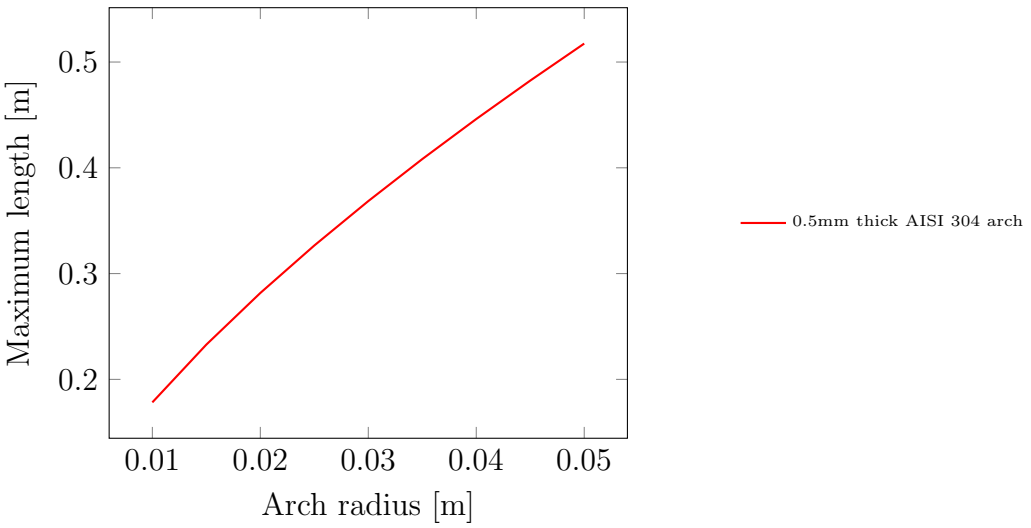

Figure 7.14: Maximum spanning length of a hollow semi circle profile treated as a beam. The maximum allowed deflection is 1/200 of the span. The arch is treated as a 0.5mm thick AISI 304 steel element.

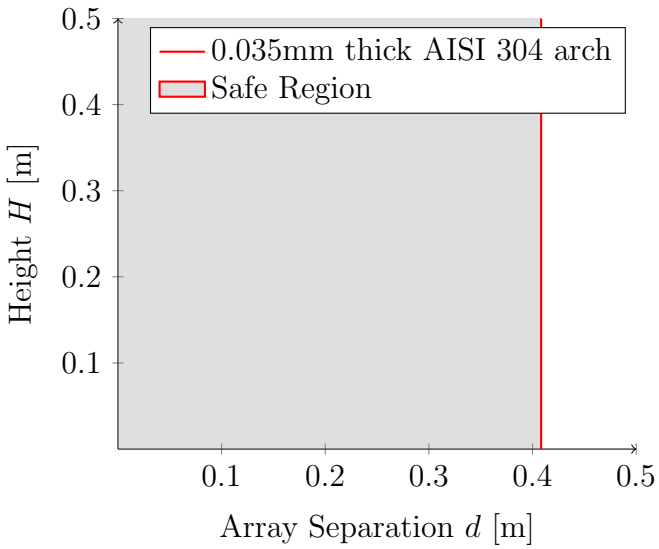

Figure 7.15: Safe design spacer element distance before the skin deflects over 1/200 of the span along the neutral axis of the arch. This is considering the face plates are supported by arch structures that bear ambient pressure and keep the face plates in tension along the horizontal axis of the arch plane.

7.5 Combination of design constraints

The previous analysis looked at three constraints individually, solid thermal conductance of the structural array, elastic buckling of the array elements and deflection of the panel's face plate. All of these providing a limit to the possible combination of array separation d and array height H.

Figures 7.16a, 7.16b, 7.16c shows these constraints individually for a 3mm thick PTFE array, and the shaded area in Figure 7.16d shows the combination of H and d which satisfies all three simultaneously. It becomes evident that PTFE is unable to sustain an array with a solid thermal conductance of 0.1 $\frac{W}{m^2K}$, but is capable of sustaining an array of 0.3 $\frac{W}{m^2K}$, albeit over a narrow region.

This analysis is meant to inform the design process, rather than indicate a definite solution. While this analysis only covers PTFE and AISI 304 Steel on a square grid, the same method can be applied to any selection of materials and structural array desired.

From these results a hollow core VIP can be reproduced in any size including all necessary elements to build it, avoiding unnecessary prototype manufacturing until desired thermal performance is achieved on a simulated case. With the interest of keeping the panel as thin as possible, further investugation is conducted on a 46mm tall, 1mm thick AISI 304 array, with rounded off ends and spaced 30cms apart; although any panel dimension is available, the standard sheet size 1.2m by 2.4m is fitting due to its area and its width to length ratio. Even though the PTFE array could only sustain a 0.3 $\frac{W}{m2K}$ conductance, or higher, it invites further investigation on the full size panel of the same dimensions but with a 46mm tall, 3mm thick PTFE square array spaced 15cms apart.

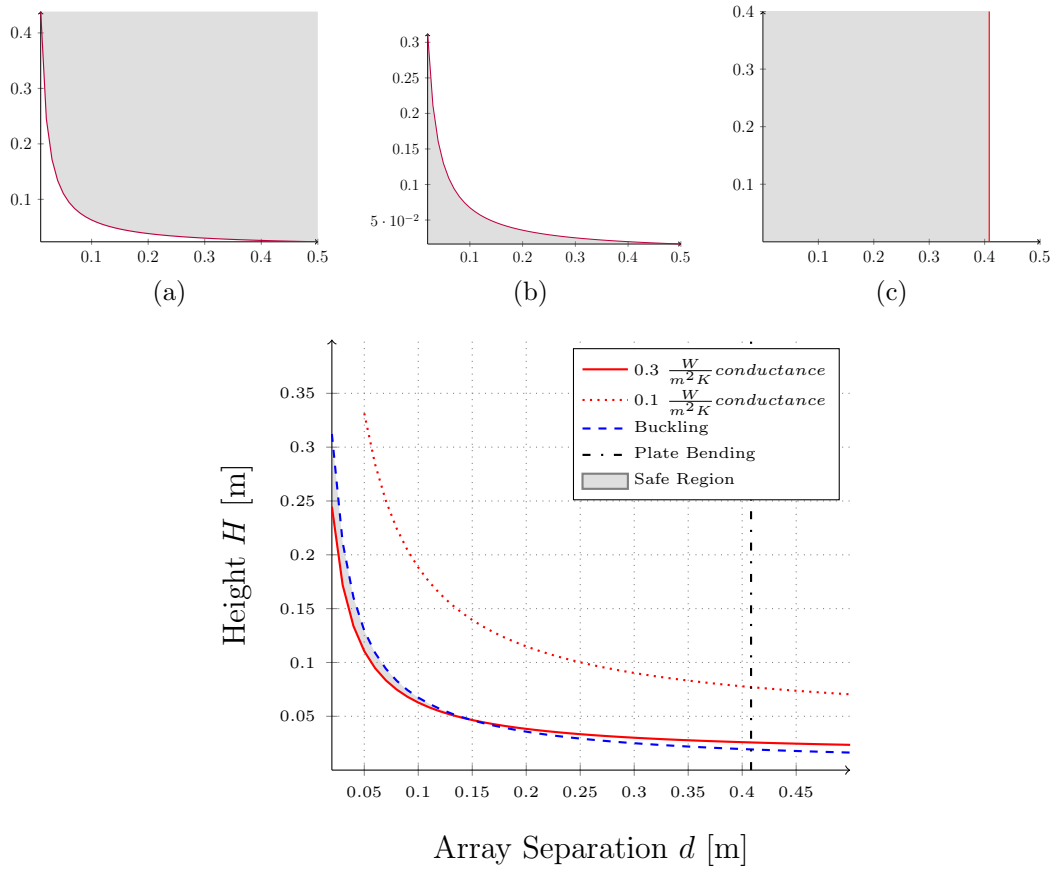

Figure 7.16: Design constraints for 3mm PTFE structural array. a) Thermal conductance b) Plate buckling c) Face plate bending d) All combined. The shaded region shows the safe combinations of H and d values. It is clear that a low array conductance of 0.1 $\frac{W}{m^2K}$ is not possible with 3mm PTFE. However, a higher solid conductance of 0.3 $\frac{W}{m^2K}$ is achievable with spacer heights as short as 46mm if these are spaced apart 15cms.

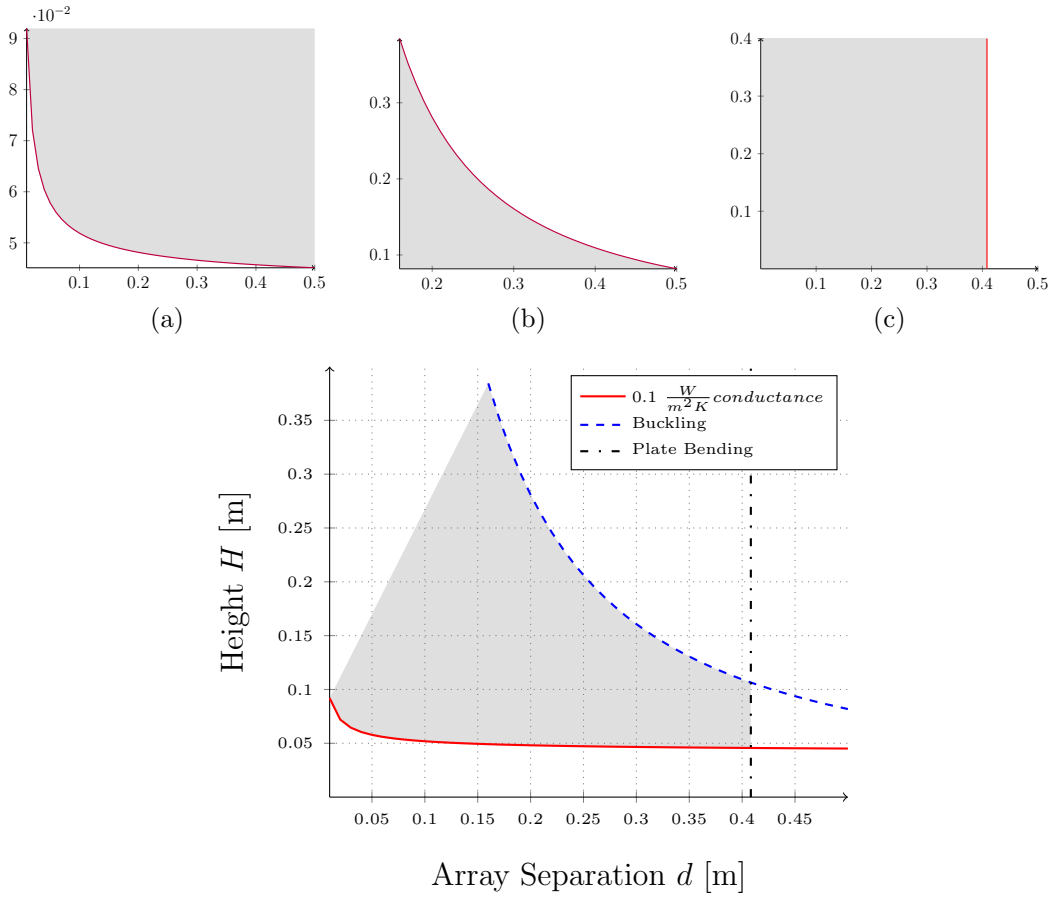

Figure 7.17: Design constraints for 1mm AISI 304 Stainless Steel with rounded off ends structural array. a) Thermal conductance b) Plate buckling c) Face plate bending d) All combined. The shaded region shows the safe combinations of H and d values. This solution, contrary to PTFE, is theoretically capable of producing a low solid conductance array, if the contact area remains small as it should for two non conforming stainless steel bodies.

7.6 Results

Several panel configurations were tested, in order to evaluate sensitivity to pressure increase, effective thermal conductivity range if an electrochromic coating was employed, and the overall performance having all panel elements included simultaneously. The following table shows the simulations performed for a PTFE and Steel array.

Table 7.1: Hollow core VIP simulations. Design constrained by structural array's thermal conductance, buckling and face plate deflection.

Array Material	**Emissivity**	**Pressure** Pa
Steel	0.595	0.01
	0.057	0.01
	0.1	0.01
	0.1	0.1
	0.1	1
PTFE	0.595	0.01
	0.057	0.01
	0.1	0.01
	0.1	0.1
	0.1	1

The PTFE array considers a 3mm thick PTFE array with a 46mm height and spaced apart 15cms. The thermal contact at the interface with the face plate of the panel is considered perfect, as such without thermal contact resistance. The steel array considers a 1mm thick AISI 304 Stainless Steel with a 46mm height and spaced apart 30cms. Due to the large panel dimensions and the small contact area, array to face plate contact is modeled as a flat 1mm thick contact instead of the rounded off edge, but introduces a thermal contact resistance that limits heat flux

to that which would be experienced over the small contact area of the rounded off edge. Hence, the contact resistance is calculated as:

$$h_c = \frac{2\kappa A_r}{H(A_f - A_r)} \tag{7.13}$$

Where the subscripts r and f indicate the rounded off or flat contact area, respectively.

All simulations include a 100 μm thick stainless steel foil that serves to seal the vacuum at the panel edge, and which could be welded to the face plate in tension to avoid deflection under pressure. Additional cases may want to consider other foils as these can be found as thin as 25 μm. Although stress distribution through the foil has not been been evaluated, experimental results demonstrate that even the 25 μm thick foil resists over $400MPa$ of tensile stress before experiencing plastic deformation [192]. Simulations were conducted for 1.2 by 2.4m size panels with temperature boundaries of 0 and 25 °C. Results from the simulations can be found in Table 7.2.

Table 7.2: Results from full size panel simulations. Simulations conducted in OpenFoam using Steady State SIMPLE algorithm.

	Emissivity	**Pressure** Pa	**Conductance** W/m2K	**Conductivity** W/mK	**Solid** %	**Gas** %	**Radiative** %
	0.595	0.01	2.26	0.104	8.2	1.1	90.7
	0.057	0.01	0.36	0.017	51.6	6.8	41.6
Steel	0.1	0.01	0.48	0.022	38.7	5.1	56.2
	0.1	0.1	0.65	0.030	28.2	30.3	41.5
	0.1	1	1.25	0.058	14.0	64.6	21.5
	0.595	0.01	2.23	0.103	16.4	0.7	82.9
	0.057	0.01	0.51	0.023	69.9	3.0	27.1
PTFE	0.1	0.01	0.62	0.029	57.7	2.4	39.8
	0.1	0.1	0.72	0.033	49.1	16.7	34.2
	0.1	1	1.10	0.051	31.4	46.3	22.4

The thermal performance of hollow core VIPs is severely limited by structural

and manufacturing necessities. Even though a structural array with a 0.1 $\frac{W}{m^2K}$ conductance is feasible, thermal transfer through the steel foil, the panel's edges, is still the biggest weakness. A 100 μm thick foil in the edges of the panel transfers as much energy as the entire steel structural array with rounded off edges as expected from the total contact area. Assuming non-conformity between the face plate and the structural element, the total contact area of the structure in the 1.2m by 2.4m panel as calculated by Hertz's equations is $1.18 \times 10^{-5} m^2$, while the contact area between the 100 μm thick edge foil and the face plate is $7.2 \times 10^{-4} m^2$. It should be noted this case is ideal as it doesn't consider bending or additional deflection from the face plate.

Ultimately, in the best of cases this represents a panel with a thermal conductance of $0.36\frac{W}{m^2K}$, and an overall effective thermal conductivity of $0.017\frac{W}{mK}$, which is slightly better than convential PUR-PIR insulation materials ($0.019\frac{W}{mK}$) but not nearly as good as aerogel or conventional VIPs ($0.004\frac{W}{mK}$) [23]. Based on these results, if we assume a 25 μm thick steel foil will reduce heat transfer through the edges by a factor of 4, the total thermal conductance and thermal conductivity of the best performing panel becomes $0.29\frac{W}{m^2K}$ and $0.013\frac{W}{mK}$, respectively. Even though these values improve hollow-core VIPs performance, they are still significantly far from superinsulators. Moreover, it should be noted that the heat bridge effect of the edges is less noticeable as the panel area increases, as such, requiring a minimum panel size to achieve decent thermal conductance, and introducing an additional limitation to the fabrication and application of hollow core VIPs.

Since the effects of the steel foil sealing the edges is significant, the difference between the PTFE and Steel arrays is narrowed. The 3mm PTFE array, with a conductance of $0.3\frac{W}{m^2K}$ produced an overall panel thermal conductance of $0.51\frac{W}{m^2K}$

with an effective thermal conductivity of $0.023\frac{W}{mK}$, close to the AISI 304 steel array panel. An important difference between these two configurations is that the PTFE panel is severly limited in its array configurations, as the array would buckle under pressure. By comparison, the steel array panel can increase its thickness or array spacing to lower the resulting thermal conductance. Nonetheless, it has been demonstrated that hollow core VIPs can function under specific configurations but are limited to a minimum panel size and thickness.

These results also indicate the panel's sensitivity to pressure increase. Increasing internal pressure from 0.01 Pa to 0.1 Pa increases thermal conductivity by nearly 20%, matching the thermal conductivity of PUR-PIR insulating materials.

Moreover, the application of an electrochromic coating on the internal surfaces of the panel, changing the emissivity from 0.057 to 0.595 [124] would increase the panel's thermal conductivity by a factor of 4. Increasing the estimated thermal conductance from $0.36\frac{W}{m^2K}$ to $2.6\frac{W}{m^2K}$. This shows great promise on the applicability of hollow core VIPs, as these can be configured to have good insulating properties with a conductive state when desired. Although the amount of heat transfered through the panel in a conductive state is not comparable to single pane windows ($5.47\frac{W}{m^2K}$ [193]) it is larger than vacuum glazing with low emittance coating ($1.3\frac{W}{m^2K}$ [77]), and provides an almost passive heating/cooling solution that can be applied to large sections of the facade.

This insulating technology is theoretically feasible, but not without its caveats. Material selection is of extreme importance, only low outgassing materials can be employed in order to maintain a high vacuum, and mechanically strong materials required to hold the panel have terrible insulating properties. However, the potential advantages of having robust, thin and self supporting insulating elements with semi-

passive heating/cooling invite further investigation into this technology.

7.7 Conclusion

The design of hollow core VIPs requires consideration of opposing qualities, structural integrity and thermal conductance. A robust panel will often represent significant heat transfer, consequently requiring careful consideration to the composition of the panel to avoid unnecessary support in favor of reduced heat exchange. Following this necessity, the composition of the panel was evaluated for solid thermal conductance and elastic buckling of the structural array, as well as deflection of the face plate. These design constraints were analyzed to produce "safe" regions with regards to the dimensions of the panel, specifically the height of the structural array and maximum spacing between array elements. This analysis was limited to consider PTFE and AISI 304 stainless steel square arrays, but it can be extended for other materials and array configurations.

The thermal conductance of the structural array was defined as a function of array dimensions and material properties. The resulting quadratic equation constrained by a thermal conductance limit was used to define array dimensions for PTFE and stainless steel structural elements.

Similarly, deflection on the face plates or fascias, and elastic buckling of the internal structural array were expressed as a function of panel dimensions and used to define array configuration limits. Deflection on the face plate was reduced by proposing a skin stiffening treatment of adjacent arches that redirect compressive stress from ambient pressure into tensile stress of a steel tie linking the arched structures. Elastic buckling of internal structural elements was studied by plate theory

and rewritten to specify limiting array dimensions under a critical load defined as ambient pressure.

The resulting "safe" dimension range of all constraints combined were very narrow for the PTFE array, and could only accommodate a thermal conductance of $0.3\frac{W}{m^2K}$, as shown in Figure 7.16d. By comparison, the steel array could theoretically have a thermal conductance of $0.1\frac{W}{m^2K}$ or lower, as shown in Figure 7.17d, if the edges were rounded off and in contact with a non-accomodating solid with the same hardness as depicted in Figure 7.8c.

The simulated performance of a large panel, 1.2m by 2.4m, using the thinnest possible configuration resulted in a total conductance of $0.36\frac{W}{m^2K}$ for the steel array, and $0.51\frac{W}{m^2K}$ for the PTFE array, with effective thermal conductivity of $0.017\frac{W}{mK}$ and $0.023\frac{W}{mK}$, respectively. The difference between the estimated array conductance and the final panel conductance is significantly affected by heat transfer through the edges sealing in the vacuum. The PTFE array, contrary to the steel array, is limited to a very narrow safe design region and has no more room for improvement. In addition to the insulating properties of the hollow core VIP, application of electrochromic coating could boost the thermal conductance of the panel by a factor of 4, thus providing a semi-passive heating/cooling solution.

This study suggests that a hollow core VIP can be manufactured to perform better than common insulating materials, but not as well as superinsulators like aerogel or conventional VIPs. However, some problems found in fumed silica VIPs could not be avoided in the hollow core application, such as significant heat transfer through the edges. Moreover, the significant participation of the edge foil sealing the vacuum requires that hollow core VIPs have a large dimension to mitigate heat bridging through the edge. Nonetheless, due to the sturdy composition of these

VIPs, employing mostly steel, some problems found in silica VIPs can be overcome, such as easy puncturing of the foil, delamination, moisture problems and pressure increase over time. In addition, these panels can be designed, with a similar analysis as presented, to be self supporting elements with a variety of geometric aspects and could potentially envelop curved facades or other vessels.

Chapter 8

Discussion and Conclusion

8.1 Introduction

The development of vacuum insulating technology for application in the building industry has continued to improve given the increasing demands of building regulations towards near zero carbon construction [194, 7]. However, thermal performance of hollow-core VIPs, which function on the same principles as vacuum glazing or composite VIPs, were never formally investigated and only the work of Nemanic [57] explored the fabrication of this type of technology.

Vacuum insulation works by reducing internal pressure of the insulating layer thus virtually eliminating convective heat transfer [96]. The resulting thermal properties of this type of insulation allow for thinner insulating layers. VIPs provide an efficient solution when insulating the building envelope with reduced impact on usable floor area by comparison to common building materials, such as mineral wool or polyurethane foams.

Hollow-core VIPs is an alternative insulating technology that could provide a

solution to some of the composite VIP's vulnerabilities, such as fragility, pressure increase over time due to water vapor permeation, narrow service temperature range and expensive filling materials [50]. Moreover, the lack of a filling material invites the possibility of altering the panel's thermal performance by use of electrochromic coatings, as has been done in vacuum glazing [73, 75, 76]. However, there is no information on design criteria, thermal performance or even the feasibility of this technology. Therefore, a study on the feasibility, configuration and thermal performance of hollow-core VIPs needs to be addressed.

The overall aim of this study was to develop and evaluate a conceptual prototype of a hollow-core vacuum insulating panel which could also posses the capacity to alternate between a conducting and insulating state, acting as a passive heating/-cooling building element.

8.1.1 The effect of varying model properties on thermal performance

Panel composition and dimensions will affect the panel's thermal resistance. Simulations were conducted on a simplified model of a hollow-core VIP to identify vulnerabilities and the most suitable channel for heat transfer manipulation. Results from initial numerical evaluation indicate hollow-core VIPs are highly sensitive to emissivity and gas pressure, but could achieve thermal conductance values lower than 0.2 $\frac{W}{m^2K}$.

Dimensions of the panel are closely linked to the necessary pressure to suppress convection by keeping the flow type in the free molecular flow regime [46]. Results indicate that panel thickness greater than $0.05m$ require pressure lower than

0.01 Pa to suppress gaseous conduction. However, while thinner panels eliminate gaseous conduction at higher pressure ($0.01Pa$), these are more vulnerable to pressure leaks, and even slight increases in pressure ($+0.04Pa$) will increase the thermal conductivity of the rarefied gas by a factor of 10. When sufficient levels of high vacuum are reached and gaseous conduction is virtually eliminated and effects of gas composition become negligible, consequently, the application of gases with lower thermal conductivity than air are not justified. The performance difference between air and Argon is below 2% at a pressure of 0.01Pa. However, at a pressure of 1Pa, where the flow has reached a slip-flow regime the difference in thermal performance between air and Argon ranges between 20% to 30% depending on panel thickness. Likewise, the difference in thermal conductance between air and Hydrogen at a pressure of 0.01Pa is negligible but increases by a factor of 5 with an internal pressure of 1Pa. Although altering pressure to control the panel's thermal conductance is an intriguing idea, and has been previously proposed by use of metal hydrides, the re-adsorption process is much slower than the hydrogen release process and requires cooling down the metal [118], which would add a delayed response to environmental conditions in addition to added complexities of incorporating the metal and its electrical components and the diffusion of the gas through the internal structure of the panel.

In addition to pressure, emissivity also has a dominant role in the overall thermal conductance of the panel. Emissivity as low as 0.07 will still have a greater effect than gaseous conduction on thermal transfer when internal gas flow is in the free molecular flow regime. High emissivity (0.8) becomes the dominant heat transfer mechanism, even when gas pressure has increased substantially and the gas is in the slip flow regime. Increasing the pressure from 0.01 Pa to 10Pa will increase

overall heat flux by a factor of 10 in a low-emissivity environment, but will only increase it by 78% in a high emissivity environment. The noticeable impact of emissivity on overall thermal conductance indicates that altering surface emissivity is the best solution towards achieving a VIP with a conductive and insulating state. Electrochromic coatings such as Nickel Oxide (NiO) and Tungsten Oxide (TiO_3) films could alter the panel's internal emissivity between 0.057 and 0.595 at the temperature range found in most building applications [124, 123, 158], potentially allowing for a thermal conductance range between 0.2 and 5 $\frac{W}{m^2K}$. Thermochromic films are discouraged from use in this type of panel since these the greatest change in emissivity is exhibited by a temperature change from 100 to 300 K, well below the expected temperature in building applications. The expected change in emissivity when temperatures changes from 250 to 310 K would only be from 0.45 to 0.55 [156], prohibiting the panel's use as an insulator.

8.1.2 Measured and Simulated thermal resistance of hollow core VIP nodes.

While a simple model provided useful information into key parameters affecting the performance of the panel, it is necessary to consider direct and indirect effects of incorporating the structural array supporting the panel. While Nemanic manufactured a hollow-core VIP with an array of staggered glass tubes [57], this study considered an orthogonal array of continuous thin plate elements, similar to a widely spaced grate.

Prototypes were manufactured in three different configurations: "box", "cross", and "box-cross", and in in two different thicknesses 25 and 50mm, to represent

sections of a full sized hollow-core VIP. Samples were manufactured from stainless steel plates, either highly polished or coated with an epoxy resin, to evaluate low and high emissivity configurations. The emissivity of these samples was measured as 0.1 for the polished stainless steel, and 0.9 for the epoxy coated plate. The structural array was manufactured from laser-cut 3mm thick PTFE sheets. These materials were chosen due to their low out-gassing properties, which makes them compatible with high-vacuum environments. The samples were placed inside a vacuum chamber and held by a testing rig that also included temperature distribution plates, platinum resistance temperature sensors, heat flux sensors, and a kapton resistance heater. The tests measured thermal conductance of the sample by rapidly increasing temperature on one side and measuring the rate of change of temperature on the opposite side, this method was proposed by Turner and Collins for measuring evacuated glazing and proved accurate by comparison to tests conducted in a guarded hot plate apparatus [173].

The testing method was calibrated against samples ($3mm$ and $8mm$ thick) of soda-lime glass. Measurements of thermal resistance showed erratic data prior to the rapid temperature increase, as measured values of ΔT and heat flux approached zero and used instrumentation lacked the necessary precision for these measurements of small magnitude. Nonetheless, measurements promptly stabilized and provided accurate data after temperature on the hot side increased.

Measurements agreed with existing theory by showing increased heat flux in high-emissivity scenarios and in areas with structural elements, which were directly affected by solid conduction. It should be noted, that effects of solid conduction were significantly affected by thermal contact conductance, which in these tests was influenced by a layer of Dow Corning high vacuum grease used as thermal

interface. Measurements of "box" samples showed thermal resistance as good as $4.75\frac{m^2K}{W}$ at center-of-sample and under low emissivity conditions. By comparison, high emissivity "box" cases showed a thermal resistance in both 25 and 50mm thick samples of $0.22\frac{m^2K}{W}$, confirming the importance of surface emissivity for either an insulating or conducting state. The lowest thermal resistance, $0.17\frac{m^2K}{W}$, was observed in the edge of the $25mm$ thick high emissivity "box" sample.

Transient simulations were modeled to match the characteristics and conditions of the measured samples, to provide detailed information that couldn't be observed during empiric tests. Simulations were model and performed in OpenFoam, using native components DSMC for molecular dynamics, and chtSimpleFoam for multi-region transient heat transfer. High emissivity cases agree in nominal thermal resistance within 5% of measured samples. Prior to inclusion of system uncertainty, nominal cases in low emissivity configurations showed a difference up to 42% between simulated and measured results. However, the uncertainty of the system was heavily influenced by thermal contact conductance amongst material thermal conductivity and surface emissivity, attaching significant error bars to nominal results. Measured and simulated results overlapped when considering system uncertainty, providing confidence in the testing and simulation methods albeit the considerable effect of uncertainty.

Simulated results complement those of laboratory tests and provide detailed information on heat flux including participation from individual heat transfer mechanisms. Even at a pressure of 0.01 Pa, gaseous conduction still accounted for $\sim 3\%$ of transfered heat in low emissivity configurations. Solid conduction and radiation share similar participation values in low emissivity scenarios in thinner panels. Thicker panel configurations (50mm) reduced solid conduction as expected by added

material resistance, but continued to account for nearly 40% of transfered heat. Similarly, increasing structural array's surface area has a detrimental effect on thermal resistance. Radiative heat transfer was shown to account for $\sim 50\%$ of heat transfered in low emissivity scenarios, and $\sim 90\%$ in high emissivity scenarios. Gathered data indicates that thermal resistance can range between ~ 0.2 to $\sim 6\frac{m^2K}{W}$ when there's no direct contact with the structural array, and from ~ 0.2 to $\sim 2\frac{m^2K}{W}$ near structural elements, considering both low and high emissivity cases.

It was found that thermal contact conductance has a significant effect on the overall performance of the panel, especially over large contact areas and with elements of high thermal conductivity. Effects from poor thermal contact conductance appear compounded when in combination with low-emissivity materials, conversely the detrimental effect of a high conductivity material is limited by poor thermal contact conductance. Observed behavior from measured samples and simulated models indicate that good thermal resistance can be achieved with low emissivity found in polished stainless steel plates and within a high-vacuum (0.01Pa) environment. However, solid conduction becomes the greatest concern even with low thermal conductivity materials such as PTFE.

8.1.3 Design constraints and performance of the hollow core VIP

It follows that design of the hollow-core VIP must balance competing requirements, structural and thermal. Plate deflection, array buckling and array thermal conductance are combined to establish limitations in the configuration of hollow-core VIPs.

The structural array was limited to a maximum thermal conductance of 0.1 $\frac{W}{m^2K}$ in an attempt to yield a maximum thermal conductance of the panel of 0.3 $\frac{W}{m^2K}$, considering that previous measurements indicated that solid conduction was accountable for 40-60 % of total heat transfered. Including participation from the foil sealing the vacuum at the edges puts an additional limitation on the design of hollow-core VIPs and stimulates the design of larger panels that mitigate participation of the edge over a large surface area. Expressing the thermal conductance of the solid array as a function of panel thickness and array separation, while including participation of the edge foil, results in a quadratic equation used to plot "safe" combinations of panel thickness and array separation that fall below a thermal conductance of 0.1 $\frac{W}{m^2K}$. It was found that PTFE, albeit having a thermal conductivity of 0.25 $\frac{W}{mK}$, requires a separation between array elements larger than 0.5m, and with a panel thickness larger 0.06m to achieve the desired performance.

The second design constraint, maximum tolerated compressive stress of the structural array, was defined as the critical buckling load of the array defined by plate theory. The tolerated dimensions for the array were obtained by rewriting the formula for maximum tolerated load in elastic buckling of plates as a function of panel thickness and array separation, and with a compressive stress defined as ambient pressure. It becomes evident that the poor mechanical properties of PTFE require a panel thickness less than 0.06m and with an array separation less than 0.2m.

The third design constraint, deflection of the face plates, was also defined according to plate theory. Maximum plate deflection was established according to Eurocodes standards for suspended ceilings, 1/200 of the span distance. Nonetheless, maximum deflection can be adjusted to fit surface coating limitations or other criteria. This equation can also be re-written in function of array separation; this

criteria is independent of panel thickness. Stiffening of the face plates is considered by incorporating a series of repeating arches tied together by the plate sealing the vacuum, and thus the limiting dimensions are evaluated by longitudinal deflection of a contiguous arch (a vault-like element).

Combination of all three design constraints yields the allowable or "safe" combination of panel thickness and array separation values to obtain an estimated thermal conductance of $0.1\frac{W}{m^2K}$. From this it was found that an array composed of 3mm thick PTFE was unable to achieve a thermal conductance below 0.1 $\frac{W}{m^2K}$ while remaining structurally sound and within elastic limits. However, using this analysis method, it is theoretically possible to achieve the desired thermal conductance with a 1mm thick stainless steel array, if the ends of the array are rounded off to reduce contact area. According to Hertz equation for non conforming cylinders [190], the hardness of stainless steel would result in a reduced contact area under the compressive load from ambient pressure and the structural array could achieve lower thermal conductance even though its thermal conductivity is much higher than PTFE.

From this analysis a panel measuring 1.2m wide and 2.4m long was configured using a stainless steel array and its performance simulated in order to evaluate sensitivity to pressure increase and effective thermal conductivity range if an electrochromic coating was included. In these conditions solid conduction through the edges remains the biggest weakness, and the 100 μm thick edge foil transfer as much heat as the entire structural array. The best simulated performance resulted in a thermal conductance of 0.36 $\frac{W}{m^2K}$ and an overall thermal conductivity of 0.017 $\frac{W}{mK}$, which is better than common insulating materials but not as good as aerogel or composite VIPs. Since the effect from the edge foil is great, the difference between the PTFE and stainless steel array is narrowed. The 3mm PTFE array resulted

in an overall panel's thermal conductance of 0.51 $\frac{W}{m^2K}$ with an effective thermal conductivity of 0.023 $\frac{W}{mK}$.

From these simulations it was also found that increasing the internal gas pressure from 0.01 Pa to 0.1 Pa increased the thermal conductivity by nearly 20%, matching the thermal conductivity of PUR-PIR insulating materials. Considering an electrochromic material with an emissivity range between 0.057 and 0.595 [124] resulted in an estimated thermal conductance range from 0.36 to 2.6 $\frac{W}{m^2K}$.

The estimated thermal conductance range is very promising showing that hollow-core VIPs can be configured to have good insulating properties with a conductive state capable of heat transfer comparable to certain types of glazing. Inclusion of variable emissivity mechanisms can alter the overall thermal conductance of the panel by a factor of 4, suggesting that this technology could be applied to large areas of the facade as a practically passive heating or cooling solution.

8.1.4 Challenges of hollow-core VIPs in building applications

Although promising, this insulating solution must address certain key aspects before becoming commercially available. Given the relatively unexplored state of the technology many things need to be improved. Nonetheless, the two main issues that need to be studied are manufacturing processes and production cost. Manufacturing processes, such as welding of the edge foil, fixing the structural array in place, panel evacuation and coating of the interior surfaces need to be studied and optimized for a large scale production of this type of technology. Prior to the manufacturing process, material selection is of extreme importance and is restricted to materials

compatible with a high-vacuum and that are mechanically strong. A cost analysis could not be extrapolated from the samples produced for laboratory measurements since these considered different materials, differed in manufacturing process and did not include the edge-foil sealing the vacuum.

8.2 Limitations

The research presented in this study encountered limitations that could have had potential impact on the findings presented and on the project's development. Regarding project design, available facilities and equipment was the most important limitation. Most of the equipment used, together with the clean room hosting the vacuum chamber needed to be manufactured and required months of intense labour. Large uncertainty bands resulted from lack of precision equipment to assist in measuring surface roughness, contact pressure, thickness of the grease layer, and similar characteristics that influence heat transfer in the system. Furthermore, funding limitations only allowed for purchase of the most necessary equipment such as the vacuum chamber and pumping system. Some measuring equipment, such as fast response heat flux sensors, chilling plate and chilling system could not be purchased. Moreover, the experimental data could have benefitted from tests including additional high performance materials such as titanium alloys and thermochromic coatings.

Another important limitation was time constraint. In addition to the time spent manufacturing the equipment and clean room, each test conducted in the vacuum chamber required over 4 hours of measurable data plus preparation time, restricting empirical tests to one per day on most occasions. Failure to achieve or maintain a

high-vacuum (chamber or pump failure is suspected) was encountered often, requiring a complete repetition of the test run. This limited the amount of permutations allowed. The facilities were also required by other researchers in the department and could not be occupied solely on this project.

Computational resources were another important limitation, as simulations are computationally expensive and would take days to conclude with the available resources. Every transient simulation would require more than 24 hrs to conclude for one hour of simulated performance. Although steady simulations were faster, the several hundreds of cases required for the uncertainty analysis took weeks to conclude. Mesh definition and meshing algorithms were limited to the minimum number of cells provided results were independent from grid size and regular hexahedral cells. Similarly, performance of the rarefied gas was simulated with pressure levels at discrete intervals separated by a factor of 10, smaller intervals could provide information with greater detail into the rate of change of the gas' thermal performance. Moreover, the modeling approach was limited in its transient behaviour as molecular dynamics had to be solved separate from the rest of the model, neglecting any feedback during a transient process affecting gas pressure.

Added to this, the initial experimental aims and objectives were broad, which lead to necessary preliminary investigation of dynamic change between insulating and conducting states to select which insulating solution was better suited for altering its thermal conductance; this led to hollow-core VIPs. Moreover, the scope of the project had to be adapted to available resources.

As described in Chapter 1, the overall aim of this research project was to conceptually develop and evaluate an insulating panel prototype capable of switching between a conducting and insulating state. Despite the aforementioned limitation, the

research here presented demonstrates the feasibility of such technology and presents its estimated performance.

8.3 Future Work

The research here presented suggests that hollow-core VIPs has potential application as a cladding element for the building industry. To further develop the technology studied here, there are some areas where future work would be greatly beneficial into leading this technology into a commercial product, while providing a more complete understanding of its characteristics, performance and limitations.

As a simulation of conditions found in VIPs, this research explored behavior of the internal vacuum by containing the entire sample in a vacuum chamber. Future work could benefit from testing a self-contained sample.

The following list presents a suggestion of areas that could further knowledge on this topic.

- Study and develop sealing and evacuation techniques, including but not exclusive to the welding of the edge foil and evacuation valve. Moreover, evaluate longevity and permeation rate of different seals;

- Study thermal conductance and its rate of change, of samples with electrochromic and selective coatings as found in solar collectors;

- Manufacture and measure thermal conductance of a stainless steel array with rounded off edges. Study how values agree with the calculated performance of non-conforming elastic solids;

- Measure thermal contact resistance in-vacuo between materials compatible with a high vacuum environment with a compressive load equal to ambient pressure and in temperature range between 275 and 320 K;
- Evaluate the structural array for response to torsion, thermal expansion and external stresses such as wind loading;
- Explore hollow-core VIPs integration to the facade or structure.

The inclusion of precision manufacturing and measuring equipment could enhance sample diversity and improve uncertainty in the system. Even though this work focused on a single structural array configuration, the method here proposed could be implemented for alternative structural solutions and even alternative applications for this technology.

Considering that this research was limited by material availability, manufacturing equipment, and computational resources it is could be greatly beneficial if further investigation is conducted under similar conditions but incorporating additional materials, such as titanium alloys, acetal and thermochromic coatings to broaden the wealth of knowledge. Simulation models can be improved by meshes with greater definition and produced with different meshing algorithms. Similarly, while a first order time scheme provided accurate results it could be useful to include a second order time scheme, especially when high conductivity materials are being used in contact with low conductivity materials. Finally, further research into creating a solver that is capable of simultaneously solving for molecular dynamics of the rarefied gas and macroscopic heat transfer of the regions with which it comes into contact, could provide a truly transient method usable for hollow-core VIPs and similar applications, and could predict performance of a deteriorating vacuum.

8.4 Conclusion

In conclusion, this study reports that hollow-core VIPs can be designed to outperform common insulating materials, but fail to achieve the insulating performance of aerogel or fumed silica VIPs. However, due to their robust composition consisting mainly of steel, hollow-core VIPs can overcome problems found in composite VIPs such as fragility of the envelope, foil de-lamination, and pressure increase over time.

The objectives presented at the beginning of this project were successfully met. Panel thickness, gas pressure, surface emissivity and thermal contact conductance were identified as key parameters influencing thermal performance of hollow-core VIPs, and their participation was quantified through transient simulations whose results match those of laboratory tests but provide detailed information. Two key parameters in structural performance were studied, elastic buckling of the internal structure and elastic bending of the envelope of the panel. The combination of competing requirements, structural and thermal, was studied to provide functional configurations for this type of panel, which resulted in limited options for PTFE structures but suggested that a stainless steel structure with limited contact area could outperform PTFE solutions. Nonetheless, further simulations of full-sized panels configured according to structural and thermal requirements indicated that solid conduction through the envelope was severe enough to narrow the gap in thermal performance between PTFE and stainless steel structures, and remains as the most limiting factor in this type of insulating panel. Simulations of full sized panels resulted in an effective thermal conductivity of $0.017\frac{W}{mK}$ for a panel with a stainless steel structure, and $0.023\frac{W}{mK}$ for a panel with a PTFE structure, providing a slight advantage over common insulating materials but short of the expected performance

from super insulating materials like aerogel. Consequently, although the hollow-core VIP can function as an insulating cladding element it still faces limitations such as very low internal emissivity requirements, reduced contact area, vacuum contamination through leaks or out-gassing, and limited material compatibility.

Beyond adequate insulating performance, hollow-core VIPs can increase their thermal conductance to act as a nearly passive space conditioning element by incorporating electrochromic coatings. Moreover, by extending the methods presented in this study, these panels could be designed to be self-supporting elements of alternative geometric configuration, potentially covering curved or irregular facades or other vessels and extending their application beyond the building industry.

References

[1] U.S. Energy Information Administration, "International Energy Outlook 2017," Tech. Rep., 2017.

[2] L. Pérez-Lombard, J. Ortiz, and C. Pout, "A review on buildings energy consumption information," *Energy and Buildings*, vol. 40, no. 3, pp. 394–398, 2008.

[3] UN General Assembly, "United Nations Framework Convention on Climate Change," 1992.

[4] ——, "Kyoto Protocol to the United Nations Framework Convention on Climate Change," 1997.

[5] Commission of the European Communities, "20 20 by 2020. Europe's Climate Change Opportunity," Brussels, 2008.

[6] J. Adamczyk and R. Dylewski, "The impact of thermal insulation investments on sustainability in the construction sector," *Renewable and Sustainable Energy Reviews*, vol. 80, pp. 421–429, 2017. [Online]. Available: http://www.sciencedirect.com/science/article/pii/S1364032117308031

[7] The European Parliament and The Council of The European Union, "Directive (EU) 2018/844 of the European Parliament and of the Council of 30 May 2018 amending Directive 2010/31/EU on the energy performance of buildings and Directive 2012/27/EU on energy efficiency," 2018. [Online]. Available: https://eur-lex.europa.eu/legal-content/EN/TXT/?uri=uriserv{\%}3AOJ.L{_}.2018.156.01.0075.01.ENG

[8] Department for Communities and Local Government, "Code for Sustainable Homes: A Step-change in Sustainable Home Building Practice," Wetherby, 2006.

[9] BRE, "The Government's Standard Assessment Procedure for Energy Rating of Dwellings - 2012 edition, version 9.92," no. June, p. 234, 2013.

[10] HM Government, "L1A - Conservation of fuel and power in new dwellings," 2016.

[11] U. S. G. B. Council, *LEED Reference Guide for Building Design and Construction*. U.S. Green Building Council, 2013, no. v. 4. [Online]. Available: https://books.google.co.uk/books?id=jvxGngEACAAJ

[12] A. M. Papadopoulos, "State of the art in thermal insulation materials and aims for future developments," *Energy and Buildings*, vol. 37, no. 1, pp. 77–86, 2005.

[13] MAG HARD INSULATORS, "Glass Wool," 2019. [Online]. Available: http://maghardinsulators.com/glasswool.php

[14] PERFORMANCE BUILDING SUPPLY, "PolarGuard EPS Foam Board," 2019. [Online]. Available: https://performancebuildingsupply.com/product/polarguard/

[15] KINGSPAN, "Thermafloor - TF70," 2019. [Online]. Available: https://www.kingspan.com/meati/en-in/product-groups/insulation/insulation-boards/therma/thermafloor-tf70

[16] W. Villasmil, L. J. Fischer, and J. Worlitschek, "A review and evaluation of thermal insulation materials and methods for thermal energy storage systems," *Renewable and Sustainable Energy Reviews*, vol. 103, no. December 2018, pp. 71–84, 2019. [Online]. Available: https://doi.org/10.1016/j.rser.2018.12.040

[17] H. R. Kymäläinen and A. M. Sjöberg, "Flax and hemp fibres as raw materials for thermal insulations," *Building and Environment*, vol. 43, no. 7, pp. 1261–1269, 2008.

[18] Insulation Shop Limited, "Glass Wool Insulation," 2019. [Online]. Available: https://www.insulationshop.co/glass{_}and{_}mineral{_}wool{_}insulation/glass{_}wool{_}insulation.html

[19] ——, "Rock Wool Insulation," 2019. [Online]. Available: https://www.insulationshop.co/glass{_}and{_}mineral{_}wool{_}insulation/rock{_}wool{_}insulation.html

[20] M. Kayfeci, "Determination of energy saving and optimum insulation thicknesses of the heating piping systems for different insulation materials," *Energy and Buildings*, vol. 69, pp. 278–284, 2014. [Online]. Available: http://dx.doi.org/10.1016/j.enbuild.2013.11.017

[21] Insulation Shop Limited, "EPS insulation," 2019. [Online]. Available: https://www.insulationshop.co/100mm{_}polystyrene{_}insulation{_}eps{_}70.html

[22] Insulation Superstore, "XPS insulation," 2019. [Online]. Available: https://www.insulationsuperstore.co.uk/product/kingspan-greenguard-gg300-r-rigid-extruded-polystyrene-100mm-3m2.html

[23] B. P. Jelle, "Traditional, state-of-the-art and future thermal building insulation materials and solutions - Properties, requirements and possibilities," *Energy and Buildings*, vol. 43, no. 10, pp. 2549–2563, 2011.

[24] Insulation Superstore, "PIR insulation," 2019. [Online]. Available: https://www.insulationsuperstore.co.uk/product/celotex-ga4100-zero-odp-rigid-insulation-board-100mm-x-1200mm-x-2400mm.html

[25] R. Baetens, B. P. Jelle, and A. Gustavsen, "Aerogel insulation for building applications: A state-of-the-art review," *Energy and Buildings*, vol. 43, no. 4, pp. 761–769, 2011. [Online]. Available: http://dx.doi.org/10.1016/j.enbuild.2010.12.012

[26] Passivhaus Store, "Spacetherm blanket," 2019. [Online]. Available: https://www.phstore.co.uk/aerogel-spacetherm-blanket

[27] S. E. Kalnæs and B. P. Jelle, "Vacuum insulation panel products: A state-of-the-art review and future research pathways," *Applied Energy*, vol. 116, no. 7465, pp. 355–375, 2014.

[28] Vacutherm Ltd, "Vacuum Insulated Panels - Products," 2019. [Online]. Available: http://www.vacuum-panels.co.uk/vacupor-products/

[29] T. L. Bergman, F. P. Incropera, D. P. Dewitt, and A. S. Lavine, *Fundamentals of Heat and Mass Transfer*, 7th ed. Wiley, 2011.

[30] E. Cuce, P. M. Cuce, C. J. Wood, and S. B. Riffat, "Toward aerogel based thermal superinsulation in buildings: A comprehensive review," *Renewable and Sustainable Energy Reviews*, vol. 34, pp. 273–299, 2014. [Online]. Available: http://dx.doi.org/10.1016/j.rser.2014.03.017

[31] M. Ozel, "Cost analysis for optimum thicknesses and environmental impacts of different insulation materials," *Energy and Buildings*, vol. 49, pp. 552–559, 2012. [Online]. Available: http://dx.doi.org/10.1016/j.enbuild.2012.03.002

[32] T. King, "The history of the Building Regulations and where we are now," in *HBF Technical Conference: The road to zero carbon is paved with Building Regulations*, 2007.

[33] NHBC Foundation, *Homes through the decades. The making of modern housing.* Milton Keynes: NHBC Foundation, 2015. [Online]. Available: http://www.nhbc.co.uk/cms/publish/consumer/NewsandComment/HomesThroughTheDecades.pdf

[34] N. Stern, *The Economics of Climate Change: The Stern Review.* Cambridge University Press, 2007.

[35] HM Government, "Innovate UK funding competition winners 2018," 2018. [Online]. Available: https://www.gov.uk/government/publications/innovate-uk-funding-competition-winners-2018

[36] R. Baetens, B. P. Jelle, J. V. Thue, M. J. Tenpierik, S. Grynning, S. Uvsløkk, and A. Gustavsen, "Vacuum insulation panels for building applications: A review and beyond," *Energy and Buildings*, vol. 42, no. 2, pp. 147–172, 2010.

[37] A. Miros, B. Psiuk, and B. Szpikowska-Sroka, "Aerogel insulation materials for industrial installation: properties and structure of new factory-made products," *Journal of Sol-Gel Science and Technology*, vol. 84, no. 3, pp. 496–506, dec 2017. [Online]. Available: https://doi.org/10.1007/s10971-017-4539-0

[38] S. B. Riffat and G. Qiu, "A review of state-of-the-art aerogel applications in buildings," *International Journal of Low-Carbon Technologies*, vol. 8, no. 1, pp. 1–6, 2013.

[39] S. R. Hostler, A. R. Abramson, M. D. Gawryla, S. A. Bandi, and D. A. Schiraldi, "Thermal conductivity of a clay-based aerogel," *International Journal of Heat and Mass Transfer*, vol. 52, no. 3-4, pp. 665–669, 2009. [Online]. Available: http://dx.doi.org/10.1016/j.ijheatmasstransfer.2008.07.002

[40] J. M. Schultz, K. I. Jensen, and F. H. Kristiansen, "Super insulating aerogel glazing," *Solar Energy Materials and Solar Cells*, vol. 89, no. 2-3, pp. 275–285, 2005.

[41] J. M. Schultz and K. I. Jensen, "Evacuated aerogel glazings," *Vacuum*, vol. 82, no. 7, pp. 723–729, 2008.

[42] NASA, "Nano-Encapsulated Aerogel," 2019. [Online]. Available: https://technology.nasa.gov/patent/MSC-TOPS-50

[43] KINGSPAN, "What is a Vacuum Insulation Panel?" 2019. [Online]. Available: https://www.kingspan.com/meati/en-in/product-groups/insulation/knowledge-base/articles/general/what-is-a-vacuum-insulation-panel

[44] J. Fricke, U. Heinemann, and H. P. Ebert, "Vacuum insulation panels—From research to market," *Vacuum*, vol. 82, no. 7, pp. 680–690, 2008.

[45] F. Zoller, "Hollow pane of glass," 1924.

[46] G. Bird, *Moelcular Gas Dynamics and the Direct Simulation of Gas Flows*. Oxford University Press, 1994.

[47] R. E. Collins and T. M. Simko, "Current status of the science and technology of vacuum glazing," *Solar Energy*, vol. 62, no. 3, pp. 189–213, 1998.

[48] Y. Fang, T. J. Hyde, F. Arya, N. Hewitt, P. C. Eames, B. Norton, and S. Miller, "Indium alloy-sealed vacuum glazing development and context," *Renewable and Sustainable Energy Reviews*, vol. 37, pp. 480–501, 2014. [Online]. Available: http://dx.doi.org/10.1016/j.rser.2014.05.029

[49] J.-S. Kwon, C. H. Jang, H. Jung, and T.-H. Song, "Effective thermal conductivity of various filling materials for vacuum insulation panels," *International Journal of Heat and Mass Transfer*, vol. 52, no. 23-24, pp. 5525–5532, 2009.

[50] M. Alam, H. Singh, and M. C. Limbachiya, "Vacuum insulation panels (vips) for building construction industry - a review of the contemporary developments

and future directions," *Applied Energy*, vol. 88, no. 11, pp. 3592–3602, 2011. [Online]. Available: http://dx.doi.org/10.1016/j.apenergy.2011.04.040

[51] Z. Chen, Z. Chen, Z. Yang, J. Hu, Y. Yang, L. Chang, L. J. Lee, and T. Xu, "Preparation and characterization of vacuum insulation panels with super-stratified glass fiber core material," *Energy*, vol. 93, pp. 945–954, 2015.

[52] R. Caps, U. Heinemann, M. Ehrmanntraut, and J. Fricke, "Evacuated insulation panels filled with pyrogenic silica powders: properties and applications," *High Temperatures-High Pressures*, vol. 33, no. 2, pp. 151–156, 2001.

[53] J. Fricke, "Materials research for the optimization of thermal insulations," *High Temperatures - High Pressures*, vol. 25, no. 4, pp. 379–390, 1993.

[54] C. Huang, Z. Lin, Y. Feng, X. Zhang, and G. Wang, "Thermal conductivity of silica nanoparticle powder: Measurement and theoretical analysis," *The European Physical Journal Plus*, vol. 130, no. 12, p. 239, 2015. [Online]. Available: http://link.springer.com/10.1140/epjp/i2015-15239-5

[55] K. Ghazi Wakili, T. Stahl, and S. Brunner, "Effective thermal conductivity of a staggered double layer of vacuum insulation panels," *Energy and Buildings*, vol. 43, no. 6, pp. 1241–1246, 2011.

[56] R. Gellert, "8 - Inorganic mineral materials for insulation in buildings," in *Materials for Energy Efficiency and Thermal Comfort in Buildings*, ser. Woodhead Publishing Series in Energy, M. R. Hall, Ed. Woodhead Publishing, 2010, pp. 193–228. [Online]. Available: http://www.sciencedirect.com/science/article/pii/B9781845695262500086

[57] V. Nemanic, "Vacuum insulating panel," *Vacuum*, vol. 46, pp. 839–842, 1995.

[58] M. Pfundstein, R. Gellert, A. Rudolphi, and M. Spitzner, *Insulating Materials: Principles, Materials, Applications*, ser. Detail practice. Edition Detail, 2008. [Online]. Available: https://books.google.com.mx/books?id=bG1MPgAACAAJ

[59] H. Zhang, W.-Z. Fang, Y. Li, and W.-Q. Tao, "Experimental study of the thermal conductivity of polyurethane foams," *Applied Thermal Engineering*, vol. 115, 2017.

[60] M. S. Al-Homoud, "Performance characteristics and practical applications of common building thermal insulation materials," *Building and Environment*, vol. 40, no. 3, pp. 353–366, 2005.

[61] I. Gnip, S. Vejelis, and S. Vaitkus, "Thermal conductivity of expanded polystyrene (EPS) at 10 degC and its conversion to temperatures within interval from 0 to 50 degC," *Energy and Buildings*, vol. 52, pp. 107–111, 2012.

[62] F. Domínguez-Muñoz, B. Anderson, J. M. Cejudo-López, and A. Carrillo-Andrés, "Uncertainty in the thermal conductivity of insulation materials," *Energy and Buildings*, vol. 42, no. 11, pp. 2159–2168, 2010.

[63] Knauf Insulation, "Rock Wool Insulation," 2019. [Online]. Available: https://www.knaufinsulation.co.uk/products/rock-mineral-wool/earthwool-building-slab-rs100

[64] Danosa, "XPS Danopren Insulation," 2019. [Online]. Available: https://portal.danosa.com/danosa/CMSServlet?node=T32{\&}lng=6{\&}site=6

[65] M. Modesti and A. Lorenzetti, "Improvement on fire behaviour of water blown PIR-PUR foams: Use of an halogen-free flame retardant," *European Polymer Journal*, vol. 39, no. 2, pp. 263–268, 2003.

[66] J. M. Lafferty, *Foundations of vacuum science and technology*. Wiley, 1998.

[67] S. Dortmund and H. O, "Patentschrift Nr. 516377," 1930.

[68] M. J. Tenpierik, J. J. M. Cauberg, and T. I. Thorsell, "Integrating vacuum insulation panels in building constructions: an integral perspective," *Construction Innovation*, vol. 7, no. 1, pp. 38–53, 2007.

[69] D. K. Benson and C. E. Tracy, "Evacuated Window Glazings for Energy Efficient Buildings," 1985.

[70] R. E. Collins and S. J. Robinson, "Evacuated glazing," *Solar Energy*, vol. 47, no. 1, pp. 27–38, 1991.

[71] R. Corruccini, "Gaseous heat conduction at low pressures and temperatures," *Vacuum*, vol. 7-8, pp. 19–29, 1957.

[72] J. P. Holman, *Heat transfer*, 7th ed. McGraw-Hill, 1989. [Online]. Available: https://books.google.co.uk/books/about/Heat{_}transfer.html?id=zCXxKEfI1gEC{\&}pgis=1

[73] Y. Fang, P. C. Eames, B. Norton, and T. J. Hyde, "Experimental validation of a numerical model for heat transfer in vacuum glazing," *Solar Energy*, vol. 80, no. 5, pp. 564–577, 2006.

[74] Y. Fang, P. C. Eames, B. Norton, T. Hyde, Y. Huang, and N. Hewitt, "The thermal performance of an electrochromic vacuum glazing with selected low-emittance coatings," *Thin Solid Films*, vol. 516, no. 6, pp. 1074–1081, 2008.

[75] Y. Fang and P. C. Eames, "Thermal performance of an electrochromic vacuum glazing," *Energy Conversion and Management*, vol. 47, no. 20, pp. 3602–3610, 2006.

[76] S. Papaefthimiou, G. Leftheriotis, P. Yianoulis, T. J. Hyde, P. C. Eames, Y. Fang, P. Y. Pennarun, and P. Jannasch, "Development of electrochromic evacuated advanced glazing," *Energy and Buildings*, vol. 38, no. 12, pp. 1455–1467, 2006.

[77] Y. Fang, P. C. Eames, B. Norton, T. J. Hyde, J. Zhao, J. Wang, and Y. Huang, "Low emittance coatings and the thermal performance of vacuum glazing," *Solar Energy*, vol. 81, no. 1, pp. 8–12, 2007.

[78] R. Collins and A. Fischer-Cripps, "Design of Support Pillar Arrays in Flat Evacuated Windows," *Australian Journal of Physics*, vol. 44, no. 5, p. 545, 1991.

[79] C. F. Wilson, T. M. Simko, and R. E. Collins, "Heat conduction through the support pillars in vacuum glazing," *Solar Energy*, vol. 63, no. 6, pp. 393–406, 1998.

[80] G. Colangelo, E. Favale, P. Miglietta, and A. De Risi, "Innovation in flat solar thermal collectors: A review of the last ten years experimental results," *Renewable and Sustainable Energy Reviews*, vol. 57, pp. 1141–1159, 2016. [Online]. Available: http://dx.doi.org/10.1016/j.rser.2015.12.142

[81] S. Suman, M. K. Khan, and M. Pathak, "Performance enhancement of solar collectors - A review," *Renewable and Sustainable Energy Reviews*, vol. 49, pp. 192–210, 2015. [Online]. Available: http://dx.doi.org/10.1016/j.rser.2015.04.087

[82] N. Ehrmann and R. Reineke-Koch, "Selectively coated high efficiency glazing for solar-thermal flat-plate collectors," *Thin Solid Films*, vol. 520, no. 12, pp. 4214–4218, 2012. [Online]. Available: http://www.sciencedirect.com/science/article/pii/S0040609011009102

[83] A. Fernández and J. A. Dieste, "Low and medium temperature solar thermal collector based in innovative materials and improved heat exchange performance," *Energy Conversion and Management*, vol. 75, pp. 118–129, 2013. [Online]. Available: http://www.sciencedirect.com/science/article/pii/S0196890413003129

[84] M. Reim, W. Körner, J. Manara, S. Korder, M. Arduini-Schuster, H.-P. Ebert, and J. Fricke, "Silica aerogel granulate material for thermal insulation and daylighting," *Solar Energy*, vol. 79, no. 2, pp. 131–139, 2005. [Online]. Available: http://www.sciencedirect.com/science/article/pii/S0038092X05001301

[85] Y. Xuan and Q. Li, "Heat transfer enhancement of nanofluids," *International Journal of Heat and Fluid Flow*, vol. 21, no. 1, pp. 58–64, 2000. [Online]. Available: http://www.sciencedirect.com/science/article/pii/S0142727X99000673

[86] L. Cindrella, "The real utility ranges of the solar selective coatings," *Solar Energy Materials and Solar Cells*, vol. 91, no. 20, pp. 1898–1901, 2007. [Online]. Available: http://www.sciencedirect.com/science/article/pii/S0927024807002784

[87] R. Moss, S. Shire, P. Henshall, F. Arya, P. Eames, and T. Hyde, "Performance of evacuated flat plate solar thermal collectors," *Thermal Science and Engineering Progress*, vol. 8, no. September, pp. 296–306, 2018. [Online]. Available: https://doi.org/10.1016/j.tsep.2018.09.003

[88] K. Chopra, V. V. Tyagi, A. K. Pandey, and A. Sari, "Global advancement on experimental and thermal analysis of evacuated tube collector with and without heat pipe systems and possible applications," *Applied Energy*, vol. 228, pp. 351–389, 2018. [Online]. Available: http://www.sciencedirect.com/science/article/pii/S030626191830936X

[89] TVP Solar, "MT-30 datasheet." [Online]. Available: http://www.tvpsolar.com/files/pagine/{\%}0A1464011780{_}MT-PowerDatasheet(v4.2x)(ver5).pdf{\%}3E(

[90] F. Kreith, R. M. Manglik, and M. Bohn, *Principles of heat transfer*, 7th ed. Stamford, CT, USA: Christopher M. Shortt, 2011.

[91] M. G. Kaganer, *Thermal insulation in cryogenic engineering.* Jerusalem: Israel Program for Scientific Translations, 1969. [Online]. Available: http://cds.cern.ch/record/103864

[92] E. Placido, M. C. Arduini-Schuster, and J. Kuhn, "Thermal properties predictive model for insulating foams," *Infrared Physics & Technology*, vol. 46, no. 3, pp. 219–231, 2005.

[93] C. K. Chan and C. L. Tien, "Conductance of Packed Spheres in Vacuum," *Journal of Heat Transfer*, vol. 95, no. 3, p. 302, 1973.

[94] J. Fricke, D. Büttner, R. Caps, J. Gross, and O. Nilsson, "Solid Conductivity of Loaded Fibrous Insulation," in *Insulation Materials, Testing and Applications*, D. McElroy and J. Kimpflen, Eds. 100 Barr Harbor Drive, PO Box C700, West Conshohocken, PA 19428-2959: ASTM International, jan 1990, pp. 66–78.

[95] M. A. Schuetz and L. R. Glicksman, "A Basic Study of Heat Transfer Through Foam Insulation," *Journal of Cellular Plastics*, vol. 20, no. 2, pp. 114–121, 1984. [Online]. Available: https://doi.org/10.1177/0021955X8402000203

[96] J. Fricke, H. Schwab, and U. Heinemann, "Vacuum Insulation Panels – Exciting Thermal Properties and Most Challenging Applications," *International Journal of Thermophysics*, vol. 27, no. 4, pp. 1123–1139, jul 2006. [Online]. Available: https://doi.org/10.1007/s10765-006-0106-6

[97] R. Mathes, J. Blumenberg, and K. Keller, "Radiative heat transfer in insulations with random fibre orientation," *International Journal of Heat and Mass Transfer*, vol. 33, no. 4, pp. 767–770, 1990. [Online]. Available: http://www.sciencedirect.com/science/article/pii/001793109090174S

[98] R. Caps and J. Fricke, "Thermal conductivity of opacified powder filler materials for vacuum insulations," *International Journal of Thermophysics*, vol. 21, no. 2, pp. 445–452, 2000.

[99] J. Kuhn, H.-P. Ebert, M. C. Arduini-Schuster, D. Büttner, and J. Fricke, "Thermal transport in polystyrene and polyurethane foam insulations," *International Journal of Heat and Mass Transfer*, vol. 35, no. 7, pp. 1795–1801, 1992. [Online]. Available: http://www.sciencedirect.com/science/article/pii/001793109290150Q

[100] C. Sprengard and A. H. Holm, "Numerical examination of thermal bridging effects at the edges of vacuum-insulation-panels (VIP) in various constructions," *Energy and Buildings*, vol. 85, pp. 638–643, 2014. [Online]. Available: http://dx.doi.org/10.1016/j.enbuild.2014.03.027

[101] S. Treml, M. Engelhardt, C. Sprengard, and W. Butko, "Determination of the internal pressure of vacuum insulation panels with the envelope lift-off technique – methods for analysing test data," *Energy and Buildings*, vol. 184, pp. 44–52, 2019. [Online]. Available: https://doi.org/10.1016/j.enbuild.2018.11.027

[102] K. Ghazi Wakili, R. Bundi, and B. Binder, "Effective thermal conductivity of vacuum insulation panels," *Building Research and Information*, vol. 32, no. 4, pp. 293–299, 2004.

[103] H. Noori, M. Jain, K. Nielsen, and F. Brandys, "Delamination in deformed polymer laminated sheet metals," *International Journal of Adhesion and*

Adhesives, vol. 85, no. June, pp. 219–224, 2018. [Online]. Available: https://doi.org/10.1016/j.ijadhadh.2018.06.014

[104] E. Fried, "Study of interface thermal contact conductance," Tech. Rep., 1964.

[105] T. Thomas and S. Probert, "Correlations for thermal contact conductance in vacuo," *Journal of ...*, pp. 141–142, 1972. [Online]. Available: http://heattransfer.asmedigitalcollection.asme.org/article.aspx?articleid=1435361

[106] T. McWaid and E. Marschall, "Thermal contact resistance across pressed metal contacts in a vacuum environment," *International Journal of Heat and Mass Transfer*, vol. 35, no. 11, pp. 2911–2920, 1992.

[107] M. Bloom, "Thermal contact resistance in a vacuum environment," Tech. Rep., 1964. [Online]. Available: http://heattransfer.asmedigitalcollection.asme.org/article.aspx?articleid=1433491

[108] E. H. Kennard, *Kinetic Theory of Gases with and Introduction to Statistical Mechanics*, first edit ed. McGraw-Hill, 1938.

[109] K. Chen, P. Chailapo, W. Chun, S. Kim, and K. Jin Lee, "The Dynamic Behaviour of a Bayonet-Type Thermal Diode," *Solar Energy*, vol. 64, no. 4-6, pp. 257–263, dec 1998.

[110] W. Chun, Y. J. Ko, H. J. Lee, H. Han, J. T. Kim, and K. Chen, "Effects of working fluids on the performance of a bi-directional thermodiode for solar energy utilization in buildings," *Solar Energy*, vol. 83, no. 3, pp. 409–419, 2009.

[111] R. Caps, J. Hetfleisch, and J. Fricke, "Vakuumwärmedämmpaneel," 1999. [Online]. Available: http://www.freepatentsonline.com/DE19647567.html

[112] M. Kimber, W. W. Clark, and L. Schaefer, "Conceptual analysis and design of a partitioned multifunctional smart insulation," *Applied Energy*, vol. 114, pp. 310–319, 2014.

[113] D. Benson and T. Potter, "Radiation-controlled dynamic vacuum insulation," 1995. [Online]. Available: http://google.co.uk/patents/US5433056

[114] H. O. Banks and R. H. Sparks, "Active heat transfer device," 1969. [Online]. Available: http://www.google.ch/patents/US3461954

[115] S. Varga, A. C. Oliveira, and C. F. Afonso, "Characterisation of thermal diode panels for use in the cooling season in buildings," *Energy and Buildings*, vol. 34, no. 3, pp. 227–235, 2002.

[116] T. Pflug, T. E. Kuhn, R. Nörenberg, A. Glück, N. Nestle, and C. Maurer, "Closed translucent façade elements with switchable U-value - A novel option for energy management via the facade," *Energy and Buildings*, vol. 86, pp. 66–73, 2014.

[117] N. Laing and I. Laing, "Variable insulation means utilizing convection generators," jun 1974. [Online]. Available: http://www.google.ch/patents/US3814175

[118] H. P. Bovenkerk, "Insulating structures with variable thermal conductivity and method of evacuation," 1965. [Online]. Available: https://www.google.es/patents/US3167159

[119] R. Horn, R. Neusinger, M. Meister, J. Hetfleisch, R. Caps, and J. Fricke, "Switchable thermal insulation: Results of computer simulations for optimisation in building applications," *High Temperatures - High Pressures*, vol. 32, no. 6, pp. 669–675, 2000.

[120] P. Bauer, "Gas pressure control for varying thermal conductivity," 1969. [Online]. Available: http://www.google.com/patents/US3450196

[121] T. Xenophou, "System of using vacuum for controlling heat transfer in building structures, motor vehicles and the like," 1976. [Online]. Available: http://www.google.com/patents/US3968831

[122] I. F. Chang, "Electrochemichromic Systems for Display Applications," *Journal of The Electrochemical Society*, vol. 122, no. 7, p. 955, 1975. [Online]. Available: http://jes.ecsdl.org/cgi/doi/10.1149/1.2134377

[123] R. J. Mortimer, "Electrochromic materials," *Annual Review of Materials Research*, vol. 41, pp. 241–268, 2011.

[124] J. S. Hale, M. DeVries, B. Dworak, and J. a. Woollam, "Visible and infrared optical constants of electrochromic materials for emissivity modulation applications," *Thin Solid Films*, vol. 313-314, pp. 205–209, 1998.

[125] W. C. Young and R. G. Budynas, *Roark's Formulas for Stress and Strain*, 2002.

[126] S. P. Timoshenko and J. M. Gere, *Theory of Elastic Stability*, second edi ed. McGraw-Hill, 1963.

[127] H. Weller, G. Tabor, H. Jasak, and C. Fureby, "A tensorial approach to computational continuum mechanics using object-oriented techniques," *Computers in Physics*, vol. 12, no. 6, 1998.

[128] P. L. Betts and I. H. Bokhari, "Experiments on turbulent natural convection in an enclosed tall cavity," *International Journal of Heat and Fluid Flow*, vol. 21, no. 6, pp. 675–683, 2000.

[129] H. Weller, "OpenFoam," 2016. [Online]. Available: https://www.openfoam.com/documentation/

[130] E. Robertson, V. Choudhury, S. Bhushan, and D. K. Walters, "Validation of OpenFOAM numerical methods and turbulence models for incompressible bluff body flows," *Computers and Fluids*, vol. 123, pp. 122–145, 2015. [Online]. Available: http://dx.doi.org/10.1016/j.compfluid.2015.09.010

[131] S. B. Lee, "A study on temporal accuracy of OpenFOAM," *International Journal of Naval Architecture and Ocean Engineering*, vol. 9, no. 4, pp. 429–438, 2017. [Online]. Available: http://dx.doi.org/10.1016/j.ijnaoe.2016.11.007

[132] M. J. Churchfield and N. R. E. L. (U.S.), *Wind Energy-related Atmospheric Boundary Layer Large-eddy Simulation Using OpenFOAM: Preprint*, ser. Conference paper. National Renewable Energy Laboratory, 2010. [Online]. Available: https://books.google.co.uk/books?id=UqM6tAEACAAJ

[133] E. De Villiers, "The Potential of Large Eddy Simulation for the Modeling of Wall Bounded Flows Eugene de Villiers," *Cycle*, 2006.

[134] H. Nilsson, "Experiences with OpenFOAM for water turbine applications," in *Proceedings of the 1st OpenFOAM International Conference*, 2007.

[135] S. Muntean, H. Nilsson, and R. Resiga, "3D Numerical Analysis of the Unsteady Turbulent Swirling Flow in a Conical Diffuser using FLUENT and OPENFOAM," in *3rd IAHR International Meeting Workgroup on Cavitation and Dynamic Problems in Hydraulic Machinery and Systems*, 2009.

[136] H. Jasak and M. Beaudoin, "OpenFOAM Turbo Tools: From General Purpose CFD to Turbomachinery Simulations," pp. 1801–1812, 2011. [Online]. Available: http://dx.doi.org/10.1115/AJK2011-05015

[137] Z. Shang, D. Emerson, and X.-J. Gu, "Numerical investigations of cavitation around a high speed submarine using OpenFOAM with LES," *International Journal of Computational Methods*, vol. 9, pp. 1–14, 2012.

[138] G. Campitelli, V. K. Krastev, W. W. Huebsch, and M. Gautam, "Two Dimensional Numerical Study of the Flow over a Bridge Deck with the Open Source CFD Tool OpenFOAM," in *43rd Fluid Dynamics Conference*, ser. Fluid Dynamics and Co-located Conferences. American Institute of Aeronautics and Astronautics, jun 2013. [Online]. Available: https://doi.org/10.2514/6.2013-3212

[139] L. Mangani, C. Bianchini, A. Andreini, and B. Facchini, "Development and validation of a C++ object oriented CFD code for heat transfer analysis," in *ASME Summer Heat Transfer*, vol. 2, 2007.

[140] A. Bansal, A. Feldick, and M. Modest, "Simulation of Hypersonic Flow and Radiation over a Mars Reentry Vehicle Using OpenFOAM," in *50th AIAA*

Aerospace Sciences Meeting Including the New Horizons Forum and Aerospace Exposition, 2012.

[141] V. Starikovičius, R. Čiegis, and A. Bugajev, "On Efficiency Analysis of the OpenFOAM-Based Parallel Solver for Simulation of Heat Transfer in and Around the Electrical Power Cables," *Informatica*, vol. 27, no. 1, pp. 161–178, 2016.

[142] N. Dongari, Y. Zhang, and J. M. Reese, "Molecular free path distribution in rarefied gases," *Journal of Physics D: Applied Physics*, vol. 44, no. 12, p. 125502, mar 2011. [Online]. Available: https://doi.org/10.1088{\%}2F0022-3727{\%}2F44{\%}2F12{\%}2F125502

[143] T. J. Scanlon, E. Roohi, C. White, M. Darbandi, and J. M. Reese, "An open source, parallel DSMC code for rarefied gas flows in arbitrary geometries," *Computers and Fluids*, vol. 39, no. 10, pp. 2078–2089, 2010. [Online]. Available: http://dx.doi.org/10.1016/j.compfluid.2010.07.014

[144] C. White, M. K. Borg, T. J. Scanlon, S. M. Longshaw, B. John, D. R. Emerson, and J. M. Reese, "dsmcFoam+: An OpenFOAM based direct simulation Monte Carlo solver," *Computer Physics Communications*, vol. 224, pp. 22–43, 2018. [Online]. Available: https://doi.org/10.1016/j.cpc.2017.09.030

[145] Z. Shang and S. Chen, "3D DSMC Simulation of Rarefied Gas Flows around a Space Crew Capsule Using OpenFOAM," *Open Journal of Applied Sciences*, vol. 03, no. 01, pp. 35–38, 2013. [Online]. Available: http://www.scirp.org/journal/doi.aspx?DOI=10.4236/ojapps.2013.31005

[146] C. Doolan, "Flow and Noise Simulation of the NASA Tandem Cylinder Experiment Using OpenFOAM," in *15th AIAA/CEAS Aeroacoustics Conference (30th AIAA Aeroacoustics Conference)*, ser. Aeroacoustics Conferences. American Institute of Aeronautics and Astronautics, may 2009. [Online]. Available: https://doi.org/10.2514/6.2009-3157

[147] O. Verhoeven, "Trailing Edge Noise Simulations using IDDES in OpenFOAM," Master Thesis, Delft University of Technology, 2011.

[148] F. Peng Kärrholm, F. Tao, and N. Nordin, "Three-dimensional simulation of diesel spray ignition and flame lift-off using openfoam and KIVA-3V CFD codes," *SAE Technical Papers*, 2008.

[149] J. H. Ferziger and M. Peric, *Computational Methods for Fluid Dynamics*, 3rd ed., 2002, vol. 91.

[150] F. Moukalled, L. Mangani, and M. Darwish, *The Finite Volume Method in Computational Fluid Dynamics*, 2016, vol. 113. [Online]. Available: http://link.springer.com/10.1007/978-3-319-16874-6

[151] D. E. Klett and R. K. Irey, "Experimental Determination of Thermal Accommodation Coefficients," in *Advances in Cryogenic Engineering*, K. D. Timmerhaus, Ed. Boston, MA: Springer US, 1969, pp. 217–223.

[152] J. Trieschmann, F. Schmidt, D. Krueger, R. P. Brinkmann, and T. Mussenbrock, "Validation And Verification Of A Kinetic Heavy Particle Transport Model," in *2017 IEEE International Conference on Plasma Science (ICOPS)*, may 2017, p. 1.

[153] E. Arlemark, G. Markelov, and S. Nedea, "Rebuilding of Rothe{\textquotesingle}s nozzle measurements with {OpenFOAM} software," *Journal of Physics: Conference Series*, vol. 362, p. 12040, may 2012. [Online]. Available: https://doi.org/10.1088{\%}2F1742-6596{\%}2F362{\%}2F1{\%}2F012040

[154] J. R. Howell, R. Siegel, and M. P. Mengüç, *Thermal Radiation Heat Transfer*, 2010.

[155] C. R. Roger, S. H. Yen, and K. G. Ramanathan, "Temperature variation of total hemispherical emissivity of stainless steel AISI 304," *Journal of the Optical Society of America*, vol. 69, no. 10, p. 1384, 1979. [Online]. Available: https://www.osapublishing.org/abstract.cfm?URI=josa-69-10-1384

[156] D. Fan, Q. Li, Y. Xuan, and P. Dai, "Variable emissivity property of magnetron sputtering thermochromic film," *Thin Solid Films*, vol. 570, no. PartA, pp. 123–128, 2014.

[157] H. Demiryont and D. Moorehead, "Electrochromic emissivity modulator for spacecraft thermal management," *Solar Energy Materials and Solar Cells*, vol. 93, no. 12, pp. 2075–2078, 2009. [Online]. Available: http://dx.doi.org/10.1016/j.solmat.2009.02.025

[158] R. J. Mortimer, D. R. Rosseinsky, and P. M. Monk, Eds., *Electrochromic Materials and Devices*. Wiley-VCH, 2015.

[159] H. O. Banks and K. K. Tang, "Thermoelectric temperature controller," 1971. [Online]. Available: http://www.google.ch/patents/US3561224

[160] Y.-X. Ji, M. Boman, G. A. Niklasson, and C.-G. Granqvist, "Thermochromics for Energy-Efficient Buildings: Thin Surface Coatings and Nanoparticle Composites," in *Nano and Biotech Based Materials for Energy Building Efficiency*, 1st ed., F. P. Torgal, C. Buratti, S. Kalaiselvam, C.-G. Graqvist, and V. Ivanov, Eds. Springer, 2016, ch. 4, pp. 71–92.

[161] Oerlikon Leybold Vacuum, "Turbolab Operating Instructions," Cologne, 2015.

[162] ——, "Turbovac Installation and Operating Instructions," Cologne, 2009.

[163] ——, "Technical Data PENNINGVAC PTR 90 N," 2016.

[164] RS Pro, "Datasheet Platinum Resistance Pt100 & Pt1000 Thin Film Detectors," 2017.

[165] Hukseflux Thermal Sensors B.V., "User Manual for HFP01 & HFP03," Delft, 2016.

[166] Omega Engineering Inc, "User's Guide KH, KHR, KHLV Series Kapton Flexible Heaters," 2017.

[167] Flow, "Mach700 Data Sheet," 2020. [Online]. Available: https://www.flowwaterjet.com/FlowWaterjet/media/Flow/8{_}Footer/Resources/Downloads/Brochures/Mach700/Flow{_}Mach700{_}DataSheet{_}EN.pdf

[168] G. A. George, G. A. Cash, and L. Rintoul, "Cure monitoring of aerospace epoxy resins and prepregs by fourier transform infrared emission spectroscopy," *Polymer International*, vol. 41, no. 2, pp. 169–182, 1996.

[169] D. A. Houtz and D. Gu, "A Measurement Technique for Infrared Emissivity of Epoxy-Based Microwave Absorbing Materials," *IEEE Geoscience and Remote Sensing Letters*, vol. 15, no. 1, pp. 48–52, jan 2018.

[170] R. P. Madding, "Emissivity measurement and temperature correction accuracy considerations," vol. 3700, pp. 393–401, 1999. [Online]. Available: http://proceedings.spiedigitallibrary.org/proceeding.aspx?articleid=987186

[171] NASA- National Aeronautics and Space Administration, "Outgassing Data for Selecting Spacecraft Materials," 2018. [Online]. Available: https://outgassing.nasa.gov/

[172] F. Siebers, P. Nass, G. Lautenschläger, and O. Becker, "Flat float Glass," pp. Patent, SCHOTT AG, US6 846 760 B2, 2005.

[173] G. M. Turner and R. E. Collins, "Measurement of heat flow through vacuum glazing at elevated temperature," *International Journal of Heat and Mass Transfer*, vol. 40, no. 6, pp. 1437–1446, 1997.

[174] T. Wentink and W. G. Planet, "Infrared Transmittance and Emittance of Polytetrafluoroethylene*," *Journal of the Optical Society of America*, vol. 51, no. 6, p. 601, 1961. [Online]. Available: https://www.osapublishing.org/abstract.cfm?URI=josa-51-6-601

[175] B. K. Tsai, D. W. Allen, L. M. Hanssen, B. Wilthan, and J. Zeng, "A Comparison of Optical Properties between High Density and Low Density Sintered PTFE," *Proceedings of SPIE Vol. 7065*, vol. 7065, pp. 1–9, 2008.

[176] C.-d. Wen and I. Mudawar, "Experimental Investigation of Emissivity of Aluminum Alloys and Temperature Determination Using," *Journal of Materials Engineering and Performance*, vol. 11, no. October, pp. 551–562, 2002.

[177] C. Y. Ho, R. W. Powell, and P. E. Liley, "Thermal Conductivity of the Elements," *Journal of Physical and Chemical Reference Data*, vol. 1, no. 2, pp. 279–421, 1972. [Online]. Available: https://doi.org/10.1063/1.3253100

[178] American Society for Metals. Metals Handbook Committee, *Metals handbook. Volume 2, Properties and selection : nonferrous alloys and pure metals*, 9th ed. Metals Park, Ohio : American Society for Metals, 1979.

[179] J. N. Sweet, E. P. Roth, and M. Moss, "Thermal conductivity of Inconel 718 and 304 stainless steel," *International Journal of Thermophysics*, vol. 8, no. 5, pp. 593–606, sep 1987. [Online]. Available: https://doi.org/10.1007/BF00503645

[180] R. S. Graves, T. G. Kollie, D. L. McElroy, and K. E. Gilchrist, "The thermal conductivity of AISI 304L stainless steel," *International Journal of Thermophysics*, vol. 12, no. 2, pp. 409–415, mar 1991. [Online]. Available: https://doi.org/10.1007/BF00500761

[181] F. Boeschoten and E. F. M. V. D. Held, "The thermal conductance of contacts between aluminium and other metals," *Physica*, vol. 23, no. 1, pp. 37–44, 1957. [Online]. Available: http://www.sciencedirect.com/science/article/pii/S0031891457902367

[182] R. C. Getty and R. E. Tatro, "Spacecraft thermal joint conduction," in *AIAA Thermophysics Specialist Conference*, no. 67, New Orleans, Louisiana, 1967. [Online]. Available: http://dx.doi.org/10.2514/6.1967-316

[183] K. Nishino, S. Yamashita, and K. Torii, "Thermal contact conductance under low applied load in a vacuum environment," *Experimental Thermal and Fluid Science*, vol. 10, no. 2, pp. 258–271, 1995.

[184] Y. Xiao, H. Sun, L. Xu, H. Feng, and H. Zhu, "Thermal contact conductance between solid interfaces under low temperature and vacuum," *Review of Scientific Instruments*, vol. 75, no. 9, pp. 3074–3076, 2004. [Online]. Available: https://doi.org/10.1063/1.1786356

[185] B. Snaith, P. W. O'Callaghan, and S. D. Probert, "Interstitial materials for controlling thermal conductances across pressed metallic contacts," *Applied Energy*, vol. 16, no. 3, pp. 175–191, 1984.

[186] U. C. Okonkwo, I. P. Okokpujie, J. E. Sinebe, and C. A. Ezugwu, "Comparative analysis of aluminium surface roughness in end-milling under dry and minimum quantity lubrication (MQL) conditions," *Manufacturing Review*, vol. 2, p. 30, 2015. [Online]. Available: http://mfr.edp-open.org/10.1051/mfreview/2015033

[187] A. Clausing and B. Chao, "Thermal contact resistance in a vacuum environment," *Journal of heat transfer*, pp. 243–250, 1965. [Online]. Available: http://heattransfer.asmedigitalcollection.asme.org/article.aspx?articleid=1433491

[188] ECSS Secretariat ESA-ESTEC, "Thermal design handbook - Part 4: Conductive Heat Transfer ECSS-E-HB-31-01 Part 4A," *European Cooperation for Space Standarization*, no. December, 2011.

[189] M. Klein, "ECSS-E-30 Mechanical Engineering Standard," *ESA bulletin. Bulletin ASE. European Space Agency*, p. 458, 2000. [Online]. Available: http://www.worldscientific.com/doi/abs/10.1142/9781860944574{_}0014

[190] K. Johnson, *Contact Mechanics*. Cambridge University Press, 1987.

[191] British Standards Institute, *UK National Annex for Eurocode. Basis of Structural Design*. B S I Standards, 2004. [Online]. Available: https://books.google.co.uk/books?id=G{_}l3PgAACAAJ

[192] Z. Ren, A. H. Heuer, and F. Ernst, "Ultrahigh-strength AISI-316 austenitic stainless steel foils through concentrated interstitial carbon," *Acta Materialia*, vol. 167, pp. 231–240, 2019. [Online]. Available: https://doi.org/10.1016/j.actamat.2019.01.018

[193] F. Arpino, G. Buonanno, and G. Giovinco, "Thermal conductance measurement of windows: An innovative radiative method," *Experimental Thermal and Fluid Science*, vol. 32, no. 8, pp. 1731–1739, 2008.

[194] The European Parliament and the Council of the Euorpean Union, "Regulation (EU) No 305/2011 of The European Parliament and of the Council," 2011. [Online]. Available: http://eur-lex.europa.eu/LexUriServ/LexUriServ.do?uri=OJ:L:2011:088:0005:0043:EN:PDF

[195] T. Holzmann, *Mathematics, Numerica, Derivations and OpenFOAM*, 2018.

[196] H. Jasak, "Error Analysis and Estimation for the Finite Volume Method with Applications to Fluid Flows," Ph.D. dissertation, Imperial College, University of London, 1996. [Online]. Available: http://citeseerx.ist.psu.edu/viewdoc/summary?doi=10.1.1.709.1639

[197] S. Pajunen, T. Välikangas, J. Baczkiewicz, S. Singh, and K. Sørensen, "Effect of natural convection and radiation inside of a hollow beam in a standard fire," 2017, pp. 121–127.

Appendices

Appendix A

DSMC Solver equations

The basic quantities considered in the molecular model are the number of molecules per unit volume and the mass, size, velocity and internal state of each molecule. These quantities are related to the distance and collision frequency to establish the effects of the collision-less interaction [46]. The number of molecules per unit volume, n_v, is independent of the composition of the gas but depends on temperature and pressure and is termed RhoN in dsmcFoam.

$$n_v = \frac{N_A p}{RT} = RhoN \tag{A.1}$$

Where N_A is Avogadro's number, p is pressure (Pa), R is the Ideal Gas Constant, and T is temperature (K). The number of simulated particles, N_S, representing a larger number of real particles is determined by the dsmcFoam variable, $nEquivalentParticles$, where V stands for the volume (m^3):

$$N_S = \frac{V * RhoN}{nEquivalentParticles} \tag{A.2}$$

The dimension of the molecule, regardless of its atomic composition, is calculated as a sphere. The Variable Hard Sphere method, VHS, employed in the simulation model relates the dimensions of the theoretic sphere to the coefficient of viscosity with temperature, accounting for accurate relative translational energy in the calculated collision cross-section. According to the Boltzmann equation the number of particles in the phase space element $dcdr$, dN, is defined as a function of position $r(x, y, z)$ and velocity $c(u, v, w)$ in orthonormal Cartesian coordinates, were Γ is the single molecule distribution function.

$$dN = \Gamma(c, r, t)dcdr \tag{A.3}$$

The number of molecules in the phase space element, dN, is related to the single molecule distribution function Γ, and the number of molecules in the phase space element dr , N, by:

$$dN = Nf(c)dc = \Gamma(c, r, t)dcdr \tag{A.4}$$

Where $f(c)$ is the distribution function in velocity space applied to the physical space element dr. Consequently, the number density, n, in the phase space element is defined as follows. It should be noted number density is defined as $nEquivalentParticles$ in dsmcFoam.

$$n = \frac{N}{dr} \tag{A.5}$$

$$nf(c) = \Gamma(c, r, t) \tag{A.6}$$

For a mono-atomic gas with binary collisions, where at most two particles will collide, the gas flow is described by the Boltzmann equation, according to position and velocity vectors [46]:

$$\frac{\partial}{\partial t}(nf) + c\frac{\partial}{\partial r}(nf) + F\frac{\partial}{\partial c}(nf) = \int_{-\infty}^{+\infty}\int_{0}^{4\pi} n^2(f^* f_1^* - f f_1)c_r \sigma d\Omega \, dc_1 \qquad \text{(A.7)}$$

Where d is the particle diameter, Ω is the solid angle, σ is the collision cross section, F is an external force, c_r is the relative velocity between colliding particles, f^* and f_1^* are the distribution functions of the particles post collision just as f is the value of the distribution function at c. This equation is a conservation equation describing a) the influx of particles due to velocity, b) the influx of particles due to an external force and c) the rate of increase of particles due to collisions.

Appendix B

Multiregion Solver equations

As with any physical process, conservation has to be respected to maintain accurate physical behavior, it is from these continuity principles that momentum, energy, enthalpy and other similar equations are derived. Following these principles the general conservation equation for an arbitrary quantity (ϕ) can be defined as [195]:

$$\frac{\partial}{\partial t}\rho\phi = -\nabla \cdot (\rho U \phi) + \nabla \cdot (D \nabla \rho) + S_\phi \tag{B.1}$$

Where D stands for the diffusion coefficient, ρ is density, U is velocity and S stands for any kind of source or sink terms influencing the quantity ϕ. Left of the equation, the first term refers to time accumulation of any given quantity, ϕ, the second term refers to the convective transport, the third term refers to diffusive transport and the final term refers to sources or sinks.

Using the previous general equation the mass conservation is derived by replacing ϕ with 1. Moreover, since mass is neither transferred by diffusion, nor transformed into energy or vice versa, the respective terms are eliminated. Finally, for incom-

pressible fluid flow, density is assumed constant and the quantity rho is taking out of the equation, resulting in the Navier-Stokes equation for incompressible fluid flow expressed as [195]:

$$\nabla \cdot \vec{U} = 0 \tag{B.2}$$

$$\frac{\partial}{\partial t} + \nabla \cdot (\vec{U}\vec{U}) = -\nabla p + v\nabla^2 \vec{U} \tag{B.3}$$

Where $\vec{U}$ is the velocity vector, p is the density-normalized or kinematic pressure and v is the kinematic viscosity.

When equation B.3 is discretized over a finite volume it is re-written as:

$$\int_V \frac{\partial \vec{U}}{\partial t}\, dV + \int_S \vec{U}\vec{U} \cdot\, d\vec{S} + \int_V \nabla p\, dV - v \int_S \nabla \vec{U} \cdot\, d\vec{S} = 0 \tag{B.4}$$

Where $d\vec{S}$ is the outward differential of the surface area vector. The non-linearity of the term $\vec{U}\vec{U}$, which would require non-linear solving at a high computational cost, is linearized by introducing flux (F) variable through each face (f), that satisfies the continuity equation B.2. In transient flows with large time-steps iteration over non-linear terms will be computationally expensive; hence smaller time-steps are preferred [196]. The linearized version of equation B.4 is expressed as [131]:

$$\frac{\partial \vec{U}}{\partial t} V_p + \sum_f F\vec{U}_f + \int_V \nabla p\, dV - v \sum_f \vec{S} \cdot \nabla_f \vec{U} = 0 \tag{B.5}$$

This previous moment conservation equation couples pressure-velocity in a system of linear equations that can be solved for steady or unsteady problems. However, as has been mentioned previously, for rarefied gases, the rate of intermolecular colli-

sions is small enough that gradients in the macroscopic properties of the fluid cannot be maintained and solving the previous equation produces invalid results [46]. Consequently, the transport implications of the rarefied gas are solved with molecular simulations, and when solving the Navier-Stokes equation during chtMultiRegionFoam simulations, the moment equations for the fluid are not solved by specifying a "frozenFlow" variable in the dictionaries and only the energy equation is solved, either by solving for enthalpy or internal energy. In this project the energy source chosen is enthalpy. Considering a frozen flow that will not update pressure or velocity in the system, only the internal energy component in enthalpy is of consequence. This problem doesn't include any internal energy sources rendering thermal energy as the only form of energy considered. I.e. This simulation is setup to only calculate thermal energy through the fluid, and according to a fixed thermal conductivity, neglecting changes in other fluid properties since the rarefied gas would only transfer energy by gas conduction and radiation.

The conserved enthalpy equation is derived from the conservation of energy equation. The total energy of the fluid is the sum of internal energy, e, and kinetic energy, K. The rate of change of kinetic energy refers to work done by viscous dissipation, pressure and external forces. Looking at the conservation of energy the terms DK/Dt, $\nabla \cdot (\sigma \cdot U), (\rho \cdot g) \cdot U$, can be identified as mechanical energy terms.

$$\rho \frac{De}{Dt} + \rho \frac{DK}{Dt} = -\nabla \cdot (q) + \rho r + \nabla \cdot (\sigma \cdot U) + \rho g \cdot U \tag{B.6}$$

If mechanical energy is neglected, the internal energy of the fluid can be expressed as:

$$\rho \frac{De}{Dt} = -\nabla \cdot (q) + \rho r + Rad \tag{B.7}$$

Also expressed in terms of local derivatives:

$$\frac{\partial(\rho e)}{\partial t} + \nabla \cdot (\rho U e) = -\nabla \cdot (q) + \rho r + Rad \tag{B.8}$$

From equation B.8, found in the source code EEqn.H, the rate of change of internal energy can be identified that as the heat transferred to the element by diffusion, $-\nabla \cdot (q)$, plus the source term, ρr, plus radiation. Since solving for enthalpy is pursued, the previous equation is rewritten, considering enthalpy (h) is defined as the sum of internal energy and kinematic pressure:

$$h = e + \frac{p}{\rho} \tag{B.9}$$

Replacing the diffusion term, $-\nabla \cdot (q)$, by Fouriers' Law [29], $q = -k\nabla T$, in equation B.7 and eliminating source terms we arrive at the enthalpy equation employed in the simulation. It should be noted that the term $\frac{D}{Dt}$ expressed as local derivative equals $\frac{\partial}{\partial t} + \nabla \cdot U$ [195].

$$\frac{\partial}{\partial t}\rho h = -\nabla \cdot (\rho U h) + \nabla \cdot (k \nabla T) + Rad \tag{B.10}$$

To derive the temperature equation, the relation to enthalpy is established as:

$$C_p = \frac{\partial h}{\partial T} \tag{B.11}$$

Where C_p is the specific heat capacity at constant pressure. Assuming constant

heat capacity and pressure the energy equation for the fluid expressed in terms of temperature is then expressed as:

$$C_p \frac{\partial}{\partial t} \rho T = -C_p \nabla \cdot (\rho U T) + \nabla \cdot (k \nabla T) + Rad \tag{B.12}$$

The radiative heat transfer can be calculated by several radiation methods; this project employs the View Factor method. Details on calculating a surface's view factor will not be discussed but can be found in [154]. The radiation model relies on the statement that the sum of view factors from a given surface must amount to unity:

$$\sum_{n=1}^{i} F_{S_i} \rightarrow F_{S_j} = 1 \tag{B.13}$$

Previous to the actual calculation an agglomeration procedure is conducted to save on computational resources. During this process, adjacent planar cells are embedded together and their view factors are assumed equal. The matrix system of equation B.13 becomes [197]:

$$Q_{rad} = C^{-1} b \tag{B.14}$$

Where C calculates the ratio between reflection and absorption, and b is the emissivity matrix:

$$b = A e_b - H_0 \tag{B.15}$$

Where A represents the agglomerated view factor matrix, e_b is the blackbody emissivity and H_0 are external radiation sources [197].

In addition to the energy of the fluid(s), the solid regions are also considered in the simulations and only their energy equation needs solving. Their energy equation states that the temporal variation of enthalpy is equal to the divergence of heat conducted through the solid:

$$\frac{\partial(ph)}{\partial t} = \nabla \cdot (\alpha \cdot \nabla h) \tag{B.16}$$

Where α is the thermal diffusivity defined as the ratio between thermal conductivity, k, and the specific heat capacity $Cp; \alpha = \frac{k}{C_p}$. Consequently, the temperature distribution within the solid is found by the relation between enthalpy and temperature described in equation B.11.

Seeing as how the solid and fluid regions are calculated using different equations, there needs to be a coupling mechanism relating both regions at the interface. The coupling between the solid and fluid regions is built around the axiom stating that temperature, T, at the interface is equal for both regions:

$$T_f = T_s \tag{B.17}$$

Moreover, this statement can be extended to say that the heat flux entering one region has to be equal to the heat flux leaving the opposing region:

$$Q_f + Q_{rad_f} = -Q_s - Q_{rad_s} \tag{B.18}$$

Appendix C

Determination of Thermal Emissivity

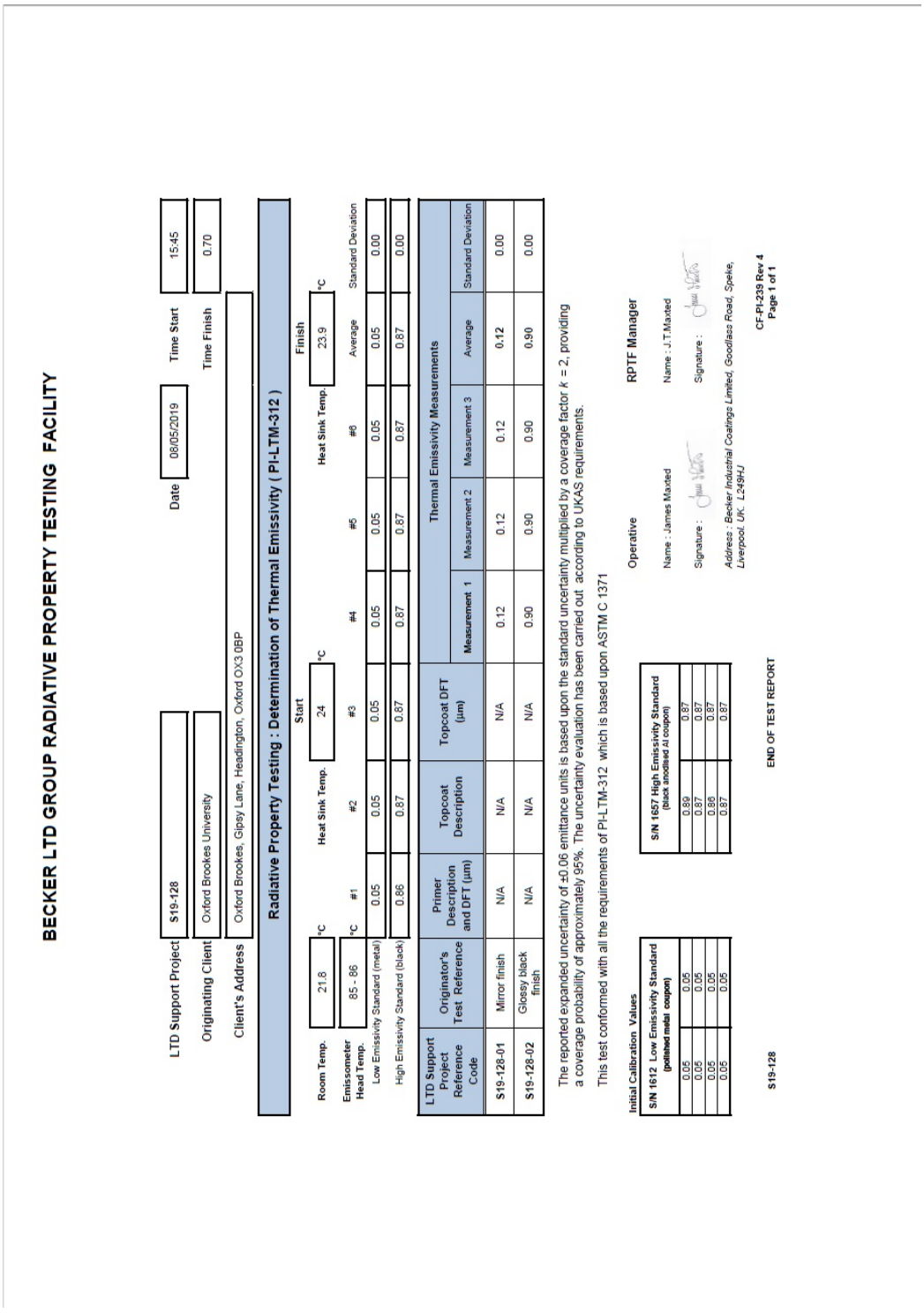

BECKER LTD GROUP RADIATIVE PROPERTY TESTING FACILITY

LTD Support Project: S19-128 | Date: 08/05/2019 | Time Start: 15:45

Originating Client: Oxford Brookes University | Time Finish: 0.70

Client's Address: Oxford Brookes, Gipsy Lane, Headington, Oxford OX3 0BP

Radiative Property Testing : Determination of Thermal Emissivity (PI-LTM-312)

			Start						Finish		
Room Temp.	21.8	°C	Heat Sink Temp.	24	°C			Heat Sink Temp.	23.9	°C	
Emissometer Head Temp.	85 - 86	°C	#1	#2	#3	#4	#5	#6	Average	Standard Deviation	
Low Emissivity Standard (metal)			0.05	0.05	0.05	0.05	0.05	0.05	0.05	0.00	
High Emissivity Standard (black)			0.86	0.87	0.87	0.87	0.87	0.87	0.87	0.00	

LTD Support Project Reference Code	Originator's Test Reference	Primer Description and DFT (µm)	Topcoat Description	Topcoat DFT (µm)	Thermal Emissivity Measurements				
					Measurement 1	Measurement 2	Measurement 3	Average	Standard Deviation
S19-128-01	Mirror finish	N/A	N/A	N/A	0.12	0.12	0.12	**0.12**	0.00
S19-128-02	Glossy black finish	N/A	N/A	N/A	0.90	0.90	0.90	**0.90**	0.00

The reported expanded uncertainty of ±0.06 emittance units is based upon the standard uncertainty multiplied by a coverage factor $k = 2$, providing a coverage probability of approximately 95%. The uncertainty evaluation has been carried out according to UKAS requirements.

This test conformed with all the requirements of PI-LTM-312 which is based upon ASTM C 1371

Initial Calibration Values

S/N 1612 Low Emissivity Standard (polished metal coupon)	
0.05	0.05
0.05	0.06
0.05	0.05
0.05	0.05

S/N 1657 High Emissivity Standard (black anodised Al coupon)	
0.89	0.87
0.87	0.87
0.86	0.87
0.87	0.87

Operative

Name : James Mawted

Signature :

Address : Becker Industrial Coatings Limited, Goodlass Road, Speke, Liverpool. UK. L249HJ

RPTF Manager

Name : J.T.Mawted

Signature :

S19-128

END OF TEST REPORT

CF-PI-239 Rev 4
Page 1 of 1

Figure C.1: Determination of thermal emissivity

Appendix D

Empiric Measurements

Table D.1: Empiric measurement results with uncertainty range. Heat Flux Q'' and and Temperatures T values are averaged after the hot plate reached stability. Subscripts $U\pm$ indicate the uncertainty adjusted value. Resistance values R are calculated as the ratio between ΔT and heat flux Q''.

		Center Sensor												**Corner Sensor**									
		Q''_{U-} $\frac{W}{m^2}$	Q" $\frac{W}{m^2}$	Q''_{U+} $\frac{W}{m^2}$	$T_{C_{U-}}$ °C	T_C °C	$T_{C_{U+}}$ °C	$T_{H_{U-}}$ °C	T_H °C	$T_{H_{U+}}$ °C	R_{U-} $\frac{m^2K}{W}$	R $\frac{m^2K}{W}$	R_{U+} $\frac{m^2K}{W}$	Q''_{U-} $\frac{W}{m^2}$	Q" $\frac{W}{m^2}$	Q''_{U+} $\frac{W}{m^2}$	$T_{C_{U-}}$ °C	T_C °C	$T_{C_{U+}}$ °C	$T_{H_{U-}}$ °C	T_H °C	$T_{H_{U+}}$ °C	R_{U-} $\frac{m^2K}{W}$	R $\frac{m^2K}{W}$	R_{U+} $\frac{m^2K}{W}$
25 mm	Low E Box	3.55	3.94	4.33	26.54	26.79	27.04	40.83	41.08	41.33	3.18	3.63	4.10	21.75	24.17	26.59	26.60	26.85	27.10	40.59	40.84	41.09	0.51	0.58	0.65
	HighE Box	39.16	43.51	47.87	30.82	31.07	31.32	40.49	40.74	40.99	0.19	0.22	0.25	50.50	56.11	61.72	30.70	30.95	31.20	40.25	40.50	40.75	0.15	0.17	0.19
	Low E Cross	32.46	36.07	39.67	27.95	28.20	28.45	40.77	41.02	41.27	0.31	0.36	0.40	5.99	6.65	7.32	27.98	28.23	28.48	43.21	43.46	43.71	2.01	2.29	2.59
	HighE Cross	43.72	48.58	53.44	29.55	29.80	30.05	40.33	40.58	40.83	0.19	0.22	0.25	37.29	41.44	45.58	29.44	29.69	29.94	40.11	40.36	40.61	0.22	0.26	0.29
	Low E Box-Cross	35.60	39.56	43.52	26.80	27.05	27.30	40.78	41.03	41.28	0.31	0.35	0.40	18.98	21.09	23.20	26.84	27.09	27.34	40.44	40.69	40.94	0.56	0.64	0.73
	HighE Box-Cross	45.74	50.82	55.90	29.68	29.93	30.18	40.45	40.70	40.95	0.18	0.21	0.24	38.92	43.25	47.57	29.52	29.77	30.02	40.25	40.50	40.75	0.22	0.25	0.28
50mm	Low E Box	3.83	4.26	4.69	20.36	20.61	20.86	40.60	40.85	41.10	4.21	4.75	5.34	22.96	25.51	28.06	20.37	20.62	20.87	40.13	40.38	40.63	0.69	0.77	0.87
	HighE Box	39.44	43.82	48.20	30.31	30.56	30.81	40.30	40.55	40.80	0.20	0.23	0.26	39.42	43.80	48.19	30.20	30.45	30.70	40.00	40.25	40.50	0.19	0.22	0.25
	Low E Cross	22.16	24.62	27.08	21.39	21.64	21.89	40.18	40.43	40.68	0.68	0.76	0.86	6.00	6.67	7.33	21.38	21.63	21.88	39.80	40.05	40.30	2.44	2.76	3.11
	HighE Cross	31.77	35.30	38.82	29.66	29.91	30.16	40.28	40.53	40.78	0.26	0.30	0.34	28.79	31.98	35.18	29.62	29.87	30.12	40.05	40.30	40.55	0.28	0.33	0.37
	Low E Box-Cross	24.50	27.22	29.95	27.85	28.10	28.35	40.80	41.05	41.30	0.42	0.48	0.54	12.56	13.96	15.36	27.89	28.14	28.39	40.43	40.68	40.93	0.78	0.90	1.02
	HighE Box-Cross	34.77	38.63	42.49	29.15	29.40	29.65	40.25	40.50	40.75	0.25	0.29	0.33	42.13	46.81	51.49	29.07	29.32	29.57	40.28	40.53	40.78	0.21	0.24	0.27

Appendix E

Uncertainty Results

Table E.1: Uncertainty analysis results for 25mm thickness configurations. Simulations conducted with OpenFoam's chtMultiRegionSimple solver. Abbrevations : GI - grease interface, MI - metallic interface, SPI - PTFE interface, AC- Aluminium conductivity, SC- Steel conductivity, PC- PTFE conductivity, AE- Aluminium emissivity, SE- Steel emissivity, RE- resin emissivity

Case	**Variable**	**Center HF [W/m2]**			**Corner HF [W/m2]**		
		U-	Nominal	U+	U-	Nominal	U+
Box Low E	GI	0.14	4.67	0.01	-11.41	36.30	5.60
	MI	0.04		-0.05	0.08		-0.09
	SPI	0.18		-0.07	-16.86		6.32
	AC	-0.01		0.01	-0.04		0.03
	SC	0.01		0.00	0.94		-0.86
	PC	0.02		-0.02	-2.24		2.12
	AE	0.07		-0.07	0.09		-0.10
	SE	-1.29		1.32	-0.99		0.99
	RE	0.00		0.00	0.00		0.00
	SUM %	**28.11%**		**28.37%**	**56.55%**		**24.26%**

continues on next page

Box High E	GI	-11.22	67.74	2.69	-15.85	74.51	5.79
	MI	0.01		-0.01	0.00		0.00
	SPI	0.11		-0.06	-18.41		7.56
	AC	-0.22		0.18	-0.10		0.08
	SC	0.07		-0.07	0.43		-0.39
	PC	0.02		-0.02	-1.81		1.72
	AE	0.07		-0.07	0.17		-0.18
	SE	0.00		0.00	0.00		0.00
	RE	-9.87		10.92	-4.20		4.46
	SUM %	**22.06%**		**16.61%**	**33.18%**		**14.31%**
Cross Low E	GI	-11.22	32.51	6.44	-0.15	5.38	0.14
	MI	0.08		-0.09	0.12		-0.13
	SPI	-17.13		7.40	0.09		-0.04
	AC	-0.05		0.04	-0.01		0.01
	SC	1.09		-0.98	0.03		-0.03
	PC	-1.07		1.02	0.01		0.00
	AE	0.07		-0.07	0.07		-0.07
	SE	-0.85		0.86	-1.46		1.48
	RE	0.00		0.00	0.00		0.00
	SUM %	**63.22%**		**30.60%**	**27.46%**		**27.78%**
Cross High E	GI	-11.99	65.75	4.52	-8.54	61.25	2.10
	MI	0.01		-0.01	0.00		0.00
	SPI	-13.65		6.11	0.06		-0.03
	AC	-0.22		0.18	-0.07		0.06
	SC	0.40		-0.35	-0.04		0.04
	PC	-1.05		1.00	0.01		-0.01
	AE	0.08		-0.08	-0.37		0.38
	SE	0.00		0.00	0.00		0.00
	RE	-4.41		4.70	-7.17		7.54
	SUM %	**28.49%**		**13.69%**	**18.22%**		**12.79%**
Box-Cross Low E	GI	-10.95	32.19	6.35	-13.73	42.60	6.71
	MI	0.00		0.01	-0.01		0.01

continues on next page

	SPI	-16.80		7.24	-21.77		8.70
	AC	-0.04		0.03	-0.03		0.03
	SC	1.08		-0.97	1.08		-1.00
	PC	-1.07		1.01	-1.88		1.79
	AE	0.06		-0.06	0.08		-0.09
	SE	-0.87		0.87	-0.82		0.83
	RE	0.00		0.00	0.00		0.00
	SUM %	**62.53%**		**30.35%**	**60.66%**		**26.31%**
	GI	-11.75		4.24	-15.57		5.57
	MI	0.02		-0.02	0.02		-0.02
	SPI	-13.38		5.98	-18.22		7.49
	AC	-0.21		0.17	-0.10		0.08
	SC	0.36	65.37	-0.31	0.41	74.12	-0.37
Box-Cross High E	PC	-1.04		0.99	-1.81		1.73
	AE	0.07		-0.07	0.18		-0.19
	SE	0.00		0.00	0.00		0.00
	RE	-4.42		4.71	-4.16		4.42
	SUM %	**28.12%**		**13.43%**	**32.91%**		**14.14%**

GI - grease interface, MI - metallic interface, SPI - PTFE interface, AC- Aluminium conductivity, SC- Steel conductivity, PC- PTFE conductivity, AE- Aluminium emissivity, SE- Steel emissivity, RE- resin emissivity

Table E.2: Uncertainty analysis results for 50mm thickness configurations. Simulations conducted with OpenFoam's chtMultiRegionSimple solver. Abbrevations : GI - grease interface, MI - metallic interface, SPI - PTFE interface, AC- Aluminium conductivity, SC- Steel conductivity, PC- PTFE conductivity, AE- Aluminium emissivity, SE- Steel emissivity, RE- resin emissivity

Case	**Variable**	**Center HF [W/m2]**			**Corner HF [W/m2]**		
		U-	Nominal	U+	U-	Nominal	U+
	MI	0.08		-0.09	0.14		-0.16
	SPI	-15.82		8.03	-19.61		9.41
	AC	-0.04		0.03	-0.04		0.03
	SC	1.02		-0.91	0.98		-0.90

continues on next page

	PC	-0.63		0.61	-1.09		1.06
	AE	0.06		-0.07	0.19		-0.20
	SE	-0.74		0.74	-0.70		0.70
	RE	0.00		0.00	0.00		0.00
	SUM %	**61.78%**		**32.87%**	**59.92%**		**29.10%**
	GI	-9.10		3.37	-12.25		4.44
	MI	0.02		-0.02	0.02		-0.02
	SPI	-11.30		6.18	-15.26		7.72
	AC	-0.17		0.14	-0.07		0.06
	SC	0.29	57.05	-0.25	0.33	64.06	-0.29
Box-Cross High E	PC	-0.62		0.60	-1.08		1.05
	AE	0.06		-0.06	0.29		-0.30
	SE	0.00		0.00	0.00		0.00
	RE	-3.28		3.42	3.13		3.26
	SUM %	**26.10%**		**13.77%**	**30.99%**		**14.91%**

GI - grease interface, MI - metallic interface, SPI - PTFE interface, AC- Aluminium conductivity, SC- Steel conductivity, PC- PTFE conductivity, AE- Aluminium emissivity, SE- Steel emissivity, RE- resin emissivity

Appendix F

Transient Results

Table F.1: Transient simulation results with uncertainty range. Values are averaged after resistance R has reached stability. Subscripts $U\pm$ indicate the uncertainty adjusted value. Resistance values R are calculated as the ratio between ΔT and heat flux Q''. Center and Corner area are approximated in size and position to the sensors used in empirical measurements.

		Center Area										**Corner Area**									
		Q''_{U-} $\frac{W}{m^2}$	U- %	Q" $\frac{W}{m^2}$	U+ %	Q''_{U+} $\frac{W}{m^2}$	T_C °C	T_H °C	R_{U-} $\frac{m^2K}{W}$	R $\frac{m^2K}{W}$	R_{U+} $\frac{m^2K}{W}$	Q''_{U-} $\frac{W}{m^2}$	U- %	Q" $\frac{W}{m^2}$	U+ %	Q''_{U+} $\frac{W}{m^2}$	T_C °C	T_H °C	R_{U-} $\frac{m^2K}{W}$	R $\frac{m^2K}{W}$	R_{U+} $\frac{m^2K}{W}$
25 mm	Low E Box	2.34	28.11	3.26	28.37	4.18	27.14	41.00	3.32	4.26	5.92	11.12	56.55	25.59	24.26	31.80	27.13	41.00	0.44	0.54	1.25
	HighE Box	35.45	22.06	45.48	16.61	53.03	29.96	41.00	0.21	0.24	0.31	31.44	31.18	45.69	14.31	52.22	29.99	41.00	0.21	0.24	0.35
	Low E Cross	10.76	63.22	29.26	30.60	38.21	27.91	41.00	0.34	0.45	1.22	3.46	27.46	4.78	27.78	6.10	27.90	41.00	2.15	2.74	3.78
	HighE Cross	28.70	28.49	40.13	13.69	45.63	30.21	41.00	0.24	0.27	0.38	32.55	18.22	39.81	12.79	44.90	30.13	41.00	0.24	0.27	0.33
	Low E Box-Cross	8.57	62.53	22.87	30.35	29.81	27.07	41.00	0.47	0.61	1.63	6.82	60.66	17.34	26.31	21.91	27.04	41.00	0.64	0.80	2.05
	HighE Box-Cross	28.23	28.12	39.27	13.43	44.54	30.39	41.00	0.24	0.27	0.38	27.10	32.91	40.39	14.14	46.10	30.33	41.00	0.23	0.26	0.39
50mm	Low E Box	3.32	27.76	4.59	28.06	5.88	21.53	41.00	3.31	4.24	5.87	9.54	60.00	23.86	29.17	30.82	21.23	41.00	0.64	0.83	2.07
	HighE Box	36.77	21.47	46.82	15.88	54.26	29.41	41.00	0.21	0.25	0.32	26.29	31.35	38.29	15.26	44.14	29.31	41.00	0.26	0.31	0.44
	Low E Cross	13.98	61.71	36.52	32.66	48.45	21.20	41.00	0.41	0.54	1.42	5.06	26.38	6.87	26.56	8.69	21.18	41.00	2.28	2.89	3.92
	HighE Cross	25.06	26.26	33.98	14.07	38.76	29.98	41.00	0.28	0.32	0.44	30.42	17.18	36.73	12.03	41.15	30.11	41.00	0.26	0.30	0.36
	Low E Box-Cross	7.03	61.78	18.40	32.87	24.44	27.73	41.00	0.54	0.72	1.89	5.50	59.92	13.72	29.10	17.72	27.78	41.00	0.75	0.96	2.40
	HighE Box-Cross	25.83	26.10	34.95	13.77	39.76	29.48	41.00	0.29	0.33	0.45	25.63	30.99	37.13	14.91	42.67	29.37	41.00	0.27	0.31	0.45